

Computational aspects of parvalbumin positive interneuron function

Jonathan Cornford

A dissertation submitted in partial fulfilment of the requirements for
the degree of Doctor of Philosophy

University College London

July 2017

Declaration

I, Jonathan Cornford, confirm that the work presented in this thesis is my own. Where information has been derived from other sources, I confirm that this has been indicated in the thesis.

Jonathan Cornford

July 2017

Abstract

The activity of neurons is dependent on the manner in which they process synaptic inputs from other cells. In the event of clustered synaptic input, neurons can respond in a nonlinear manner through synaptic and dendritic mechanisms. Such mechanisms are well established in principal excitatory neurons throughout the brain, where they increase neuronal computational ability and information storage capacity. In contrast for parvalbumin-positive (PV^+) interneurons, the most common cortical class of inhibitory interneuron, synaptic integration is thought to be either linear or sub-linear in nature, facilitating their role as mediators of precise and fast inhibition.

This thesis addresses situations in which PV^+ interneurons integrate synaptic inputs in a nonlinear manner, and explores the functions of this synaptic processing. First, I describe a form of cooperative supralinear synaptic integration by local excitatory inputs onto PV^+ interneurons, and I extend these results to show how this augments the computational capability of PV^+ cells within spiking neuron networks. I also explore the importance of polyamine-modulation of synaptic receptors in mediating sublinear synaptic integration, and discuss how this expands the array of mechanisms known to perform similar functions in PV^+ cells. Finally, I present work manipulating PV^+ cells experimentally during epilepsy. I consider these findings together with recent scientific advances and suggest how they account for a number of open questions and previously contradictory theories of PV^+ interneuron function.

Contents

1	Introduction	13
1.1	Synaptic input and integration	13
1.1.1	Synaptic input location	14
1.1.2	Synaptic clustering	16
1.1.3	Inhibition - excitation interaction	19
1.1.4	Active conductances in dendrites	20
1.2	PV ⁺ Interneurons	22
1.2.1	Morphology and connectivity	22
1.2.2	Passive properties	25
1.2.3	Active properties	27
1.2.4	Synaptic receptor expression	30
1.3	PV ⁺ interneuron network function	33
1.3.1	Feedforward inhibition	33
1.3.2	Feedback inhibition	36
1.4	PV ⁺ interneurons and pathology	38
1.4.1	Epilepsy	38
1.4.2	Schizophrenia	39
1.5	Thesis Overview	40
1.6	Acknowledgement of contributions	41
2	Methods	42
2.1	Electrophysiology	42
2.1.1	Mouse lines	42
2.1.2	Slice Preparation and electrophysiological recording	43
2.1.3	Two-Photon Imaging and Uncaging	44
2.1.4	Pharmacological dissection of NMDA receptor conductance	47
2.1.5	Data Analysis and Statistics	48
2.2	Multi-Compartmental modelling	49

2.2.1	Hippocampal CA1 PV ⁺ interneuron model	49
2.2.2	Synaptic receptors	51
2.2.3	Simulation protocol	52
2.3	Network Modelling	52
2.3.1	Spiking single neuron models	53
2.3.2	Network structure	54
2.3.3	Synaptic modelling	55
2.3.4	External input	60
3	Cooperative synaptic integration of local feedback connections by PV⁺ interneurons	62
3.1	Introduction	62
3.2	Results	65
3.2.1	Stratum oriens dendrites show supralinear synaptic integration	65
3.2.2	NMDA receptors mediate stratum oriens dendrite supralinear synaptic integration	75
3.2.3	Dendritic morphology does not fully account for dendrite specific synaptic integration	86
3.2.4	Differential NMDA receptor expression and dendritic morphology explain dendrite specific synaptic integration	93
3.2.5	The network-level roles of supralinear integration of feedback connections	97
3.3	Discussion	112
3.3.1	Glutamate-uncaging experiments	113
3.3.2	Network simulations	116
4	Polyamine modulation of AMPA receptors	119
4.1	Introduction	119
4.2	Results	122
4.2.1	Kinetic model of CP-AMPA receptors	122
4.2.2	Polyamine-modulation of CP-AMPA receptors mediates sublinear synaptic integration	125
4.3	Discussion	131
5	PV⁺ interneurons and epilepsy	133
5.1	Introduction	133
5.2	Methods	137
5.2.1	Pilocarpine epilepsy model	137

5.2.2	Experimental design	138
5.2.3	Feature extraction	139
5.2.4	Random Forests	143
5.2.5	Performance metrics	143
5.2.6	Chronic tetanus toxin epilepsy model	144
5.2.7	Hidden Markov models	146
5.2.8	Forward-backward algorithm	147
5.2.9	Obtaining emission probabilities with cross-validation	150
5.2.10	Obtaining emission probabilities with Bayes' rule	152
5.3	Results	154
5.3.1	Pilocarpine network-state classifier performance	154
5.3.2	The effect of PV ⁺ interneuron activation on seizure duration is time-dependent	156
5.3.3	Tetanus toxin model spontaneous seizure detection	159
5.4	Discussion	162
5.4.1	Pilocarpine network-state classifier	162
5.4.2	Time dependent bi-phasic effect of PV ⁺ interneuron activation	162
5.4.3	Spontaneous seizure detection	164
6	Discussion	165
6.1	General discussion	165
6.2	Concluding remarks	169
6.3	Bibliography	169

List of Figures

1.1	PV ⁺ cell morphology	23
1.2	The distribution of synaptic inputs onto PV ⁺ , CB ⁺ and CR ⁺ interneuron dendrites	24
1.3	Feedforward inhibition enforces pyramidal cell temporal precision	34
1.4	Feedforward inhibition enhances dynamic range and entrains pyramidal cell populations	35
1.5	Feedback inhibition	36
2.1	Recording from PV ⁺ cells	43
2.2	Measuring dendritic integration	46
2.3	Model kinetic scheme glutamate-receptor comparison	52
2.4	Izhikevich model neurons	53
2.5	Network architecture	55
2.6	Modelling input cooperation onto PV ⁺ cells	59
2.7	NMDA receptor current-voltage relationship	59
2.8	External input distributions across pyramidal cells	61
3.1	Comparison of uEPSP to spontaneous activity	66
3.2	Oriens dendrites support supralinear synaptic integration	67
3.3	Input-output functions by cell	69
3.4	Unscaled input-output comparison	70
3.5	Comparison of maximum theoretical summations	71
3.6	Dendritic location vs synaptic integration nonlinearity and expected maximum uEPSP	73
3.7	NMDA receptors mediate supralinear stratum oriens dendrite synaptic integration	78
3.8	uEPSP amplitude synaptic integration in APV and TTX	79
3.9	Pharmacology cumulative frequency plots of uEPSP integration nonlinearity	80
3.10	Unscaled input-output comparison for APV and TTX experiments	81

3.11	Comparison of maximum theoretical summations in APV	82
3.12	Comparison of maximum theoretical summations in TTX	83
3.13	Uncaging distance from soma vs uEPSP integration nonlinearity and maximum arithmetic compound uEPSP in APV	84
3.14	Uncaging distance from soma vs uEPSP integration nonlinearity and maximum arithmetic compound uEPSP in TTX	85
3.15	Multi-compartmental modelling of synaptic integration	88
3.16	Simulated synaptic responses in stratum oriens	89
3.17	Simulated synaptic responses in stratum radiatum	90
3.18	NEURON model amplitude and integral non-linearities	91
3.19	NEURON model nonlinearity vs distance from soma	92
3.20	Model EPSP integration nonlinearity vs NMDA conductance	92
3.21	Pharmacological dissection of NMDAR and AMPAR conductances from feedforward and feedback inputs	95
3.22	NEURON model amplitude and integral nonlinearity with unequal NMDA receptor conductance	96
3.23	Model spiking neuron network response to external input	99
3.24	Example currents on neurons during network simulations	100
3.25	NMDA receptor recruitment by external input pattern	103
3.26	NMDARs help to maintain a sparse and sharp representation of a 'hump' of excitation to the feedback circuit shown	104
3.27	Subnetworks driven by clustered or disperse inputs, with and without NMDA receptors	105
3.28	Subnetworks driven by clustered temporally consistent or inconsistent inputs, with and without NMDA receptors	106
3.29	Summary data for competing subnetwork simulations	107
3.30	Competing subnetworks with external input noise - varying NMDA receptor strength	109
3.31	Competing subnetworks with external input noise - varying AMPA receptor strength	110
3.32	Dominant network flip rate vs NMDAR and AMPAR conductance.	111
4.1	CP-AMPA receptor rectification properties	120
4.2	Model CP-AMPA receptor	123
4.3	Model CP-AMPA current-voltage relationships	124
4.4	Model PV ⁺ cell and with synaptic locations	126
4.5	EPSP summation with and without polyamines	127

4.6	Inter-synaptic delay and synaptic integration nonlinearity	128
4.7	Polyamines mediate sublinear synaptic integration for distributed synaptic inputs:	130
5.1	Neocortical focal epilepsy model and recording setup	137
5.2	Typical pilocarpine model induced epileptiform discharges	138
5.3	Extracting baseline periods of recordings	140
5.4	Peaks and troughs	140
5.5	Signal dataset	141
5.6	Wavelet spectrogram of signal dataset	142
5.7	Tetanus toxin induced spontaneous seizure	145
5.8	Trellis diagram for a hidden Markov model	146
5.9	Graph diagram for a hidden Markov model	147
5.10	Diagram of a HMM in which Hidden States "inter-ictal" and "ictal" emit "baseline" and "seizure" observations	151
5.11	Precision-recall curves for pilocarpine-model dataset	155
5.12	Temporal dependence of PV ⁺ depolarisation on the duration of ictal-like discharges	157
5.13	Bi-directional effect of PV ⁺ interneuron activation	158
5.14	Forward-backward algorithm posterior probabilities	160

List of Tables

2.1	Parameters used for NEURON model and simulations	50
2.2	Izhikevich model parameters	54
2.3	Network synaptic parameters	56
5.1	Pilocarpine network-state classifier performance	154
5.2	Random forest performance on chronic tetanus toxin model ECoG recordings without hidden Markov model	161
5.3	Algorithm performance with hidden state emission probabilities of classifier output	161
5.4	Algorithm performance using $p(Z_t X_t)/p(Z_t)$	161

Chapter 1

Introduction

This thesis mainly addresses the physiology and function of a type of parvalbumin expressing (PV^+) interneuron, fast-spiking basket cells. It builds on a large body of work to investigate how these interneurons integrate excitatory synaptic inputs and seeks to place these findings at the neuronal network and circuit level. The objective of this introduction is to provide an overview of the relevant scientific literature, and to highlight open questions. I first provide a general overview of synaptic integration by neurons, before addressing PV^+ interneuron physiology specifically, finally ending with a discussion of PV^+ interneuron functions in networks and pathology.

1.1 Synaptic input and integration

Neurons, the electrically active cells of the brain, maintain a voltage across their cell membrane. The preservation of neuronal membrane potentials accounts for roughly half of the brain's total energy expenditure (Howarth et al., 2012) or $\approx 10\%$ of that of the entire body. Communication between neurons revolves around affecting this electrical potential difference, with the aim of driving the cell towards or away from a membrane potential threshold at which the cell produces an action potential, a brief all-or-none reversal of membrane potential polarity.

Fast chemical communication between neurons occurs at synapses, which are ei-

ther excitatory or inhibitory depending on their driving of the postsynaptic membrane towards or away from the action potential threshold. In the field of neural networks, neurons are reduced to the level so far described: the output of each neuron is calculated by passing its summed inputs through a simple function that typically incorporates an activation threshold below which there is no output (McCulloch and Pitts, 1943). In biology, the function describing the input-output relationship of a neuron is far more complex.

Central to the neuronal input-output function are the receptive surfaces of neurons, their dendrites, whose diverse and intricate structure forms the location for the majority of synaptic inputs onto a cell. Within the dendrites, synaptic inputs not only interact with each other, but also with the active elements of the dendritic membrane itself, yielding elaborate integrative properties. The functional role of these properties has been the topic of much study and interest. One view holds that they are simply elaborate mechanisms by which the cell regularises the summation of inputs across its dendritic tree, a necessary solution to the physical way by which neurons must connect. In contrast, intricate integrative rules and processing may be of fundamental importance to the function of neurons and the circuits in which they are embedded (Häusser and Mel, 2003). It is likely that dendrites serve different roles for different cells, collapsing inputs as if made onto a single compartment for some neurons, whereas for others, dendrites may implement processing of inputs upstream of the cell body and the action potential initiation zone.

1.1.1 Synaptic input location

Dendrites conduct synaptic potentials towards the soma with a remarkable degree of voltage amplitude attenuation, for example, the difference between distal synaptic and somatic voltage is at least 40-fold for neocortical layer 5 pyramidal cells (Williams and Stuart, 2002). This distance-dependent attenuation is due to both the loss of charge directly through the membrane, which is determined by the ratio of axial resistance to membrane resistance, and by capacitive filtering of the voltage response by the membrane, which is greater for faster signals. Therefore, due to attenuation, synapses of unit conductance distributed along a passive dendritic tree will elicit smaller somatic voltage responses the farther they are from the soma.

Synapse location is therefore an important component of the synaptic signal at the soma. Proximal synapses quickly and powerfully influence the somatic membrane potential, but distal inputs may still be important for setting the overall state of the neuron, as a significant portion of depolarising charge reaches the soma from remote synapses. In contrast, however, location-dependent distortions may be sub-optimal for a neuron that is required to integrate inputs in a more democratic way, and as a result, neurons implement a variety of mechanisms to mitigate the effects of synaptic location. Importantly, these biophysical strategies are not limited to countering attenuation, instead they often go beyond this. Therefore, distance-dependent attenuation constitutes a major driver of complexity in the neuronal input-output function.

In the 1970s, experiments investigating cat spinal motor neuron physiology (Iansek and Redman, 1973) found somatic EPSP sizes that were independent of synaptic input location. One way in which this may be achieved, and the distance-dependent attenuation overcome, is via boosting of the synaptic current by voltage-dependent ion channels located in the dendritic tree (Cook and Johnston, 1999). Synapses farther from the soma experience larger local input resistances due to dendrite morphology, and the voltage change elicited by a distal synaptic current is therefore larger. As a result, distal inputs are better able to recruit active elements of the dendritic membrane than proximal inputs, and are boosted more than proximal synapses (Cook and Johnston, 1999).

A number of the voltage-dependent conductances (reviewed 1.1.4) both generate, and are activated by, membrane depolarisation. As a consequence, if these conductances are expressed with enough density, it is possible for distal synapses, either alone or together, to initiate a regenerative dendritic "spike" (Llinás et al., 1968). These events are typically much more powerful than an individual synaptic input, and enable distal locations to perform dendritic processing upstream from the soma (Manita et al., 2017).

A simpler strategy, found in pyramidal neurons in the CA1 region of hippocampus, is to implement "synaptic democracy" through distance-based scaling of synaptic conductance (Magee and Cook, 2000), thereby countering the increased attenuation experienced by distal synapses. However, it is unclear how synaptic democracy reliant on conductance scaling is maintained when a number of synapses are active, for example during the high levels of synaptic activity seen in vivo, or during shunting inhibition (defined below, section 1.1.3) (Koch et al., 1990). The very nature of

conductance-based synapses, discussed below in section 1.1.2, results in a reduction in dendritic membrane resistance when synapses are active. This membrane resistance decrease accentuates the attenuation experienced by distal synapses, necessitating a steeper synapse-scaling than what is required for more quiescent states (London et al., 2001). In response, Magee et al suggest synaptic conductance scaling and nonlinear voltage-dependent conductances may interact to overcome some of these limitations (London et al., 2001).

1.1.2 Synaptic clustering

The issues surrounding the summation of spatially clustered synapses also drive neuronal input-output function complexity. As noted by Rall in 1964, if two adjacent excitatory synapses are active on a passive dendrite within a narrow time-window, the depolarisation generated by the first synapse reduces the electrical driving force for the second. Additionally, by opening a conductance in the membrane, the first synapse reduces the local input resistance seen by the second synapse. As a result of these two factors, the size of the second input is smaller than if it were active in isolation from the first - synaptic integration is non-linear and saturating in its nature.

In a manner similar to the mitigation of distance-dependent synaptic attenuation, voltage-dependent conductances present in dendrites are able to amplify the size of summated synaptic potentials and counteract sublinear integration. Furthermore, synapses are often equipped with NMDA receptors, which are blocked by extracellular Mg^{2+} at hyperpolarised potentials but not at depolarised potentials, generating further boosting (Schiller and Schiller, 2001). As a result, in many cell types, clustered synapses are able to cooperate with each other to recruit an amplification that goes beyond linearising synaptic summation that would otherwise be sublinear. Indeed, the ability of dendritic regions to engage in local electrogenesis in response to clustered inputs is well documented (Larkum and Nevian, 2008).

In contrast, however, to synaptic cooperation, which relies on synaptic clustering, an alternative theory asserts that neurons rely on distributed synaptic inputs, ideally on different dendritic branches, to promote purely linear synaptic summation (Yuste, 2011) - which has been seen in some studies (Cash and Yuste, 1999). This has led to controversy over whether functionally-related synapses cluster on dendrites,

which would facilitate the recruitment of non-linearities and is thought to enhance information storage by dendrites (Poirazi and Mel, 2001; Kastellakis et al., 2015).

Studies of synaptic clustering can be divided non-exclusively into two aspects: anatomical clustering, whereby synapses group closely together in small regions relative to an average density across the dendrite, and functional clustering, in which neighbouring synapses are activated synchronously during activity. Evidence for experience-driven anatomical clustering on principal neurons was first found in barn owls reared using prisms to cause chronic displacement of their visual fields (McBride et al., 2008). Furthermore, in the hippocampus, the synapses between CA3 and CA1 were found to be distributed in a highly non-random and clustered manner, with neurons sharing similar developmental time windows displaying the most clustering (Druckmann et al., 2014). Finally, in the context of experience-induced plasticity, pyramidal neuron synapses in the barrel cortex were found to potentiate in clusters (Makino and Malinow, 2011).

With regards to functional clustering of synapses, calcium imaging of hippocampal organotypic slice cultures revealed that bursts of spontaneous activity tend to activate different sets of synapses, but that the activity of synapses close together on the dendritic tree were correlated with each other (Kleindienst et al., 2011). These findings were corroborated in CA3 pyramidal cells *ex-vivo*, and also during spontaneous activity in barrel cortex *in-vivo* (Takahashi et al., 2012). *In-vivo* experiments have also found evidence for functional clustering. Calcium imaging of pyramidal neurons in layer 2/3 of the ferret visual cortex found evidence for orientation-specific clustering of synaptic inputs, and that the neuron's orientation selectivity was correlated with the density of dendritic functional clustering (Wilson et al., 2016). In addition, a separate imaging study in the visual cortex found that inputs representing similar features of the visual space were more likely to cluster on neighbouring spines (Iacaruso et al., 2017).

In contrast, there are also *in-vivo* studies from the Konnerth laboratory, investigating a number sensory areas of the brain: visual cortex (Jia et al., 2010), barrel cortex (Varga et al., 2011), and the auditory cortex (Chen et al., 2011), that do not find evidence for the co-tuning of neighbouring synapses to similar input features. Instead, these experiments indirectly support a distributed linear model of synaptic integration (Cash and Yuste, 1999), with random microcircuit connection rules determined purely by axon and dendrite arbour overlap, also known as Peters' rule (Peters

et al., 1976).

However, these studies, which show a lack of orientation, sound frequency, and whisker combination co-tuning when comparing nearby synapses (Jia et al., 2010; Chen et al., 2011; Varga et al., 2011), assume that the dendritic topographic map should be ordered along the continuum of the elementary sensory feature in question, i.e synapses along a dendrite should encode smoothly varying frequencies or orientations. These particular experiments could potentially be reconciled with the clustering hypothesis if this smooth topographical organisation is not assumed. Instead clusters may be formed from combinations of these features, such as frequencies that are contained in naturalistic behaviourally relevant sounds. Furthermore, it is possible that synapses were electrically active, but did not show a Ca^{2+} signal. In these circumstances, co-tuning of synapses would not be detected.

Finally, dendritic spikes can also be regarded as a read-out of synaptic clustering, due to the clustered input generally required to elicit them. In addition to in-vitro recordings, reviewed in (Larkum and Nevian, 2008), multiple studies suggest a functional role for dendritic spikes in sensory perception in-vivo (Manita et al., 2017). For example, in the barrel cortex, NMDAR-dependent non-linearities were found to contribute to tuning of layer 4 neurons by enhancing the neurons' preferred angular directions (Lavzin et al., 2012). In addition, in the primary visual cortex, regenerative dendritic spikes enhance orientation selectivity (Smith et al., 2013).

In conclusion, there is a preponderance of evidence suggesting that anatomical and functional synaptic clustering occurs in neuronal circuits, where it plays a functional role. However, like synaptic democracy, it should not be expected that all neurons use identical information processing approaches. Indeed, while non-linear dendritic integration theoretically enhances the computational capabilities of neurons, such as pattern discrimination capacity (Poirazi and Mel, 2001), the field of neural networks also provides clear examples of sophisticated computation from linear integration (Hopfield, 1982; Hopfield and Tank, 1986).

1.1.3 Inhibition - excitation interaction

The interaction between inhibitory and excitatory synaptic currents in dendrites is also complex. Fast inhibition is typically mediated by GABA_A receptors, which have a reversal potential that is often close to the resting potentials of neurons. As a result, the opening of large inhibitory conductances in the membrane may produce negligible currents, due to small electrical driving forces. However the short-circuit introduced in the membrane is able to scale down EPSPs in a divisive, nonlinear manner. This strong "shunting" inhibition was shown to occur in neurons of cat primary visual cortex, where experiments found somatic input resistance decreased by more than three times in response to certain bar orientations (Borg-Graham et al., 1998).

In addition to being nonlinear in nature, shunting inhibition is particularly precise. First, temporally, as synaptic conductances are shorter-lived than the synaptic potentials they elicit, and as pure shunting inhibition is only inhibitory when the conductance is open, shunting inhibition acts over just a few milliseconds (Staley and Mody, 1992). Second, as the space constant for conductance is half that of voltage (Williams, 2004), shunting inhibition is also spatially restricted, and is able to affect only specific subregions of the cell.

The effectiveness of shunting inhibition is also critically dependent on the relative locations of the excitatory and inhibitory synapses. In general, inhibitory synapses are more effective if they are in the same region as excitatory synapses, or located closer to the soma, than if they are on the other side of the excitatory synapse, away from the soma - where the divisive effect of inhibition falls off sharply (Hao et al., 2009). This arrangement is known as "On-path" (Rall, 1964; Koch et al., 1983), and forms the standard model for excitation-inhibition interactions. In extrema, it is possible for inhibitory synapses located between the soma and a distal dendrite branch to effectively veto excitatory signals (Liu, 2004).

Interestingly, in contrast to the On-path model, *in silico* work first showed that Off-path inhibition can, in some situations, be more effective at dampening active dendritic events than On-path inhibition (Gidon and Segev, 2012). This is due to the asymmetrical morphology (tapering) of the dendritic tree, and its resulting electrotonic structure in which the soma forms a "sink". These simulations were then supported by experiments comparing the effect of On- and Off-path inhibition on

dendritic spike threshold in layer 5 pyramidal neurons (Jadi et al., 2012). Therefore, the effectiveness of inhibition, with regards to synaptic location, is also dependent on the type of excitatory activity being dampened.

Inhibitory synapses also act more conventionally through hyperpolarising synaptic currents. In this case, hyperpolarising inhibition acts simply as a linear subtraction (Rall, 1964). However, relatively small changes in the membrane potential can dramatically affect the driving force across the inhibitory synaptic receptor, and thereby cause large changes in the synaptic current. In contrast, this variability is not observed as strongly with excitatory synaptic receptors due to their depolarised reversal potential of ~ 0 mV. Furthermore, there is evidence that during periods of sustained inhibition intracellular Cl^- can accumulate, especially in spatially restricted regions such as the axon initial segment, thereby weakening the inhibitory driving force and reducing the effectiveness of hyperpolarising inhibition. The strength of inhibition is therefore also somewhat dependent on the history of the inhibitory synapse.

1.1.4 Active conductances in dendrites

Dendritic membranes often express conductances that are sensitive to, and are activated by, changes in the membrane potential. While a comprehensive review of all voltage gated ion channels is beyond the scope of this introduction, a number of these conductances are particularly important in the context of synaptic integration.

Na^+ channels are one of the active conductances most commonly found in neuronal dendrites. Depending on the particular neuron-type in question, these channels not only contribute to synaptic potential amplification (Schwindt and Crill, 1995), but have also been shown to play a role in the propagation of action potentials away from the soma, backwards into the dendritic tree (Stuart and Sakmann, 1994), as well as underlying dendritic Na^+ spikes that are initiated by synaptic inputs before somatic action potentials (Losonczy and Magee, 2006).

In addition to Na^+ channels, voltage gated Ca^{2+} channels are another type of regenerative cationic conductance commonly found in dendrites (Stuart et al., 2008) and generally underlie more prolonged inward currents. The channels that mediate Ca^{2+} conductances occur in a number of subtypes: L, N, P/Q, R and T-type.

These subtypes typically have different sub-cellular distributions, and display distinct kinetics and voltage dependences. The particular combination and expression of subtypes often determines the specific function of dendritic Ca^{2+} channels. For example, low voltage threshold T-type Ca^{2+} channels, are activated close to resting membrane potential, and therefore are able to amplify postsynaptic potentials (Markram and Sakmann, 1994). In contrast, high voltage threshold channels, such as L-type, are activated at more depolarised potentials and elicit more prolonged spikes and Ca^{2+} influx. These dendritic Ca^{2+} spikes can generate bursts of somatic action potentials (Larkum et al., 1999), and dendritic plateau potentials have also been shown to underlie place cell formation (Bittner et al., 2015). Finally, as Ca^{2+} is an intracellular messenger in its own right, Ca^{2+} channels also play important roles in a wide variety of intracellular processes, such as synaptic plasticity (Golding et al., 2002), and can even mediate dendritic neurotransmitter release (Ludwig and Pittman, 2003).

In contrast to Na^+ and Ca^{2+} channels, which enhance the excitability of dendrites, voltage-gated K^+ channels dampen dendritic excitability and reduce the size of postsynaptic potentials (Hoffman et al., 1997). K^+ conductances are mediated by a number of different channels channels, with functions ranging from limiting action-potential back-propagation (Goldberg et al., 2003) and enhancing EPSP waveform acceleration and temporal precision (Fricker and Miles, 2000), to synaptic plasticity regulation (Buchanan et al., 2010). Consistent with other dendritic conductances, K^+ channels are found in a variety of cellular and sub-cellular distributions. For example, K^+ conductance increases with distance from the soma in CA1 pyramidal cells (Hoffman et al., 1997), but not in layer 5 pyramidal cells (Bekkers, 2000).

Lastly, hyperpolarisation-activated cation conductances (I_h/HCN) are another commonly expressed dendritic conductance with a relatively depolarised reversal potential. Interestingly, I_h is generally active at rest, but is deactivated by depolarisation of the membrane potential. In this way, I_h channels can also reduce excitability and postsynaptic potential duration, thereby decreasing the time-window for temporal summation (Magee, 1998). Furthermore, in pyramidal neurons, I_h is generally expressed with increasing density with distance from the soma, normalising the effective R_m along the dendrite (Williams and Stuart, 2003). Finally, as I_h channels form a biological source of inductance, they are able to somewhat mitigate capacitive artefacts and mediate amplitude resonance at theta frequency (Vaidya and Johnston, 2013).

1.2 PV⁺ Interneurons

Neurons can be roughly separated into two species: excitatory glutamatergic principal neurons and inhibitory GABAergic interneurons, so named for the neurotransmitters they release, glutamate and GABA (γ - aminobutyric acid) respectively, and the actions these transmitters have on their downstream targets. In comparison to glutamatergic neurons, which account for ~80-90% of the total neuronal population, GABAergic interneurons are a minority of the neurons found in the forebrain, constituting only ~10-20% of the total neuron number (Freund and Buzsáki, 1998). Within the CA1 region of the hippocampus experimental observations of GABAergic numbers range from 7-11% (Bezaire and Soltesz, 2013).

Despite their relative scarcity, GABAergic interneurons serve many critical functions, without which the activity of cortical circuits breaks down, resulting in pathologies such as seizures (Kandel et al., 2000). Furthermore, interneurons exhibit a cellular diversity not found amongst the principal cell population (Klausberger and Somogyi, 2008), implying specialised functions. Understanding this diversity is generally aided by considering a given interneuron in the context of its morphology, molecular expression profile, and functional characteristics. This thesis is focussed on PV⁺ interneurons, so named for their expression of the calcium-binding protein parvalbumin, in the CA1 region of the hippocampus, where they comprise roughly 2% of the regional neuronal population (Bezaire and Soltesz, 2013). PV⁺ cells are equipped with both the ability to strongly suppress local principal cell activity and to sample from a range of excitatory input sources. They are therefore powerfully positioned to gate signal flow and sculpt the dynamics of the network in which they are found (Hu et al., 2014a).

1.2.1 Morphology and connectivity

In contrast to other interneurons present within the CA1 region of the hippocampus, such as cholecystokinin (CCK⁺) or somatostatin (SOM⁺) expressing interneurons, the somata of PV⁺ interneurons are found most frequently among the cell bodies of the principal pyramidal cells in the stratum pyramidale (PV⁺ : 70%, CCK⁺: 20%, SOM⁺: 0%) and the majority of remaining PV⁺ cell bodies are located in the stratum oriens (23.9%) (Bezaire and Soltesz, 2013).

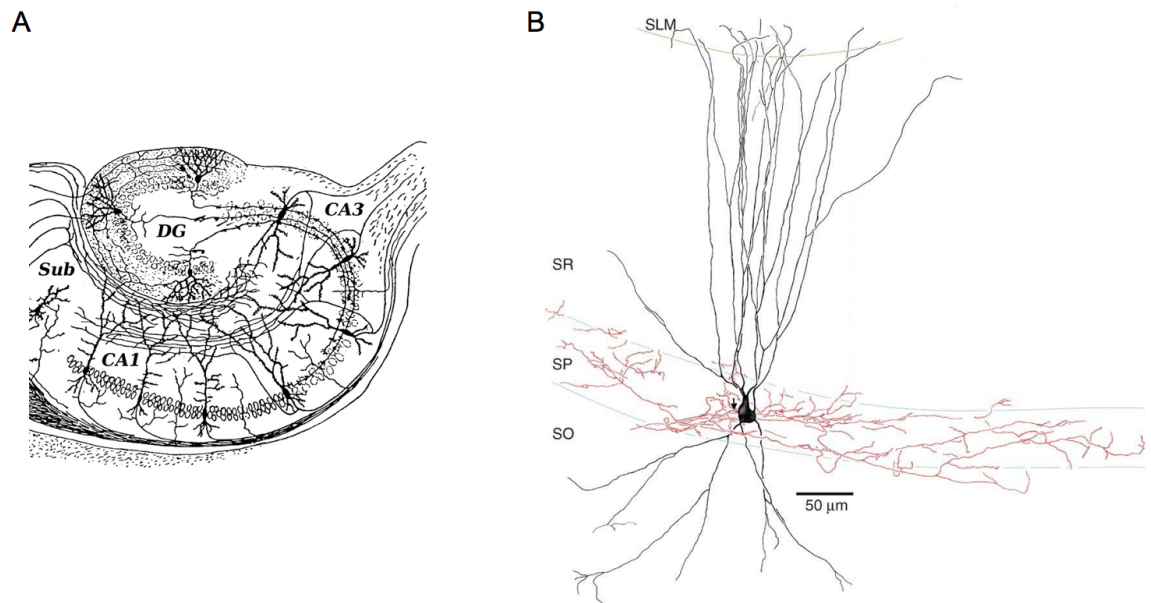


Figure 1.1. PV⁺ cell morphology: (A) Diagram of hippocampus. (B) Reconstruction of CA1 PV⁺ interneuron. Note dendrites located in all strata. Figure panel altered from Lapray et al. (2012)

Further similarity with the local excitatory pyramidal cells is found in the extent and connectivity of the PV⁺ cell's dendritic arborisation, which runs radially through all of the layers of the CA1 region, from the stratum oriens, to the stratum radiatum and into the stratum lacunosum-moleculare (Gulyás et al., 1999). This contrasts with other interneuron subtypes, such as oriens lacunosum-moleculare or neurogliaform interneurons, which have dendrites largely constrained to just one layer of the CA1 region. As a result of their extensive dendrites, PV⁺ cells receive excitatory inputs from all the major excitatory afferent pathways present in the CA1 region. Local feedback connections are found on basal PV⁺ cell dendrites in the stratum oriens, long-range Schaffer-collateral inputs from CA3 are located on both the dendrites in the strata oriens and radiatum, and finally the perforant pathway, from the entorhinal cortex, makes synaptic connections on the dendrites in the stratum lacunosum-moleculare (Klausberger and Somogyi, 2008; Bezaire and Soltesz, 2013).

PV⁺ interneuron dendrites are typically smooth and aspiny. Excitatory synapses therefore make connections directly onto the dendritic shafts of PV⁺ cells, as opposed to the spines found on principal cell dendrites. The lack of spine neck, and associated electrical resistance, is thought to facilitate the fast rise and decay of postsynaptic potentials on these dendrites (Geiger et al., 1997). A further implication of smooth dendrites is the lack of biochemical compartmentalisation between synapses (Blood-

good and Sabatini, 2007), which plays an important role in synaptic plasticity. As might therefore be expected, PV⁺ interneurons express significantly different synaptic plasticity mechanisms than those seen mediating plasticity in pyramidal cells (Kullmann and Lamsa, 2007).

PV⁺ interneuron dendrites also show a high density of excitatory synaptic contacts, compared to other interneuron subtypes such as calbindin (CB⁺) or calretinin (CR⁺) expressing interneurons (Gulyás et al., 1999). Figure 1.2 shows excitatory and inhibitory synapse density on dendrite reconstructions from serial ultra-thin sections of PV⁺, CB⁺ and CR⁺ interneuron dendrites. As shown in Figure 1.2 this study found PV⁺ interneurons had a high density of contacts, roughly 300 excitatory synapses per 100 μm of dendrite averaged across the entire dendritic tree (and 400 excitatory inputs per 100 μm in the dendritic strata investigated in this thesis) which was >4 fold the density of excitatory inputs onto CB⁺ and CR⁺ interneuron dendrites.

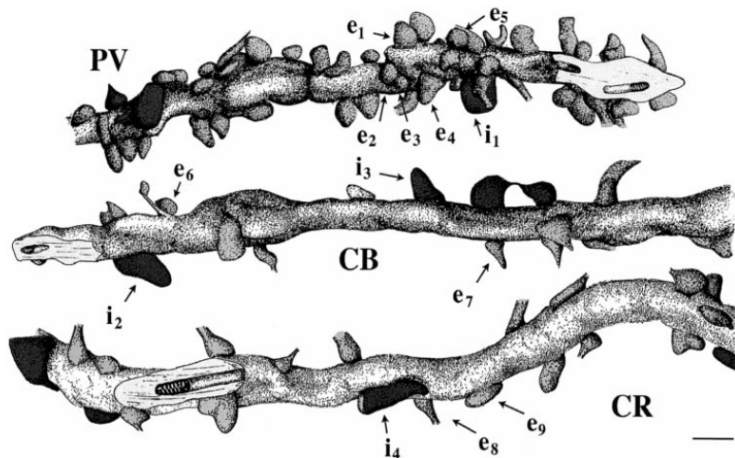


Figure 1.2. The distribution of synaptic inputs onto PV⁺, CB⁺ and CR⁺ interneuron dendrites. GABA-negative axon terminals labelled with 'e' and GABA-positive 'i'. Scale bar denotes 1 μm . Figure from (Gulyás et al., 1999).

PV⁺ interneurons often display a large and extensively arborised axon, in opposition to historical anatomical views on GABAergic interneurons, in which interneurons were defined by their short axons (DeFelipe, 2002). PV⁺ cells in the CA1 region can be subdivided into three main subclasses - largely based on axonal structure. The most common type of PV⁺ interneuron is the basket cell, which accounts for 60% of the PV⁺ cells in the CA1 region. PV⁺ basket cell axons typically innervate the soma and proximal dendrites of the surrounding principal cells in massive numbers, each forming roughly 10,000 synapses in CA1 (Sik et al., 1995), providing powerful, divergent inhibition to the surrounding excitatory cell population. PV⁺ axo-axonic cells,

also referred to as chandelier cells, make up 14% of the CA1 PV⁺ cell population, and specifically target the axon initial segments of principal cells. This specialised configuration, coupled with the small volume of the axon initial segment, has led to a controversial theory in which axo-axonic cells become excitatory during periods of heightened network activity, and are even able to elicit axonal action potentials, due to Cl⁻ reversal potential changes (Szabadics et al., 2006). Finally, PV⁺ bistratified cells make up 24% of CA1 PV⁺ cells and their dendrites target the dendrites of local pyramidal cells (Bezair and Soltesz, 2013).

Finally, PV⁺ interneurons within both the hippocampus and neocortex form a syncytium, with dendrites connected to one another by gap junctions (Galarreta and Hestrin, 1999). This structural organisation allows PV⁺ cells to respond to inputs onto neighbouring cells, widening the area over which the neuron effectively samples synaptic inputs (Galarreta and Hestrin, 2001). In addition, as gap junctions effectively increase the amount of dendrite, EPSP decay time will be accelerated due to redistribution of charge into adjacent neuron dendrites (Koch et al., 1996).

1.2.2 Passive properties

The passive properties of PV⁺ interneurons lay the foundation of the cell type's specialised electrical nature for fast input-output processing. The most basic of these properties is input resistance (R_{in}), which in PV⁺ interneurons is around 60 M Ω (64.3 ± 8.6) (Aponte et al., 2006). This is low in comparison to other large interneurons, such as CCK⁺ basket cells or CA1 pyramidal cells, which both have input resistances that are typically over 100 M Ω (Bartos and Elgueta, 2012; Spruston and Johnston, 1992).

Input resistance is dependent on total membrane area: the addition of membrane can be conceptualised as adding conductance to a cell, and therefore larger cells will generally have a lower input resistance than small cells. To distinguish between a small cell with a "leaky" membrane, which still has a relatively high input resistance, and a large cell with a "tight" membrane, which has a comparatively low input resistance, the term specific membrane resistance can be used (R_m), and refers to the resistance of a given membrane area (and likewise for specific membrane capacitance, C_m). For PV⁺ interneurons, the low input resistance is the product of both a low specific membrane

resistance and a large total membrane area. However, dual soma-dendrite recordings of dentate gyrus PV⁺ interneurons suggest that the specific membrane resistance is not uniform throughout the cell: distal dendrites have a 10x higher specific membrane resistance than proximal dendrites (Nörenberg et al., 2010), which is opposite to the gradient of R_m found in pyramidal cells (Golding et al., 2005; Stuart and Spruston, 1998). Increased R_m is expected to lead to increased synaptic waveform filtering. However, if distal dendrites mainly receive low frequency activity, for example theta frequency activity from entorhinal cortex, increased filtering may be less important than charge loss through the membrane.

A primary effect of low specific membrane resistance exhibited by PV⁺ interneurons is to set the membrane time constant ($\tau_m = R_m C_m$), which in PV⁺ interneurons is generally ≈ 10 ms. τ_m defines the lower-bound for the rate at which the voltage across the cell's membrane can change as a result of current flow (Koch et al., 1996). Therefore, synaptic currents in PV⁺ interneurons generally elicit faster voltage responses than synaptic currents in cells that have larger membrane time constants, such as pyramidal cells, which have time constants of around 30-70 ms (Jonas et al., 2004). As a result, PV⁺ interneurons can be driven to voltage threshold for action-potential generation quickly, facilitating rapid input-output signalling.

τ_m is also related to the corner frequency (f_c), or cut-off frequency, of the low pass RC filter formed by the cell's membrane by $f_c = 1/2\pi R_m C_m$. f_c is the frequency at which the filter will start to rapidly attenuate higher frequency signals. As can be seen from the formula, the smaller the membrane time constant, the faster the signal can be before filtering occurs. As a result, the dendrites of PV⁺ interneurons will filter and smear fast synaptic EPSPs less than cells with slower membrane time constants. Therefore, EPSPs arriving at the PV⁺ cell soma typically have short half durations of (4-10 ms at physiological temperature (Jonas et al., 2004)).

A general trade-off made by a reducing R_m for a fast τ_m , is increased attenuation of synaptic currents as they propagate along a dendrite. This is commonly assessed by the length constant, λ , which is a measure of the steady state (DC) dissipation of voltage with distance, and is defined as $\lambda = \sqrt{R_m/R_i}$, where R_i is the intracellular resistivity (and therefore dependent on dendrite diameter). Note, however, synaptic currents are transient, and the effective λ is dependent on the speed of the synaptic current. In this case $\lambda_{AC} = \sqrt{R_m/R_z}$, where R_z is the specific membrane impedance, composed of ohmic resistance and also of capacitive reactance, which decreases with

increasing signal frequency. Very fast currents will therefore reduce λ_{AC} to negligible distances, regardless of R_m . However, for the range of signal frequencies found in interneuron communication this does not occur, and cells with low membrane resistances generally show greater EPSP attenuation than more resistive cells.

While significant EPSP attenuation, due to a short λ , may have useful processing properties, for example by constraining EPSPs to the dendritic tree and thereby promoting functional compartmentalisation, PV⁺ interneurons have a relatively large λ . This comparatively large λ is due to the large diameter of PV⁺ cell dendrites - thicker than other interneurons (Emri et al., 2001). As a direct result, axial resistance to current flow is reduced, increasing λ . Remarkably, PV⁺ interneurons are therefore relatively electrically compact, displaying comparatively small morphotonic dendritic lengths (Larkman et al., 1992).

One final passive biophysical property is the dendritic conduction velocity. For a passive cylindrical cable this approximates to $v = 2\lambda/\tau_m$ (Agmon-Snir and Segev, 1993). Therefore, PV⁺ interneurons can be considered to be maximising conduction velocity: a low specific membrane resistance reduces τ_m , and a large dendritic diameter increases λ . As a result, it is expected that PV⁺ interneuron dendrites support faster EPSP conduction than typical principal neurons.

The passive properties of PV⁺ interneurons therefore build up a clear impression of a cell primarily built for speed and input coincidence detection, as opposed to input cooperation. Long thick dendrites, formed of low-resistance membrane, conduct EPSPs to the soma with low latency, where they arrive with short half-widths, due to a fast τ_m , and with relatively little amplitude attenuation, due to a large λ . This defines a narrow time-window during which somatic EPSPs can interact, as the EPSP peaks are sharp and decay rapidly. As a result, the window for temporal summation of somatic postsynaptic currents in PV⁺ cells is approximately 5 ms (Geiger et al., 1997).

1.2.3 Active properties

The active properties of PV⁺ interneurons further build upon the foundation of passive properties to render the PV⁺ interneuron a fast input-output signalling device. Most

striking is the depolarised resting potential that PV⁺ interneurons typically display, around -60 mV, placing the interneuron in a "ready-to-fire" mode, near the action potential threshold. Resting membrane voltage is a reflection of the conductances that are active when the cell is at rest, as each pulls the membrane potential towards its own reversal potential. Generally, this resting conductance is dominated by K⁺, as either inwardly rectifying K⁺ channels or two-pore domain K⁺ channels form the primary neuronal leak conductance (Goldstein et al., 2001). However, in the case of PV⁺ interneurons, this raises a paradox: they have a low R_m, suggestive of a significant leak conductance, but a resting potential closer to -60 mV, substantially depolarised from the K⁺ reversal potential of around -90 mV.

Hyperpolarisation-activated cation channels (HCN or I_h) are thought to be responsible for the combination of a depolarised resting potential and low R_m found in PV⁺ interneurons. In one study application of the I_h blocker ZD7288 increased input resistance from 64.3±8.6 MΩ to 106.6±15 MΩ, and hyperpolarised the membrane potential by 5.7±1.5 mV (Aponte et al., 2006). Generally, the presence of a "sag" in the voltage response to a hyperpolarising current is considered to be a reliable indication of HCN channel expression (Pape, 1996). However, despite significant I_h, PV⁺ cells do not exhibit this response to current injection. Two factors are suggested by Aponte et al to explain the lack of sag: first, the activation of I_h has a relatively shallow voltage dependency implying a modest change in open channel probability in response to hyperpolarising current pulses, and second, the activation kinetics of I_h could be obscured by the PV⁺ cell membrane time constant measured when I_h is blocked (11.2 ms in control vs 66.4 ms in ZD7288). Off-target actions of ZD7288 (Chen, 2004; Chevaleyre and Castillo, 2002), for example blockade of K⁺ channels, could also explain the increase in PV⁺ cell input resistance upon ZD7288 application. However, this explanation is not consistent with the recorded membrane hyper-polarisation or the lack of effect on action-potential half-width (Aponte et al., 2006).

CA1 PV⁺ interneuron dendrites do not actively support regenerative events, unlike most principal cells, such as CA1 pyramidal cells. Action-potential back-propagation into the dendritic tree diminishes rapidly with distance from the soma, as reported by direct recordings (Hu et al., 2010) and calcium imaging (Camire and Topolnik, 2014; Chiovini et al., 2010). This is in contrast to principal cells, where back-propagation is generally active (Stuart and Sakmann, 1994) and forms the basis for spike-timing dependent plasticity rules (Bi and Poo, 1998). In addition, PV⁺ interneuron dendrites do not typically support dendritic spikes, in response to either direct current injec-

tion or synaptic stimulation (Hu et al., 2010); however, massive glutamate uncaging experiments on dendrites in the CA1 stratum radiatum suggests that this is not so clear-cut (Chiovini et al., 2014).

The passive dendritic nature of PV⁺ interneurons is due to a low density of voltage gated Na⁺ channels, which is coupled with a high density of voltage gated K⁺ channels (Hu et al., 2010). This ratio is another characteristic property that distinguishes PV⁺ interneurons from other interneurons and principal cells, and further supplements their rapid input-coincidence detection properties. The lack of dendritic spikes limits input cooperation within the dendritic tree, and failure of action potential back-propagation prevents previous activity from interacting with incoming signals. Furthermore, the significant K⁺ conductance in the dendrites will sharpen the EPSP waveforms by effectively decreasing their decay time constants, thereby counteracting temporal filtering by the dendrites, and promoting short somatic EPSP half-widths.

K_v3 channels are the dominant conductance found in PV⁺ interneuron dendrites, and are well suited for EPSP waveform acceleration due to their high activation threshold and fast activation and deactivation kinetics (Rudy and McBain, 2001). EPSPs arriving on dendritic locations with large local input resistances, such as thin dendrites or locations closer to sealed ends - both typically further from the soma - will generate local EPSPs with large peak amplitudes, which are able to efficiently recruit the dendritic K⁺ conductance, speeding their decay. The increased EPSP waveform filtering, due to the increased R_m of distal dendrites, (Nörenberg et al., 2010) could also be countered in this way. However, PV⁺ interneurons also express K⁺ conductance in a location dependent manner, decreasing with distance from the soma (Hu et al., 2010), complicating this analysis. Spatially clustered inputs will also be more effective at recruiting K⁺ channels than distributed inputs. PV⁺ cells may therefore be less sensitive to clustered inputs, especially if the inputs are not exactly coincident in time, as the K⁺ conductance will reduce the peak of the summated EPSP amplitude more for clustered inputs than for spatially distributed ones.

Further to their role in the dendrites of PV⁺ interneurons, K_v3 channels in the axon initial segment are critical for conferring perhaps the most recognisable feature of PV⁺ interneurons: their fast-spiking phenotype and action-potential waveform. The large bi-phasic afterhyperpolarisation is determined by K_v3 expression, while a high density of axonal Na⁺ channels, greater than that required for reliability (Hu et al., 2014b), underlies the rapid rising-phase. K_v3 channel kinetics enable fast membrane

repolarisation and Na⁺ channel de-inactivation, facilitating reliable repetitive spiking without changing the spike initiation threshold or spike amplitude (Rudy and McBain, 2001).

In addition to K_v3 channels, K_v1 channels are also expressed by PV⁺ interneurons in the axon initial segment. K_v1 channels are thought to be responsible for the subtle diversity of firing-patterns observed between PV⁺ cells, namely delay-type, continuous, and stutter firing. The exact pattern depends on K_v1 subunit composition, for example K_v1.1 has faster kinetics than K_v1.2, and on the subcellular expression profile (Goldberg et al., 2008). In general, at the onset of a current pulse K_v1 channels activate, depolarising the voltage threshold for action-potential initiation. With prolonged membrane depolarisation K_v1 channels slowly inactivate, hyperpolarising the voltage threshold and leading to delayed spiking. During spiking, the large afterhyperpolarisation that follows action potentials accelerates de-inactivation of K_v1 channels, again depolarising the action potential voltage threshold and cutting off firing. This cycle then repeats, resulting in a bursting, or stuttering, firing pattern (Sciamanna and Wilson, 2011).

K_v1 channel expression has a number of functional consequences, further to the cell's response to a square wave current pulse. For example, generally only sufficiently large and fast synaptic inputs are able to outrun the K_v1 activation (Goldberg et al., 2008). In this way, K_v1 channels constitute yet another mechanism of coincidence detection in PV⁺ cells. However, previous sub-threshold synaptic inputs can inactivate K_v1 channels, attenuating the K_v1-dependent input gating (Goldberg et al., 2008). Finally, PV⁺ cell intrinsic excitability can be regulated by modulation of K_v1 channel expression. This has been shown to occur when K_v1 channels are down-regulated in response to high-frequency stimulation and metabotropic glutamate receptor activation (Campanac et al., 2013).

1.2.4 Synaptic receptor expression

Excitatory synaptic currents are generally commonly composed of two glutamate gated ion channels, AMPA and NMDA receptors (He et al., 1998). AMPA receptors are heterotetramers, formed from a combination of four AMPA receptor subunits, GluA1-4 (Traynelis et al., 2010). In contrast to most principal cells, PV⁺ interneu-

rons express very low levels of the mRNA for GluA2, and their AMPA receptors are mainly composed of GluA1 and GluA4 subunits (Geiger et al., 1995). The lack of GluA2 subunits confers a number of important properties upon PV⁺ AMPA receptors. Distinctively, their Ca²⁺ permeability is an order of magnitude larger than that of GluA2 containing receptors (Geiger et al., 1995), which has resulted in the use of term calcium-permeable (CP-AMPA) to describe GluA2-lacking receptors. In addition, the overall channel conductance of CP-AMPA receptors is significantly higher than that of AMPA receptors that contain the GluA2 subunit (Bowie, 2012), and the synaptic currents from the receptors exhibit faster rise and decay kinetics (Lalanne et al., 2015).

Another striking feature of CP-AMPA receptors is their sensitivity to blockade by intracellular polyamines such as spermine, spermidine, and putrescine. This blockade is voltage dependent: at depolarised potentials polyamines block the channel pore, resulting in an inwardly rectifying current-voltage (IV) relationship. At extremely positive potentials the positively charged intracellular polyamine is driven through the pore and into the extracellular space, resulting in a characteristic cubic shaped IV relationship (Bowie and Mayer, 1995; Koh et al., 1995; Bowie et al., 1998). The degree of channel sensitivity to polyamine blockade can be modulated by auxiliary AMPA receptor subunits, for example, the transmembrane AMPA receptor regulatory protein (TARP) stargazin decreases the CP-AMPA receptor's affinity for polyamines (Soto et al., 2007, 2014).

The NMDA receptor is a second class of excitatory synaptic receptor. NMDA receptors also form tetramers, but from a combination of only three subunits: GluN1-GluN3. Of these subunits, two of the GluN1 subunits are obligatory for channel formation (Vyklicky et al., 2014). NMDA receptor activation generally requires two molecules of glutamate, which bind to the GluN2 subunits, and also the co-agonist glycine or D-serine, which binds to the GluN1 and GluN3A/B subunits. As a result, receptors composed of just GluN1 and GluN3 subunits only require glycine for activation - although these receptors have a very low calcium permeability (Pachernegg et al., 2012).

Like AMPA receptors that lack GluA2 subunits, NMDA receptors are Ca²⁺ permeable and their conductance is voltage dependent. However, in place of modulation by intracellular polyamines, the NMDA receptor channel-pore is blocked by extracellular Mg²⁺ ions, with maximal blockade at hyperpolarised potentials and a relief of block

at depolarised membrane potentials (Nowak et al., 1984). The resulting outwardly rectifying IV relationship of NMDA receptors is therefore in direct contrast to that of CP-AMPA receptors. The two receptors can therefore be described as detectors of opposing modalities: NMDA receptors promote input cooperativity and clustering, as inputs cooperate to relieve the Mg²⁺ channel block; whereas, in contrast, CP-AMPA receptors produce maximal responses from sparse input (Kullmann and Lamsa, 2007).

The kinetics of NMDA receptors differ dramatically from those of AMPA receptors. While AMPA receptor activation elicits a brief, rapidly rising and decaying conductance, typically occurring within a few milliseconds, NMDA receptor conductances have much slower rise and decay constants, typically an order of magnitude slower than those elicited by AMPA receptors, such that the NMDA receptor mediated current often persists for around 100 ms (Traynelis et al., 2010). The specific synaptic rise and decay time constants are highly temperature sensitive, scaled by a factor of 2-3 for a 10°C increase (Q10 factor), complicating interpretation of experimental measurement (Postlethwaite et al., 2007; Cais et al., 2008). Furthermore, the Q10 factor is not uniform for all of the state transitions underlying the recorded synaptic current, for example, while glutamate binding to, and channel opening of, NMDA receptors were found to vary with a low Q10 factor, receptor re/de-sensitisation have a much stronger temperature sensitivity and a corresponding high Q10 factor (Cais et al., 2008). Complications aside, at near-physiological temperature, PV⁺ interneurons express, relative to principal neurons, fast NMDA and AMPA receptors, with decay time constants of around 19 and 0.77 ms for NMDA and AMPA receptors respectively (Geiger et al., 1997).

Finally, the expression of NMDA receptors by PV⁺ interneurons is generally thought to be sparse, particularly on PV⁺ dendrites in the Stratum Radiatum of the CA1 region, although the NMDA receptor expression on dendrites in the Stratum Oriens is more variable (Nyíri et al., 2003). Despite their rarity, paradoxically, NMDA receptors on PV⁺ have been heavily implicated in pathology, most strikingly linked to schizophrenia and deficits in gamma oscillations (Gonzalez-Burgos and Lewis, 2012). A non-uniform expression of NMDA receptors at feedback vs feedforward synapses may go some way to resolving this apparent paradox, as long term potential experiments have previously shown NMDA receptor mediated plasticity at feedback but not at feedforward synapses (Le Roux et al., 2013; Grunze et al., 1996).

1.3 PV⁺ interneuron network function

Individual PV⁺ interneurons do not exist in isolation: they are embedded within networks of neurons with often highly specific connectivity rules. When considering the place of inhibition within these networks, a classical distinction between feedforward and feedback microcircuits is often made to aid discussion. These two terms refer to the situations in which the excitatory drive to the inhibitory cells originates either from outside the local area, which is termed feedforward inhibition, or from the local excitatory cells, referred to as feedback inhibition (Kullmann and Lamsa, 2007). It should be emphasised that the feedforward-feedback distinction is ultimately of limited use: neuronal circuits are generally composed of recurrent feedback loops, thus blurring the division. Nevertheless, considering inhibitory cells in the context of feedforward-feedback roles provides a useful reference-point for discussion.

As might be expected from their extensive dendritic arborisation, in contrast to many GABA-ergic interneurons, such as oriens lacunosum-moleculare cells, PV⁺ interneurons are typically involved in both feedforward and feedback inhibition. What are their particular network functions within these two circuit-motifs, and what is the relevance of their array of rapid signalling mechanisms to these network functions?

1.3.1 Feedforward inhibition

In the hippocampal area CA1, feedforward recruitment of PV⁺ interneurons is primarily mediated by Schaffer collaterals from CA3 and perforant path input from the entorhinal cortex. Stimulation of Schaffer collaterals efficiently recruits PV⁺ interneurons with low latency (~ 2 ms), before the pyramidal cell population is driven to voltage threshold. As a result, Schaffer collateral stimulation elicits a combined excitatory and inhibitory current at CA1 pyramidal cells (Fig. 1.3 B) (Pouille and Scanziani, 2001).

In principle, the long τ_m of many pyramidal neurons should allow synaptic inputs to summate over long periods of time. In this case, somatic spiking would simply reflect the average amount of synaptic input over that integration window, as opposed to being temporally precise. The rapid signalling properties of PV⁺ interneurons

however, which allow the neuron to fire rapidly in response to the Schaffer collateral input, enforce temporal precision of local pyramidal cells (Fig. 1.3 C).

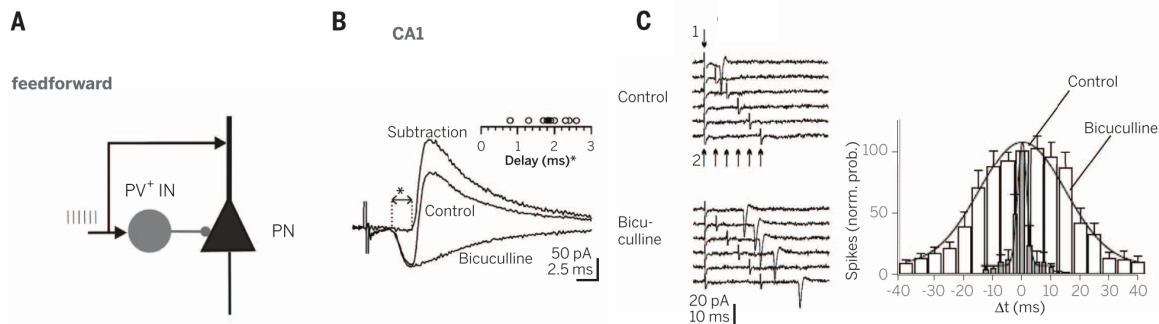


Figure 1.3. Feedforward inhibition enforces pyramidal cell temporal precision: (A) Schematic of feedforward inhibition. (B) Voltage clamp recordings from CA1 pyramidal cell during Schaffer collateral stimulation. Inhibitory current, blocked by bicuculline, is elicited 2 ms after collateral stimulation. (C) Two stimulating electrodes in Schaffer collateral pathway and cell-attached pyramidal cell recording. Blocking feedforward inhibition widens coincidence detection window. Panels of figure adapted from (Pouille and Scanziani, 2001; Hu et al., 2014a)

Rapid recruitment of feedforward inhibition is not limited to simply sharpening principal cell recruitment. An essential issue faced by excitatory circuits with divergent axonal projections is the input range that the network can represent. The number of active upstream neurons that are required to activate just a few downstream neurons is surprisingly similar to the number needed to recruit almost all of the downstream population. For example, if the pre-post connection probability is 15%, and each postsynaptic neuron requires 40 active inputs to reach threshold, 200 presynaptic neurons will recruit just 2% of the postsynaptic population, whereas 400 will recruit >99% (Pouille et al., 2009).

While network saturation may be a useful computation in of itself - for example providing a simple threshold, Pouille et al. found that the rapid recruitment of feedforward inhibition by incoming activity effectively normalised the impact of an individual afferent input to the total size of the upstream activity (Pouille et al., 2009). As afferent activity increased, so too does the strength of feedforward inhibition, increasing the EPSC size required to recruit the postsynaptic cell. Feedforward inhibition can therefore makes the range of inputs that the postsynaptic population

can represent dynamic. As a result of such a mechanism, networks are both able to remain sparsely activated in response to strong afferent activity and also to be responsive to weak stimuli - for example the wide range of active neurons seen in response to sensory stimuli (Fig. 1.4A)(Pouille et al., 2009).

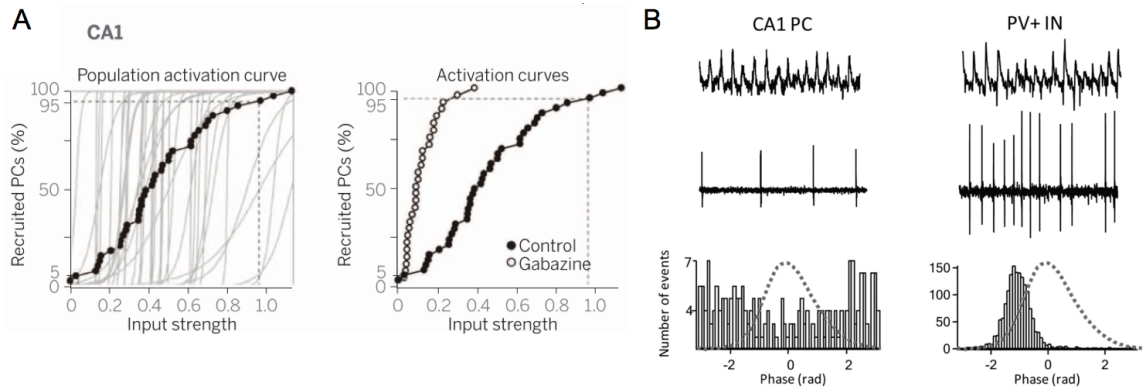


Figure 1.4. Feedforward inhibition: (A) Feedforward inhibition enhances the dynamic range of pyramidal cell (PC) populations. Left, % PC recruitment vs input strength. Grey individual cells, black average. Right, comparison of population range in control (solid) and inhibitory-blockade (open) conditions (Pouille et al., 2009). (B) Spiking activity of CA1 PCs and PV⁺ cells during carbachol induced oscillations. Top: local field potential (LFP) recording, middle: cell attached recording, bottom: Firing probability vs LFP phase. PCs (left) are most likely to fire at troughs of gamma oscillation. In contrast, PV⁺ cells (right) fire just before the peak (Zemankovics et al., 2013).

Finally, rapid feedforward inhibition also plays a role in network entrainment by upstream areas. In the hippocampus both CA3 and entorhinal cortex are thought to generally entrain the CA1 region at gamma frequencies, via Schaffer collaterals and perforant-path axons respectively (Bragin et al., 1995; Colgin et al., 2009). There is also, however, evidence that CA1 can generate its own gamma oscillations (Craig and McBain, 2015; Pietersen et al., 2014). In line with the rapid feedforward inhibition so far discussed, PV⁺ cells are recruited first by these entraining inputs. For example, during CA3-CA1 entrainment, the synchronous excitatory drive from CA3 primarily recruits PV⁺ interneurons, such that the firing phase of the local CA1 cells is at the trough of the CA3 input (Zemankovics et al., 2013).

1.3.2 Feedback inhibition

PV⁺ interneurons are also involved in feedback inhibition, forming both recurrent and lateral connections with local principal cells (Hu et al., 2014a). For example, in the medial entorhinal cortex, quadruple patch-clamp recordings showed reciprocal connectivity between stellate cells and PV⁺ interneurons of around 26% percent. In hippocampal CA1, PV⁺ cells receive the most input from superficial local pyramidal cells, but provide stronger inhibition to deep pyramidal cells (Lee et al., 2014).

Paradoxically, despite substantial, strong feedback connections (Csicsvari et al., 1998; Marshall et al., 2002), PV⁺ cells do not generally inherit the specialised firing characteristics of local principal cells. For example, in the entorhinal cortex, where grid cells predominate, PV⁺ interneurons show broad spatial tuning (Buetfering et al., 2014). Likewise, in the CA1 hippocampus, where many of the neurons are place cells, which have narrow receptive fields to the animal's position in space, PV⁺ interneurons generally display much broader place fields, if at all (Fig. 1.5B) (Wilson and McNaughton, 1993). However, they do inherit phase precession, implying coupling to individual place cells (Maurer et al., 2006). Therefore, the broad tuning of PV⁺ cells is thought to be due to inheritance of spatial preferences from a number of principal neurons with a range of receptive fields (Hu et al., 2014a).

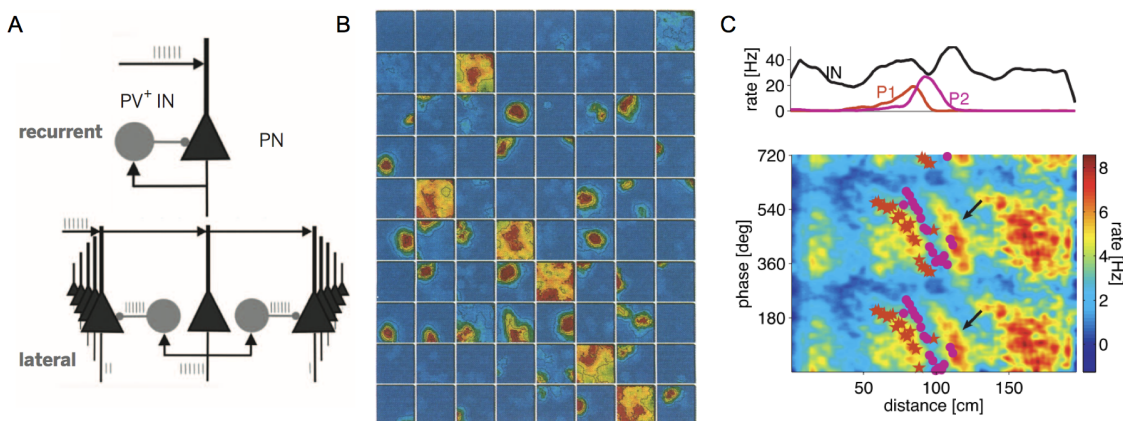


Figure 1.5. Feedback inhibition: (A) Schematic of recurrent and lateral inhibitory circuits. (B) Comparison of CA1 pyramidal cell place fields and PV⁺ interneuron receptive fields. PV⁺ cell fields are full boxes. Image from (Wilson and McNaughton, 1993). (C) PV⁺ interneurons separate between cell assemblies. Firing of PV⁺ interneuron and pyramidal cell 1 are anti-correlated with pyramidal cell 2. Taken from Fig. 4 (Geisler et al., 2007).

One simplistic function of feedback inhibition is to provide network stabilisation (Tsodyks et al., 1997), however, the lateral and recurrent feedback connections also implement a "winner-takes-all" mechanism. The principal cells with the most excitation recruit feedback inhibition to prevent action-potential firing in the remaining population of cells. Therefore in this case, the term "winner" actually refers to the number of cells that have fired to recruit the inhibition ("k"-winners - de Almeida et al., 2009a), and this number is determined by parameters such as excitatory input distribution, principal cell τ_m , and the speed of feedback inhibition.

Winner-takes-all mechanisms are thought to be important for a range of functions: for example contributing to sparse coding (Pernia-Andrade and Jonas, 2014) and pattern separation (Leutgeb et al., 2007) in the dentate gyrus, and grid to place field conversion (de Almeida et al., 2009b). In addition, in hippocampal CA1, where PV⁺ interneurons regulate place fields (Royer et al., 2012), these winner-takes-all structures may allow segregation of place cell assemblies (Geisler et al., 2007; Trouche et al., 2016).

While the contribution of PV⁺ cell rapid signalling mechanisms and coincidence detection towards functions involving feedforward inhibition is relatively clear, it is arguably less so for feedback inhibitory functions. While the speed of inhibition recruitment is clearly important to a meaningful definition of "winner" (de Almeida et al., 2009a), the general sparse mode by which the brain operates (Babadi and Sompolinsky, 2014) raises questions over how a small population of principal cells, with large τ_m and resultant jitter, are able cooperate to recruit a cell specialised to handle large numbers of coincident inputs.

1.4 PV⁺ interneurons and pathology

As may be expected from their wide ranging roles in network function, PV⁺ interneurons are thought to play key roles in a number of pathologies, ranging from disorders historically associated with inhibition, such as epilepsy, to more complex psychiatric diseases such as schizophrenia.

1.4.1 Epilepsy

Epilepsy is a set of neurological disorders characterised by repeated epileptic seizures that often form the endpoint of pathologies such as tumours, infections, stroke and traumatic injury. Seizures are ultimately network-level events and it is likely that multiple, diverse mechanisms overlap to contribute towards seizure likelihood. However, early observations lead to a simple model of epilepsy in which inhibition and excitation act analogously to brakes and an accelerator of an engine. Congruent with this model, GABAergic antagonists enhance seizure likelihood whereas GABAergic agonists broadly suppress ictogenesis, and correspondingly are used as anti-epileptic drugs. In addition, strong activation of glutamatergic synapses increases seizure probability. Furthermore, in mouse models of epilepsy, optogenetic activation of PV⁺ interneurons suppresses seizures and promotes their early termination (Krook-Magnuson et al., 2013).

As might be expected, however, this model is oversimplified (Cossart et al., 2005). While drugs, such as benzodiazepines, are effective in ~80% of patients, simply increasing inhibition fails in ~20% of cases (Kwan et al., 2011). This may be explained by inhibitory cells entering a state such as depolarisation-induced-block, or a failure of hyperpolarising inhibition at the postsynaptic site - for example if Cl⁻ accumulates intra-cellularly and erodes the GABA receptor driving force. However, there are other features of epilepsy, such as its episodic nature, that do not sit with such a crude concept as general inhibitory failure (Pavlov et al., 2013).

Finally, it is becoming clear that treating inhibition as a homogeneous population of interneurons is also simplistic, instead, the role of fast somatic inhibition by PV⁺ cells is likely distinct from the slower inhibition mediated by dendritic targeting

interneurons, such as SOM⁺ neurons (Khoshkhoo et al., 2017). It is also probable that the role of inhibition, and the underlying interneuron subtype, is context dependent. For example, in a study in which PV⁺ interneurons were optogenetically activated either during ictal, or interictal phases, of 4-AP induced seizures, uncovered respectively anti-epileptic or ictogenic roles of PV⁺ cells (Assaf and Schiller, 2016).

1.4.2 Schizophrenia

Despite schizophrenia's etymology, translating from Greek as "splitting of the mind", and public perception, schizophrenia is not characterised by split personalities. Instead, schizophrenia is a complex psychiatric disorder characterised by disordered thoughts, delusions, and abnormal social behaviour. Schizophrenic symptoms are often classified as either positive or negative: positive aspects include hallucinations, delusions and cognitive deficits, whereas behaviours including social withdraw and lack of motivation are referred to as negative symptoms and generally respond poorly to medication.

A leading hypotheses in schizophrenia research is one of NMDA receptor hypofunction. NMDA receptor blockers, such as ketamine and MK-801, induce a range of schizophrenic symptoms in control volunteers (Krystal et al., 1994), and reinstate previous symptoms in stabilised schizophrenic patients (Lahti et al., 1995). Another dominant pathophysiological observation is impaired GABAergic signalling, this is based on post-mortem studies that show reductions in cortical PV, GABA, and GAD, the enzyme that synthesises GABA (Perry et al., 1979).

Several lines of evidence suggest that impaired signalling by NMDA receptors specifically in PV⁺ interneurons underlies some features of schizophrenia. First, the loss of interneurons is mainly restricted to PV⁺ interneurons (Zhang and Reynolds, 2002). Second, repeated administration of NMDA receptor blockers reduces GAD67 and parvalbumin in PV⁺ interneurons (Behrens et al., 2007). Finally, mice with genetic deletion of NMDARs from PV⁺ interneurons exhibit many symptoms of schizophrenia, altered gamma oscillations, and the schizophrenic behavioural effects of the NMDA receptor blocker MK-801 are occluded (Belforte et al., 2010; Carlén et al., 2012) - though this is controversial (Bygrave et al., 2016).

1.5 Thesis Overview

This thesis addresses the general physiology and function of PV⁺ interneurons, but most specifically how they handle synaptic inputs. I first present work showing they integrate feedback excitatory synaptic input in a NMDAR-dependent nonlinear manner, which adds a number of computational properties to the networks in which they are embedded. I also explore sublinear synaptic integration due to polyamine modulation of CP-AMPA receptors using computational simulations. Synaptic summation dictates how neurons behave both during physiology and pathology, and finally, I discuss work investigating PV⁺ interneuron activity during epilepsy.

Chapter 2 provides an overview of the methodology used to investigate PV⁺ interneuron synaptic integration and its functions. This chapter is relevant for **chapters 3 & 4**. There are three main methodological areas: first, electrophysiological techniques were used to interrogate synaptic integration rules and the underlying mechanisms; second, multicompartmental modelling, using the NEURON simulation environment, augmented and provided deeper insights into the electrophysiological experiments; and finally, networks of spiking model neurons were used to investigate the network-level functions of supralinear synaptic integration at feedback connections.

Chapter 3 addresses the integration of synaptic inputs by PV⁺ interneuron dendrites using glutamate-uncaging. Here, we show that dendrites in the stratum oriens, which receive recurrent collaterals from local pyramidal cells, display NMDAR-dependent supra-linear integration, whereas stratum radiatum dendrites sum inputs linearly. This difference is dependent on a combination of morphological differences, and an imbalance of NMDA receptor conductance, between the two dendritic locations. Finally, we investigate the role of these synaptic integration rules in the context of winner-takes-all networks.

Chapter 4 explores the role polyamine modulation of PV⁺ interneuron CP-AMPA receptors may have in augmenting the array of electrophysiological mechanisms, already known to be expressed by PV⁺ cells, that contribute to input sublinearity and coincidence detection.

Chapter 5 documents time-dependent anti- and pro- epileptic properties of PV⁺ interneurons in an acute in vivo model of seizure activity. The later part of the

chapter is concerned with extending this work to a spontaneous model of epilepsy. For this project, my main contributions were the development and implementation supervised learning analysis workflows. As such, this workflow forms the main body of the chapter, and secondary methods discussion is also included to extend chapter 2.

Finally, in **Chapter 6**, I discuss implications and caveats of this work as a whole, and draw insights from the distinct lines of research presented in this thesis.

1.6 Acknowledgement of contributions

It is hard, and perhaps improper, to claim sole responsibility for the insights, hypotheses, and, indeed, successful experiments that constitute this thesis. Instead, ultimately, this thesis is the product of innumerable discussions with the people that I have been lucky enough to meet throughout the course of this PhD. Of these, I'd like to highlight the contributions of the following people: Professor Dimitri Kullmann, Professor Michael Hausser, Dr. Vincent Magloire, Dr. Marion Mercier, Dr. Marco Leite, Dr. Matej Macak, Dr. Arnd Roth, Dr. Christian Wilms, Dr. Christoph Schmidt-Hieber, Dr. Beverly Clark, Dr. Forrest Collmann, Dr. Kristina Micheva, Matt Hoddinott, Soyon Chun, Dr Yamina Bakiri, Dr. Kaiyu Zheng, Dr. Lucie Bard, Dr. Piotr Mikhaluk.

There are, however, those that have contributed directly to the work presented in this thesis. I gratefully acknowledge the assistance and collaboration with Dr. Marco Leite in developing the spiking neuron network simulations presented in chapter **Chapter 3**, and I thank Dr. Marion Mercier for the in vitro field-stimulation experiments investigating NMDA receptor-mediated conductances at feedforward and feedback excitatory inputs onto PV⁺ cells, also presented in **Chapter 3**. I also thank Dr. Vincent Magloire for the pilocarpine epilepsy model surgeries, experiments, and network-state annotations presented in **Chapter 5**, and to Albert Snowball for providing the data from the tetanus-toxin epilepsy model, also presented in **Chapter 5**.

Chapter 2

Methods

2.1 Electrophysiology

2.1.1 Mouse lines

All procedures were carried out in accordance with the UK Animals (Scientific Procedures) Act, 1986.

Hippocampal slices were obtained from postnatal day 14-24 male and female mice group-housed under a standard non-reversed light/dark cycle, allowed access to food and water *ad libitum*. Experimental mice were obtained from breeding pairs that consisted of a homozygous mouse expressing Cre under the PV promoter (Jackson Labs: B6;129P2-Pvalb^{tm1(cre)Arbr}) and a homozygous Ai9 Cre reporter mouse (Jackson Labs: B6.Cg-Gt(*ROSA*)26Sor^{tm9(CAG-tdTomato)Hze}) resulting in heterozygous experimental animals with red fluorescent protein variant tdTomato in neurons expressing PV. Due to the age-dependence of PV-Cre-driven recombination (Carlén et al., 2012), weak tdTomato expression is expected 13 days postnatal (Carlén et al. 2012 Fig. 1A), however, using wide-field fluorescence PV expressing cells could be reliably identified.

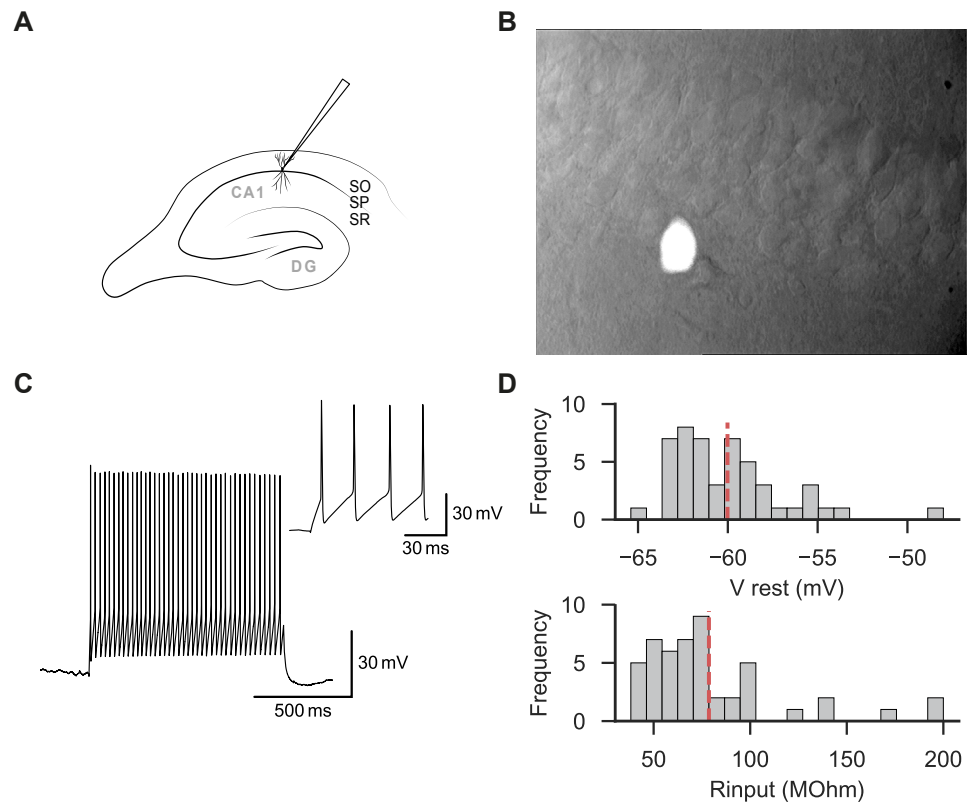


Figure 2.1. Recording from PV⁺ cells: (A) Recording schematic (B) Overlay of Dodt contrast and epifluorescence image (C) Firing response of an example PV⁺ cell to 500 pA somatic current injection. Top right, blow-up of first 4 spikes. (D) Histograms of resting membrane potentials (mV) of recorded cells upon break-in and their input resistances (MΩ). Red lines denote means, n = 49

2.1.2 Slice Preparation and electrophysiological recording

Acute sagittal brain slices (300 μm) were prepared using a Vibratome (Leica VT1200 TS). Slices were cut in an ice-cold artificial cerebrospinal fluid (ACSF) solution, containing (in mM): NaCl (119), KCl (2.5), NaH_2PO_4 (1.25), NaHCO_3 (25), Glucose (20), CaCl_2 (1.5), MgSO_4 (1.3), saturated with 95 % O_2 and 5% CO_2 gas. Slices were allowed to recover at 32°C for 15 minutes after slicing, before subsequent storage in ACSF at room temperature.

Electrophysiological experiments were carried out in ACSF, as prepared for slice preparation, saturated with 95% O_2 and 5% CO_2 gas and maintained at 30-32°C. Slices were placed in a submerged recording chamber with single perfusion tubing and perfused with ACSF at a rate of 2-3 ml/min. Wide-field epifluorescence was used for targeted whole-cell patch clamp recordings of PV⁺ cells in the stratum pyrami-

dale of CA1 hippocampus. The presence of a fast-spiking firing response to square wave current injection was used to confirm accurate recording. Electrophysiological properties of recorded cells were typical for fast-spiking interneurons (Lamsa et al., 2007): $V_{\text{rest}} = -60.0 \pm 0.45$ mV, $R_{\text{input}} = 78.6 \pm 5.2$, n=49 cells, (Fig. 2.1).

Somatic whole-cell recordings were acquired with custom LabVIEW software (Professor Dimitri Kullmann) using a Multiclamp 700B amplifier (Molecular Devices), digitised at 20 kHz and low-pass filtered at 5 kHz. Patch pipettes of 3-4 M Ω were filled with a KGlu-based internal solution, containing (in mM): K-Gluconate (140), K-OH-HEPES (10), EGTA (0.2), NaCl (8), Mg-ATP (2), Na-GTP (0.3), Mg-ATP (5). Series resistance of recordings was typically less than 20 M Ω .

2.1.3 Two-Photon Imaging and Uncaging

For two-photon imaging and uncaging slices were mounted on an upright microscope with a 25x water immersion objective (Olympus FV1000MPE: Upright Microscope BX61, Olympus; objective Olympus XLPlan N 25x 1.05 NA, FV10-ASW Software Olympus). Simultaneous two-photon imaging and uncaging of 4-Methoxy-7-nitroindolyl-caged-L-glutamate (MNI-caged glutamate) (Matsuzaki et al., 2001) was performed with two Ti-sapphire lasers tuned to 800 nm and 720 nm for imaging and glutamate uncaging respectively (Chameleon, Coherent; Mai-Tai, Spectra Physics). Laser-light deflection was achieved via two separate galvanometer scanning mirror sets controlled by a voltage command (Olympus).

For both imaging and uncaging laser scanning units calibration procedures were as follows. First, we used 6 μm fluorescent beads were used for rough alignment - we acquired a z-stack to ensure that the centre of the fluorescent bead did not move laterally as z position was varied. Then, for finer adjustment and assessment of psf (theoretical two-photon psf of objective $\sim 300 \times 1350 \mu\text{m}$ (Yang and Yuste, 2017)) 150 nm beads were used for the z-stack. In order to ensure overlay of the x, y coordinates for the two scanning systems (required to co-register uncaging spots and structural images), x and y voltage offsets between the two scanning systems were checked and adjusted regularly by imaging 6 μm beads with both scanning units.

MNI-caged-glutamate-TFA (3 mM; Femtonics) was dissolved in the recording

ACSF solution and recycled around the bath in a closed perfusion system (~7 ml). For structural visualisation of the recorded cell Alexa-594 (50 μM ; ThermoFischer) was included in the internal KGlu-based internal recording solution. In a subset of experiments D(-)-2-Amino-5-phosphonopentanoic acid (APV) (100 μM) and tetrodotoxin (TTX) (0.1 μM) were added to the ACSF to respectively block NMDA receptors and voltage gated Na^+ channels.

After obtaining whole-cell patch clamp configuration and waiting ~5 minutes for the Alexa-594 in the pipette solution to diffuse into the cell, 800 nm laser-light (5-10 mW) was used to excite the Alexa-594 and visualise the cell. A dendritic region of interest was then selected between 40 and 250 μm from the soma. Locations for uncaging were selected either side of the dendritic region of interest, separated by 2-3 μm and within 1 μm of the dendrite. These uncaging spots were placed in a (experimenter determined) pseudo-randomized order to prevent direction specific summation artefacts due to dendritic tapering (Branco et al., 2010). All uncaging-evoked EPSPs (uEPSPs) were evoked using 0.5 ms long pulses of 720 nm laser-light. To account for differing depths of dendritic segments, uncaging-laser intensity was adjusted using a Pockels Cell (Conoptics), between 15-60 mW, to produce uEPSPs of comparable size to spontaneous EPSPs.

We measured the summation of uEPSPs evoked at the different dendritic regions by recording somatic potentials while uncaging at increasing numbers of uncaging locations. In detail, k (8-12) glutamate-uncaging spots were activated in increasing numbers over k number of "trials", starting with one location, with an additional location recruited per trial until all uncaging spots were stimulated. Within each trial, activation of uncaging locations was separated by an interval of 1 ms (0.5 ms dwell-time, 0.5 ms wait). The set of trials from 1 to k active uncaging spots was defined as a cycle. Within a cycle, trials were separated by a delay of a 10 s. Cycles were occasionally aborted if significant "drift" from the original image position was noted, or if photo-damage occurred. At least three cycles were generally recorded per dendritic location. Uncaging times and locations were controlled by a combination of Olympus software (FV10-ASW) and a pulse generator connected to the Pockels cell (Berkeley Nucleonics, Model 575 2-channel Pulse Generator).

To compare the measured uEPSP summation with theoretical compound uEPSPs we generated expected uEPSPs by arithmetic summation of individual uEPSP waveforms. First, individual uEPSPs were evoked by stimulation of uncaging spots

with an inter-uncaging interval of 200 ms. Acquisition of these uEPSP responses was interleaved with the cycles of uEPSP integration described in the previous paragraph. Next off-line, after the experiment, we summed the individual uEPSP waveforms with the k^{th} waveform delayed by k ms. This delay was required to match the experimental delay imposed by the 0.5 ms laser dwell time, and 0.5 ms wait-time between uncaging spot activations (Figure 2.2). uEPSP integrals were calculated over the 50 ms following glutamate uncaging of filtered traces. For comparison of uEPSPs to spontaneous EPSPs, time to peak was calculated as the time from manual start time annotation to the maximum filtered EPSP.

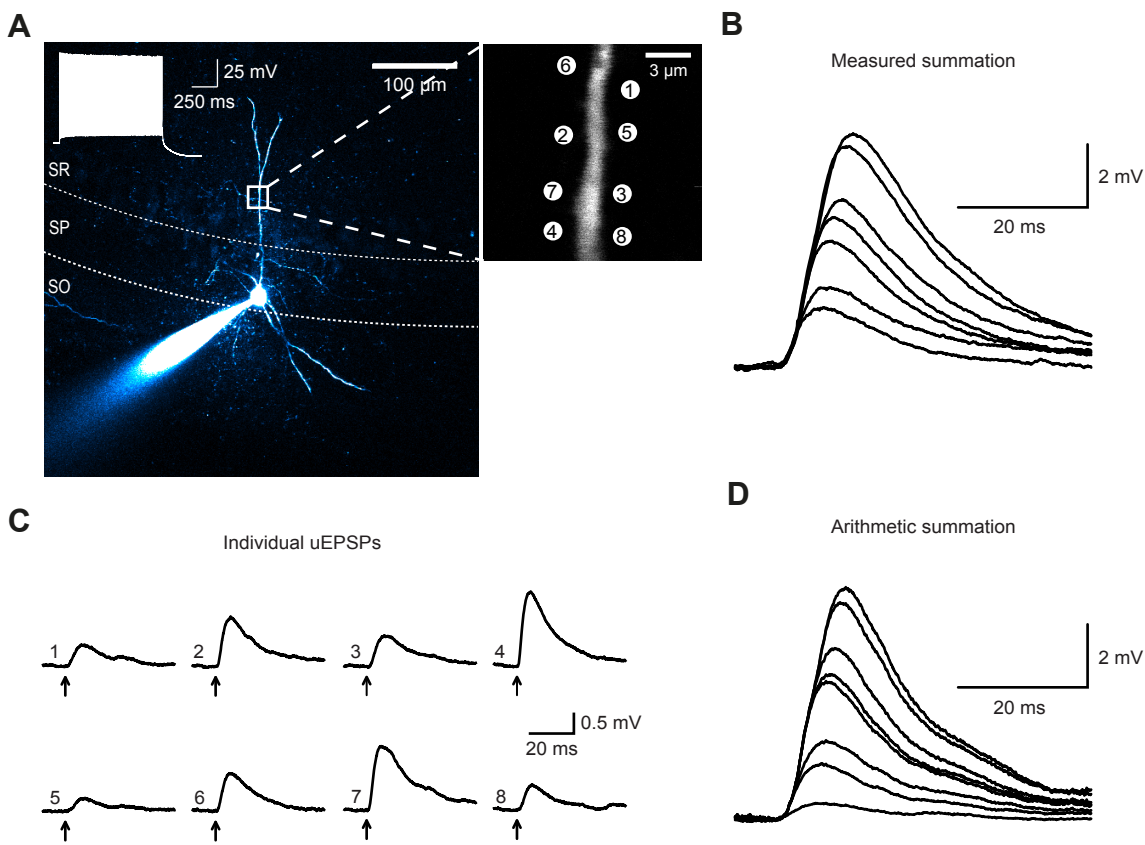


Figure 2.2. Measuring dendritic integration: (A) Two-photon z-stack of PV⁺ interneuron in CA1. Box and inset, dendritic region of interest and uncaging locations. (B) uEPSP waveforms measured after activation of increasing numbers of uncaging locations. (C) Individual responses to the uncaging locations 1-8. (D) Arithmetic uEPSP waveforms calculated by cumulatively adding waveforms in (C).

2.1.4 Pharmacological dissection of NMDA receptor conductance

These experiments were performed to investigate the ratio of NMDA receptor-mediated conductance at feedforward and feedback inputs onto PV⁺ interneurons. They were carried out in collaboration with Dr. Marion Mercier. Experimental design and pilot data acquisition were done in collaboration, but the rest of the data presented were gathered by Dr. Marion Mercier. I analysed the data.

For field stimulation experiments, concentric bipolar stimulating electrodes (FHC), coupled to constant current stimulus isolation units (Digitimer), were placed in the alveus and stratum radiatum of CA1. Stimulation of the electrode placed in the radiatum therefore recruited feedforward Schaffer collateral fibres, whereas stimulation of the electrode placed in the alveus evoked antidromic local pyramidal cell feedback inhibition (Pouille and Scanziani, 2004). Stimuli were delivered to each pathway at 0.05 Hz, and alternated between the two pathways.

During field stimulation, PV⁺ cells (recorded as in section 2.1.2) were held at -60 mV, close to their resting potential, in order to minimise space-clamp errors. In order to record NMDA receptor conductance at this membrane potential, a modified ACSF containing 0.1 mM MgSO₄ was used. At this concentration of external Mg²⁺ it is expected that NMDA receptors will be half relieved from Mg²⁺ block at -60 mV (Jahr and Stevens, 1990). Feedback and feedforward inhibitory currents were prevented by inclusion of the GABA_A and GABA_B receptor blockers picrotoxin (100 μM) and CGP 55845 (1 μM) in the ACSF. In addition, to reduce the likelihood of recurrent seizure-like activity the CA3 region was micro-dissected. Finally, in these low external Mg²⁺ conditions, Schaffer collateral stimulation often elicited feedback excitation; the HCN channel blocker ZD7288 (30 μM) was therefore also included in the ACSF in order to hyperpolarise local pyramidal cells and thereby reduce this rebound CA1 activity (Pavlov et al., 2011).

Under these conditions, baseline glutamatergic responses were obtained from both stimulation sites. NBQX (10 μM) was then added to the ACSF in order to block AMPA receptors and isolate the NMDA receptor component of the response. After 20 minutes of recording, APV (100 μM) was added to the ACSF to block NMDA receptors.

For analysis of NMDA and AMPA receptor ratios, isolated NMDA and AMPA receptor traces were extracted via subtraction of EPSC waveforms. In order to isolate the AMPA receptor component, responses recorded in the presence of NBQX were subtracted from those recorded during baseline. To isolate the NMDA receptor component, responses recorded in both NBQX and APV were subtracted from those recorded in NBQX only. The total NMDAR- or AMPAR-dependent charge was then calculated by integrating the first 300 ms or 50 ms, respectively, of these isolated traces.

2.1.5 Data Analysis and Statistics

Data analysis was performed using custom code written in Python. As described in section **2.1.3**, in order estimate arithmetic uEPSP summation, the individual membrane potential waveforms were first shifted by the experimental intra-uEPSP delay of 1 ms and then summed linearly to construct an arithmetic uEPSP. The difference between these arithmetic uEPSPs and measured uEPSPs was quantified in terms of nonlinearity for each dendritic location using the following equation:

$$\text{nonlinearity \%} = \sum_{i=2}^n \left(\frac{M_i}{A_i} - 1 \right) / (n - 1) \times 100$$

where:

- M_i is the amplitude of the i th measured uEPSP (composed of i individual uncaging spots)
- A_i is the amplitude of the i th constructed arithmetic summed uEPSP, and n is the total number of uncaging locations

The same analysis method was used to quantify uEPSP integral nonlinearity, which was calculated over 50 ms. A Savitzky-Golay filter was applied before taking the integral of the traces.

Statistical significance was assessed using Student's paired or unpaired t-tests unless otherwise stated, and was considered significant when $p < 0.05$. Datasets are

presented as mean \pm SEM, unless stated otherwise. The t-test was deemed a suitable test due to its robustness to departures from normality of the sample population. This is because it assumes that the means of repeated samples are normally distributed, which, due to central limit theorem, is true for large samples of even extremely non-normal data (Lumley et al., 2002).

When analysing correlations, for example between uncaging distance from soma and uEPSP integration nonlinearity, Pearson correlation coefficients were calculated to measure the linear relationship between two variables. The coefficient is denoted with r in the text and figures. The formula for the Pearson correlation coefficient between two variables x and y is:

$$r = \frac{\Sigma(x_i - \bar{x})(y_i - \bar{y})}{\sqrt{\Sigma(x_i - \bar{x})^2 \Sigma(y_i - \bar{y})^2}}$$

Where \bar{y} and \bar{x} denote the sample means.

2.2 Multi-Compartmental modelling

Multi-compartmental modelling simulations were performed with the NEURON (version 7.4) simulation environment (Hines and Carnevale, 1997) in combination with Python (version 3.5).

2.2.1 Hippocampal CA1 PV⁺ interneuron model

The soma and dendrites of a PV⁺ interneuron were reconstructed using the TREES toolbox in MATLAB (Cuntz et al., 2010). The axon was not included in the reconstruction. As PV⁺ interneuron dendrites are generally smooth, addition of spines or correction of synaptic responses for spines was deemed unnecessary. The number of segments per section was constrained to odd numbers and set according to the d-lambda rule (Carnevale and Hines, 2009) to have a length no more than 10% of alternating current length constant at 1 kHz. The model contained 500 segments in

total with a maximal segment length of $8.7 \mu\text{m}$. Adequate spatial discretisation was also verified by increasing the number of sections by a factor of 3, which caused very minimal changes in the voltage response of the model to simulations, when recorded both at the dendrite and the soma.

Table 2.1. Parameters used for NEURON model and simulations

Parameter	Proximal	Distal	Units
C_m	0.9	0.9	$\mu\text{F cm}^{-2}$
R_{axial}	170	170	$\Omega \text{ cm}^{-1}$
R_m	5.55	55.5	$\text{k}\Omega \text{ cm}^2$
e_{leak}	-65	-	mV
e_{gK}	-90	-	mV
e_{gNa}	55	-	mV
v shift	-12	-12	mV
$g_{\text{k dend}}$	300	300	$\text{pS } \mu\text{m}^{-2}$
$g_{\text{Na dend}}$	200	100	$\text{pS } \mu\text{m}^{-2}$
$g_{\text{Na soma}}$	2000	-	$\text{pS } \mu\text{m}^{-2}$

Note: here, "e" refers to reversal potential, C_m and R_m are specific membrane capacitance and resistance.

The biophysical parameters were based on previously published models of dentate gyrus PV⁺ basket cells (Nörenberg et al., 2010; Hu and Jonas, 2014). The specific membrane capacitance (C_m) and intracellular resistance (R_i) were assumed to be spatially uniform (for values see table 2.1). In contrast, the specific membrane resistance (R_m) was assumed to vary as a step function with distance from the soma. R_m at distal dendrites was 10 times larger than at proximal dendrites, and R_m was chosen so the model cell's input resistance was $78 \text{ M}\Omega$, the mean experimentally recorded input resistance ($78.6 \pm 5.2 \text{ M}\Omega$). The border between proximal and distal dendrites was defined to be $120 \mu\text{m}$ from the soma, in line with previous models of dentate gyrus PV⁺ basket cells (Nörenberg et al., 2010).

Wang and Buzsaki (WB) Na⁺ and K⁺ channels were inserted in the model neuron to confer a fast-spiking action potential phenotype (Wang and Buzsáki, 1996). However, in order to produce a realistic firing frequency current injection relationship a hyperpolarising voltage shift was included in the WB implementation. This inadequacy of unadjusted WB mechanism has been previously been discussed (Ferguson et al., 2013).

All simulations were run with an initial resting membrane potential of -65 mV , a

time-step of 0.01 ms, and temperature set to 32 °C, unless otherwise stated.

2.2.2 Synaptic receptors

NMDA and AMPA receptor conductances were implemented using kinetic state models that were connected to a simple step function glutamate release mechanism. NMDA receptors were modelled using a 10 state gating model (Branco et al., 2010), whereas AMPA receptors were modelled using a 6 state scheme. Glutamate release lasted 0.5 ms and was varied between 1-3 mM depending on the simulation. Maximal peak conductances (used to multiply the receptor open fraction) for the mechanisms were chosen to produce a peak synapse current of $\approx \leq 50$ pA at -60 mV, and were varied depending on the simulation in the range 0-5 nS and 0-8 nS for AMPA and NMDA receptors respectively.

The rates, and kinetic scheme, used for the AMPA receptor model, were taken from a kinetic scheme of GluR6(Q) receptors (Bowie et al., 1998), and it is therefore technically a kainate receptor. This approach was initially taken in order to model the effects of polyamine modulation of glutamate receptors (detailed in Chapter 4). However, we then compared the model receptor to a commonly used alternative AMPA receptor model (Destexhe et al., 1998), but found the GluR6 receptor to be more suitable for modelling AMPA receptor currents on PV⁺ cells, as it had a faster decay time constant (Figure 2.3).

For the NEURON simulations in which we investigated the effects of polyamine blockade of CP-AMPA receptors, described in Chapter 4, voltage dependent polyamine binding was modelled as detailed in the study from Bowie et al., 1998. The equations describing the on and off rate constants as a function of voltage (V) for polyamine binding were:

$$k_{on} = a \exp(V/b)$$

$$k_{off} = c \exp(V/d)$$

Where:

- $a = 48.5 \mu\text{M}^{-1}\text{sec}^{-1}$
- $b = 98.8 \text{ mV}$
- $c = 132.3 \text{ sec}^{-1}$
- $d = -18.1 \text{ mV}$

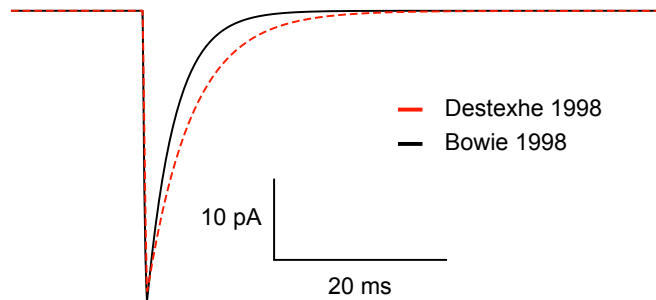


Figure 2.3. Model kinetic scheme glutamate-receptor comparison

2.2.3 Simulation protocol

NEURON simulations were used to investigate the effect that dendrite morphology might have on experimental results. Therefore, simulations closely followed experimental protocol. In line with experimental distances, sites on the dendritic tree that were located between 50 and 250 μm from the soma were chosen as the centre of uncaging locations. Simulations replicated the experimental uncaging protocol detailed above. At each dendritic site, 15 synapses were placed within a distance of 30 μm . Each synapse was activated individually and the arithmetic sum calculated from the somatic membrane potential. Synapses were then activated in increasing numbers, in a random order, with an interval of 1 ms between activations, and the integral (50 ms) and amplitude of these measured responses compared to the calculated arithmetic responses. Quantification of dendritic nonlinearity was identical to experimental data (section 2.1.5).

2.3 Network Modelling

The work presented involving network modelling was done in collaboration with Dr. Marco Leite.

2.3.1 Spiking single neuron models

Network simulations were run using simple two dimensional Izhikevich neuron (Izhikevich, 2003) models of CA1 PV+ interneurons and CA1 pyramidal cells (Fig. 2.4). Izhikevich-like models for these two CA1 neurons have previously been parameterised from experimental data (Ferguson et al., 2013, 2014). In line with this work, neuron models were slightly modified from (Izhikevich, 2003), in order to reproduce a narrow PV+ interneuron spike width, and had the following form:

$$C_m \frac{dv}{dt} = k(v - v_r)(v - v_t) - u + I_{applied}$$

$$\frac{du}{dt} = a[b(v - v_r) - u]$$

if $v \geq v_{peak}$, then $v = c, u = u + d$

Where $k = k_{low}$ if $v \leq v_t$; $k = k_{high}$ if $v > v_t$

The variable v (mV) is the membrane potential, and u (pA) represents a slow refractory current that is responsible for firing frequency adaptation. u is increased by d when the neuron fires, and decays at a rate determined by a . The parameter b controls the sensitivity of u to subthreshold voltage fluctuations. This refractory current can be interpreted as an abstract representation of K^+ channel activation and Na^+ channel inactivation.

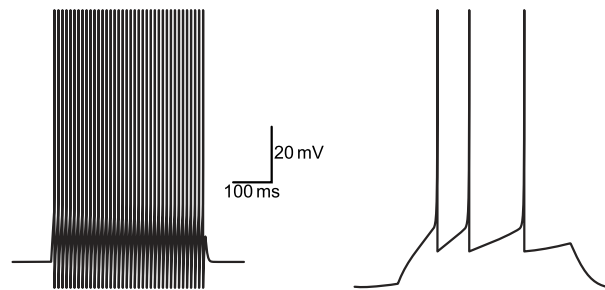


Figure 2.4. Izhikevich model neurons used in network simulations. Figure shows the voltage response of a 300 pA current injection to a model FS PV+ interneuron (left), and a 50 pA application to a model pyramidal cell (right). Parameters describing neurons are found in Table 2.2.

The specific values used for the model Izhikevich neurons are shown in Table 2.2. Model parameters are as follows:

- C_m (pF) is the cell's membrane capacitance
- k (nS/mV) is a scalar
- v_r (mV) is the resting membrane potential
- v_t (mV) is the spike initiation threshold potential
- $I_{applied}$ (pA) is the applied current, comprised of synaptic input to the cell
- a (ms^{-1}) is the recovery inverse time constant of the refractory current, u .
- b (nS) is the sensitivity of u to subthreshold voltage fluctuations
- c (mV) is the voltage reset value
- d (pA) is the amount of current generated by the after-spike behaviour

Table 2.2. Izhikevich model parameters

Parameter	FS PV ⁺	Pyramidal	Units
C_m	90	115	pF
k_{high}	14	3.3	nS/mV
k_{low}	1.7	0.1	nS/mV
v_r	-60.6	-65.8*	mV
v_t	-43.1	-57	mV
$I_{applied}$	-	-	pA
a	0.1	0.0012	ms^{-1}
b	-0.1	3	nS
c	-67	-65.8	mV
d	0.1	10	pA

* denotes a value change from reference paper (Ferguson et al., 2013, 2014). Pyramidal cell v_r changed from 61.8 to 65.8 mV as the original 61.8 mV resulted in a rheobase of 0 pA.

2.3.2 Network structure

Networks were composed of 250 pyramidal cells and one PV⁺ interneuron unless otherwise stated. Both the pyramidal cells and PV⁺ interneurons received external

input (detailed in section 2.3.4). In brief, external synaptic inputs to each neuron were modelled as being drawn from individual Poisson processes, with neuron specific intensity parameters that dictated the probability of presynaptic spikes (this is shown as the Gaussian curve marked "External input" in 2.3.4). External input to the PV⁺ interneuron was modelled as a scaled sum of the input to the pyramidal cell population. The pyramidal cell population was connected to the PV⁺ interneuron with both AMPAR- and NMDAR-like synapses, which recurrently inhibited both the pyramidal cell population and itself. Figure 2.5 shows a diagram of network structure.

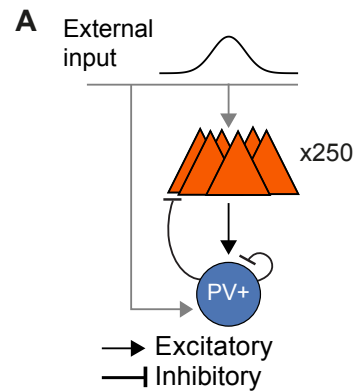


Figure 2.5. Network architecture: (A) 250 pyramidal cells connected recurrently to a single PV⁺ interneuron. Both the pyramidal cell population and the PV⁺ interneuron receive excitatory external input.

2.3.3 Synaptic modelling

All synaptic connections between neurons were modelled as conductance based synapses, with synaptic conductances described by a difference of two exponentials (Roth and van Rossum, 2009). Rise and decay time constants for the two exponentials for the different synapses are shown in Table 2.3. Synaptic currents therefore had the following bi-exponential form:

$$I_{syn} = g(t)(E_{syn} - v) \quad (2.1)$$

$$g(t) = G \frac{1}{\tau_1 - \tau_2} \left(e^{-\frac{t}{\tau_1}} - e^{-\frac{t}{\tau_2}} \right) \quad (2.2)$$

Where:

- E_{syn} (mV) is the synaptic reversal potential
- G (nS) is the total conductance integral.
- τ_1 (ms) is the decay exponential time constant
- τ_2 (ms) is the rising exponential time constant
- t is time (ms).

Table 2.3. Network synaptic parameters

Parameter	FS PV ⁺	Pyramidal	Units
$\tau_{1 \text{ GABA}}$	2.5	6.5	ms
$\tau_{2 \text{ GABA}}$	0.3	0.26	ms
$\tau_{1 \text{ AMPA}}$	0.77	1.7	ms
$\tau_{2 \text{ AMPA}}$	0.25	2	ms
$\tau_{1 \text{ NMDA}}$	60	-	ms
$\tau_{2 \text{ NMDA}}$	2	-	ms

These parameters were based on the values and references detailed in (Roth and van Rossum, 2009).

2.3.3.1 NMDA receptor modelling

NMDA receptors present at the feedback connections from CA1 pyramidal cells onto CA1 PV+ interneurons were modelled in an abstract manner. All co-active inputs from the population of n pyramidal cells were assumed to have a degree of cooperation, or functional clustering (Wilson et al., 2016). A distance matrix, $D^{N \times N}$, was used to describe this cooperation and was defined as a Toeplitz matrix, with the i_{th} element of the row vector $D_{\frac{n}{2}}$ equal to:

$$D_{\frac{n}{2},i} = \frac{1}{\sqrt{2\sigma^2\pi}} e^{-(i-n/2)^2/2\sigma^2}$$

Where the parameter σ^2 controlled the specificity of local cooperation. This distance matrix, shown in Figure 2.6 C, was inspired both by functional clustering of synapses (Wilson et al., 2016), and by the electrotonic structure of neurons, in which

neighbouring synapses on a dendritic branch interact more than synapses further away. These synaptic relationships can be seen in the steady state electronic signature that can be calculated from neuron morphology (Figure 2.6 B (Cuntz et al., 2010)). Defining the cooperativity matrix, D , as described above allowed us to approximate the electrotonic structure and synaptic clustering in a simple manner.

The PV⁺ interneuron postsynapses were modelled as patches of membrane containing both AMPA and NMDA receptors. In order to calculate the NMDAR conductance for a given postsynaptic location, the degree of Mg⁺ dependent NMDAR block was calculated from the postsynaptic membrane patch voltage according to equation 2.5 (IV relationship shown in Figure 2.7). The time evolution of the i th membrane patch voltage was determined by equation 2.3. To obtain current flowing into the i th patch, the i th patch voltage was used as the driving force for the sum of all patch conductances weighted by the distance matrix (Eq. 2.4). The somatic membrane potential was then used to calculate the driving force for the somatic currents originating from each postsynaptic patch.

The equations describing the postsynaptic membrane voltage, for the i th synapse, were therefore:

$$C^{syn} \frac{dv_i^{syn}}{dt} = k^{syn} I_i^{syn} + g^{leak} (e^{leak} - v_i^{syn}) \quad (2.3)$$

$$I_i^{syn} = \sum_{j=1}^n D_{i,j} (g_j^{ampa} + g_j^{nmda}(v_j^{syn})) (e^{glu} - v_i^{syn}) \quad (2.4)$$

$$g_i^{nmda}(v) = gmax_i^{nmda} \left(\frac{1}{2} \cdot \tanh \left[\frac{v_i^{syn} + 50mV}{10mV} \right] + \frac{1}{2} \right) \quad (2.5)$$

Where $gmax_i$ comes from equation 2.2, and the equations describing $I_{applied}$ for the soma were:

$$\begin{aligned} I_{applied} = & k^{ampa} \sum_{i=1}^{n_{yr}} g_i^{ampa} (e^{glu} - v) \\ & + k^{nmda} \sum_{i=1}^{n_{pyr}} g_i^{nmda} (v_i^{syn}) (e^{glu} - v) \\ & + k^{gaba} \sum_{i=1}^{n_{pv+}} g_i^{gaba} (e^{gaba} - v) \\ & + k^{ext} \sum_{i=1}^{n_{pyr}} g_i^{ext} (e^{glu} - v) \end{aligned} \tag{2.6}$$

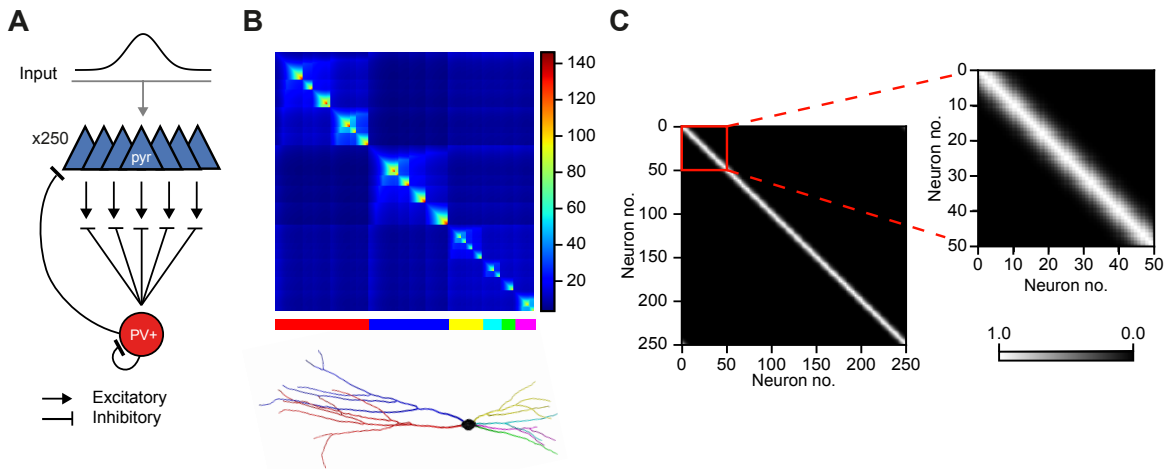


Figure 2.6. Modelling input cooperation onto PV⁺ cells: **(A)** Network schematic showing postsynaptic membrane patches of PV cell. Patches received neighbouring patch conductances weighted by matrix in panel C. **(B)** Steady state electrotonic inter-connectivity for a reconstructed PV⁺ interneuron used in NEURON simulations using TREES toolbox (Cuntz et al., 2010). The matrix shows the electrotonic 'proximity' of neighbouring patches of membrane on the dendritic tree (colour scale: $\mu\text{V}/\text{pA}$). The main branches of the dendritic tree are indicated at the bottom. **(C)** Cooperativity "distance" matrix used in simulations. Inset shows zoomed view of the cooperativity matrix for the neurons in range 0-50.

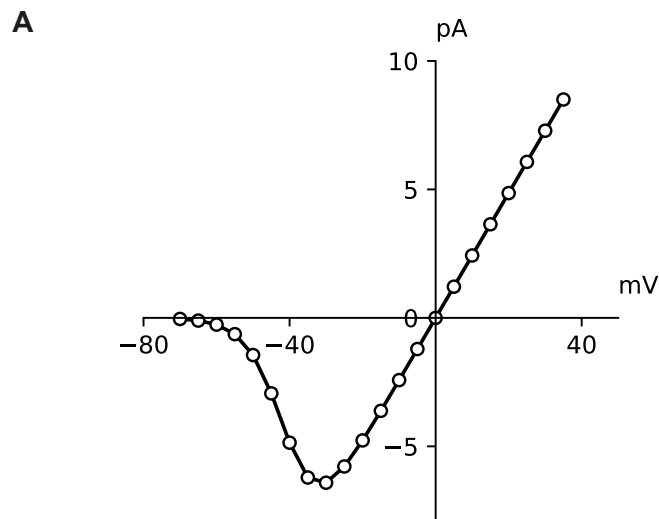


Figure 2.7. NMDA receptor current-voltage relationship: **(A)** Current voltage relationship for NMDA receptors due to Mg^{2+} block described by equation 2.5

2.3.4 External input

Spike times for external input to the i_{th} neuron were modelled as being generated by a homogeneous Poisson process:

$$P(n) = \frac{k_i \lambda^n e^{-k_i \lambda}}{n!}$$

Here $P(n)$ describes the probability of n spikes in a time interval. λ is a homogeneous intensity parameter defining the expected number of spikes in an interval. In addition, k was a neuron specific scaling factor representing a Gaussian receptive field of the neuronal population to an abstract stimulus, and was defined for the i_{th} neuron as:

$$k_i = \frac{1}{\sqrt{2\sigma_k^2\pi}} e^{-(i-\mu_k)^2/2\sigma_k^2}$$

- σ_k^2 dictates the width of the receptive field
- μ_k is the location of the neuron at the centre of the receptive field.

At the peak of the receptive field, neurons received around five thousand external input spikes per second. The spike times for each neuron were then convolved with the neuron's AMPA receptor conductance waveform to generate an external conductance input matrix. We modified the external input spike distribution to produce three input patterns (Fig. 2.8): 1. clustered and temporally consistent, 2. clustered but temporally inconsistent, 3. dispersed but temporally consistent.

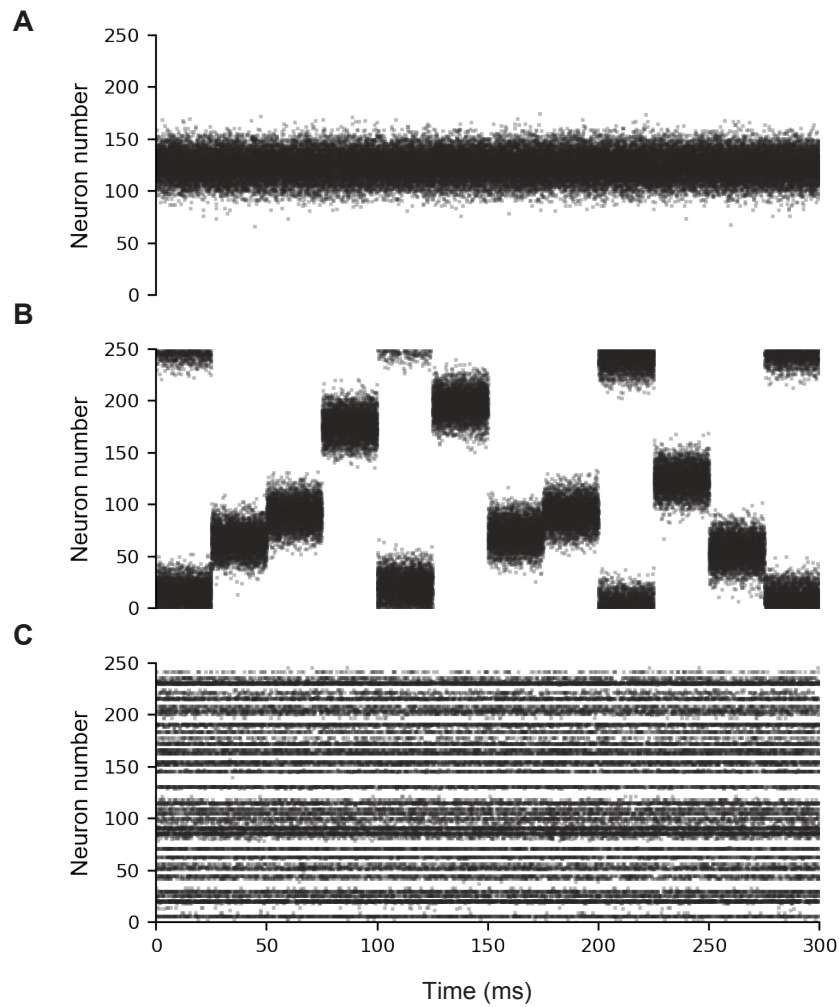


Figure 2.8. External input distributions across pyramidal cells: (A) Clustered, temporally consistent input. (B) Clustered, temporally inconsistent input generated from A by shuffling sections randomly. (C) Dispersed, temporally consistent input, generated from A by shuffling the Gaussian distribution.

Chapter 3

Cooperative synaptic integration of local feedback connections by PV⁺ interneurons

3.1 Introduction

The existence of supralinear synaptic and dendritic mechanisms (Stuart and Spruston, 2015) in response to clustered synaptic input (Takahashi et al., 2012; Wilson et al., 2016), is well established in principal neurons throughout the brain, where they increase neuronal computational ability and information storage capacity (Poirazi and Mel, 2001). In contrast, for PV⁺ interneurons, the most common cortical class of interneuron (~50%), dendritic integration is thought to be linear or sublinear (Hu et al., 2010; Nörenberg et al., 2010), underscoring their role as fast signalling devices, specialised for coincidence input detection and rapid feedforward inhibition (Pouille and Scanziani, 2001).

How these specialized signalling properties facilitate the role of PV⁺ interneurons in feedback circuit motifs, which often form "winner-takes-all" (WTA) microcircuits, (Geisler et al., 2007) is not as well established. While fast and strong feedback inhibition restricts the number of winning neurons (de Almeida et al., 2009*a*), how local principal neurons that are concurrently under feedforward inhibitory control cooper-

ate together to recruit PV⁺ interneurons is unclear.

The role of NMDA receptors on PV⁺ cells is a second area of some controversy. Multiple lines of evidence implicate NMDA receptor dysfunction on PV⁺ interneurons as underlying altered network oscillations (Polepalli et al., 2017) and neurological disorders such as schizophrenia (Jadi et al., 2016). However, these reports, and the importance they assign to PV⁺ NMDA receptors, sit somewhat paradoxically with the theory of fast passive synaptic integration by PV⁺ interneurons: not only do NMDA receptors mediate slow conductances, but they also typically underlie synaptic amplification (Schiller and Schiller, 2001). Furthermore, NMDA receptor content at excitatory to PV⁺ cell synapses is thought to be small (Nyíri et al., 2003), though see (Jones and Bühl, 1993).

There is also evidence that the NMDA receptor content at feedback and feedforward excitatory synapses onto PV⁺ interneurons is not equal. Historically, Grunze et al. found that local recurrent CA1 inhibition could be potentiated in an NMDA receptor-dependent manner (Grunze et al., 1996). More recently, using precise targeting of hippocampal CA1 PV⁺ interneurons, Le Roux et al. again found NMDA receptor-dependent hebbian LTP at feedback synapses, in contrast to feedforward Schaffer collateral inputs that expressed only "anti-hebbian" LTP, dependent on CP-AMPA (Le Roux et al., 2013). According to Le Roux et al., these differing plasticity rules were mediated by enriched NMDA receptor content at feedback connections, relative to feedforward inputs. They presented voltage clamp recordings showing larger NMDAR : AMPAR ratios at feedback synapses than at feedforward synapses (Le Roux et al., 2013).

These ratios were, however, obtained at clamp potentials of +60 and -60 mV, in order to measure NMDA receptor conductances without Mg²⁺ blockade. Unfortunately, this approach is not free of pitfalls: PV⁺ interneurons are large, with long dendrites, and typically display low membrane resistances (additionally, their input resistance decreases at positive potentials - experimental observations), making them unsuitable for whole-cell voltage clamp. Moreover, the dendrites that receive feedback inputs, in the stratum oriens, are shorter than the dendrites in the stratum radiatum, and are therefore potentially less subject to space-clamp errors. Given the well documented issues of obtaining accurate voltage clamp recordings in non-spherical cells (Williams and Mitchell, 2008), which are compounded by the electrophysiological nature of PV⁺ cells, it is possible these ratios are the product of experimental limitations, as opposed

to reflecting NMDA receptor expression differences at the two inputs.

We therefore sought to investigate whether NMDA receptors contributed to differential handling of synaptic responses from feedforward or feedback excitatory inputs by PV⁺ interneurons, and how this affected PV⁺ recruitment in a network setting. To do this we used glutamate uncaging, and made use of the physical separation between the location of feedforward synapses, which are found predominantly on stratum radiatum dendrites (though also in the stratum oriens) and feedback synapses, which are found at dendrites in the stratum oriens (Bezair and Soltesz, 2013; Andersen, 2007).

3.2 Results

3.2.1 Stratum oriens dendrites show supralinear synaptic integration

Two-photon glutamate uncaging was used to mimic synaptic input onto PV⁺ interneuron dendrites in either the stratum oriens or the stratum radiatum (Figure 3.1). Laser power was adjusted to account for varying depths of the dendrite section of interest within the slice, with the aim of eliciting uncaging evoked EPSPs (uEPSPs) of roughly similar amplitude to spontaneous events (sEPSP). sEPSPs were compared to uEPSPs offline (Figure 3.1), both groups exhibited large variability (uEPSP vs sEPSP, minimum amplitude: 0.3 mV vs 0.2 mV, maximum amplitude: 3.3 mV vs 4.4 mV, mean amplitude: 1.11 ± 0.04 mV vs 1.10 ± 0.06 mV, $p = 0.98$, $n = 78$ vs 210, 4 cells). Spontaneous events were faster than uEPSPs however, both time to peak amplitude and half amplitude duration were significantly smaller (uEPSP vs sEPSP, time-to-peak: 4.5 ± 0.13 ms vs 3.1 ± 0.09 ms, $p < 0.0001$, half amplitude duration: 13.5 ± 0.47 ms vs 10.5 ± 0.32 ms, $p < 0.0001$, $n = 78$ vs 210, 4 cells).

Although analysis of a subset of recordings (4 cells) showed on average that uEPSPs were slower than spontaneous events, the overall similarity between uEPSP and sEPSP shapes, and the variability of recorded waveforms, supports the use of glutamate uncaging to investigate dendritic integration. An alternative, possible comparison could have been made between uEPSPs and miniature EPSPs (spontaneously recorded EPSPs in the presence of TTX). A caveat of using spontaneous EPSPs is that a presynaptic cell may potentially make multiple synaptic connections with the PV⁺ interneuron, resulting in large compound EPSPs. However, it is also thought that miniature events may be mediating specific functions distinct from action-potential driven spontaneous release, such as underlying network and synapse stability, and make use of different pre and postsynaptic machinery (Kavalali et al., 2011). Furthermore, pyramidal cells are thought to mainly form single synaptic contacts with PV⁺ interneurons (Gulyás et al., 1993; Sik et al., 1993), thus justifying the use of spontaneous EPSPs.

In order to assess the type of synaptic integration performed by the two dendritic locations we compared the dendritic input-output functions. These functions

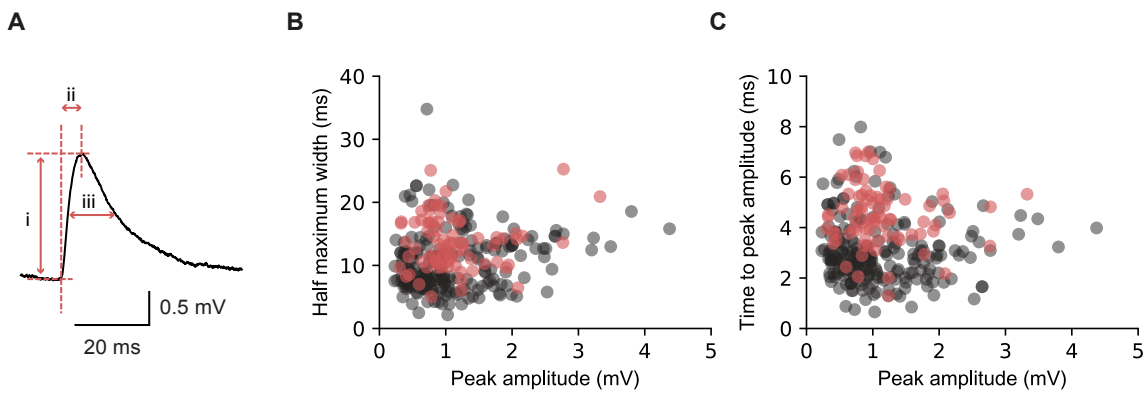


Figure 3.1. Comparison of uEPSP to spontaneous activity: **(A)** uEPSP with overlay of the three comparative measurements: i) peak amplitude (mV), ii) time to peak amplitude (ms), iii) half maximum width (ms) **(B)** half maximum width vs peak amplitude, **(C)** time to peak amplitude vs peak amplitude. $n = 210$ sEPSPs (grey), $n = 78$ uEPSPs (red), 4 cells.

were measured by comparing the theoretical linear summation of individual uEPSPs with the actual summation recorded when uncaging glutamate at locations near-simultaneously (as detailed in methods section 2.1.3).

We found that dendrites in the stratum oriens can integrate synaptic inputs in a cooperative nonlinear manner, whereas dendrites in the stratum radiatum tend to sum inputs linearly. An example cell with paired recordings from two dendrites displaying these two types of integration is shown in Figure 3.2A. In this recording the predicted summations of individual somatic uEPSPs from stratum radiatum inputs (Figure 3.2B) largely matched the actual recorded summation waveforms. In contrast, for the stratum oriens dendrite, the summation initially matches the theoretical waveforms, but, as more uncaging locations are activated, the summation waveform becomes progressively larger and more rounded than expected, consistent with the recruitment of a voltage sensitive conductance in the dendrites (Figure 3.2C&D).

In total, somatic responses were recorded from uncaging at 23 dendritic locations 35 - 250 μm from the soma, with between 8 - 12 uncaging locations at each dendritic region of interest. Overall, the mean percentage peak amplitude nonlinearity (quantified as detailed in methods, section 2.1.5) for stratum oriens locations was $24.0 \pm 4.5\%$, $n = 14$, whereas stratum radiatum dendrites showed linear synaptic integration: $3.8\% \pm 5.0\%$, $n = 9$ ($p = 0.0083$). Furthermore, we also compared theoretical and measured uEPSP waveform integrals (50 ms). Similar to uEPSP amplitude, there were also a significant difference between oriens and radiatum dendrite uEPSP inte-

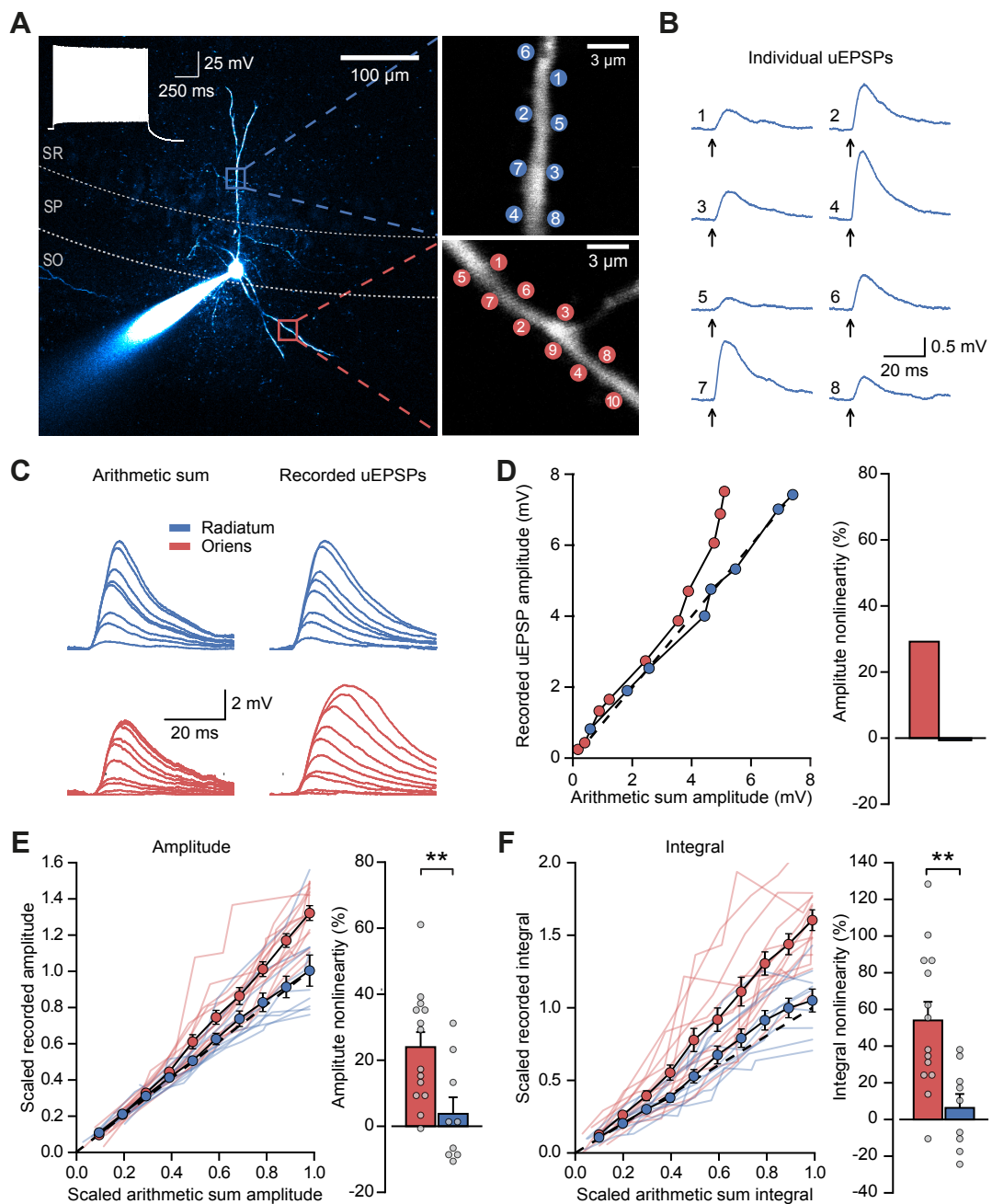


Figure 3.2. Oriens dendrites support supralinear synaptic integration: (A) Two photon image of a PV⁺ interneuron filled with alexa-594 with two dendritic regions of interest at higher magnification. (B) Individual uEPSP responses from a dendritic location in the radiatum. (C) Comparison of arithmetic and measured uEPSP waveforms from uncaging locations in stratum radiatum (blue) and oriens (red). (D) Peak amplitudes of recorded uEPSPs (y-axis) vs arithmetic waveforms (x-axis) for the two regions shown in panel A. (right) bar chart showing quantification of the amplitude nonlinearity as detailed in section 2.1.5. (Red) oriens, (blue) radiatum (E&F) Summary scaled amplitude and integral (50 ms) comparisons for all cells, n = 23. Oriens locations n = 14, Radiatum locations n = 9. Filled circles and error bars display mean and SEM of a linear interpolation between scaled data points

grals: mean oriens integral nonlinearity was 54.0 ± 10.1 % compared to 6.3 ± 7.6 % for dendrites in the radiatum ($p = 0.0027$). One sample t-tests against the null hypothesis of linear integration (0%): oriens amplitude $p = 0.00015$, oriens integral $p = < 0.00014$, radiatum amplitude $p = 0.47$, radiatum integral $p = 0.43$.

We expected individual locations within the same cell to be relatively uncorrelated, due to varied dendritic morphology and distances from the soma, thus justifying their use as individual experimental units. However, in order to avoid potential pseudo-replication errors, we present the data averaged by cell for both percentage integral and amplitude nonlinearity (Figure 3.3A & B). Here, of the 11 cells, 6 had at least one recording from both strata oriens and radiatum. Both paired and unpaired statistics showed significant differences between the two strata for peak amplitude (Oriens vs Radiatum all data including unpaired recordings: 26.0 ± 6.0 % s.o. vs 5.4 ± 5.4 % s.r., $n=9$ vs $n=8$, $p=0.022$, and Oriens vs Radiatum paired recordings only: 29.6 ± 8.7 % s.o. vs 6.4 ± 6.7 % s.r. $n = 6$, $p = 0.012$) and uEPSP integral comparisons (Oriens vs Radiatum all data including unpaired recordings: 49.1 ± 8.5 % s.o. vs 0.28 ± 9.4 % s.r., $n=9$ vs $n=8$, $p=0.0043$, and Oriens vs Radiatum paired recordings only: 59.3 ± 16.5 % s.o. vs 13.1 ± 9.6 % s.r., $n = 6$, $p = 0.035$). There were insufficient recordings to assess intra-cell clustering relative to the full data set, however, in general, the scores for the two strata in the same cell were related, i.e. a relatively low radiatum score and a relatively low oriens score. This dataset therefore implies that the cell has a global degree of synaptic integration nonlinearity, and that the integration of the two dendritic locations is relative to this value.

We also show the nonlinearity quantifications for individual dendritic locations as cumulative frequency plots. Here significance was assessed non-parametrically using the Kolmogorov - Smirnov test (uEPSP amplitude nonlinearity, oriens vs radiatum: $p = 0.023$, ks statistic 0.59; uEPSP integral nonlinearity, oriens vs radiatum: $p = 0.013$, ks statistic 0.64).

Figure 3.4 displays the comparison between theoretical and measured uEPSP waveforms without scaling for the maximum theoretical size of the uEPSPs. The scaled graphs, shown in Figure 3.2, are preferred as somatic size is an unreliable estimate of local uEPSP size. It is therefore potentially futile to consider how multiple dendritic locations are integrating synaptic inputs at "5 mV" for example. However, for completeness, these graphs are included.

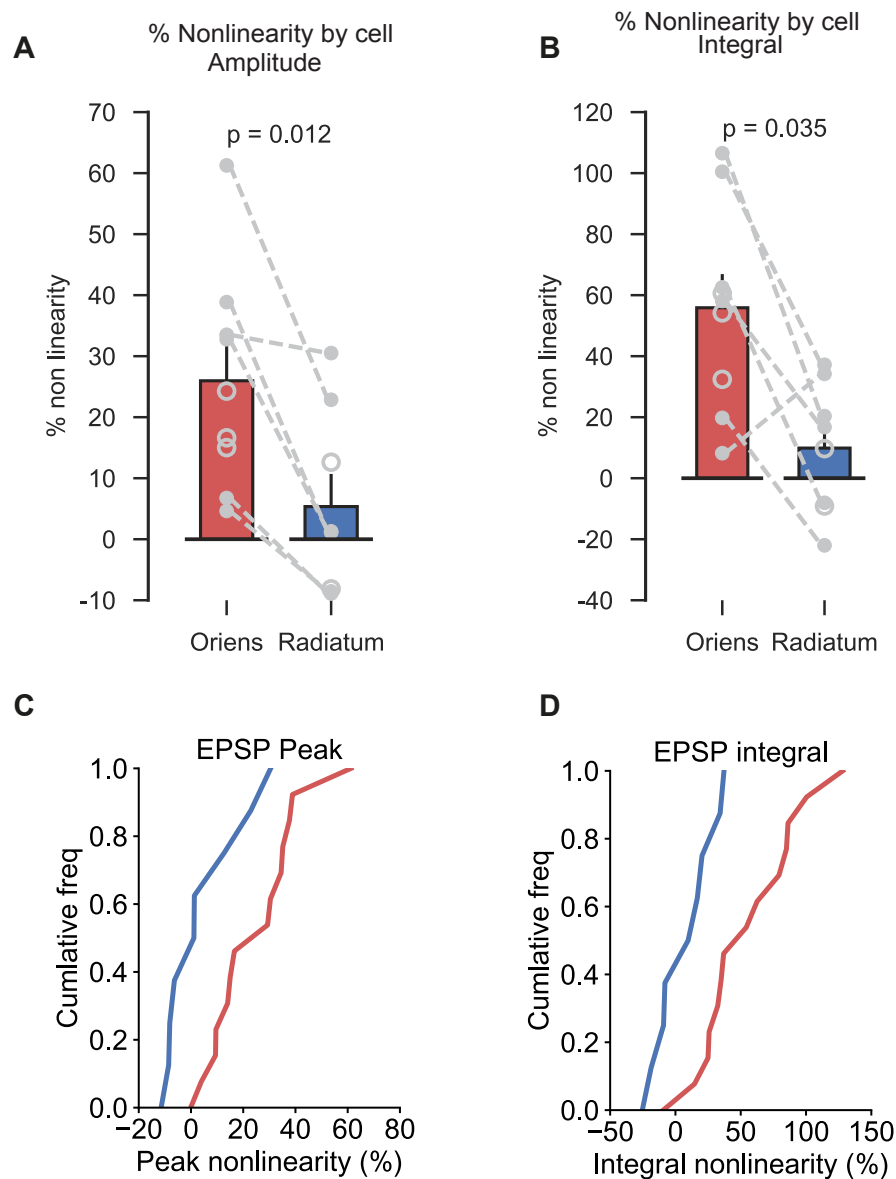


Figure 3.3. (A) Peak amplitude nonlinearity by cell. (B) Integral nonlinearity by cell. For panels A & B closed markers denote paired recordings, open unpaired recordings. In total, recordings from 11 cells are displayed, of which 6 were paired with both radiatum and oriens recordings. There are also 3 unpaired recordings from oriens dendrites, and 2 unpaired recordings from radiatum dendrites. (C&D) Cumulative frequency plots of individual dendrite nonlinearity percentages shown in Figure 3.2. (C) peak-amplitude, (D) integral.

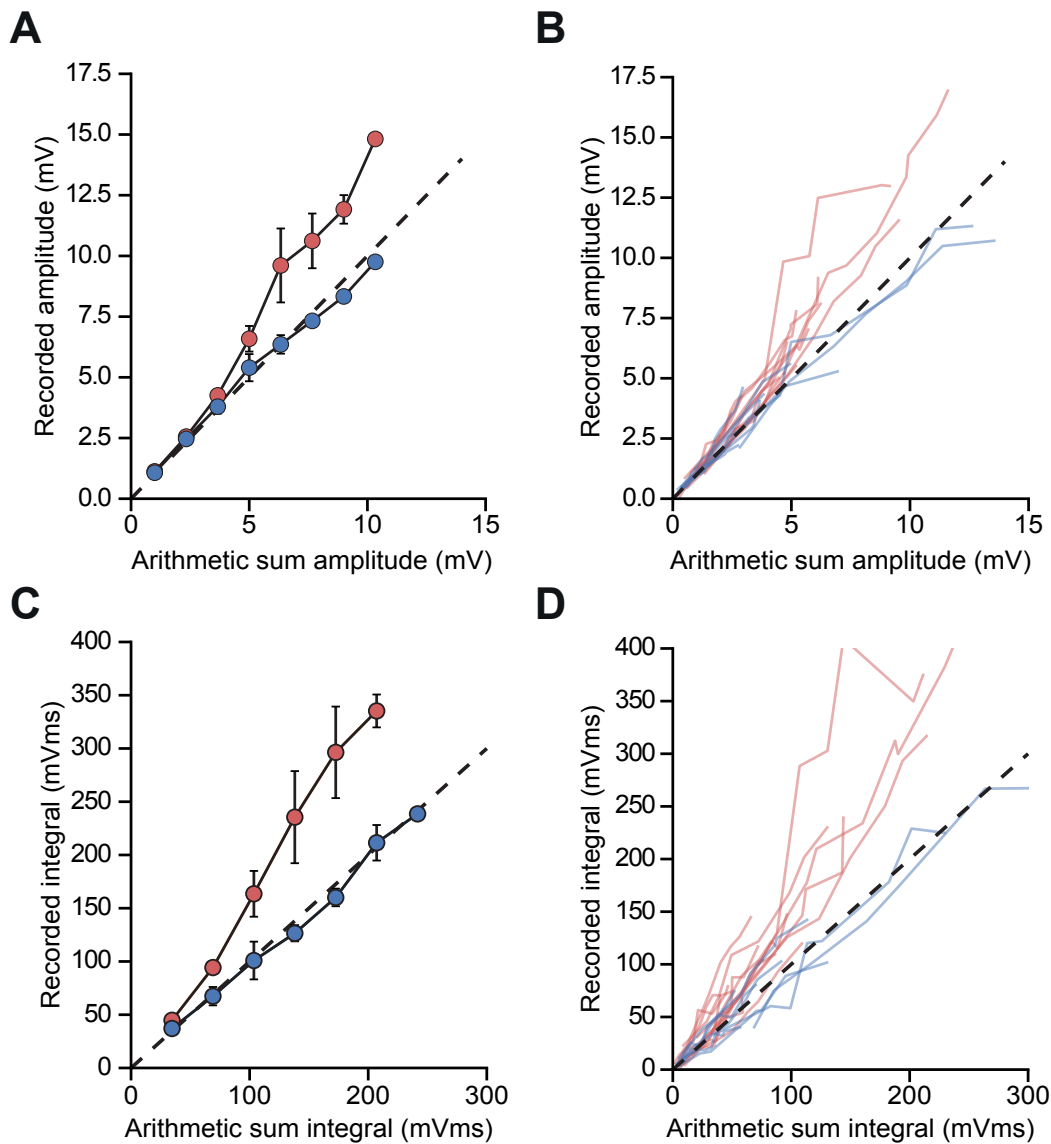


Figure 3.4. Unscaled input-output comparison: recorded (y axis) vs theoretical (x axis). Oriens: $n = 14$ (red) radiatum: $n = 9$ (blue) (A) peak-amplitude comparison (B) integral comparison. (C&D) mean values \pm SEM using linear interpolation between points. Note unequal number of data points at each location.

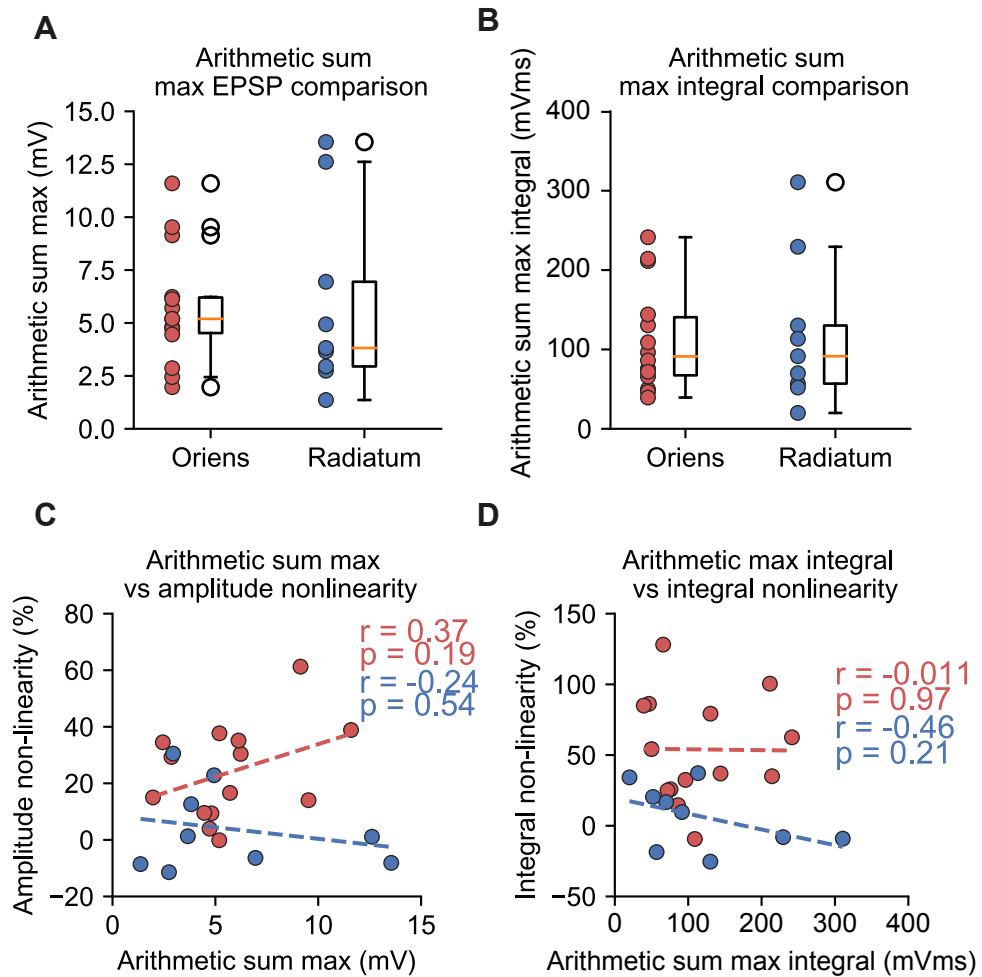


Figure 3.5. Comparison of maximum theoretical summations: stratum oriens (red) stratum radiatum (blue), (A) peak amplitude comparison, (B) integral comparison. Box plots show means and interquartile ranges excluding outliers shown as open circles. These data points were included for t-tests and calculation of sample means reported in text. (C & D) regression analysis of either peak amplitude or integral with dendritic synaptic integration nonlinearity. r - Pearson correlation coefficient.

One possible explanation for the difference in synaptic integration that we observed is a lack of sufficient local depolarisation in stratum radiatum dendrites. It might be possible to obtain a similar dataset from potentially very active dendrites if the uncaging evoked radiatum inputs were deliberately kept small, so as to not recruit any voltage gated channels. While somatic uEPSP size is not a reliable estimate of the actual local depolarisation, it is true that a larger local depolarisation will generally elicit a larger somatic depolarisation. We therefore compared the maximum expected peak amplitudes and integrals of the theoretical uEPSP summations to see if there was a bias between the two locations (Figure 3.5 A & B). Overall there was no significant difference between the mean size of either the maximum expected uEPSP amplitude, or expected uEPSP integral, measured as a result of uncaging glutamate at the two dendritic locations (strata Oriens vs Radiatum, peak-amplitude: 5.7 ± 0.73 mV s.o. vs 5.8 ± 1.5 mV s.r., $p = 0.93$, integral: 113 ± 17.8 mVms s.o. vs 119.3 ± 31.3 mVms s.r., $p = 0.852$).

Furthermore, there was no statistically significant relationship between the maximum expected amplitude, or integral, of the uEPSPs and the degree of synaptic integration nonlinearity observed (Figure 3.5 C&D) (amplitude vs nonlinearity: stratum oriens - $r = 0.37$, $p = 0.19$; stratum radiatum - $r = -0.24$, $p = 0.54$; integral vs nonlinearity: oriens - $r = -0.011$, $p = 0.97$; radiatum - $r = -0.46$, $p = 0.21$). This finding implies that were there to have been a difference in uncaging-evoked somatic EPSP sizes by stratum, it would still not have explained the the synaptic integration difference. However, as discussed, somatic depolarisation is an unreliable measure of local depolarisation, and it is still possible that local depolarisation of radiatum dendrites was less than that of oriens dendrites for comparable somatic uEPSPs.

Uncaging-location distance from the soma is another potential source of experimental bias. For example, typically PV⁺ cells were recorded at the base of the pyramidal cell layer, on the border between the strata oriens and pyramidale, as targeted recording was slightly easier in this location. As a result, the apical PV⁺ dendrite generally passed through the pyramidal cell layer before entering the stratum radiatum. Therefore, the closest radiatum locations to the soma were slightly farther from the soma than the closest oriens locations.

For passive dendrites, local input resistance increases with distance from the soma due to dendritic morphology. In addition, as reviewed in section 1.1.4, sub-cellular expression of active conductances is often dependent on location. Therefore, it might

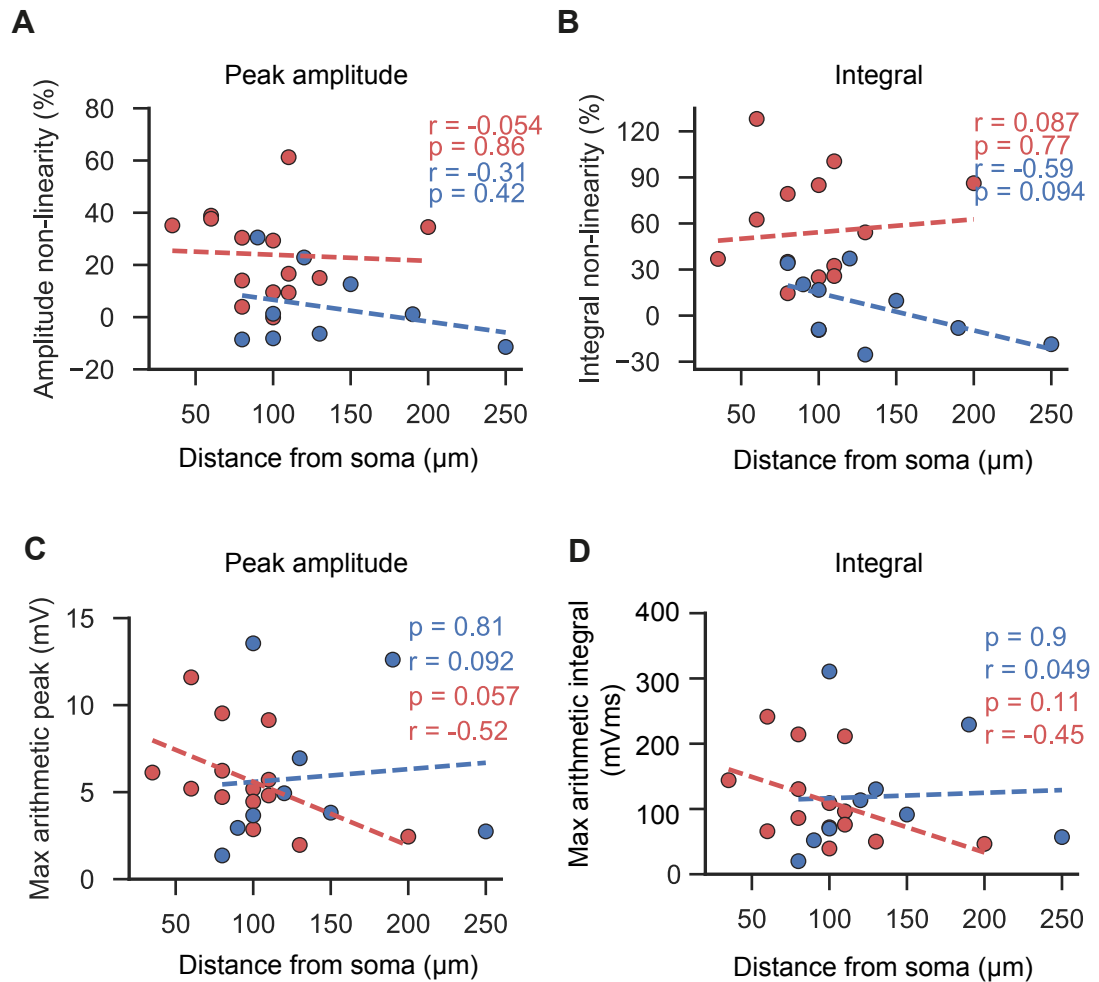


Figure 3.6. Dendritic location vs synaptic integration nonlinearity and expected maximum uEPSP: oriens (red) $n=14$, radiatum (blue) $n = 9$. **(A)** uEPSP amplitude nonlinearity vs distance from soma. **(B)** uEPSP integral nonlinearity vs distance from soma. **(C)** Expected maximum amplitude of compound uEPSP vs distance from the soma. **(D)** Expected maximum integral of compound uEPSP vs distance from the soma. r - Pearson correlation coefficient.

reasonably be expected that a relationship exists between uncaging location and synaptic integration nonlinearity. However, we did not see a significant correlation between distance from the soma and percentage nonlinearity of either peak or integral nonlinearity (Figure 3.6A: amplitude nonlinearity vs distance: oriens $r = -0.05$, $p = 0.86$; radiatum $r = -0.31$, $p = 0.42$; Figure 3.6B: integral nonlinearity vs distance: oriens $r = 0.087$, $p = 0.77$; radiatum $r = -0.59$, $p = 0.094$).

3.2.2 NMDA receptors mediate stratum oriens dendrite supra-linear synaptic integration

Having established that basal PV⁺ dendrites, which receive local feedback connections, are able to integrate synaptic inputs in a cooperative nonlinear manner, we next sought to understand the mechanism underlying the observed supralinear synaptic integration. We hypothesised that a dendritic voltage-sensitive conductance was being recruited locally by the uEPSPs, and therefore performed experiments with pharmacological blockade of either NMDA receptors or Na⁺ channels using APV and TTX respectively.

Figure 3.7 A & B show an example recording in the presence of APV. In this case the theoretical uEPSP summation waveforms and recorded uEPSP summation waveforms are very similar. In Figure 3.7 C summary data for all experimental recordings in APV are presented, and the nonlinearity quantification is shown relative to control oriens dendrites. Overall, with APV included in the ACSF, there was no observable difference in the synaptic integration between dendrites in the stratum oriens or stratum radiatum (Figure 3.7 C and Figure 3.8 A) (strata oriens vs radiatum, uEPSP amplitude nonlinearity: 1.9 ± 2.7 % s.o. vs 7.3 ± 2.5 % s.r., $p = 0.26$, uEPSP integral nonlinearity: 2.5 ± 3.0 % s.o. vs 3.3 ± 2.6 % s.r., $p = 0.88$, $n = 10$ oriens vs $n = 4$ radiatum). We also compared uEPSP integration in APV to control conditions. Here the uEPSP integration amplitude and integral of radiatum dendrites was comparable in APV to control (amplitude $p = 0.66$, integral $p = 0.80$). In contrast, the uEPSP integration of stratum oriens dendrites was altered in the presence of APV (amplitude $p = 0.001$, integral $p = 0.0004$). One sample t-tests against the null hypothesis of linear integration in the presence of APV: oriens amplitude $p = 0.51$, oriens integral $p = < 0.42$, radiatum amplitude $p = 0.07$, radiatum integral $p = 0.30$.

In contrast to APV, in the presence of TTX, PV⁺ dendrites in the stratum oriens continued to integrate uEPSPs supra-linearly (Figure 3.7 D & Figure 3.8 B) (strata oriens vs radiatum, uEPSP amplitude nonlinearity: 22.6 ± 5.2 % s.o. vs 2.9 ± 3.9 % s.r., $p = 0.016$, uEPSP integral nonlinearity: 40.1 ± 5.6 % s.o., vs 9.4 ± 3.3 % s.r., $p = 0.0007$, oriens $n = 16$ vs radiatum $n = 9$). Furthermore, when compared to control, addition of TTX to the ACSF did not statistically change the synaptic integration nonlinearity at either dendrite location (oriens control vs oriens APV: amplitude $p = 0.84$, integral $p = 0.23$. radiatum control vs APV: amplitude $p = 0.89$, integral p

= 0.71). One sample t-tests against the null hypothesis of linear integration in the presence of TTX: oriens amplitude $p = 0.0006$, oriens integral $p = < 0.0001$, radiatum amplitude $p = 0.48$, radiatum integral $p = 0.021$.

Figure 3.9 also shows the nonlinearity quantifications in APV and TTX for individual dendritic locations as cumulative frequency plots. Here significance was assessed non-parametrically using the Kolmogorov - Smirnov test (Figure 3.9 A&B APV uEPSP amplitude nonlinearity oriens vs radiatum: $p = 0.34$, ks statistic 0.5; uEPSP integral nonlinearity oriens vs radiatum: $p = 0.91$, ks statistic 0.3. Figure 3.9 C&D TTX uEPSP amplitude nonlinearity oriens vs radiatum: $p = 0.025$, ks statistic 0.58; uEPSP integral nonlinearity: $p = 0.0002$, ks statistic 0.83).

Figure 3.10 displays the peak-amplitudes and integrals of recorded uEPSP waveforms plotted against the theoretical uEPSP waveforms, without being scaled to the maximum theoretical integral or peak-amplitude, as shown in Figure 3.7 C&D and Figure 3.8 A&B. Limits on axes are set to match control graph values.

Figure 3.11 shows a comparison of the maximum expected peak-amplitudes (Figure 3.11 A) and maximum expected integrals (Figure 3.11 B) between somatic responses evoked from dendrites in strata oriens and radiatum in APV. There was no observed statistical difference in the mean of these measures of the uncaging evoked responses (Oriens vs Radiatum, expected uEPSP amplitude in APV: 7.4 ± 0.91 mV s.o. vs 4.9 ± 0.45 mV s.r., $p = 0.11$, expected uEPSP integral: 158.9 ± 20.4 mVms s.o. vs 131.7 ± 12.7 mVms s.r., $p = 0.81$). Furthermore, as in control conditions, there was also no statistically significant relationship between either the expected, theoretical maximum compound uEPSP amplitude or expected compound integral with percentage integration nonlinearity (nonlinearity amplitude vs expected compound amplitude: oriens - $r = -0.25$, $p = 0.49$; radiatum - $r = -0.32$, $p = 0.68$; nonlinearity integral vs expected compound integral: oriens - $r = 0.56$, $p = 0.094$; radiatum - $r = -0.51$, $p = 0.49$).

Similarly, Figure 3.12 shows a comparison of the maximum expected arithmetic compound uEPSP amplitudes (Figure 3.12 A) and maximum expected arithmetic uEPSP integrals (Figure 3.12 B) of somatic responses evoked by uncaging at dendrites in strata oriens and radiatum in the presence of TTX. We observed no statistical difference by location between the means of the expected maximum uEPSP amplitudes (Oriens vs Radiatum, maximum uEPSP amplitude: 6.0 ± 0.61 mV s.o. vs $5.4 \pm$

1.07 mV s.r., $p = 0.58$) or expected maximum uEPSP integrals (Oriens vs Radiatum, maximum uEPSP integral: 113.5 ± 16.1 mVms s.o. vs $113.5.1 \pm 21.3$ mVms s.r., $p = 0.75$). Interestingly, in contrast to control and APV conditions, negative trends were observed between the maximum expected uEPSP integrals or amplitudes and uEPSP integration nonlinearity, which in one case was statistically significant (uEPSP amplitude nonlinearity vs expected maximum amplitude: oriens $r = -0.55$, $p = 0.026$; radiatum $r = -0.61$, $p = 0.08$; uEPSP integral nonlinearity vs expected maximum integral: oriens $r = -0.45$, $p = 0.077$; radiatum $r = -0.62$, $p = 0.074$). This might be indicative of a role for Na^+ channels in balancing driving force loss, or the activation of K^+ conductances.

We did not observe any significant relationships between the uncaging site distance from the soma and the uEPSP integration nonlinearity recorded, either in APV (Figure 3.13A: uEPSP amplitude nonlinearity vs distance: oriens $r = -0.36$, $p = 0.3$; radiatum $r = -0.89$, $p = 0.11$; Figure 3.13B: integral nonlinearity vs distance: oriens $r = 0.017$, $p = 0.65$; radiatum $r = 0.89$, $p = 0.14$) or in TTX (Figure 3.14A: amplitude nonlinearity vs distance: oriens $r = -0.031$, $p = 0.91$; radiatum $r = -0.15$, $p = 0.7$; Figure 3.14B: integral nonlinearity vs distance: oriens $r = -0.025$, $p = 0.93$; radiatum $r = 0.27$, $p = 0.48$).

We also did not observe statistically significant relationships between the maximum theoretical compound uEPSP and the uncaging distance from the soma, either in APV (Figure 3.13 C: max. compound uEPSP amplitude vs distance: oriens $r = -0.096$, $p = 0.79$; radiatum $r = 0.29$, $p = 0.71$; Figure 3.13 D max. compound uEPSP integral vs distance: oriens $r = 0.0002$, $p = 1.0$; radiatum $r = -0.4$, $p = 0.25$) or in TTX (Figure 3.14 C: max. compound uEPSP amplitude vs distance: oriens $r = 0.055$, $p = 0.84$; radiatum $r = -0.48$, $p = 0.19$; Figure 3.14 D max. compound uEPSP integral vs distance: oriens $r = 0.33$, $p = 0.21$; radiatum $r = -0.52$, $p = 0.15$).

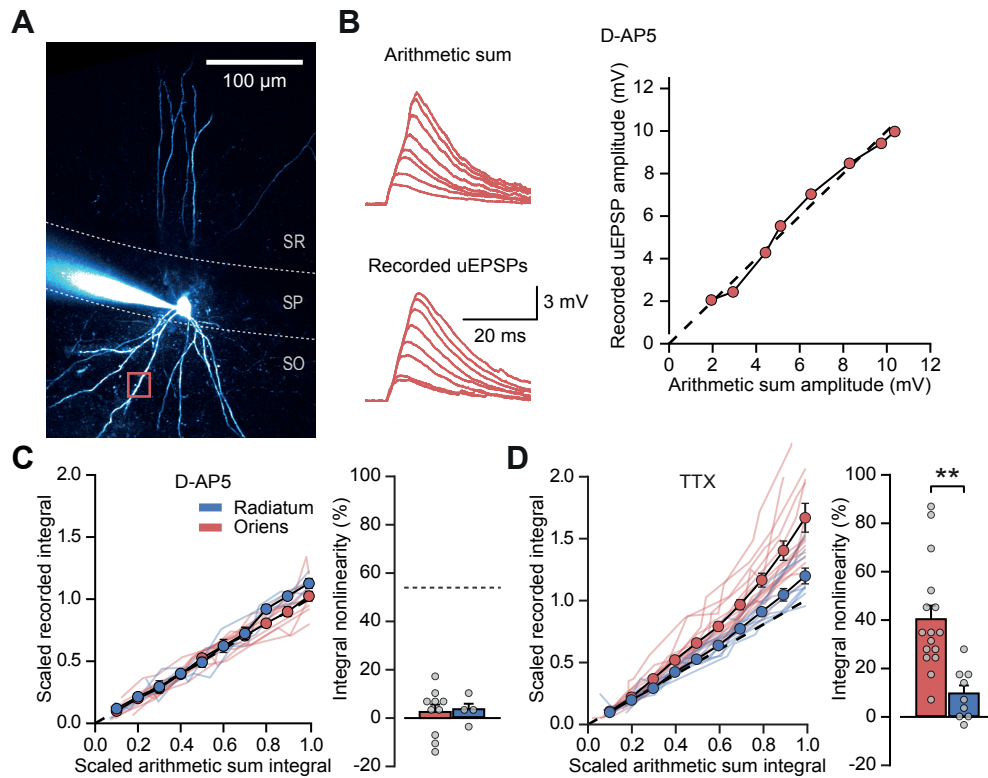


Figure 3.7. NMDA receptors mediate supralinear stratum oriens dendrite synaptic integration: (A) Two photon z-stack of PV⁺ cell in CA1 region of hippocampus. Red box marks glutamate uncaging location. (B) Comparison of theoretical and recorded uEPSP summation waveforms in the presence of APV. (Right) peak recorded amplitude vs peak theoretical amplitude. (C) Summary data for 14 dendritic locations recorded with APV in the ACSF, $n = 10$ oriens $n = 4$ radiatum. (Right) synaptic integration nonlinearity quantified as a percentage, dashed line marks control oriens nonlinearity. (D) Summary data for 25 dendritic locations recorded with TTX in the ACSF, $n = 16$ oriens $n = 9$ radiatum. (Right) synaptic integration nonlinearity quantified as a percentage.

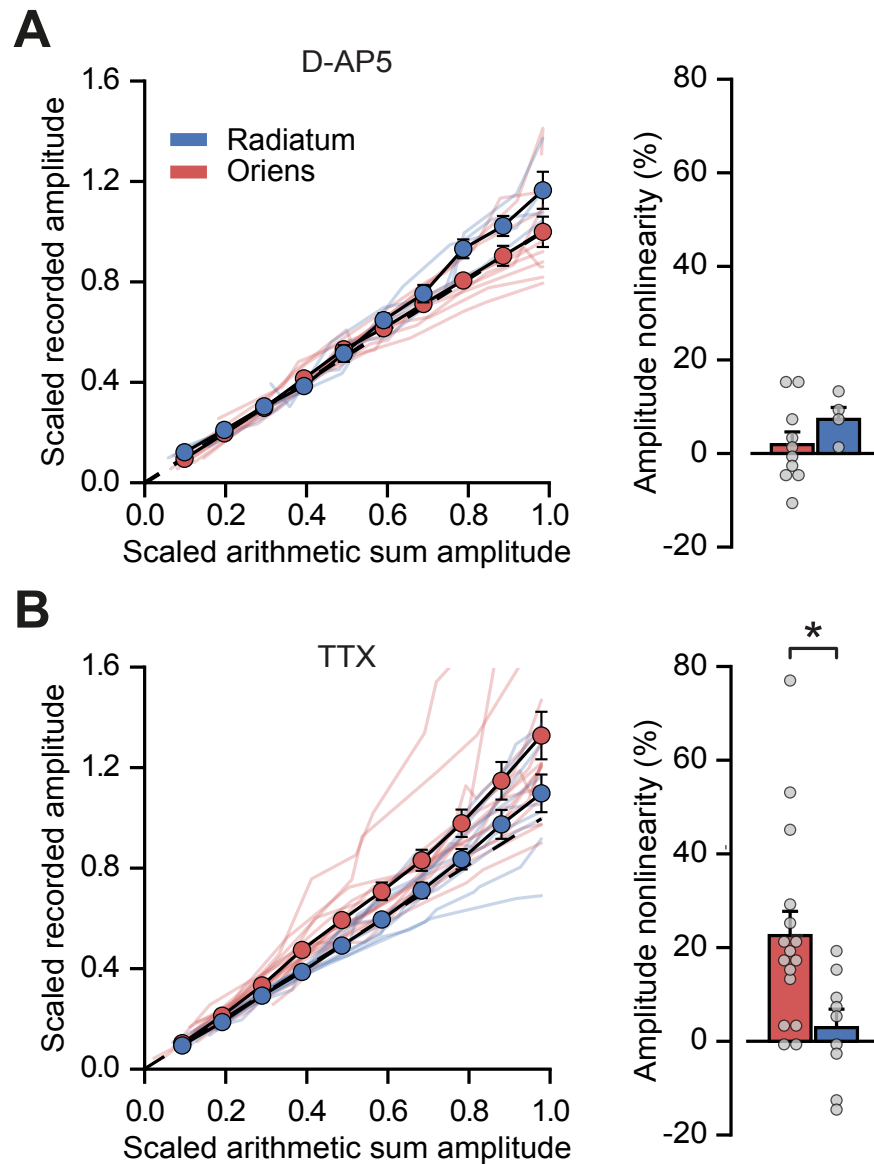


Figure 3.8. uEPSP amplitude synaptic integration in APV and TTX: **(A)** scaled recorded uEPSP integration vs scaled expected uEPSP integration in APV. (right) uEPSP amplitude integration nonlinearity quantified as a percentage in APV. **(B)** Scaled recorded uEPSP integration vs scaled expected uEPSP integration in TTX. (right) uEPSP amplitude integration nonlinearity quantified as a percentage in TTX.

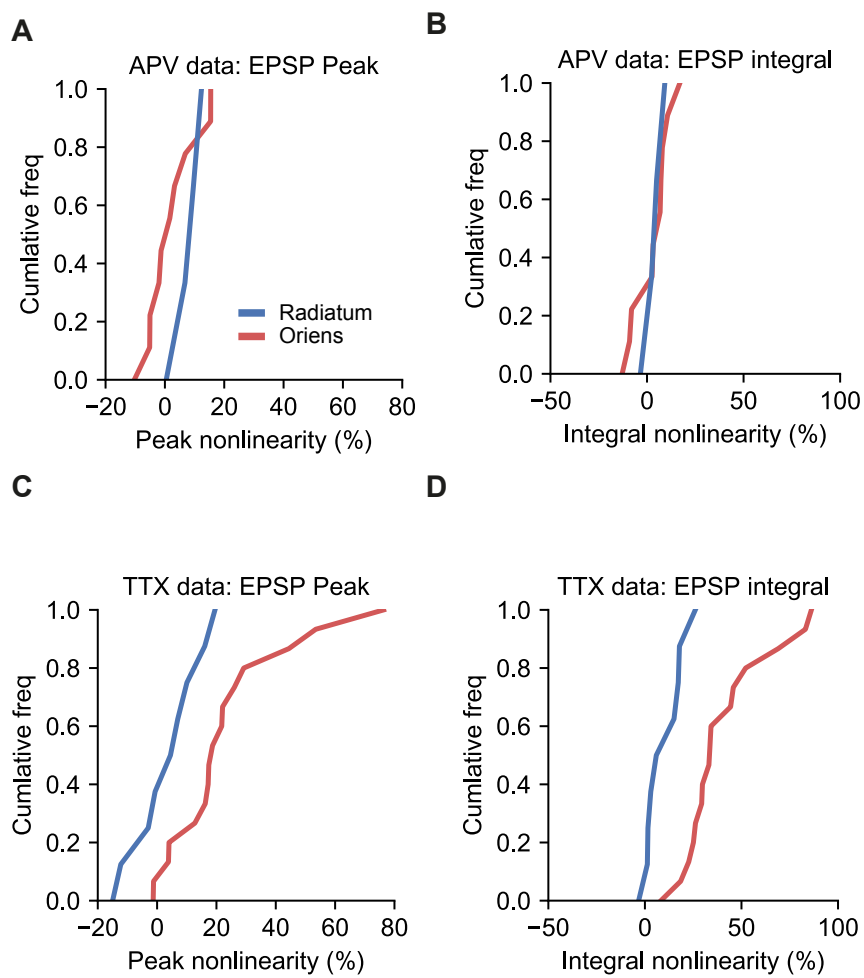


Figure 3.9. Pharmacology cumulative frequency plots of uEPSP integration nonlinearity: uEPSP integration nonlinearity in APV (**A**) amplitude and (**B**) integral. uEPSP integration nonlinearity in TTX (**A**) amplitude and (**B**) integral.

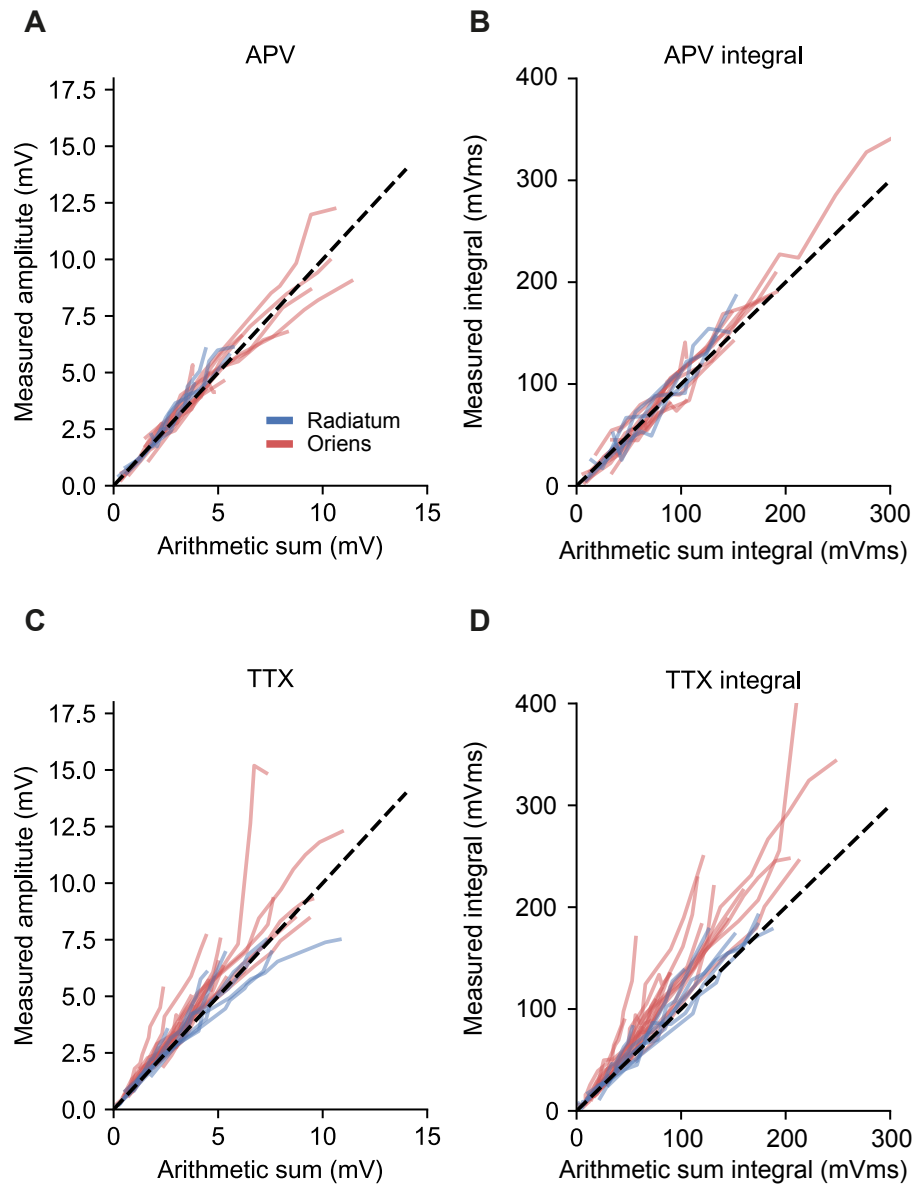


Figure 3.10. Unscaled input-output comparison for APV and TTX experiments: recorded (y axis) vs theoretical (x axis) uEPSP waveforms. (A&B) APV. Oriens: $n = 10$ (red) radiatum: $n = 4$ (blue) (A) uEPSP amplitude comparison (B) uEPSP integral comparison. (C&D) TTX. Oriens: $n = 16$ (red) radiatum: $n = 9$ (blue) (C) uEPSP amplitude comparison (D) uEPSP integral comparison.

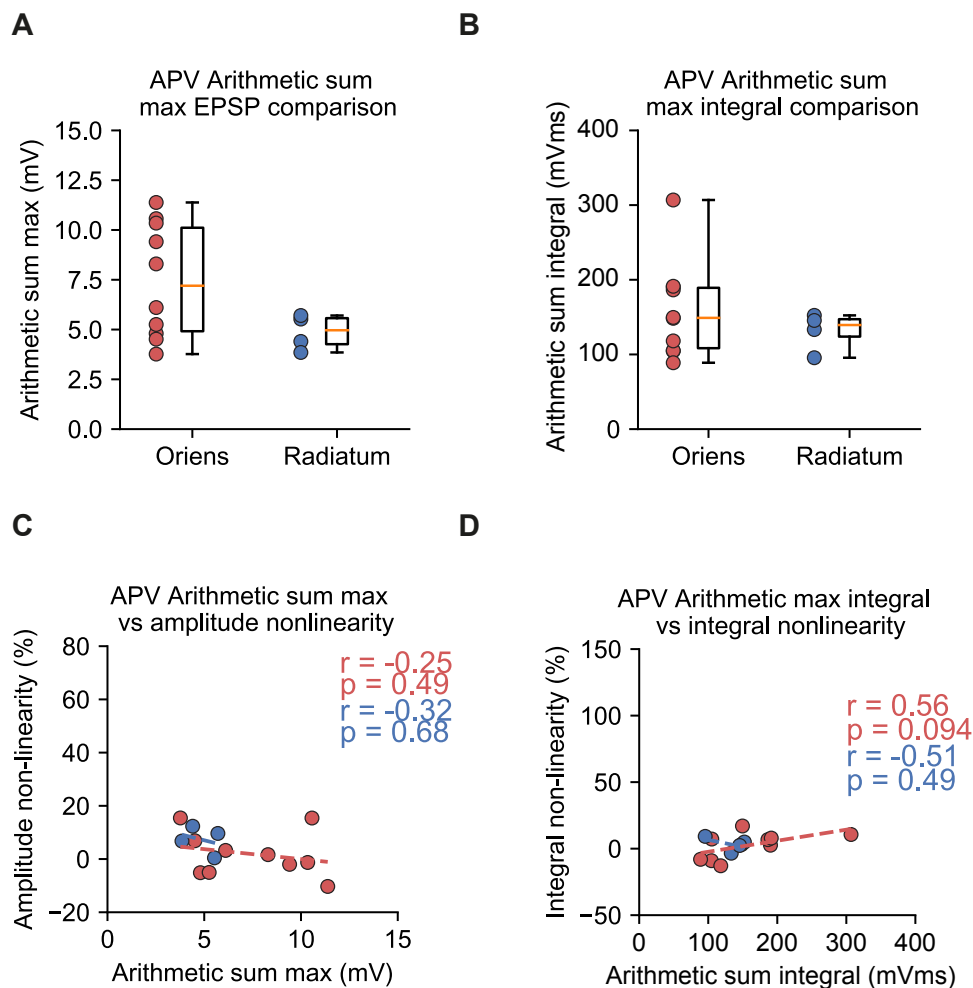


Figure 3.11. Comparison of maximum theoretical summations in APV: oriens (red) radiatum (blue), (**A**) uEPSP expected maximum compound amplitude comparison by stratum, (**B**) uEPSP expected maximum compound integral comparison by stratum. Box-plots show means and interquartile ranges. (**C&D**) regression analysis of either expected compound uEPSP amplitude (**C**) or integral (**D**) with uEPSP integration non-linearity. r - Pearson correlation coefficient.

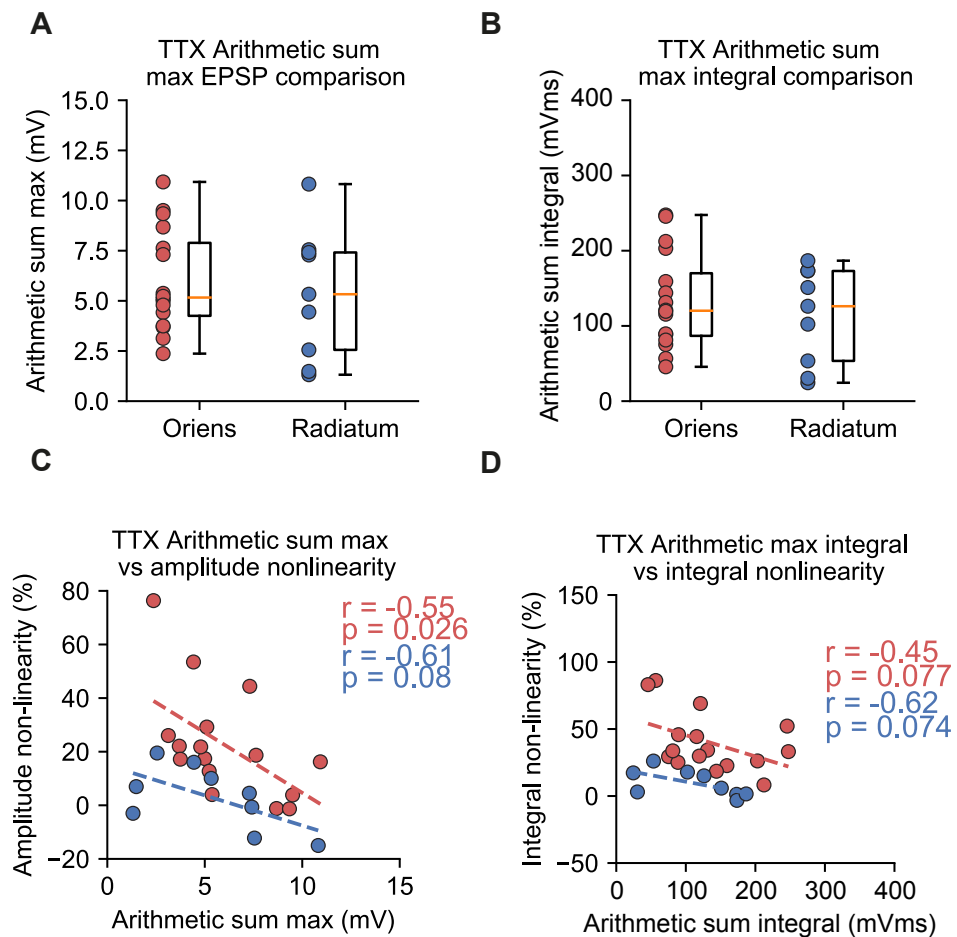


Figure 3.12. Comparison of maximum theoretical summations in TTX: oriens (red) radiatum (blue), **(A)** uEPSP expected maximum compound amplitude comparison by stratum, **(B)** uEPSP expected maximum compound integral comparison by stratum. Box-plots show means and interquartile ranges. **(C&D)** regression analysis of either expected compound uEPSP amplitude **(C)** or integral **(D)** with uEPSP integration non-linearity. r - Pearson correlation coefficient.

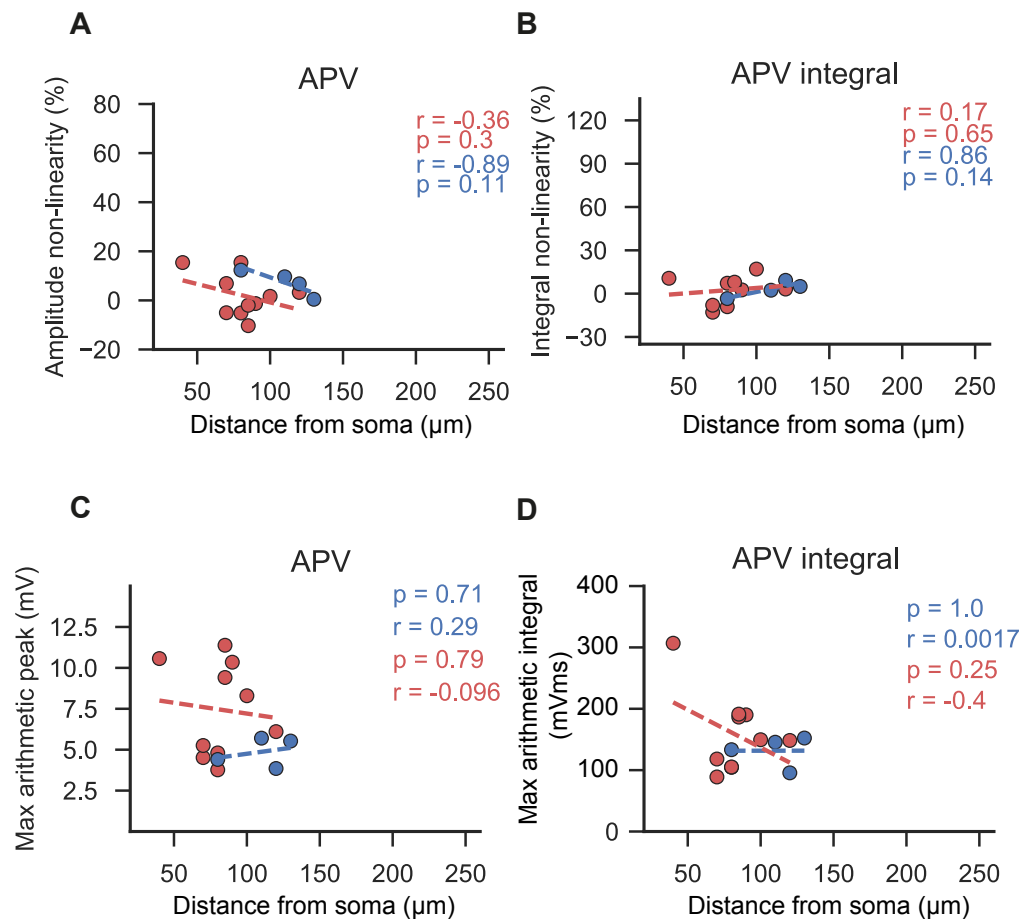


Figure 3.13. Uncaging distance from soma vs uEPSP integration nonlinearity and maximum arithmetic compound uEPSP in APV: oriens (red) $n=10$, radiatum (blue) $n = 4$. **(A)** uEPSP integration amplitude nonlinearity vs uncaging distance from soma. **(B)** uEPSP integration integral nonlinearity vs uncaging distance from soma. **(C)** Maximum expected compound uEPSP amplitude vs uncaging distance from soma. **(D)** Maximum expected compound uEPSP integral vs uncaging distance from soma. r - Pearson correlation coefficient.

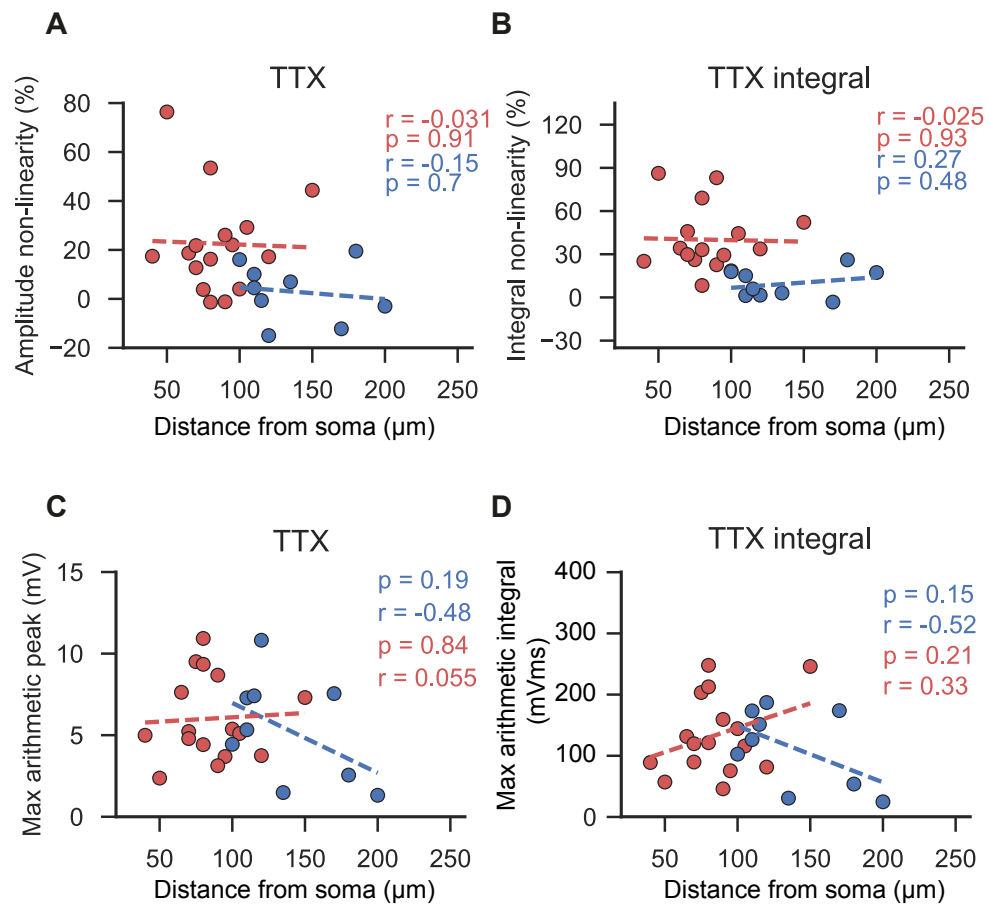


Figure 3.14. Uncaging distance from soma vs uEPSP integration nonlinearity and maximum arithmetic compound uEPSP in TTX: oriens (red) $n=10$, radiatum (blue) $n = 4$. **(A)** uEPSP integration amplitude nonlinearity vs uncaging distance from soma. **(B)** uEPSP integration integral nonlinearity vs uncaging distance from soma. **(C)** Maximum expected compound uEPSP amplitude vs uncaging distance from soma. **(D)** Maximum expected compound uEPSP integral vs uncaging distance from soma. r - Pearson correlation coefficient.

3.2.3 Dendritic morphology does not fully account for dendrite specific synaptic integration

We next sought to understand why NMDAR-dependent supralinear uEPSP integration was found only at oriens dendrites. Starting from the null hypothesis that NMDA receptor content was uniform across the cell, we investigated whether NMDA receptors might be preferentially recruited by synaptic inputs onto oriens dendrites, in comparison to radiatum dendrites. Experimental observations suggested that typically the dendrites found in the stratum radiatum are slightly thicker and longer than the dendrites in the stratum oriens. As a result, from the perspective of a synaptic conductance at a given distance from the soma, the input impedance of oriens dendrites would be larger than that of radiatum dendrites. Therefore, when compared with radiatum dendrites, synaptic currents on oriens dendrites would generate larger local EPSPs, which would in turn facilitate the relief from Mg^{2+} dependent NMDA receptor blockade.

In order to investigate the contribution of dendritic morphology to NMDA receptor recruitment, we reconstructed a CA1 PV^+ interneuron (Figure 3.15A) as detailed in section 2.2 for use in NEURON environment simulations. Model synapses, containing both NMDA and AMPA receptors, were placed in clusters of 15 synapses, in the range of distances from soma that was measured experimentally (40 - 250 μm , Figure 3.15B). Simulations then closely followed experimental procedures, and NMDA and AMPA conductances were hand-tuned to produce similar responses as experimental recordings (Fig. 3.15C).

Figures 3.16 and 3.17 show the model PV^+ neuron's response to the activation of all 15 synapses at progressively more distal locations in the stratum oriens and stratum radiatum. For both the stratum radiatum and stratum oriens, the somatic responses remain broadly similar as the synaptic locations are moved distally from the soma. In contrast to the somatic membrane potential, the local dendritic response becomes progressively larger with distance - as correspondingly the local input resistance increases. In addition, proximal synapses do not recruit as much NMDA receptor conductance, or as strongly activate the potassium and sodium conductances present in the dendrites, as more distal synapses. When comparing the distal stratum oriens locations (Figure 3.16 C), and distal stratum radiatum locations (Figure 3.17 C), stratum radiatum locations recruit relatively smaller amounts of NMDA receptor

conductance and dendritic conductance.

Figure 3.18 presents the results of the input-output simulations for all synaptic cluster locations, in the format of the experimental data analysis. Both peak-amplitude (Figure 3.18 A) and integral (Fig. 3.18 B) synaptic integration nonlinearity were significantly different between the two locations, supporting a role for dendritic morphology in underlying differential recruitment of NMDA receptors - in line with experimental observations (oriens vs radiatum, $n = 28$ vs $n = 16$, peak-amplitude: 12.5 ± 1.1 vs 8.4 ± 1.2 , $p = 0.0018$, integral: 42.54 ± 3.5 vs 23.9 ± 2.3 , $p = 0.0005$). However, in contrast to experimental observations, the magnitude of the EPSP integration difference between the two locations was relatively modest, with model stratum oriens EPSP integration amplitude nonlinearity or integral nonlinearity being 1.5 and 1.8 times stratum radiatum nonlinearity, whereas the experimental ratios were 6.4 and 8.5 respectively.

In further contrast to experimental recordings, model simulations also showed a clear relationship between synaptic integration nonlinearity and distance from the soma (Fig. 3.19). This relationship, which is expected theoretically, was not seen in the experimental data. However, the decrease in EPSP amplitude nonlinearity after $140 \mu\text{m}$ from the soma in Figure 3.19 A may provide some insight into this and will be discussed further in section 3.3.1.

We also investigated the relationship between the EPSP integration nonlinearity of the two dendritic locations and NMDA receptor conductance. This is shown in Figure 3.20. As the NMDA receptor conductance is reduced from its baseline value, which was chosen to approximate experimental observations, the mean nonlinearity percentage reduces for both dendritic locations. However, this reduction is more severe for the integration nonlinearity of stratum oriens synaptic clusters than radiatum clusters. At 20 % of baseline NMDA receptor conductance the mean EPSP integration is lower for oriens dendrites than radiatum dendrites. These simulation results are in line with larger dendritic EPSPs in the oriens than in the radiatum dendrites, produced as a result of larger local input resistances in the thinner, shorter oriens dendrites. The larger oriens dendritic EPSPs are better able to recruit NMDA receptors, causing supralinear integration if they are present with sufficient conductance, but if not, the oriens dendritic EPSPs cause more local driving-force shunting and recruitment of K^+ channels. As a result, without sufficient NMDAR conductance oriens inputs generate more integration sublinearity than radiatum synapses.

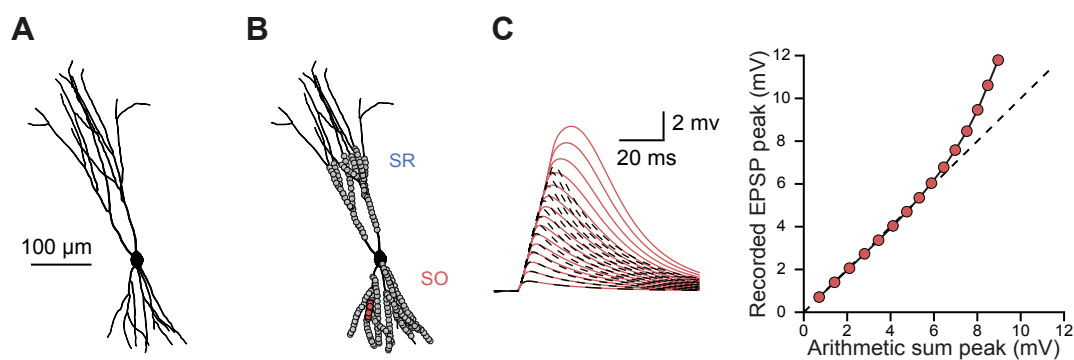


Figure 3.15. Multi-compartmental modelling of synaptic integration: (A) Reconstruction of PV⁺ interneuron, not including axon. (B) Positions of synapses in grey, bounded by experimental glutamate uncaging distances from the soma. Synapses were composed of 44 clusters, 28 in the oriens and 16 in radiatum. (C) Example simulated uncaging experiment at the synapses in (B) marked with red circles. Red solid lines, recorded summation, dashed black lines arithmetic summation waveforms calculated from individual synaptic responses. (Right) plot of peak recorded EPSP waveforms vs peak theoretical EPSP waveforms.

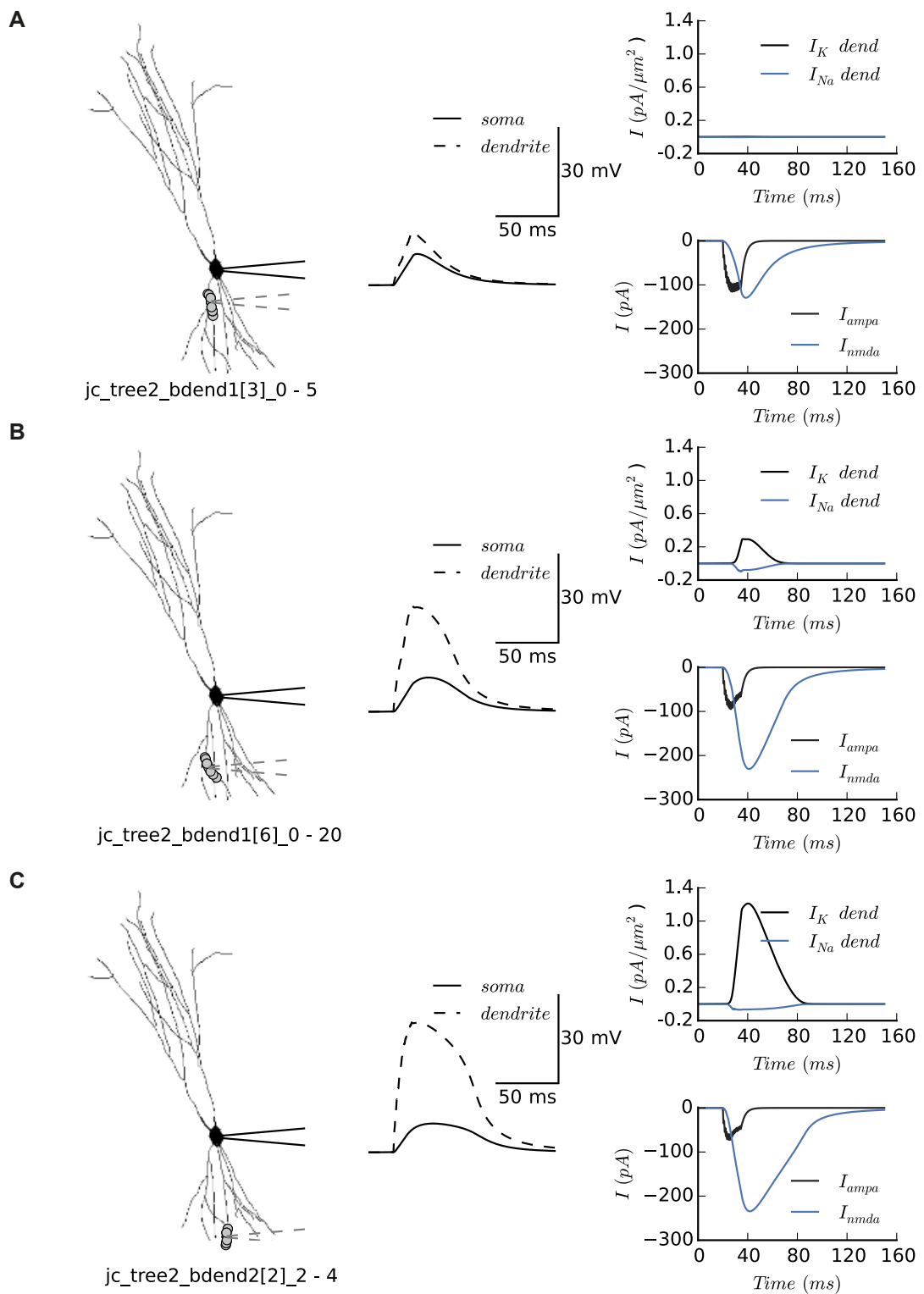


Figure 3.16. Simulated synaptic responses in stratum oriens: (A, B, C) Show the simulation runs in which synapses are located at increasing distances from the soma. (Left) location of the synapses on the cell and position of dendritic recording electrode (dashed grey). (Middle) Somatic and dendritic voltage responses to activation of synapses. (Right upper) Dendritic potassium and sodium current response. (Right lower) Sum of current mediated by synaptic AMPA and NMDA receptors

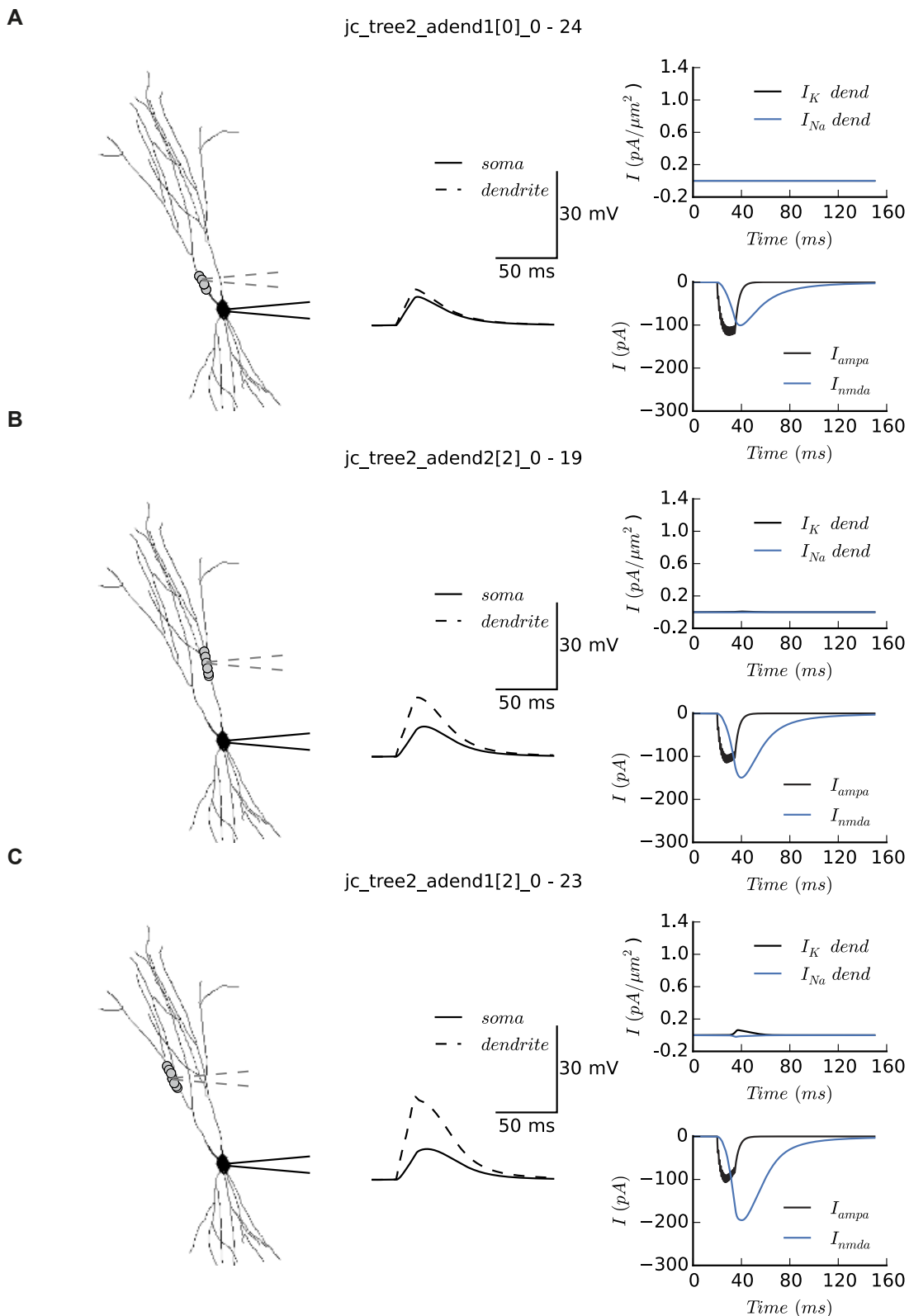


Figure 3.17. Simulated synaptic responses in stratum radiatum: (A, B, C) Show the simulation runs in which synapses are located at increasing distances from the soma. (Left) location of the synapses on the cell and position of dendritic recording electrode (dashed grey). (Middle) Somatic and dendritic voltage responses to activation of synapses. (Right upper) Dendritic potassium and sodium current response. (Right lower) Sum of current mediated by synaptic AMPA and NMDA receptors

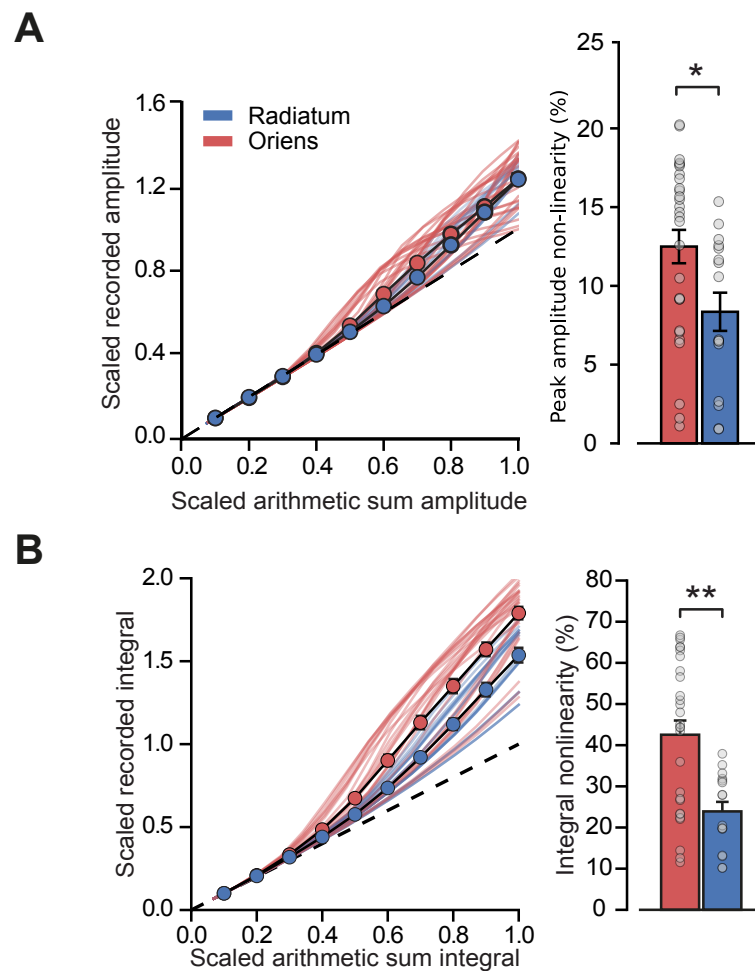


Figure 3.18. NEURON model scaled amplitude and integral non-linearities: $n=28$ oriens, $n=16$ radiatum (**A**) scaled recorded peak amplitude vs scaled theoretical peak amplitude, (right) comparison of the percentage amplitude nonlinearity. (**B**) scaled recorded integral vs scaled theoretical integral, (right) comparison of the percentage integral nonlinearity.

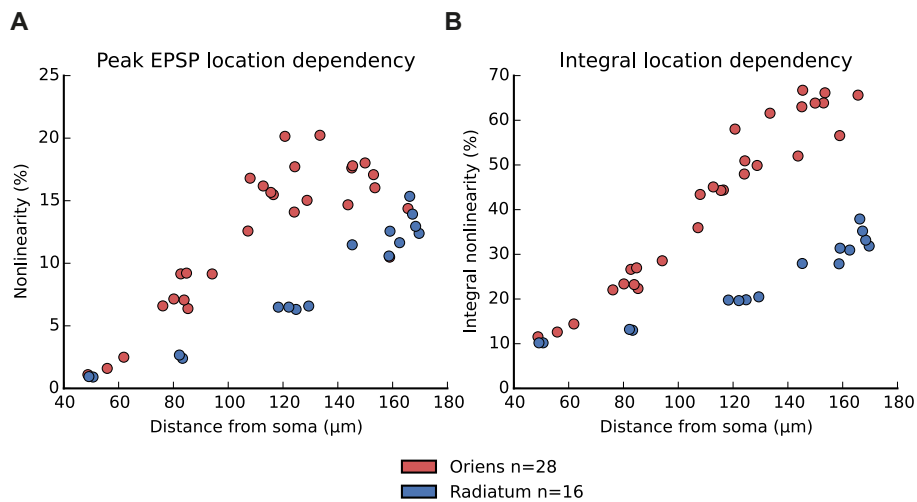


Figure 3.19. NEURON model nonlinearity vs distance from soma: (A) EPSP amplitude nonlinearity vs cluster distance from soma. (B) EPSP integral nonlinearity vs cluster distance from soma.

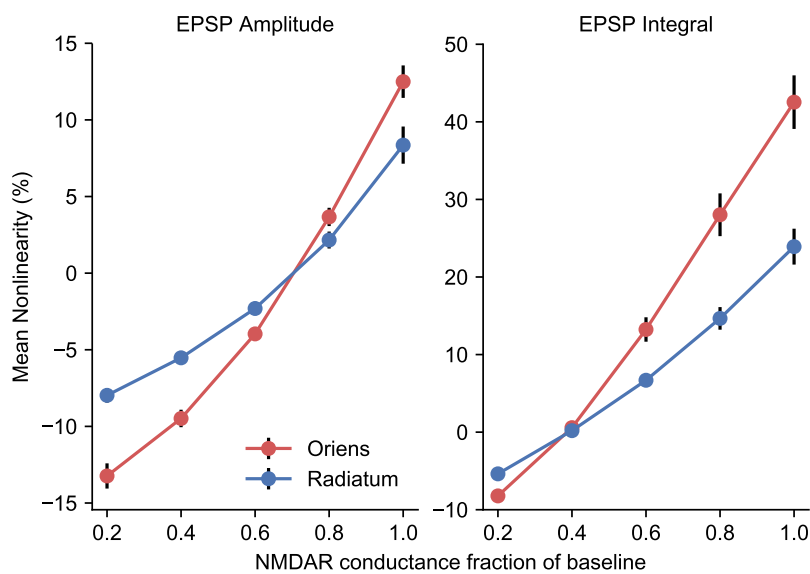


Figure 3.20. Model EPSP integration nonlinearity vs NMDA conductance. Plots show mean EPSP integration nonlinearity over all locations as NMDA receptor conductance is varied. Left - EPSP amplitude nonlinearity, right - EPSP integral nonlinearity.

3.2.4 Differential NMDA receptor expression and dendritic morphology explain dendrite specific synaptic integration

As mentioned in section 3.1, there is evidence from studies investigating the plasticity of excitatory connections onto PV⁺ cells that a larger NMDA receptor conductance is found at feedback inputs, which are found on stratum oriens dendrites, than at feedforward synapses. However, this result is based on voltage clamp experiments that measure NMDA receptor-mediated currents at +60 mV. PV⁺ interneurons typically display input resistances much less than 100 M Ω at rest, and this further decreases as the clamp potential is depolarised from resting membrane potential (experimental observations, not shown). Furthermore, the dendrites receiving the two synaptic inputs have different morphology (stratum radiatum dendrites are longer for example). Inferences drawn from these experiments could therefore be undermined by voltage clamp errors.

In order to probe the relative NMDA receptor conductance at feedforward and feedback connections, we pursued a pharmacological approach that permitted quantification of NMDAR conductances at resting membrane potentials. External Mg²⁺ was reduced to partially unblock NMDA receptors, and the cell was clamped close to resting membrane potential, at -60 mV. AMPA and NMDA receptor blockers were then used to dissect out the currents associated with the two receptors. Figure 3.21 A shows the experimental set-up, with stimulating electrodes placed in the alveus in order to antidromically activate local pyramidal cell axons (Pouille and Scanziani, 2004), and in the stratum radiatum to recruit feedforward Schaffer-Collateral fibres. Figure 3.21 B shows example traces obtained using synaptic receptor blockers, and these were then used to calculate isolated NMDA and AMPA receptor currents at feedforward and feedback synapses (Figure 3.21 C).

Consistent with the report from Le Roux et al, we also found that the ratio of NMDA to AMPA receptor conductance at feedback synapses was larger than at feedforward synapses. This is shown in Figure 3.21 D. NMDA and AMPA receptor currents were integrated in order to calculate the charge ratio. The charge ratio for all paired recordings (Fig.3.21 D right) was significantly greater for feedback synaptic inputs than feedforward (n = 10, charge ratio 3.5 ± 0.7 vs 1.3 ± 0.3 , $p = 0.0017$).

In line with these findings, we revisited the multi-compartmental NEURON model and reduced the NMDA receptor conductance at synaptic cluster locations in the stratum radiatum to 65% of that at stratum oriens locations. With this modification, the ratio between stratum radiatum and stratum oriens synaptic integration non-linearity was similar in magnitude to that which we experimentally observed. Figure 3.22 shows these simulation results (oriens vs radiatum, $n = 28$ vs $n = 16$, peak-amplitude: 12.5 ± 1.1 vs -1.3 ± 0.17 , $p = \ll 0.001$, integral: 42.54 ± 3.5 vs 8.5 ± 0.8 , $p = \ll 0.001$).

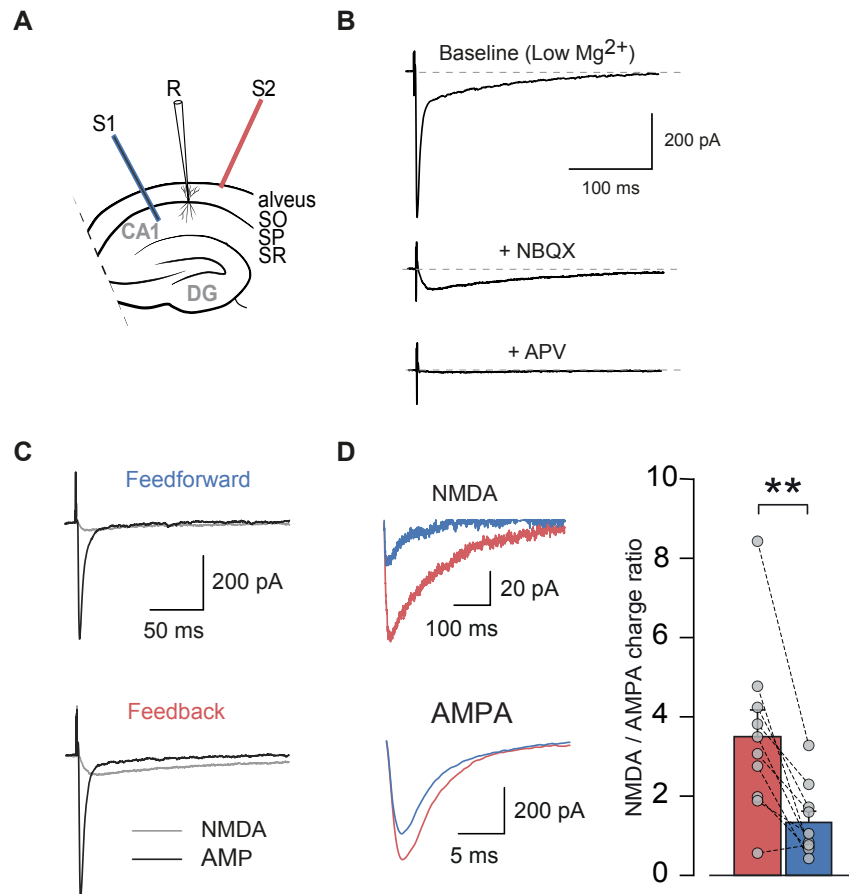


Figure 3.21. Pharmacological dissection of NMDAR and AMPAR conductances from feedforward and feedback inputs: (A) simplified schematic of experimental set up. Two stimulating electrodes were placed in the alveus (S2) and radiatum (S1) to stimulate feedforward and feedback connections onto PV⁺ cell respectively. (B) Example currents elicited from a stimulating electrode at baseline, with NBQX, and NBQX & APV in the ACSF. (C) Example NMDAR & AMPAR currents, dissected from traces seen in (B), elicited from stimulation of either feedforward (blue) or feedback (red) connections. (D) (Left) comparison of feedforward and feedback NMDAR and AMPAR currents. (Right) Summary NMDA:AMPA receptor-mediated charge ratio data. n=10

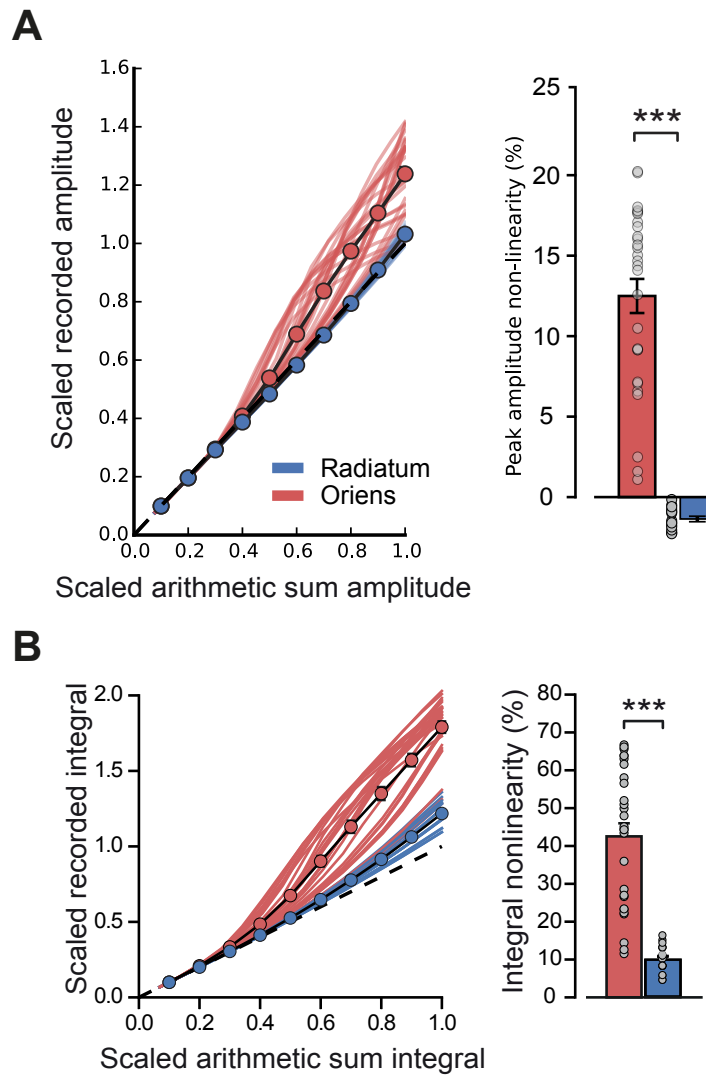


Figure 3.22. NEURON model amplitude and integral nonlinearity with unequal NMDA receptor conductance: $n = 28$ oriens, $n = 16$ radiatum (**A**) scaled recorded peak amplitude vs scaled theoretical peak amplitude, (right) comparison of the percentage amplitude nonlinearity. (**B**) scaled recorded integral vs scaled theoretical integral, (right) comparison of the percentage integral nonlinearity.

3.2.5 The network-level roles of supralinear integration of feedback connections

What might the function of a cooperative synaptic integration mechanism be for feedback connections onto PV⁺ cells? To address this question, we considered what properties would be beneficial for networks of local CA1 pyramidal neurons that innervate PV⁺ cells. As CA1 pyramidal neurons are thought to form assemblies that encode representations of the animals position in space (Wilson and McNaughton, 1993), one function might be to fine-tune the spatial receptive field. Another attribute could be the ability to lock onto temporally stable and spatially tight inputs, perhaps encoded by a population of afferents converging onto pyramidal cells. NMDA receptors on PV⁺ cells mediate cooperative supralinear synaptic responses, making them good candidates to underlie these types of processing.

In order to investigate the network-level properties of cooperative synaptic integration at feedback connections onto fast inhibition, we built a network model of Izhikevich-like neurons including a representation of synaptic integration (see section 2.3). Figure 3.23 shows the response of this network to external input, distributed as a Gaussian centred at pyramidal cell 125, over 300 ms. Figure 3.23 B shows a raster plot of pyramidal cell firing (in orange) in relation to PV⁺ interneuron firing (blue). Pyramidal cells are first driven to firing threshold by external input, after which they recruit the PV⁺ cell and recurrent inhibition, generally preventing firing of the pyramidal cell population until the GABAergic current has sufficiently decayed. The PV⁺ cell fires at low gamma frequency, approximately 40 Hz. The firing relationship between pyramidal cell 125, which is the most strongly activated pyramidal cell in this simulation, and the PV⁺ cell is shown in Fig. 3.23 C. The pyramidal cell fires, on average, every other cycle, and predominantly just before the interneuron (4 out of 5 cycles).

The progressive recruitment of NMDA receptor-like conductance can also be seen in the reduction of the number of "k"-winners per PV⁺ interneuron firing cycle (de Almeida et al., 2009a) section 1.3.2. As the NMDA receptor-mediated current builds up, fewer presynaptic spikes are required to drive the PV⁺ cell to firing threshold, reducing the number of active principal cells during each gamma cycle. Figure 3.26 also shows this effect: with NMDA receptors on the PV⁺ interneuron, the distribution of active pyramidal cells is narrower at the end of the simulation compared

to when the interneuron is modelled as not containing NMDA receptors.

Figure 3.24 shows the currents acting on the PV⁺ interneuron (panel A) and the central pyramidal cell (panel B) during the simulation shown in figure 3.23. For the PV⁺ cell, AMPA receptor currents from pyramidal cells gradually recruit more NMDA receptor current, which eventually lasts across oscillation cycles, with AMPA receptor currents riding on-top to cause PV⁺ cell firing. In contrast, pyramidal cells only receive one source of excitatory input, which is relatively constant across time, but get phasic GABAergic inhibition from the PV⁺ cell. As all synaptic inputs are modelled as conductances, cell firing causes transient driving force changes, resulting in the spikes seen in the current traces (particularly prominent in Fig. 3.24 B).

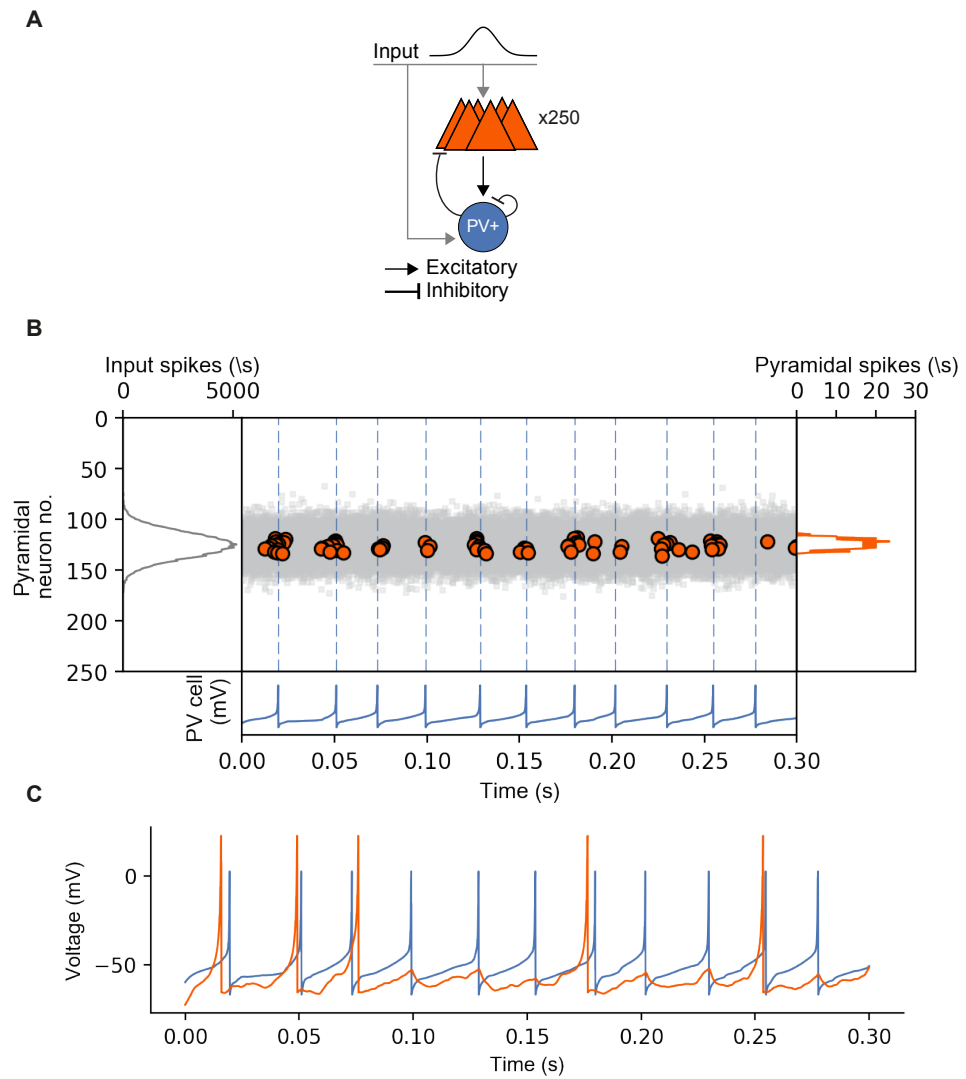


Figure 3.23. Model spiking neuron network response to external input: **(A)** Schematic of network structure. **(B)** Summary plot of network simulation showing, external input distribution (grey), pyramidal cell firing (orange, circles) and interneuron firing (blue). **(C)** Voltage traces of interneuron (blue) and pyramidal cell no. 125 (orange), which was the most strongly activated pyramidal cell.

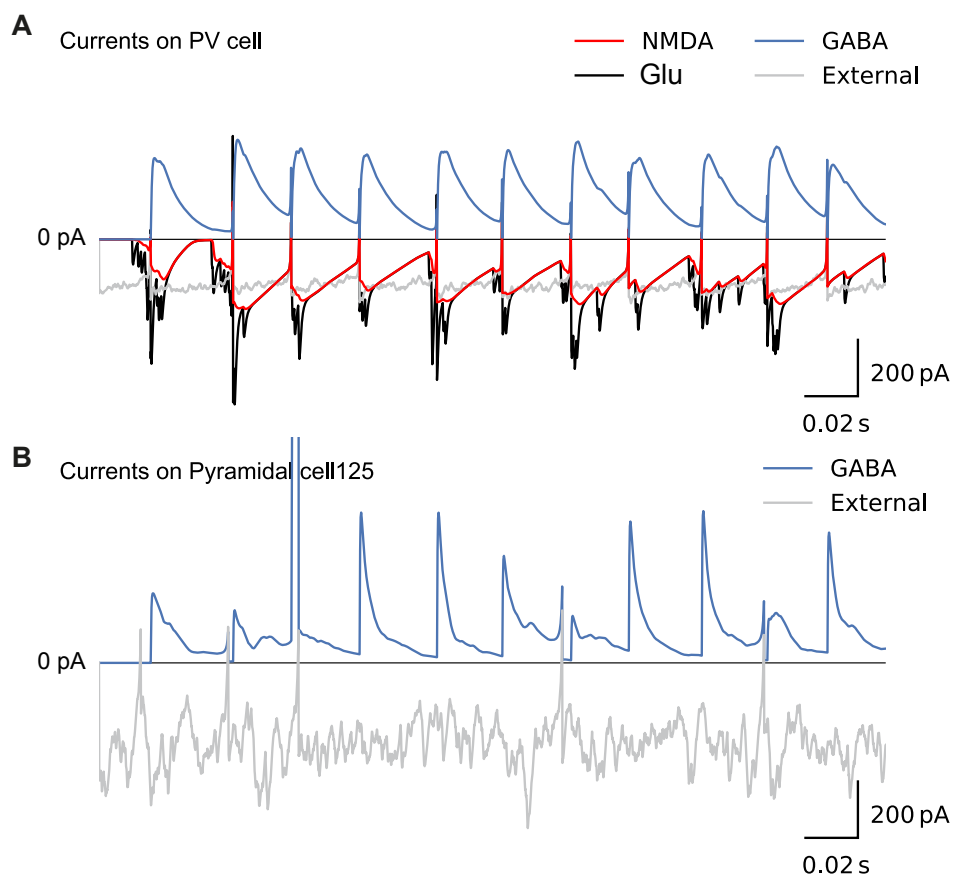


Figure 3.24. Example currents on neurons during network simulations (simulation fig. 3.23): (**A**) Current inputs onto the PV⁺ cell: (red) NMDAR, (black) glutamatergic, (blue) GABAergic, (grey) external. (**B**) Current inputs onto Pyramidal cell no.125: (blue) GABAergic, (grey) external.

We then investigated the response of the network to three different external input distributions, representing inputs that were either: clustered and temporally consistent, clustered but temporally inconsistent, and finally, distributed but temporally consistent. These input patterns are shown in methods, Figure 2.8. We hypothesised these different input patterns would generate network behaviour that resulted in the recruitment of differing amounts of NMDA receptor current by pyramidal cells.

Figure 3.25 shows the recruitment of the NMDA receptor-like conductance, per spike, by feedback inputs onto the model PV⁺ cell, for each of the external input distributions. As might be expected, the temporally consistent and clustered input recruits the most NMDA receptor current (0.622 pC per spike), followed by clustered but temporally inconsistent (0.072 pC per spike), and finally distributed but consistent (0.028 pC per spike). These values reflect the relative, and consistent, firing of "neighbouring" pyramidal cells, which is required to depolarise the postsynaptic membrane-patches and relieve NMDA receptors of Mg²⁺ blockade.

Local pyramidal cells often form cell assemblies, into which PV⁺ interneurons can be incorporated (Geisler et al., 2007), forming winner-takes-all lateral inhibition arrangements between cell assemblies (Trouche et al., 2016). We next investigated the result of competition between two sub-networks, driven by different external input distributions - with and without cooperative synaptic integration of feedback connections (NMDA receptors). Sub-network 1 was composed of neurons 1-250 and sub-network 2 of neurons 251-500 (Fig. 3.27). In these simulations, the PV⁺ interneurons of the two subnetworks provided lateral inhibition that was three times as strong as the recurrent inhibition of the sub-network to which it belonged. PV⁺ to PV⁺ interneuron inhibition was the same strength as auto inhibition.

Figure 3.27 shows two example simulation runs between two subnetworks, driven either by clustered or disperse input, with and without NMDA receptors on the PV⁺ cells. In Figure 3.27 A, network 1, which is driven by clustered external input, suppresses the activity of network 2, which is driven by disperse external input. In contrast, in Figure 3.27 B, without NMDA receptors, network 2 suppresses activity in network 1 - although not completely. Note that the winning network is also dependent on variation between simulations, in addition to NMDA receptors: Figure 3.29 A&B shows summary data for 500 simulation runs. Without NMDA receptors, there is equal chance (51.2%) that either network suppresses the activity of the other. In contrast, with NMDA receptors, the likelihood of network one winning increases to

75.2%. Furthermore, the ratio of pyramidal cell spikes from network 1 compared to network 2 becomes greater (3.29B), indicating more of a complete suppression of the losing network.

Figure 3.28 shows two example simulation runs between two subnetworks driven either clustered temporally consistent or inconsistent inputs, with and without NMDA receptors. Unlike in the simulations shown in Figure 3.27, the pyramidal neurons of the two networks are not driven equally by the external inputs. This is due to the temporally inconsistent input effectively "wasting" excitatory current (in driving the pyramidal cells to fire) when it switches location. To somewhat account for this, in these simulations the pyramidal neurons of network 2 received 5% stronger external input current.

In Figure 3.28 A, with NMDA receptors, network 1, which is driven by temporally consistent input, suppresses the activity of network 2, which is driven by temporally inconsistent external input. In contrast, in Figure 3.28 B, without NMDA receptors, neither of the two networks succeed in suppressing the other. Again, however, the winning network is also dependent on variation between simulations, in addition to NMDA receptors: Figure 3.28 C&D shows summary data for 500 simulation runs. Without NMDA receptors, there is roughly equal chance (58.3%) that either network suppresses the activity of the other. In contrast, with NMDA receptors, the likelihood of network one winning increases to 82.0%. In addition, similar to the clustered and disperse input simulations, the ratio of pyramidal cell spikes from the winning network compared to losing network becomes greater (3.28B).

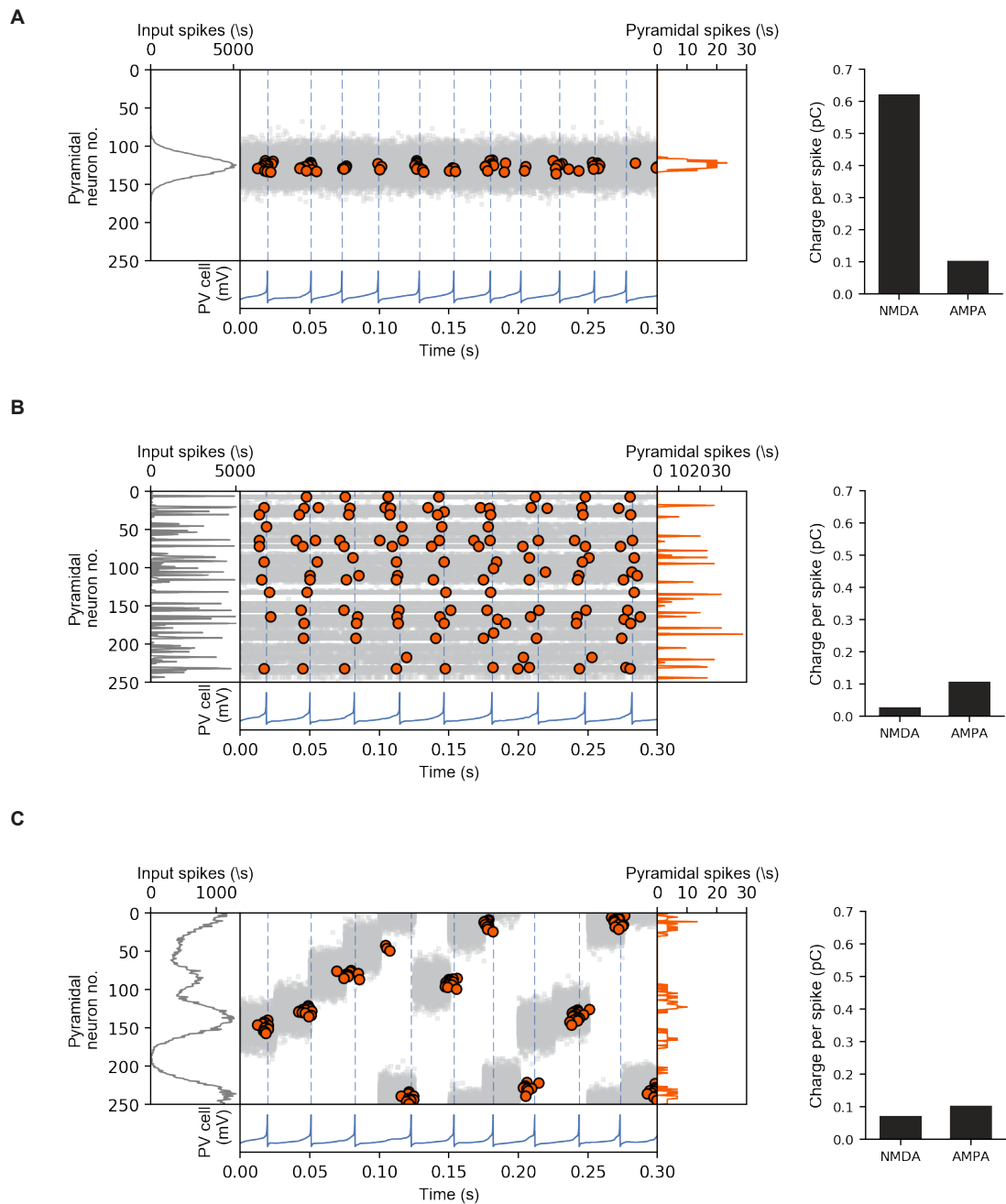


Figure 3.25. NMDA receptor recruitment by external input pattern: Response of network and NMDA receptor charge per spike of (A) clustered consistent (B) unclustered consistent and (C) clustered inconsistent input patterns.

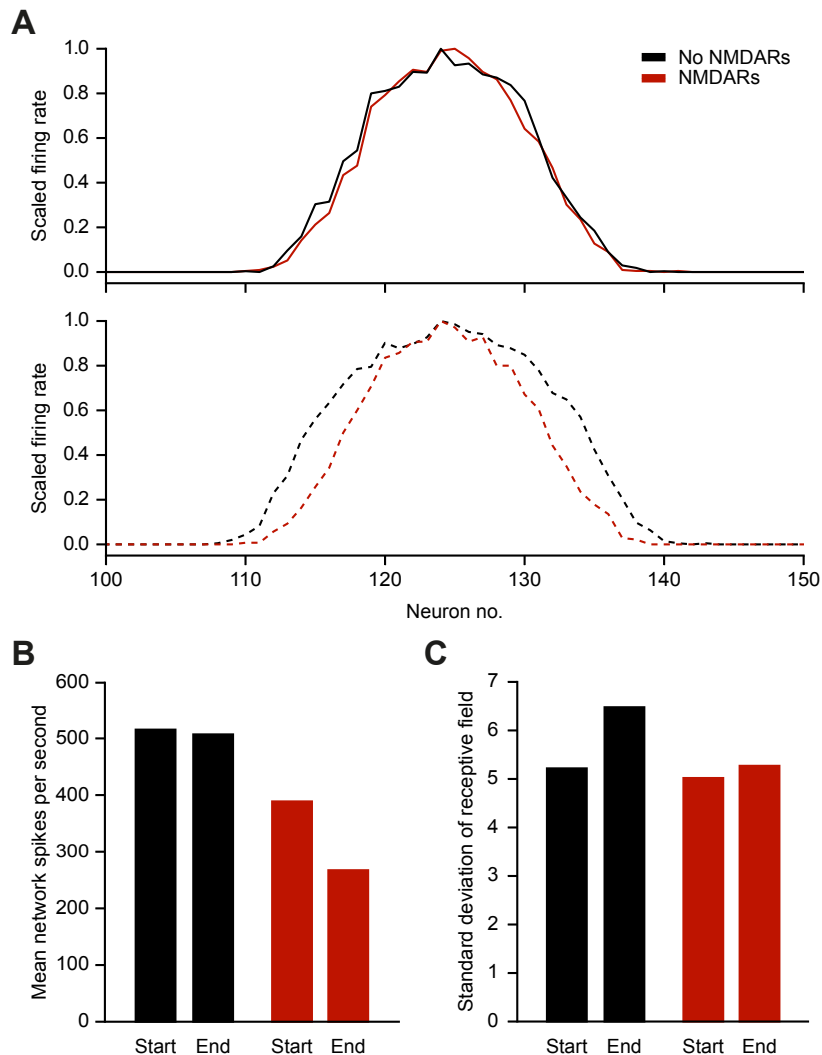


Figure 3.26. NMDARs help to maintain a sparse and sharp representation of a 'hump' of excitation to the feedback circuit shown. (A) Mean firing rate by neuron during the first 75 ms (top) and last 75 ms (bottom) of one hundred 300 ms - long simulations. The hump of excitation was centred on neuron 125, whose firing rate was used to normalize the firing rates of neurons 100 - 150 (other neurons are not shown). Black: without NMDARs; red: with NMDARs. (B) Mean network firing rates during first and last 75 ms of network simulation runs. (C) Standard deviation of average network "receptive field" during first and last 75 ms of simulation runs.

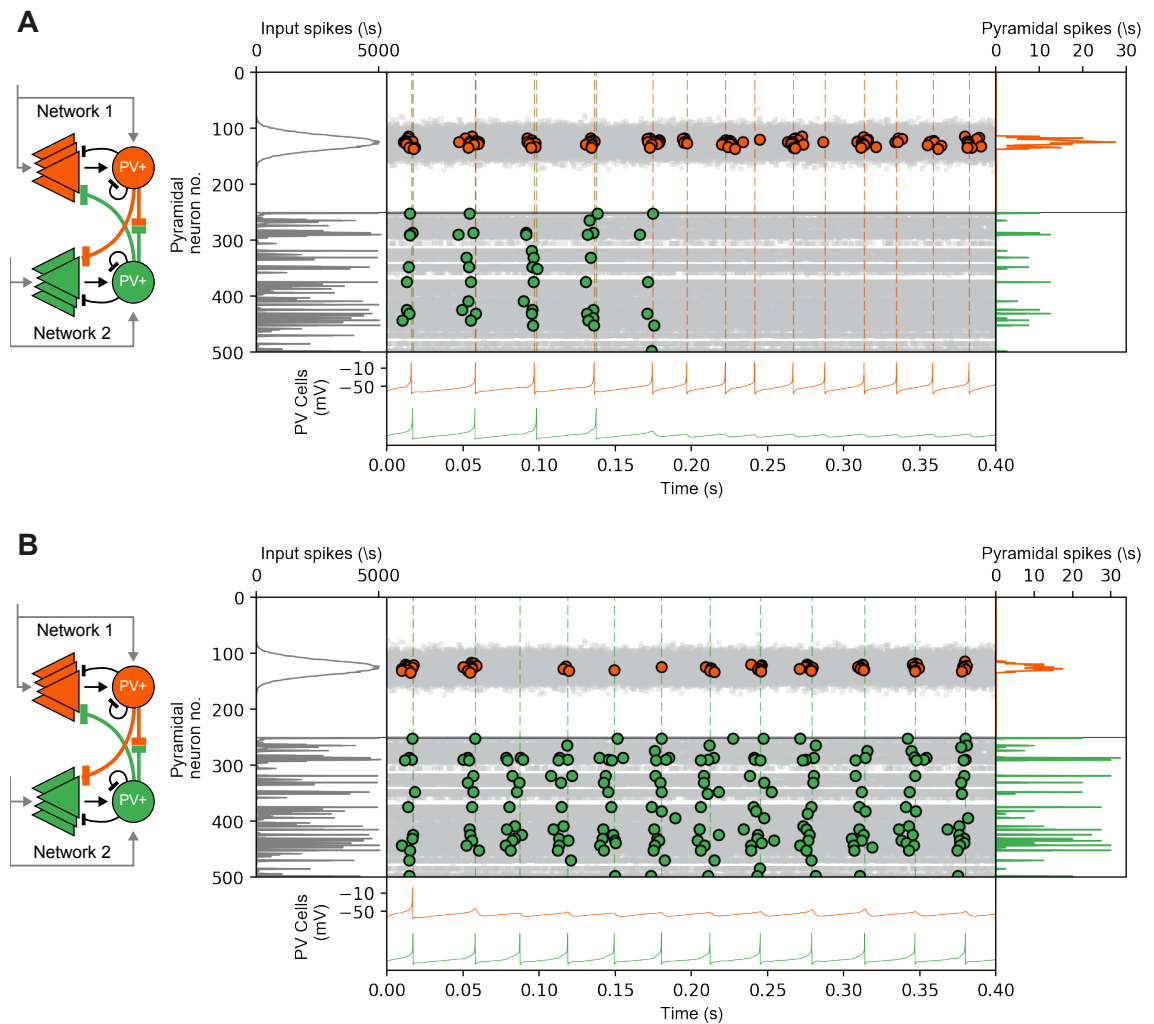


Figure 3.27. Subnetworks driven by clustered or dispersed inputs, with and without NMDA receptors: neurons 1-250 belong to network 1, and 251 to 500 to network 2. **(A)** With NMDA receptors onto PV⁺ cells. **(B)** Without NMDA receptors onto PV⁺ cells.

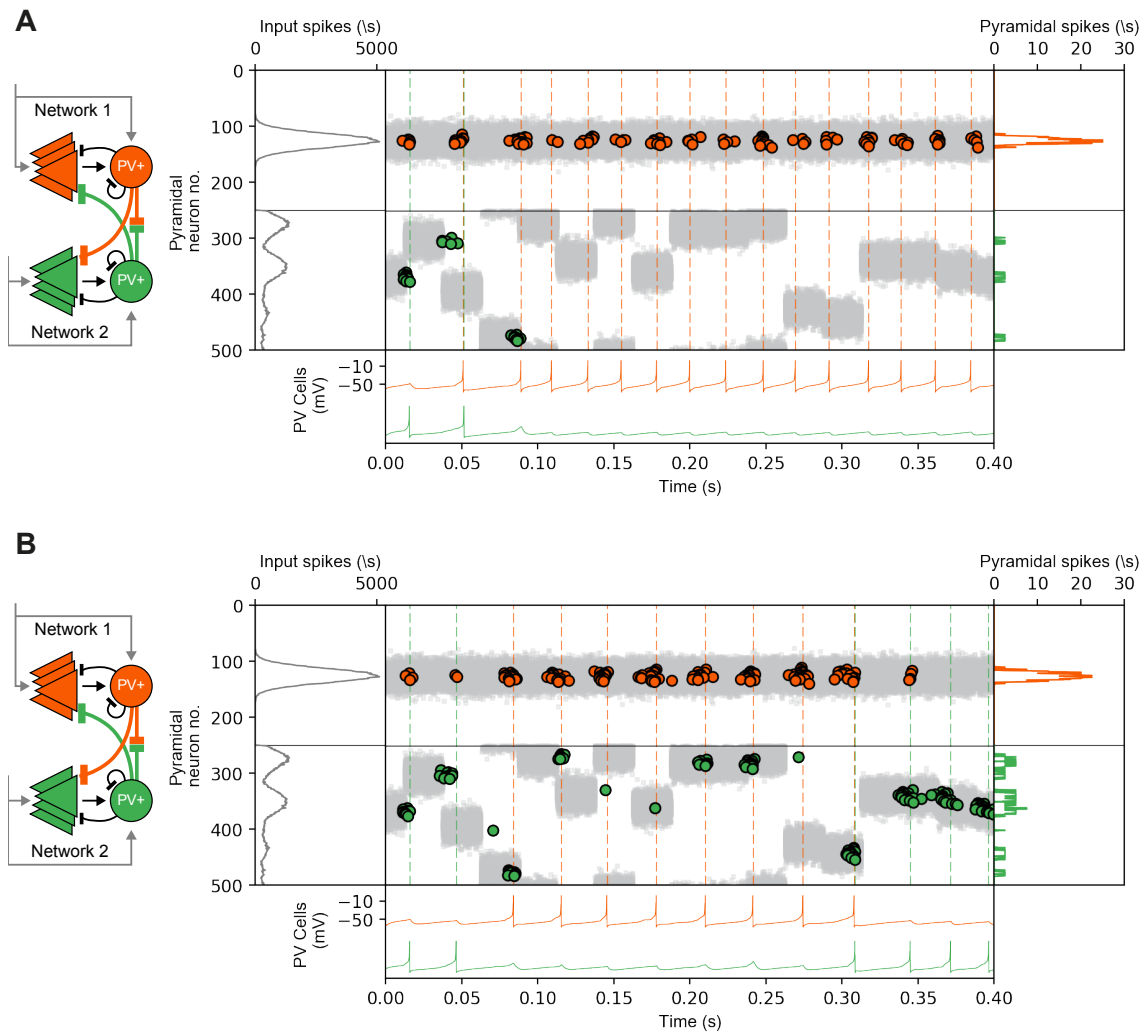


Figure 3.28. Subnetworks driven by clustered temporally consistent or inconsistent inputs, with and without NMDA receptors: neurons 1-250 belong to network 1, and 251 to 500 to network 2 (A) With NMDA receptors onto PV⁺ cells. (B) Without NMDA receptors onto PV⁺ cells.

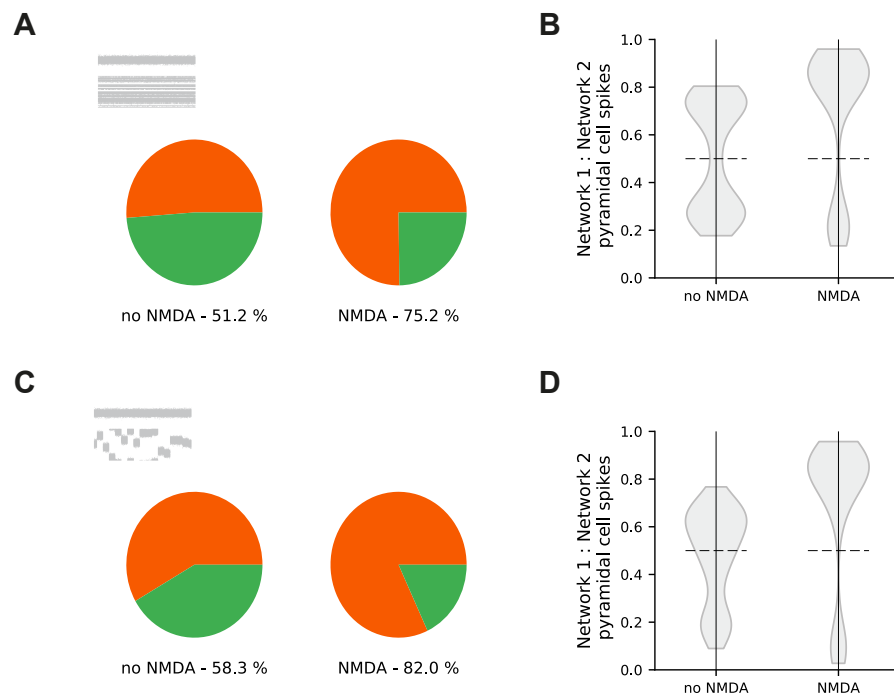


Figure 3.29. Summary data for competing subnetwork simulations: **(A)** Pie charts showing the probability of the network with clustered input (orange) suppressing the activity of the network with disperse input (green). **(B)** Violin plots showing the pyramidal neuron firing ratio of network 1 (clustered) vs network 2 (disperse). **(C)** Pie charts showing the probability of the network with temporally consistent input (orange) suppressing the activity of the network with inconsistent input (green). **(D)** Violin plots showing the pyramidal neuron firing ratio of network 1 (consistent) vs network 2 (inconsistent).

As NMDA receptor-mediated conductances are long lasting, we hypothesised that once a sub-network managed to dominate the competition between two competing subnetworks, the NMDA receptor-mediated conductance would make the winning subnetwork robust to noise in the external input. In contrast, in a system without NMDA receptors, fluctuations in external input could more easily elicit a flip in the dominant subnetwork. To investigate this we added stochastic noise to the homogeneous Poisson process generating the external input spikes, and ran simulations for 5 seconds, while varying the ratio of AMPA and NMDA receptors.

Figures 3.30 A and 3.31 A show example simulations in which the dominant network flips regularly. In this simulation, peak NMDA receptor current per synapse (at +60) is 3.6 pA, and AMPA receptor current per synapse (at +60) -92.9 pA. In Figure 3.30 B & C, NMDA receptor strength is increased to respectively 14.6 pA and 58.3 pA. With modest NMDA receptor current, the same as in subnetwork simulations, the dominant network flips less, only four times instead of eleven (Figure 3.30 B). Increasing NMDA receptor strength further results in the dominant network identity only switching once.

Figure 3.31 shows the results of increasing peak AMPA receptor current from -92.9 pA, to -185.7 pA (Fig.3.31B) and 371.42 pA (Fig.3.31C). In contrast to increasing NMDA receptor strength, increasing AMPA the did not make the dominant subnetwork more robust to noise in the external drive to the network. Figure 3.32 Shows average dominant network flip rate as NMDA receptor and AMPAR receptor conductances are varied.

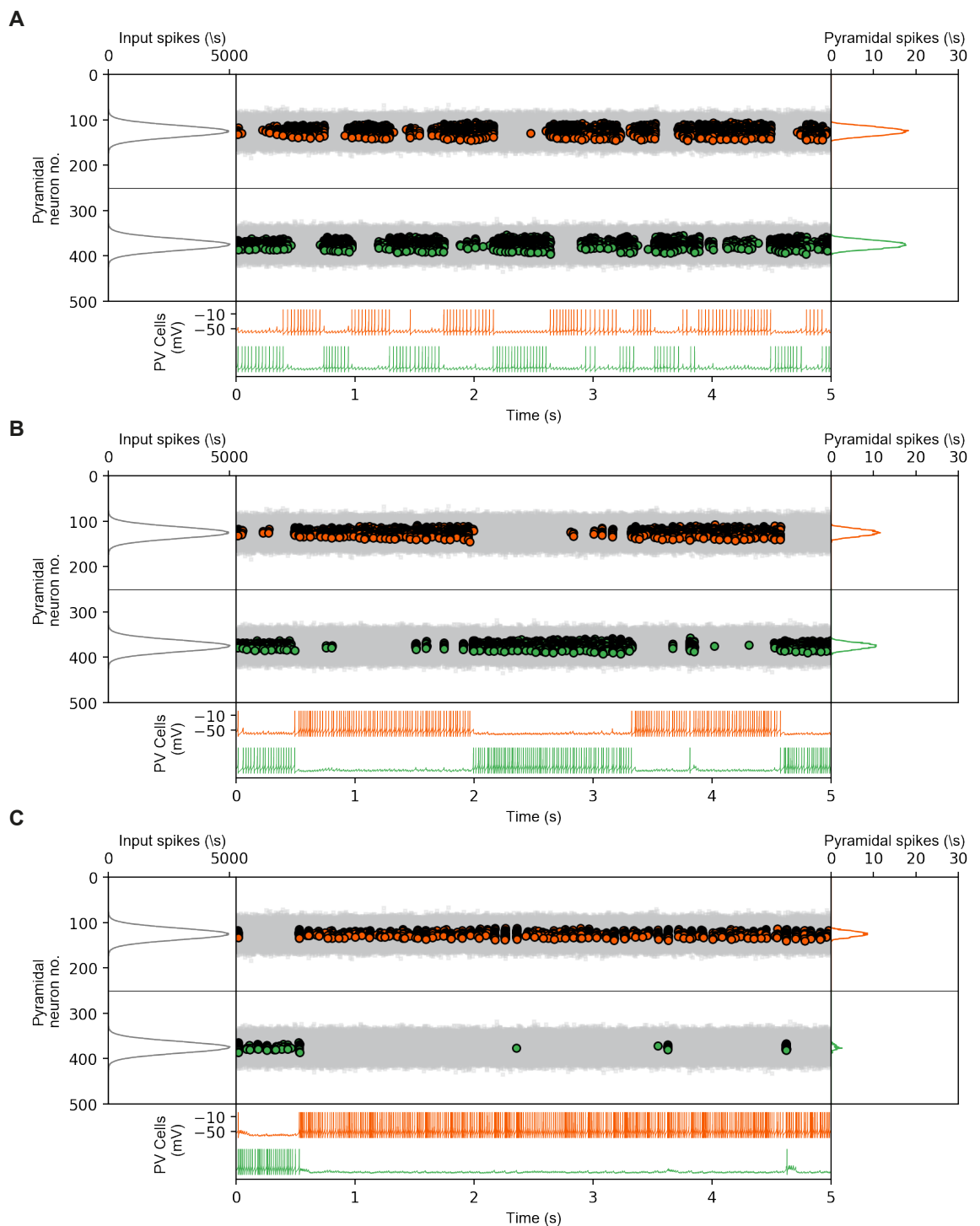


Figure 3.30. Competing subnetworks with external input noise - varying NMDA receptor strength: peak AMPAR current held at -92.9 (-60 mV) while NMDAR strength changed (A) Low (peak amplitude 3.6 pA $+60$ mV) (B) modest (peak amplitude 14.6 pA $+60$ mV) (C) large (peak amplitude 58.3 pA $+60$ mV).

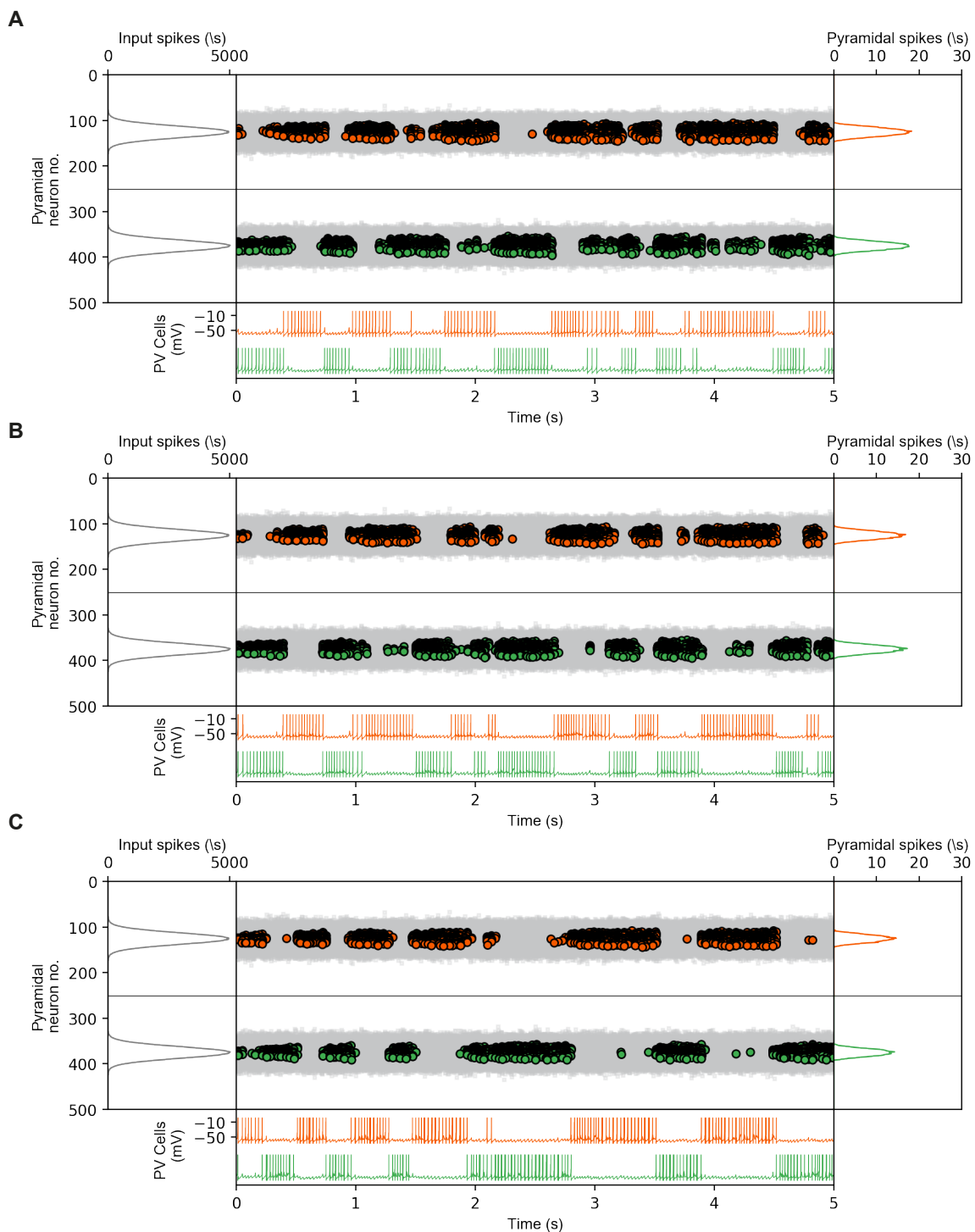


Figure 3.31. Competing subnetworks with external input noise - varying AMPA receptor strength: peak NMDA receptor current held at 3.6 (+60 mV) while AMPAR strength changed (**A**) control (peak amplitude -92.9 pA -60 mV) (**B**) modest (peak amplitude -185.7 pA -60 mV) (**C**) large (peak amplitude -371.42 pA -60 mV).

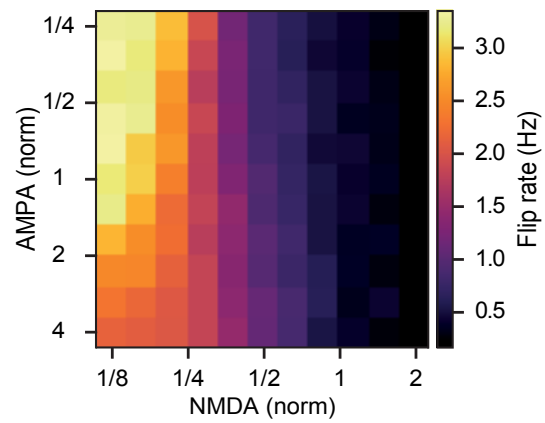
A

Figure 3.32. Dominant network flip rate vs NMDAR and AMPAR conductance.

3.3 Discussion

Here we show that the dendrites of PV⁺ interneurons that receive local excitatory feedback inputs are able to summate uncaging-evoked EPSPs in a NMDAR-dependent supralinear manner, whereas dendrites that solely receive feedforward inputs integrate inputs linearly. We reproduce work showing that feedback connections onto PV⁺ cells express a larger NMDA receptor conductance than feedforward inputs, and hypothesise that this imbalance in NMDA receptor expression, coupled with their preferential recruitment due to stratum oriens dendrite morphology, underlies the differential synaptic integration shown by the two dendrites. Extending this notion of cooperative local feedback synapses to the network-level, we show that the presence of an NMDA receptor-like conductance onto fast inhibition grants a reduced network the ability to discriminate between the spatial and temporal consistency of input distributions. When placed in a winner-take-all configuration, clustered and temporally consistent networks are able to most effectively recruit NMDA receptor-like conductance, facilitating their dominance. Furthermore, we show that NMDA receptors are able to stabilise the winning sub-network in the face of distracting inputs and noise.

This description of NMDA receptor-dependent synaptic integration by PV⁺ interneurons, and its role at the network level, brings together a number of somewhat disparate observations, and builds on one other study (Chiovini, 2013) in enriching the linear synaptic integration and fast coincidence detection mediated by PV⁺ interneurons (Hu et al., 2014*a*). Until now, the observation of Hebbian NMDAR-dependent LTP at feedforward synapses (Le Roux et al., 2013) has stood somewhat alone from theories of how PV⁺ cells handle synaptic inputs. Furthermore, the lines of evidence implicating NMDA receptors on PV⁺ cells in pathology and network disorders have, to a certain degree, lacked traction due to the absence of a prescribed, clear function of NMDA receptors in synaptic integration by these cells. If one considers the role of NMDA receptors purely in the feedforward function of PV⁺ cells, the slow NMDA receptor conductance is indeed paradoxical. However, by considering the role of NMDA receptors at feedback connections, where they are enriched, and in the larger temporal context of oscillations, the ability of NMDA receptors to facilitate feedback excitation recruitment becomes clearer and more meaningful.

3.3.1 Glutamate-uncaging experiments

Of the assumptions underpinning our conclusions, perhaps the most important is the synaptic nature of uEPSPs, or the contribution of feedback synapses to the uEPSPs elicited on stratum oriens dendrites. With regards to the synaptic nature of uEPSPs, the synaptic density onto parvalbumin interneuron dendrites is particularly high, as shown in Figure 1.2, around $4 \mu\text{m}^{-1}$ (Gulyás et al., 1999), and the lack of spines decreases the dendritic surface area relative to other cell types. In addition, the theoretical two-photon uncaging lateral psf is approximately half a micron. We also show in section 2.1.3 (Figure 3.1) that spontaneous somatic uEPSP waveforms can be similar to the somatic waveforms elicited by glutamate uncaging, supporting a synaptic receptor origin of uEPSPs - though the rise and decay times are slower. In general, it is therefore perhaps not surprising that glutamate uncaging generally produced synaptic-like responses, and that silent uncaging locations were relatively rare (though we did not exclude these sites in case they were silent-synapses, without an AMPA receptor component).

However, it remains an experimental caveat of glutamate uncaging is that significant numbers of extra-synaptic glutamate receptors may be activated by an uncaging event. Furthermore, if stratum oriens dendrites were to express more extra-synaptic NMDA receptors than stratum radiatum dendrites this provides an alternative explanation for our experimental results (independent of feedforward/feedback pathways). Differential extra-synaptic receptor expression would follow if a specialised function of oriens dendrites was to sense glutamate spillover from synapses, for example in order to mediate local-network stabilisation, or if the extra-synaptic NMDA receptors expressed oriens were composed of subunits with a greater affinity for glutamate.

Differing synaptic density between oriens and radiatum dendrites also provides a separate, thematically related, alternative explanation for our results. For example, if oriens dendrites expressed a higher density of receptors, glutamate uncaging would lead to stronger activation of oriens dendrites: the general proximity of uncaging spots to synaptic receptors would be expected to be greater, resulting in less silent uncaging locations and more poly-synaptic activations (if they occurred). Radiatum dendrites could therefore be lower down on the voltage-dependent "recruitment" curve of the NMDAR-mediated nonlinearity. In this case stronger activation of radiatum dendritic locations, independent of feedforward or feedback pathway considerations, would be

able produce similar uEPSP integration to that seen in the oriens. One way in which this potential caveat could be experimentally addressed would be to require saturation of the compound uEPSP, either through more uncaging sites or stronger uncaging laser powers, as saturation would indicate that the local dendritic location was significantly depolarised. Unfortunately, in general we did not observe uEPSP saturation, and often compound uEPSP sizes were close to causing the cell to fire action potentials, imposing an upper limit on compound uEPSP size. Indeed, in general we can only conclude the NMDARs to be operating in the mode of uEPSP boosting (Schiller and Schiller, 2001), rather than generating saturating feed-forward NMDAR-dominated "spikes". However, evidence from electron microscopy studies indicates that stratum oriens and radiatum dendrites seem to have similar synaptic densities, ~ 400 per $100 \mu\text{m}$ of dendrite, in the sub-cellular areas we investigated (Gulyás et al., 1999, Table 4). Finally, although somatic potentials are poor estimates of local dendritic potentials, somatic responses were comparable for both locations.

Further uncaging experiments, to detect synaptic "hotspots" or the degree of glutamate spread upon uncaging may help address the above questions. However, glutamate uncaging's activation of synaptic receptors is ultimately imprecise. A potential solution to these general experimental limitations would be to use electrical stimulation for all experiments, not just those investigating NMDAR ratios at feedforward and feedback synapses. Electrical stimulation could be achieved either with field stimulation experiments, or with local stimulation of axons near a dendritic region of interest, for example using theta-glass pipettes. However, while the synaptic origin of responses is essentially guaranteed, detailed assessment of integration would be more difficult relative to glutamate uncaging. Electrical stimulation is unable to precisely control the number of synaptic locations recruited, and independent activation of synapses is not possible. Furthermore, field stimulation does not guarantee that synaptic clusters will be recruited, so dendritic integration mechanisms may not be engaged. In contrast, while local stimulation of axons near a dendrite does improve synaptic clustering, pathway selectivity - one of the main strengths of field stimulation - is lost. In addition, intense local stimulation may also generate glutamate spillover from synapses, re-engaging the previously discussed extra-synaptic receptor activation concerns. Finally, in our hands, stimulation of Schaffer collaterals produced significant recurrent activation of PV⁺ cells by local CA1 pyramidal cells with very modest intensity, further complicating experimental design. It is therefore not clear that electrical stimulation is a better choice to investigate synaptic integration.

The existence of synaptic clustering on PV⁺ cells is a fundamental assumption of both the uncaging experiments and the network modelling, as it is required for the cooperative recruitment of NMDA receptors. While there are multiple lines of evidence for synaptic clustering in principal cells, reviewed in section 1.1.2, this is still an active area of research, and the functional clustering assumed by our conclusions is controversial. In addition, to our knowledge, there are no comparable studies investigating synaptic clustering on PV⁺ interneurons, and, while we believe assuming similar clustering on PV⁺ interneurons is a fair assumption, it remains possible that these clustering rules are different between principal cells and interneurons.

The network modelling, which builds on the results of the uncaging experiments, assumes that the uEPSP nonlinearity is mediated by NMDARs at feedback synapses. Unfortunately, the proportional contribution of feedback synaptic receptors to the uncaging evoked responses from stratum oriens dendrites is unclear. However, the field stimulation experiments showed feedforward synapses mediate small NMDA receptor conductances, and radiatum dendrites, which only receive feedforward inputs, display linear integration. Therefore, the heterogeneity of feedforward and feedback synapse types on oriens dendrites should dilute supralinear integration of uEPSPs. As a result, perhaps the strongest argument for our activation of significant numbers of feedback synapse receptors, in support of the network modelling, is simply that stratum oriens dendrites are able to summate uEPSPs in an NMDAR-dependent, supralinear manner.

We also did not investigate, or include in the NEURON modelling, the potential role of a Ca²⁺ conductance in uEPSP integration, which likely plays an active role. For example, Ca²⁺ conductances may explain the somewhat unexpected linear integration shown by radiatum dendrites, and oriens dendrites in the presence of APV. While roughly linear integration by passive dendrites in response to spatially dispersed inputs is an accepted theory (Yuste, 2011), we elicited spatially clustered uncaging-evoked inputs. Each preceding input is therefore expected to reduce the electrical driving force and effective input resistance seen by the following input, resulting in sublinear integration. Furthermore, a significant K⁺ conductance is expressed in PV⁺ cell dendrites, which should further contribute to sublinear integration. A feedforward nonlinear conductance is therefore needed to arrest and linearise the seemingly inevitable sublinear integration. Na⁺ channels are unlikely candidates, both due to their sparse expression in PV⁺ cells (Hu et al., 2014a) and the lack of an effect of TTX in significantly altering uEPSP integration. Instead, in some manner, finely

tuned Ca^{2+} conductances, likely balanced by K^+ channels, may underlie linear stratum radiatum integration, and we expect are also recruited by NMDA receptors in the oriens.

The absence of a clear relationship between distance from soma and integration nonlinearity was a surprising result. As expected, in the NEURON model this relationship was clearly observed. However, the tail-off in peak-amplitude non-linearity with distance from the soma, seen in the NEURON model, may also provide an explanation - as synaptic input location becomes more distal, the larger local EPSPs will be more able to recruit hyperpolarising conductances, such as potassium, and generate greater reductions in electrical driving force per synaptic input. Furthermore, synaptic inputs will elicit relatively larger shunts of the local membrane resistance. As a result, we may expect a sigmoid or parabola shaped relationship between distance-from-soma and integration nonlinearity for a single dendrite. While the NEURON modelling is a single cell, experimental data was obtained from a mixture of dendritic morphologies. The relationship between, for example, $45 \mu\text{m}$ and $50 \mu\text{m}$, which is a straightforward in the model and along the same dendrite, is not known in terms of heterogeneous dendritic morphologies. Whatever the true distance-nonlinearity relationship, $45 \mu\text{m}$ and $50 \mu\text{m}$ may not be comparable between cells. The distance-nonlinearity plots could therefore be seen as random samplings from many overlapping distance-nonlinearity relationships, which are unique for each physical dendrite.

3.3.2 Network simulations

In the network simulations described in this chapter we investigated possible functions that cooperative supralinear feedback connections onto fast inhibition might have in the context of cell assembly competition. Evidence for assembly competition, and the involvement of PV^+ interneurons, comes from a number of studies. One study, which used c-fos activation to tag the subset of CA1 cells active in a spatial environment, showed that silencing active cells uncovered the firing of a different population of cells that encoded an alternative spatial representation, which were previously suppressed (Trouche et al., 2016). While this study did not directly identify PV^+ cells as mediating the suppression of the alternative cell assembly and its spatial representation, they are the likely candidate. Furthermore, previous studies have indicated that PV^+ cells mediate lateral inhibition between principal cells (Geisler

et al., 2007).

The most straight-forward of these functions is the sharpening of a clustered, consistent external input, with regards to the number of "k-winners" per gamma cycle (de Almeida et al., 2009a). Here, the NMDA receptor-like conductance ramps up, reducing the number of pyramidal cells that are required to recruit the feedback inhibition. As a result, fewer pyramidal cells fire before the population as a whole is inhibited, and only the most driven pyramidal cells are able reach threshold in time. By scaling up the AMPA conductance a similar "iceberg" effect could also be achieved, however, this would not be dynamic, dependent on the presence of a clustered consistent signal. In addition, simply scaling the AMPA conductance might render the system more vulnerable to noise, as every input would be more able to drive the PV⁺ cell to firing threshold. This function may be important for PV⁺ roles such as facilitation of sparse coding in the dentate gyrus, and place cell field regulation - which is known to be less spatially precise when NMDA receptors on PV⁺ cells are absent (Korotkova et al., 2010).

We also show that the NMDA receptor-like conductance on PV⁺ cells allows signals that are clustered and temporally consistent to dominate over more inconsistent or disperse signals that are represented by competing cell assemblies. The likelihood that two inputs with such different statistics as those used in the simulations drive competing cell assemblies in a physiological situation is low. However, instead, these simulations provide a set of clear examples for the general principal of differential exploitation of the NMDAR dependent supra-linear synaptic integration by assemblies driven by different input statistics. Simulations with both more balanced statistics and differing input strengths would be interesting avenues of further work.

An alternative way in which this type of lateral network-competition could be implemented is through slower inhibition, from example an inhibitory connection with a large GABA_B component. However, by placing the NMDA receptors on the PV⁺ cell, the feedback connections cooperate to recruit a fast source of inhibition and the networks would be able to rapidly switch - for example if a signal to one subnetwork dissipated. In contrast, slower inhibition would take longer to stop inhibiting the now valid signal.

Simulations also show that NMDA receptors increase the winning network's stability in the face of variations in external input drive. This occurs as consistent

feedback inputs from the winning network become relatively more powerful than the opposing network's feedback inputs, as NMDA receptor conductance ramps up with repeated, neighbouring synaptic activations. Therefore, the dominant network needs fewer pyramidal cells to fire in order to recruit its interneuron.

This result is interesting in terms of pathologies involving PV⁺ cells, such as schizophrenia. One of the core symptoms of schizophrenia is disordered thinking, a general inability to focus on a sensory input in concentrated manner, when patients seem almost to flicker between input streams. It is interesting to note that without NMDA receptors, albeit in our very reduced model, we uncovered an effect that resembles these symptoms, at least at a very high level. It is therefore exciting to speculate if a mechanism somewhat akin to that of our model underlies the mounting evidence implicating particularly PV⁺ cells and NMDA receptor loss in schizophrenia.

Chapter 4

Polyamine modulation of AMPA receptors

4.1 Introduction

AMPA receptors that either lack or contain unedited GluA2 subunits are orders of magnitude more permeable to Ca^{2+} than AMPA receptors that do not (Geiger et al., 1995). While these calcium-permeable AMPA (CP-AMPA) receptors can sometimes be found at excitatory inputs onto principal cells, for example in early development and during pathologies such as epilepsy (Liu and Savtchouk, 2012), CP-AMPA receptors are most commonly seen at excitatory inputs onto interneurons, in particular PV^+ fast-spiking interneurons (Lalanne et al., 2015).

As discussed in section 1.2.4, the lack of an edited GluA2 AMPA receptor subunit alters an AMPA receptor's properties in a number of ways, in addition to increasing calcium permeability. CP-AMPA receptors typically show faster desensitisation and larger single channel conductances (Swanson et al., 1997) than calcium-impermeable AMPA receptors, and are sensitive to polyamine blockade at depolarised potentials. Of these changes, wrought by the lack of an edited GluA2 subunit, generally, most attention is given to the faster channel kinetics (Lalanne et al., 2015), or the Ca^{2+} conductance, for example the role of CP-AMPA receptors in the mediation of synaptic plasticity and "anti-hebbian LTP" (Lamsa et al., 2007; Camire and Topolnik, 2014).

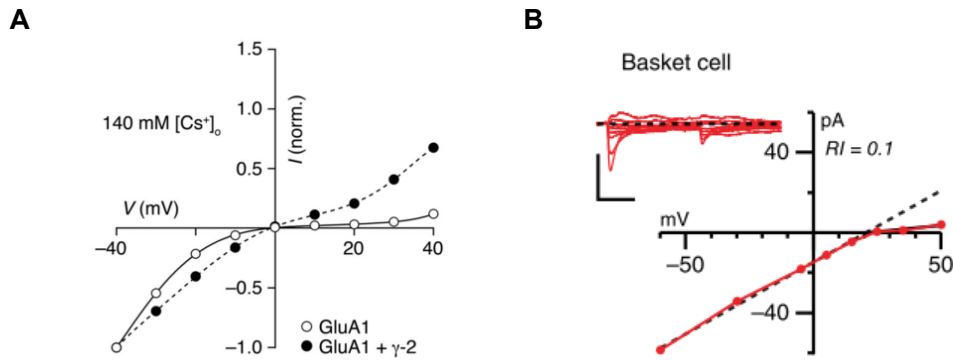


Figure 4.1. CP-AMPA receptor rectification properties: **(A)** polyamine-induced rectification is reduced by association with TARPs (Soto et al., 2014) **(B)** Inward-rectification only seen at depolarised potentials in whole-cell patch clamp. (Lalanne et al., 2015)

In contrast, polyamine modulation of receptor conductance, and the inward rectification of the current-voltage relationship that it causes, is often seen more as a diagnostic tool, to be used for identification of CP-AMPA receptor expression (Bowie, 2012), than of functional importance - for example in synaptic integration. This relative lack of attention may be partly due to experiments showing either weak rectification in outside-out patches (Koh et al., 1995; Jonas et al., 1994), or emphasizing strongly depolarised clamp potentials, >0 mV, for rectification. (Lalanne et al., 2015). However, analysis of recombinant CP-AMPA and CP-kainate receptor currents in HEK cells suggests substantial attenuation of current flow closer to resting potential (Bowie and Mayer, 1995), supporting a functional role for CP-AMPA receptors.

Auxiliary transmembrane AMPAR regulatory proteins (TARPs) strongly affect AMPA receptor properties, including the sensitivity of CP-AMPA receptors to polyamine blockade (Fig. 4.1 A; Soto et al., 2014). Association with TARPs is therefore one possible explanation for the weak rectification seen in some experiments, as is the disruption of the cytoplasmic gating mechanisms in the outside-out patch recording configuration (Bowie and Mayer, 1995). However, whole-cell voltage clamp experiments record polyamine mediated rectification, but only at more positive potentials (Fig. 4.1 B; Lalanne et al., 2015). This inconsistency might be due to the difficulties of attaining voltage clamp in cells with dendrites (Williams and Mitchell, 2008), and, substantial rectification may therefore also be apparent at more hyperpolarised potentials.

Chapter Aims

The work presented in this chapter aims to determine whether polyamine modulation of channel pore conductance might have a functional role in the synaptic integration performed by PV⁺ interneurons.

As direct measurement of CP-AMPA receptor rectification in neurons, such as PV⁺ interneurons, is complicated by the issues described above, we took a simplistic approach and asked, using multi-compartmental modelling, whether a functional readout would be expected given a generous degree of rectification seen in cell culture experiments (Bowie et al., 1998).

4.2 Results

4.2.1 Kinetic model of CP-AMPA receptors

In order to investigate polyamine modulation of CP-AMPA receptors in a multi-compartmental model, we first required a model CP-AMPA receptor. To our knowledge, however, no CP-AMPA receptor exists for use in NEURON-model simulations. We therefore built a NEURON compatible receptor-model using a published glutamate receptor kinetic scheme (Fig. 4.2A; Bowie et al., 1998). Figure 4.2 B displays the flux of model through states in response to a square pulse of glutamate (1 mM 0.5 ms) after 20 ms, note that polyamines bind to the model before glutamate is presented (blue traces). In order to verify the model receptor current adequately reflected experimentally measured responses, we compared it to an uncaging evoked voltage clamp current from of a proximal location, in the presence of APV. This comparison is shown in Figure 4.2 C.

Figure 4.3 shows model receptor current-voltage (IV) relationships. For all simulations polyamines were modelled as a concentration of 100 μM , in line with intracellular estimates and previous work (Lalanne et al., 2015). Without polyamines, the model receptor shows a linear IV relationship, similar to that of calcium impermeable receptors, in contrast, polyamines caused significant inward rectification in the IV relationship. As polyamines bind to the receptor before glutamate presentation (Fig. 4.2B), they reduce the available receptor conductance. Therefore, in order to compare between receptors with, and without polyamines, we scaled up the maximum conductance of the model receptor when polyamines were included in the simulations (4200 nS vs 2000 nS). The model-receptor IVs shown in Figure 4.3 are obtained with this scaling, in order to match peak-currents at clamped hyperpolarised membrane potentials.

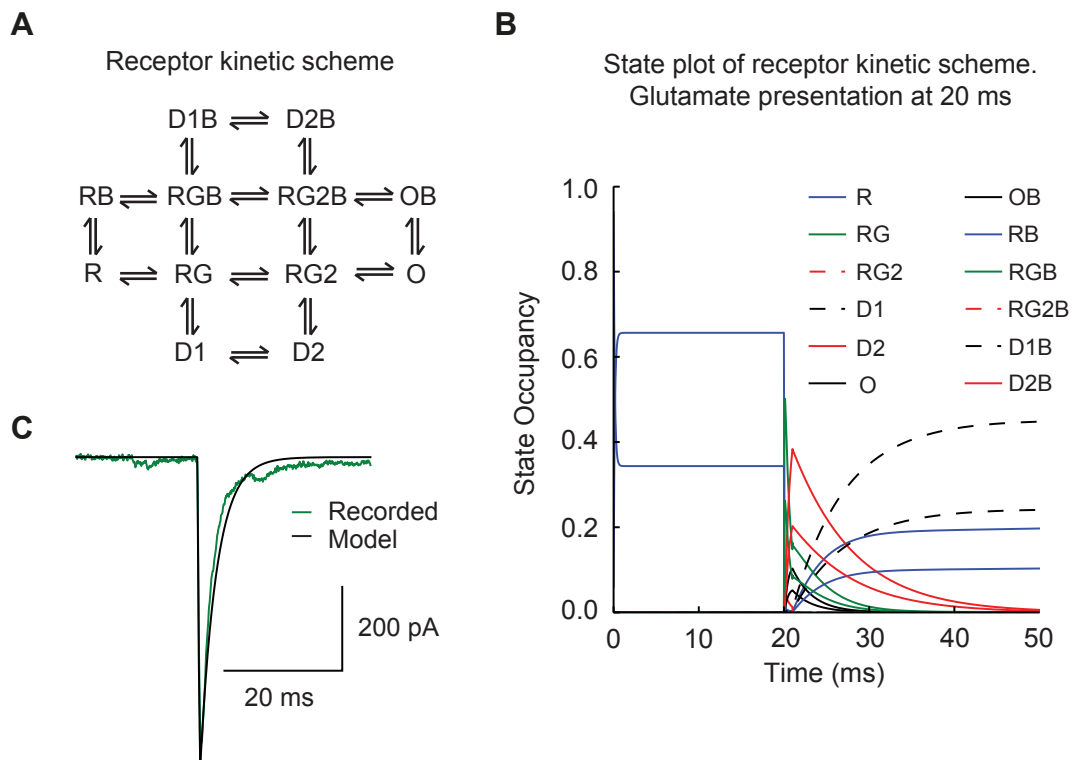


Figure 4.2. Model CP-AMPA receptor: **(A)** Receptor kinetic scheme from Bowie et al. G: glutamate, B: polyamine, D:desensitised, O: open, R:receptor. (Bowie et al., 1998). **(B)** Plot showing flux of model through receptor states in response to a square pulse of glutamate at 20 ms (1 mM 0.5 ms). **(C)** Comparison of model receptor current (black) to uncaging evoked current (green)

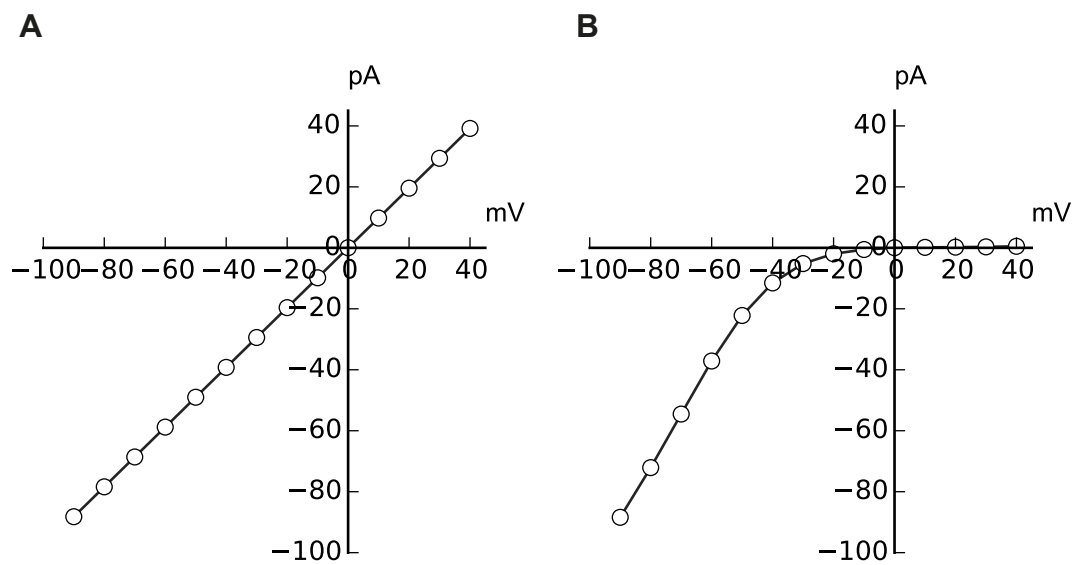


Figure 4.3. Model CP-AMPA current-voltage relationships: (A) without polyamines (B) with polyamines.

4.2.2 Polyamine-modulation of CP-AMPA receptors mediates sublinear synaptic integration

In order to explore synaptic integration by PV⁺ cells, with polyamine-mediated rectification, we simulated synaptic inputs onto a passive dendritic tree, and quantified synaptic integration nonlinearity as described in section 2.1.5. Fifteen synapses were placed at a dendritic location of the model PV⁺ cell (Figure 4.4) and we compared EPSP summation waveforms to their expected summation, calculated arithmetically from individual EPSPs. Presenting synaptic inputs with a delay of 0.5 ms (Fig. 4.4 A) resulted in sublinear integration (due to an absence of NMDARs and Na⁺ channels) both without and with polyamines, though the percentage sublinearity was greater with polyamines (-10.0 vs -23.0 %). Without polyamine-mediated rectification, the expected maximum somatic potential was 5.9 mV, and the recorded summated input was 5.0 mV. With polyamine-rectification (and scaled up synaptic conductance), the expected maximum somatic potential was 6.4 mV, however the recorded summated input was even lower than control, only 4.2 mV.

Figure 4.5 B, C, D, shows simulations in which synapses were activated with increasing inter-synaptic delays: respectively 1, 2, and 4 ms. Consistent with results of simulations with inter-synaptic intervals of 0.5 ms, polyamine-mediated rectification of synaptic currents resulted in increased integration sublinearity. However, as inter-synaptic delay was increased, the relative difference between integration nonlinearity with polyamines, or without, decreased. In addition, as expected from passive cable theory, the overall synaptic integration sublinearity for both inputs decreases with increased inter-synaptic delay.

Figure 4.6 displays summary data showing the relationship between synaptic integration, with and without polyamines, and inter-synaptic input delay. At synaptic delays of 0.5 ms or less, the difference between the peak voltage of expected arithmetic summation and recorded summation is particularly broad, but becomes more negligible after delays of 4 ms (Fig 4.6 A). For all simulations, polyamine inclusion resulted in greater sublinearity of synaptic integration, particularly for small delays (Fig 4.6 B).

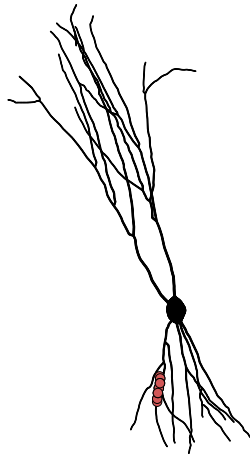
A

Figure 4.4. Model PV⁺ cell and with synaptic locations

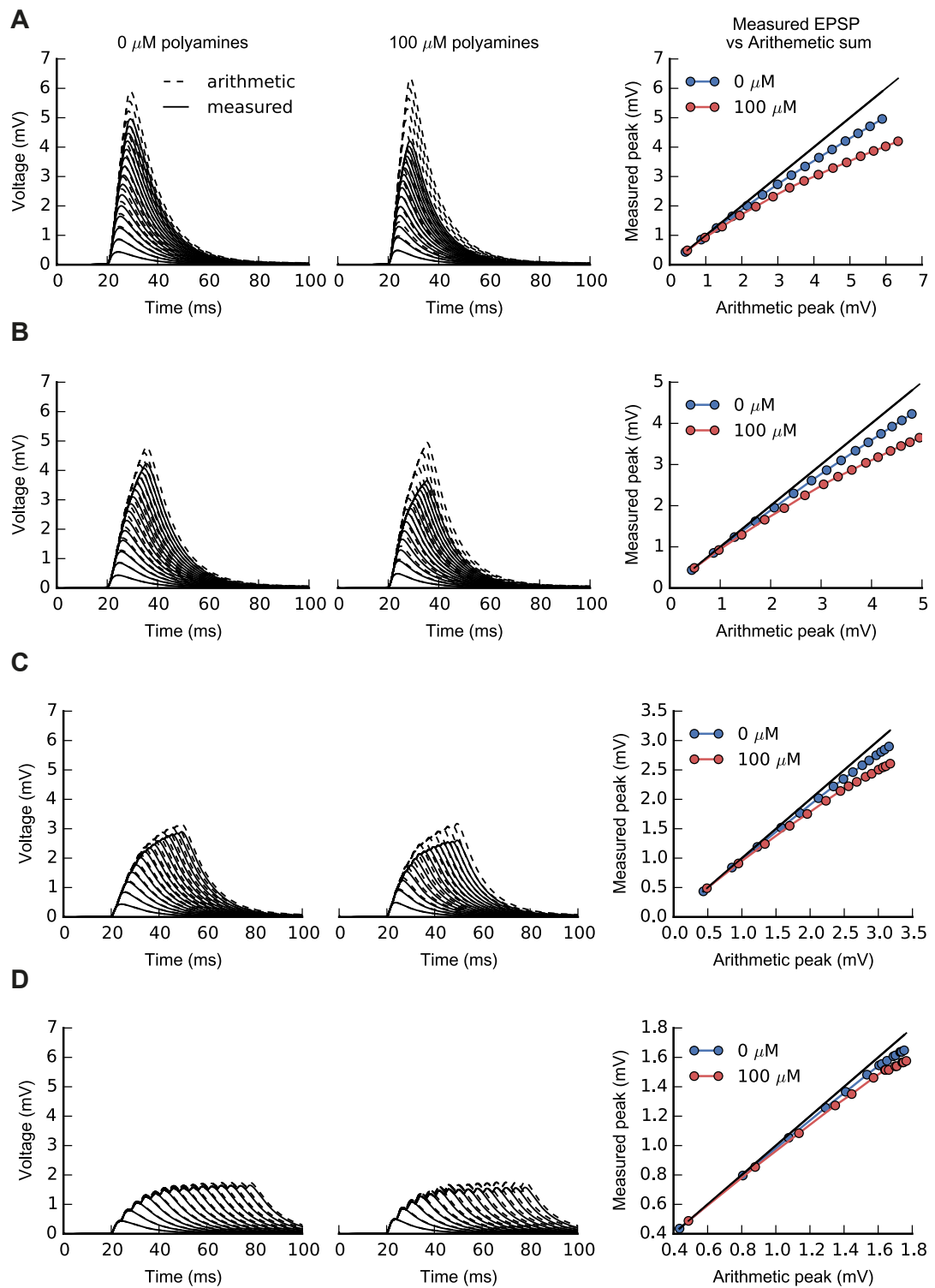


Figure 4.5. EPSP summation with and without polyamines: panels show various delays between synaptic inputs (**A**) 0.5 ms, (**B**) 1 ms, (**C**) 2 ms, (**D**) 4 ms. (Left) plots show recorded synaptic summation (solid lines) and arithmetic summation (dashed lined). (Right) plot of peak recorded EPSPs vs peak arithmetic EPSPs.

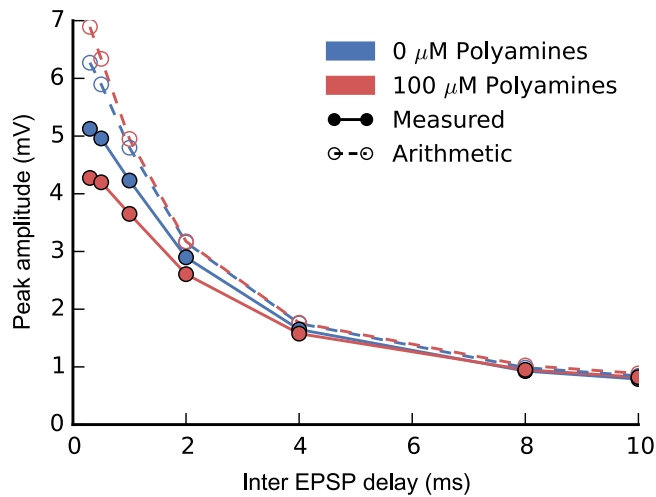
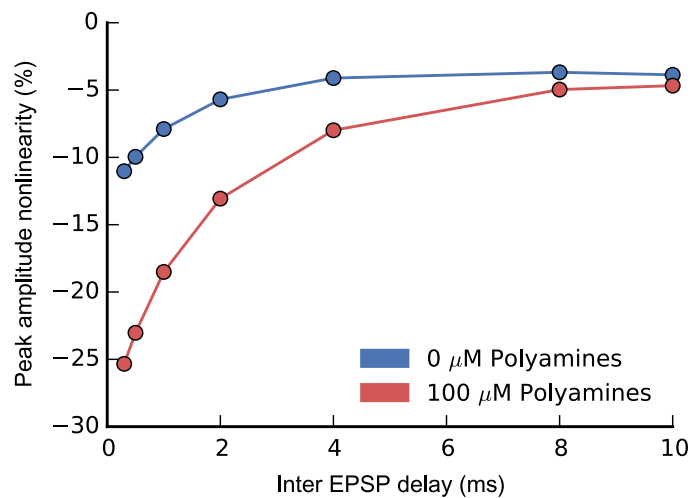
A**B**

Figure 4.6. Inter-synaptic delay and synaptic integration nonlinearity: **(A)** Peak amplitude vs inter-synaptic delay of recorded (solid lines) and arithmetic (dashed lines) synaptic integration, for simulations without polyamines (blue) and with polyamines (red). **(B)** Peak amplitude integration nonlinearity % vs inter-synaptic delay. (blue) with polyamines, (red) without polyamines.

We next sought to address whether polyamine receptor modulation would also increase integration sublinearity when synaptic inputs were not clustered on small patches of dendrite. In order to test this, 300 hundred synaptic inputs were distributed across either the apical or basal the dendritic tree, in two groups of 150 synapses (referred to in figures as stim 1 and stim 2 - as they were inspired by stimulating electrodes). These groups were then activated independently from each other, at separate times, to calculate expected arithmetic summation waveforms, and simultaneously, to obtain measured EPSPs.

Figure 4.7 shows the integration of the two synaptic groups, with and without polyamines. As for previous simulations, the cell was passive, and synaptic integration was therefore sublinear both with and without polyamines. However, as for clustered input, polyamines exacerbated the sublinear integration. Synapses distributed across the apical dendrites produced EPSPs that were 6 mV individually, and summated to 10.7 mV together (-11.4 %; Fig. 4.7A). When polyamines were included, the synaptic integration sublinearity roughly doubled (-21.9%) - individual inputs of 5.6 and 5.7 mV summed to 8.8 mV. Similarly, when synapses were placed on the basal dendrites without polyamines, synapse groups composing stims 1&2 elicited EPSPs that were 7.4 mV individually, and 13.0 mV together (-11.9%). With polyamines, these groups generated EPSPs that were 7.2 and 7.3 mV in size individually, but only 11 mV together (-22.3 %; Fig. 4.7B).

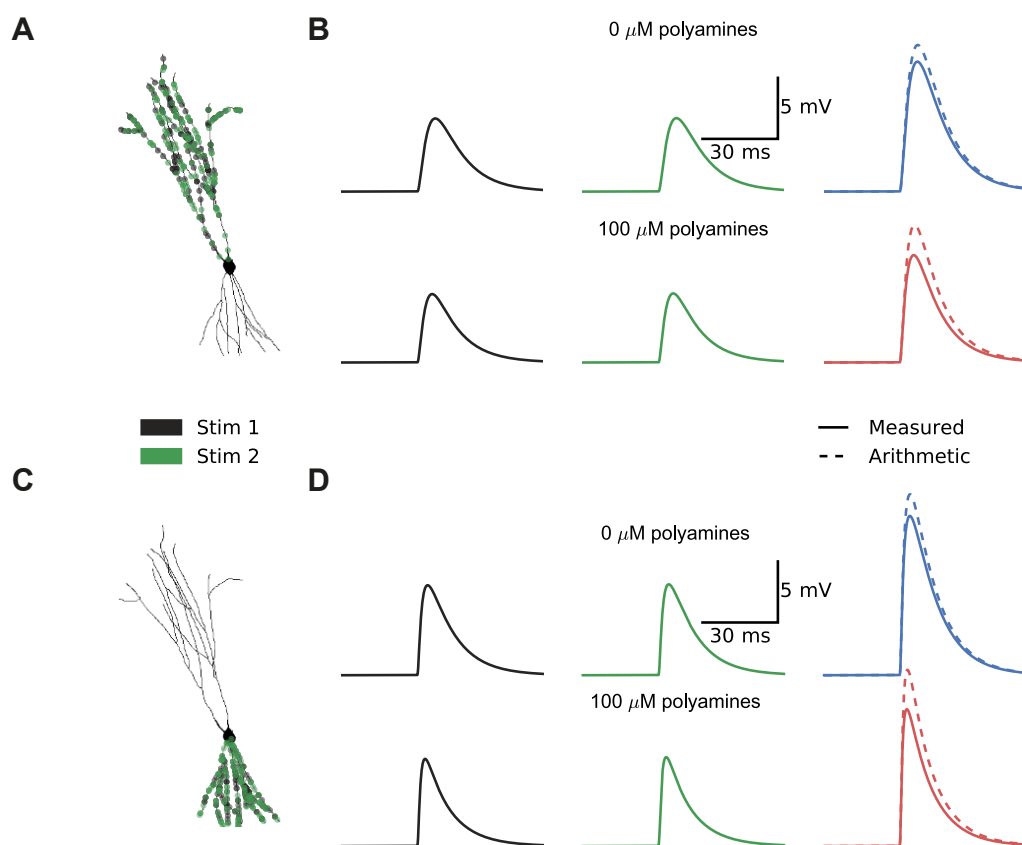


Figure 4.7. Polyamines mediate sublinear synaptic integration for distributed synaptic inputs: (A) Synapses distributed across apical dendrites in stratum radiatum. (B) Somatic EPSPs recorded when synaptic groups active together (right) or separately (left), with (bottom) and without (top) polyamines. (C&D) As for A&B, but for basal dendrites, in stratum oriens.

4.3 Discussion

The work presented in this chapter is composed of exploratory NEURON simulations that suggest polyamine modulation of CP-AMPA receptors contributes towards sub-linear synaptic integration for both large numbers of synapses distributed across the dendritic tree, and for smaller numbers of clustered inputs. These predictions can be tested experimentally, either using glutamate uncaging, or with stimulating electrodes. This work therefore constitutes one aspect of a power test, as it provides an indication for the expected magnitude of effect. Further experiments are required to measure experimental variability in synaptic integration nonlinearity under passive conditions.

In the context of PV⁺ cells, polyamine modulation of CP-AMPA receptors constitute yet another mechanism whose function is to limit input cooperation, and facilitate the handling of large excitatory barrages without the cell entering into depolarisation induced block. Other adaptations are reviewed in section 1.2, but, for example, consist of significant dendritic K⁺ conductances and an electrotonic structure that limits input cooperation. Unlike the cell's passive structure, polyamine modulation can be considered in the same vein as dendritic K⁺ conductance, as it is an activity-dependent damper of excitation.

This inhibitory role for polyamines is also interesting in the context of the activity dependent CP-AMPA receptor switch seen in hippocampal pyramidal cells after insults such as stroke and epilepsy (Liu and Savtchouk, 2012). While there are a number of interacting factors, such as channel kinetics, intracellular calcium signalling and altered channel conductance; CP-AMPA receptors, if modulated by polyamines to facilitate sublinear synaptic integration as described in this chapter, may be beneficial for protecting a cell from pathological barrages of glutamatergic input that occur in epileptic networks.

There are a number of limitations and assumptions made in these conclusions, however. The most important of these is the strong degree of rectification shown by the model receptor, for which there is sparse, if any, experimental data from whole-cell patch clamp of neurons. Further work investigating the effect of more modest rectification, for example by varying intracellular polyamine concentration, would be useful to assess polyamine function in these conditions.

One other limitation with the work presented in this chapter is the non-equal maximum conductances of the receptors. This was required to compare the conditions with and without polyamines. Polyamines cause a large fraction of the model receptor state "R" to be unavailable to glutamate binding, reducing the possible open conductance (Fig. 4.2). While there are a number of possible arguments that one could make for this, for example the larger channel conductance displayed by CP-AMPA receptors (Swanson et al., 1997) and general existence of homeostatic scaling mechanisms (Turrigiano, 1999), ideally polyamine modulation would be assessed with equal baseline receptor conductance.

Furthermore, all simulations were carried out with a passive NEURON model, without K^+ , Ca^{2+} or Na^+ conductances, and also without NMDA receptors. This approach was taken in order to simplify synaptic integration to allow better dissection of the specific role of polyamine modulation of AMPA receptors. However, it is not clear how important the modest integration sublinearity conferred by polyamine modulation is, relative to these other active conductances, not included in the model.

Chapter 5

PV⁺ interneurons and epilepsy

5.1 Introduction

A shift in the normal excitation-inhibition (E-I) ratio towards excitation has long been implicated in, and associated with, epileptic disorders (Stief et al., 2007; Holmes, 1995). Consistent with this hypothesis, antagonists of GABAergic signalling, such as bicuculline, are ictogenic in nature (Connors, 1984), whereas positive allosteric modulators of GABAergic action, such as benzodiazepines, have been successfully used to treat epilepsy (Greenfield, 2013) since the 1960s. However, despite their efficacy, between 20 and 30% patients do not respond adequately to anti-epileptic drugs (Kwan et al., 2011) and alternative surgical procedures often have significant negative consequences (Polkey, 2009). Furthermore, in addition to underlying unwanted clinical side effects, the powerful pro-GABAergic nature of many anti-epileptic drugs is particularly concerning for the cognitive development of children suffering from epilepsy (Lagae, 2006). As a mediator of powerful somatic inhibition throughout the brain, fast-spiking PV⁺ interneurons, which account for 40% of cortical interneurons (Tremblay et al., 2016), are primary candidates for alternative, more precise, cell-specific therapeutic strategies.

An enhanced understanding of the mechanisms that underlie epilepsy, particularly the precise dysfunction of individual cell-types, is integral to the promise of targeted, cell-specific, therapies. For fast-spiking PV⁺ interneurons, this understanding remains

incomplete. In line with a simplistic view of E-I imbalance, closed-loop optogenetic activation of PV⁺ interneurons significantly shortened seizures in an *in vivo* kainic acid model of epilepsy (Krook-Magnuson et al., 2013). Furthermore, feedforward recruitment of PV⁺ cells is thought to be critical for defining the "ictal penumbra", restricting the propagation, and eventual generalisation, of focal seizures (Cammarota et al., 2013; Trevelyan et al., 2006).

Unfortunately, however, despite the attraction and historical effectiveness of emphasising neuronal E-I balance and its disruption, it is now clear that glutamate and GABA do not have such direct relationships with ictogenesis as initially thought. For example, glutamatergic synapses drive both glutamatergic and GABAergic neurons, and decreasing glutamatergic signalling may therefore have a negligible net effect - due to a concurrent decrease in feedback inhibition. Likewise, for GABAergic signalling, excessive synchronisation of principal cells is ictogenic, and can be caused by powerful inhibition, such as that mediated by PV⁺ cells (Scharfman, 2007). In addition, the chloride reversal potential that underlies the hyperpolarising current mediated by GABA receptors can be eroded by the intracellular Cl⁻ accumulation that occurs during periods of intense activity, such as seizures, damping the effectiveness of inhibition; in extrema, the Cl⁻ reversal potential is thought to become slightly depolarising, potentially contributing to the maintenance of seizure states (Ellender et al., 2014). Cl⁻ ion build-up is particularly relevant during development, when incomplete expression of the K⁺-Cl⁻ transporter (KCC2) renders cells more vulnerable to Cl⁻ accumulation (Dzhala et al., 2005).

Consistent with an enriched view of GABAergic signalling in the context of ictogenesis, fast spiking PV⁺ interneurons have also been shown to have pro-epileptic effects in addition to their classical anti-epileptic actions. In an optogenetic "kindling" epilepsy model, activation of PV⁺ interneurons failed to attenuate seizures as expected. Instead, PV⁺ interneuron inhibition was found to be effective in reducing seizure duration (Khoshkhoo et al., 2017), in direct contrast to previous work (Krook-Magnuson et al., 2013). However, an explanation may lie in the precise timing of PV⁺ activation and inhibition, relative to the seizure evolution. For example, later in seizure, depolarisation-induced block of PV⁺ interneuron firing, or excitatory GABAergic signalling due to Cl⁻ accumulation, both explain the anti-epileptic effect of optogenetic PV⁺ interneuron inhibition.

Chapter Objectives

The overarching aim of the work presented in this chapter was to determine the function of PV⁺ interneurons during seizures, and to determine their suitability as therapeutic targets for intervention strategies. My contribution to this work was to design and implement software to detect and categorize electrocorticographic (ECoG) recordings, and to help analyse a effects of PV⁺ interneuron activation.

We hypothesised that the pro- or anti- epileptic roles of PV⁺ interneurons were functions of time and seizure progression. To test this hypothesis, we used an acute pilocarpine model of cortical focal seizures in awake behaving mice, and used amplitude-crossings from a recording electrode to trigger, with varying delays, optogenetic depolarisation of PV⁺ cells. As is typical for epilepsy models, pilocarpine injection induces a spectrum of epileptiform discharges (see Fig. 5.2). Therefore, in order to restrict our analysis to a consistent "network-state", across animals and in an objective manner, we used a supervised learning approach to categorise the pilocarpine-induced activity.

The first section of this chapter addresses the role of PV⁺ interneurons in pilocarpine induced epileptiform activity. However, while the acute epileptiform activity induced by pilocarpine injection is useful for studying of epileptic seizures, it is not a model of the chronic epilepsy that occurs in humans (Loscher, 2011). We therefore sought to investigate the role of PV⁺ interneurons in a chronic model of epilepsy with spontaneous seizures. However, seizure detection and analysis of recordings from chronic, spontaneous, epilepsy models, such as the model of refractory focal neocortical epielpsy generated by injection of tetanus toxin (Nilsen et al., 2005), is typically done in a manual or semi-automated way. This analysis work-flow imposes a limit on research efforts, due to the number of hours required to analyse recordings, and prohibits meaningful closed-loop detection experiments - which naturally follow from high precision off-line seizure detection.

Unfortunately, analysis of spontaneous seizures is also an ongoing issue for many projects within the laboratory, and indeed multiple laboratories across the world. While automated seizures analysis has been pursued since the early 1980's (Gotman, 1982; Tzallas et al., 2012), and is now a mature field in which regular crowd-sourced competitions are held (Baldassano et al., 2017), these efforts have typically been focussed on multi-channel EEG data acquired at high sample-rates from humans

or large animals such as dogs, in order to aid clinical diagnoses and treatment of humans. Though seizures do share conserved patterns across species and brain areas (Jirsa et al., 2014), nevertheless, they vary both spatially and temporally; and their appearance is also dependent on the type of recording equipment used (Hunyadi et al., 2017). As a result, this work is of limited relevance to the analysis challenge faced by our laboratory and others like it.

Instead, in contrast to work with the aim of augmenting clinical diagnoses and annotations, relatively little attention has been paid to seizure detection from single-channel, low sampling frequency, recordings from rodents (Hunyadi et al., 2017) relevant for laboratories. The few papers that do address this issue often focus on absence seizures (Aghazadeh et al., 2015) and spike-wave discharges (Ovchinnikov et al., 2010), which are typically detected with higher accuracy than other seizure types due to their consistent manifestation (Buteneers et al., 2013). Furthermore, seizure detection is a highly unbalanced classification task, as seizures typically make up less than 1% of the data. As a result, approaches that report a high specificity (true negative rate) and recall (true positive rate or sensitivity), may still return many false positives per seizure or poor precision, which is unsuitable for closed-loop experiments (these metrics are defined in section 5.2.5).

The work presented in this chapter is primarily concerned with the development of a supervised learning approach to classify pilocarpine-model recording epochs into example hand-annotated network-states. Results from these experiments are presented. The epoch-based approach used for the pilocarpine-model was then adapted and extended to the detection of spontaneous seizures from chronic intra-cranial electrode recordings of a rat tetanus toxin model by application of Hidden Markov Models. This work is ongoing and the preliminary results are reported.

All animal surgeries, data acquisition, and network-state annotation related to the acute pilocarpine epilepsy model were carried out by Vincent Magloire. Surgeries, data acquisition and seizure annotations for the chronic tetanus toxin model were carried out by Albert Snowball.

5.2 Methods

5.2.1 Pilocarpine epilepsy model

Focal cortical seizures were induced in awake mice by acute injection of pilocarpine dissolved in sterile saline ($0.2 - 0.4 \mu\text{L}$, 3 M , 100 nl min^{-1}), into the visual cortex of mice via an implanted cannula guide. Experimental mice were obtained by crossing PV-Cre mice (section 2.1.1) with Ai32 mice for Cre dependent EYFP-tagged ChR2 expression (Jackson Labs:B6;129S - *Gt(ROSA)26Sor^{tm32}(CAG-COP4*H134R/EYFP)Hze*). Wireless ECoG recording electrodes (Open Source Instruments Inc., USA) were implanted onto the dura above the injection site, with a reference electrode positioned on the contra-lateral hemisphere. ECoG was recorded at a sampling rate of 512 Hz. An optic fibre (0.22 NA , $200 \mu\text{m } \varnothing$, Multimode 190-1200 nm, Thorlabs, Inc.) was positioned at the same depth as the injection needle and connected to a laser light source (470 nm). Epileptiform activity was observed roughly ten minutes after recovery from the pilocarpine injection, which was performed under isoflurane-induced anaesthesia.

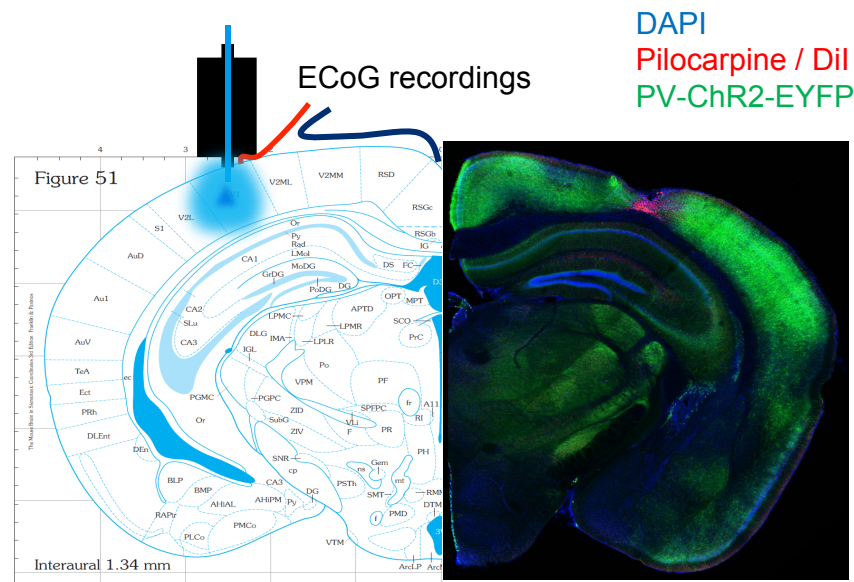


Figure 5.1. Neocortical focal epilepsy model and recording setup: Left: diagram of injection site and experimental setup. Right: immunohistochemistry image showing PV⁺ interneurons expressing YFP tagged ChR2 (green), nuclei DAPI staining (blue), and DiL that was co-injected with pilocarpine (magenta).

We categorised the activity elicited by acute pilocarpine injection into four sub-

types: baseline (Fig. 5.2 grey trace); state 1, which was characterised by periods of baseline interrupted by large negative shocks (Fig. 5.2 black traces); state 2, in which the negative spikes seen in state 1 are followed by transient oscillatory activity (Fig. 5.2 red traces); and finally, state 3, which was the most heterogeneous state, generally composed of continuous activity (Fig. 5.2 blue traces). We used a training dataset of 740 ten second hand-annotated epochs of recordings to train our classifier, and a testing dataset of 204 segments for verification.

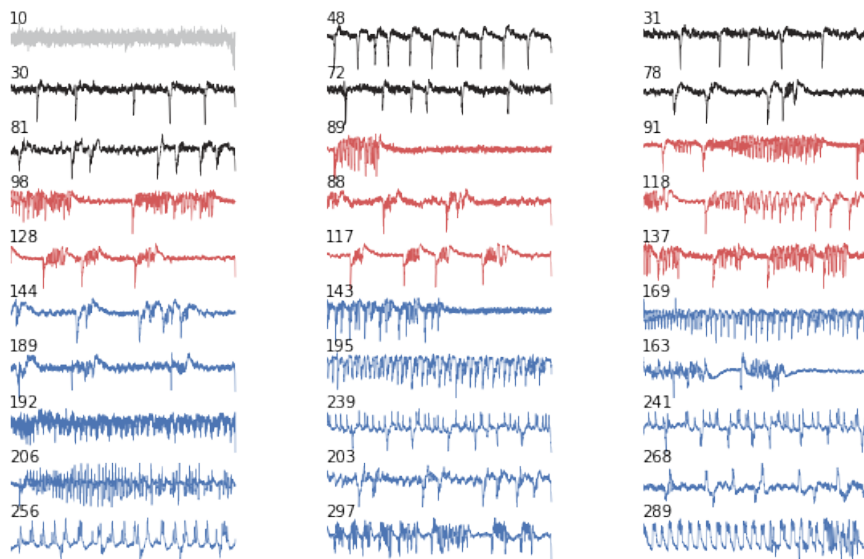


Figure 5.2. A selection of typical pilocarpine model induced epileptiform discharges. Data points are scaled between 0-1 and traces are 10 seconds in length. Grey: baseline, Black: state 1, inter-ictal events, Red: state 2, ictal-like events, Blue: state 3, aberrant or continuous epileptiform activity. Class assignments were hand annotated.

5.2.2 Experimental design

In order to investigate the role of PV^+ interneurons throughout seizures, closed-loop optogenetic activation of PV^+ interneurons for ten seconds was triggered from negative amplitude crossings of the ECoG recording with varying delays of 0, 0.5, 2 and >2 seconds. As a result of this simple criteria, light pulses, and resultant PV^+ activation was induced across all of the network states shown in Figure 5.2. We therefore, offline, after the experiment, used the ten preceding seconds of recorded ECoG before a light

pulse, to classify the recording into a network-state. Only epochs that were deemed to be of state 2, were carried through for subsequent analysis.

5.2.3 Feature extraction

As is typical of many automated EEG approaches that do not rely on neural networks (Tzallas et al., 2012), the first step in our classification approach was feature extraction. We prioritised feature interpretability, excluding such a black-box approach and extracted 21 features from recordings. First, the ten second epochs were normalised between 0-1 by Min-Max scaling according to the following equation:

$$trace_{norm} = \frac{trace - trace_{min}}{trace_{max} - trace_{min}}$$

Having standardised the range of the recorded ECoG to between 0 - 1, a rolling standard deviation value, calculated with a sliding window of 100 data points, and a threshold of 0.04 was used to determine baseline data points. These are shown in red on the selection of sample traces (Fig. 5.3). Three features were extracted from this analysis: 1, number of baseline data points out of the 5120. 2, the mean time difference between baseline data points. 3, the skew of the time difference between data points.

Second, we detected the peaks and troughs in the recordings, shown in Figure 5.4. This yielded five more features for each epoch: 1 & 2, total number of peak and troughs; 3 & 4, mean peak and trough values; 5, the average range between peaks and troughs.

We then calculated more standard statistical features from our ECoG recordings, these were: mean, std deviation, kurtosis, skew, and sum of the absolute difference between each data point - which is also referred to as line-length. In order to standardise the comparison between epochs with varying number of "events" such as the state 1's with varying numbers of negative spikes, before calculating these features, the baseline data points were subtracted, creating a "signal" dataset. Line length was also calculated relative to the total number of data points. In the case of a period of baseline, these features could not be calculated, and the average feature value for all

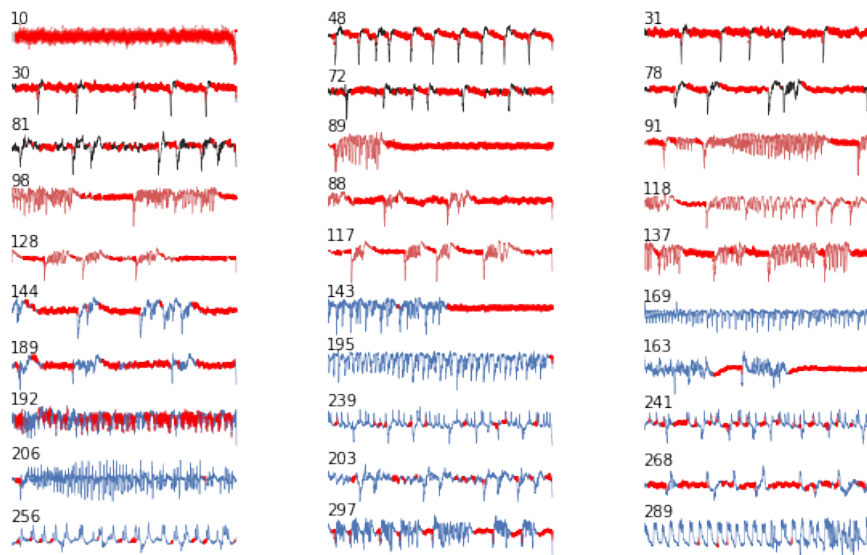


Figure 5.3. Extracting baseline periods of recordings: Baseline periods of recordings (red) were extracted by calculating a sliding std. deviation value using a window of 100 data points. Data points deemed to be non-baseline were those whose corresponding std. deviation value exceeded a threshold of 0.04.

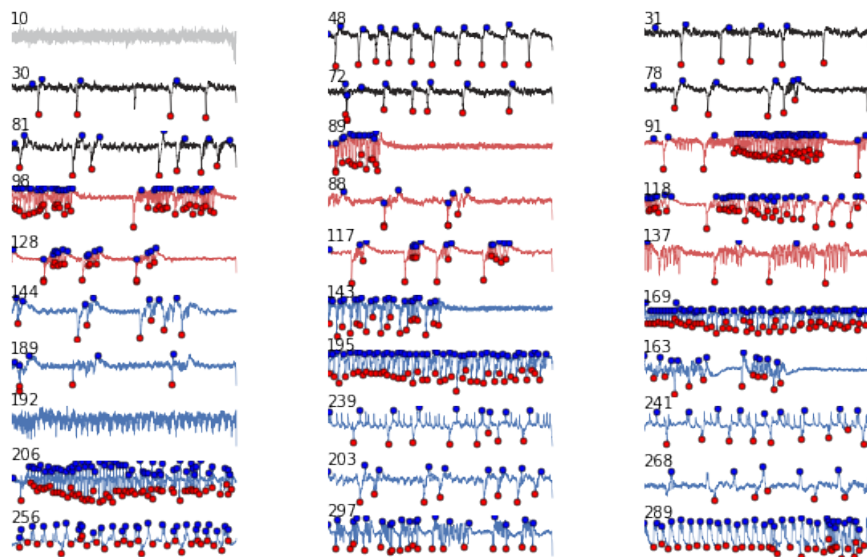


Figure 5.4. Peaks and troughs

epochs was used instead.

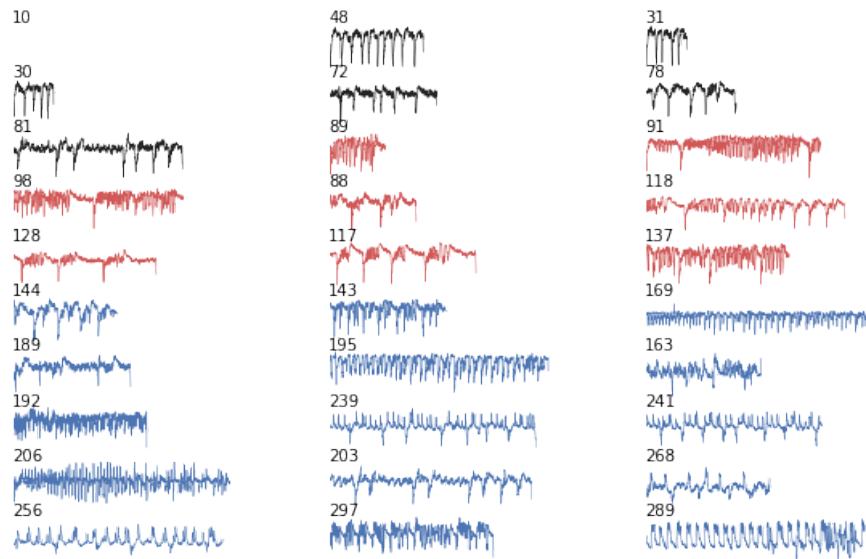


Figure 5.5. Signal dataset, after subtraction of baseline data points. This allowed more consistent comparison of states with a varying number of events, such as states 1 and 2.

Finally, we convolved the signal dataset with a family of complex Morlet wavelets, centred at frequencies of 1, 5, 10, 15, 20, 30, 60 and 90 Hz. Mean power of the signal dataset at each frequency was used as a feature. Wavelet spectrograms generated from this analysis are shown in Figure 5.6.

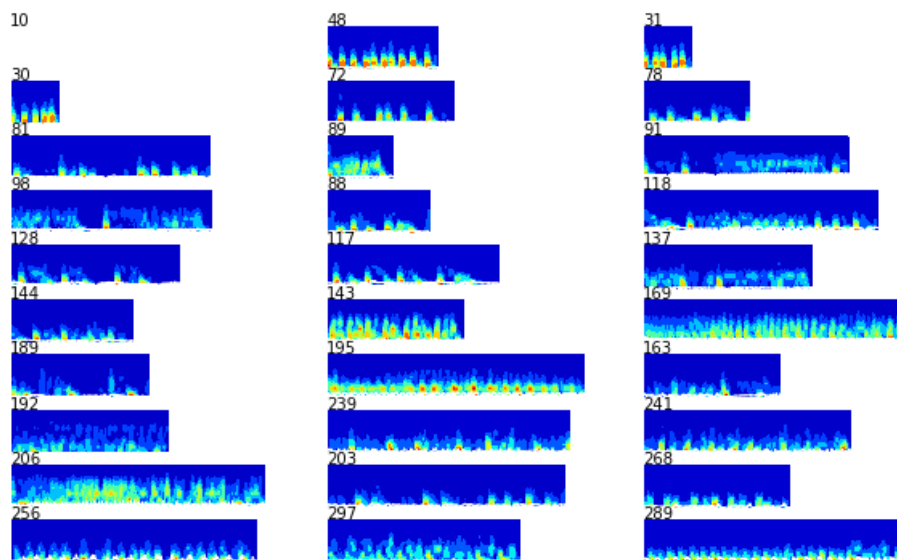


Figure 5.6. Wavelet spectrogram of signal dataset: plots power calculated from convolution with a family of complex Morlet wavelets, centred at frequencies of 1, 5, 10, 15, 20, 30, 60 and 90 Hz.

5.2.4 Random Forests

Having extracted features from our hand-annotated dataset, we then trained a random forest classifier on the features and network-state labels. A random forest is a type of ensemble classifier, introduced in the early 2000's (Breiman, 2001), that consists of many unpruned decision trees, forming a "forest" of trees, that classify examples based on majority vote. Decision trees, even when correctly pruned, generally suffer from high variance: slight differences in training data can cause large alterations in the final trained model. However, by averaging across many such trees, each with different variance, the overall variance is reduced. In addition to this majority vote, random forests employ two further techniques to decorrelate individual trees: first, each tree in the forest is trained on a bootstrapped version of the training data (with replacement), which is known as bagging, and second, at each node (or split) only a random subset of features is considered.

The simple approach yields surprisingly powerful classifiers, that do not depend on careful hyper-parameter tuning, and are robust to over-fitting training datasets (Breiman, 2001). In a study comparing the performance of popular classifiers across many datasets, using a number of performance metrics, random forests were second only to one other algorithm - boosted trees (Caruana and Niculescu-Mizil, 2006). Since this comparison in 2006, much work has gone into artificial neural networks, however, random forests still offer state-of-the art performance with little effort.

5.2.5 Performance metrics

The performance of the pilocarpine network-state classifier, and spontaneous seizure detection (described next), were evaluated in terms of precision and recall metrics. Accuracy was not used, as though it is the perhaps the most intuitive performance measure, being simply the fraction of correct predictions from the total number of examples, it is a poor metric for imbalanced datasets such as seizures. For example, in the case of seizures, baseline periods constitute $> 99\%$ of the dataset, and an accuracy $> 99\%$ can therefore be achieved by a classifier that predicts baseline for every epoch.

Precision is the a measure of how exact a classifier is in its predictions. It is defined

as the number of correct positive predictions (TP) divided by the total number of positive predictions that were made. Therefore, high precision also corresponds to a low false positive (FP) rate per true positive, or correctly labelled seizure.

$$\text{Precision} = \frac{TP}{TP + FP}$$

Recall measures the percentage of positive epochs or seizures that were correctly picked up by the classifier. It is also called sensitivity or true positive rate. A low recall therefore indicated that there are many false negatives, as many positive examples have been missed.

$$\text{Recall} = \frac{TP}{TP + FN}$$

Finally, the F1 score, or F-measure, is a weighted average of precision and recall scores.

$$\text{F1 Score} = 2 \times \frac{\text{Precision} \times \text{Recall}}{\text{Precision} + \text{Recall}}$$

5.2.6 Chronic tetanus toxin epilepsy model

We next sought to extend our work to closed-loop experiments with chronic, spontaneous models of epilepsy, again activating PV⁺ cells with different time delays relative to seizure onset. However, to do this, we first had to alter our supervised learning approach for a chronic epilepsy model (Figure 5.7). We therefore used data acquired from a tetanus toxin epilepsy model, which is established in the laboratory (Wykes et al., 2012). Before closed-loop experiments could be attempted, we first aimed for strong off-line seizure detection performance.

A dataset comprising 2 weeks of continuous ECoG recordings from 10 epileptic rats was provided by Albert Snowball, another member of the lab. Seizure start and end times had been hand annotated using a semi-automated analysis process currently in use by the lab (Wykes et al., 2012), and verified by comparison with video recordings. For this dataset epochs of 5 seconds were classified as either seizure or baseline and total performance was calculated against the precise hand-annotated start and end times. The main modification to the approach used for the pilocarpine dataset was to incorporate information from the classification of surrounding epochs using hidden

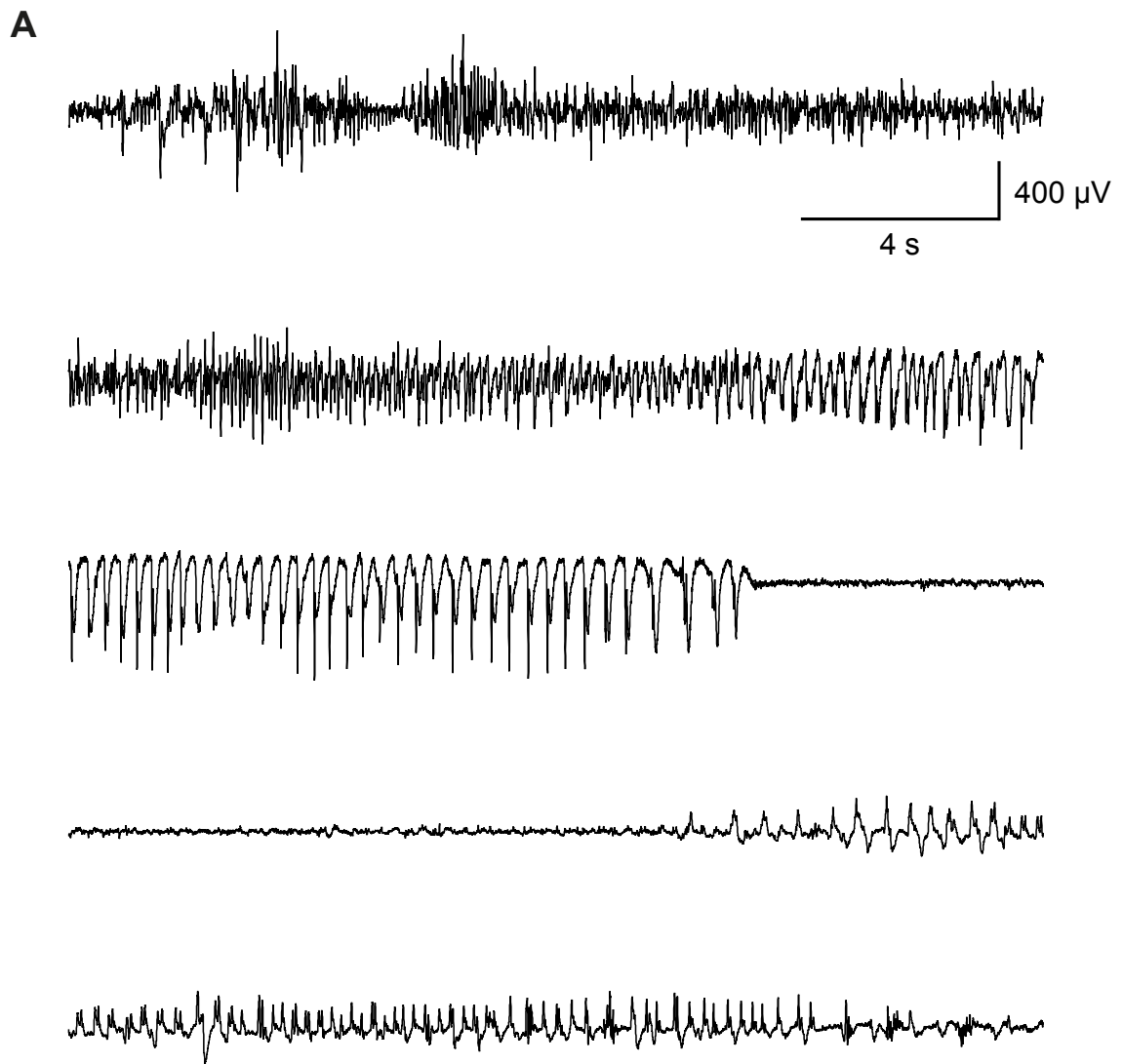


Figure 5.7. Tetanus toxin induced spontaneous seizure: Consecutive 20 second segments of a typical ECoG recording of a spontaneous seizure. Note the characteristic progression from high frequency activity to large, low frequency complexes, followed by a period of suppression.

Markov models, described below. However, the feature extraction was also altered; baseline data points were still calculated, but not subtracted from the epochs, and Fourier transform band-powers for frequencies of, in Hz, (1-4), (4-8), (8-12), (12-30), (30-50), (50-70), (70-120), (120-160) were used instead of wavelet convolutions. Finally, instead of min-max scaling, recordings were normalised, per hour, by the mode standard deviation.

5.2.7 Hidden Markov models

In order to take advantage of the sequential nature of the ECoG epochs, we modelled the relationship between epochs using hidden Markov models. In the related Markov model, the probability of an observation at time $t + 1$ is dependent on the previous observation at time t . However, for a hidden Markov model, observations at times t and $t + 1$ are independent of each other, given knowledge of a latent state variable at time t (Fig. 5.8). Hidden Markov models have been widely used, for example in the fields of speech recognition, handwriting recognition and DNA sequence analysis (Bishop, 2007) and are reviewed below.

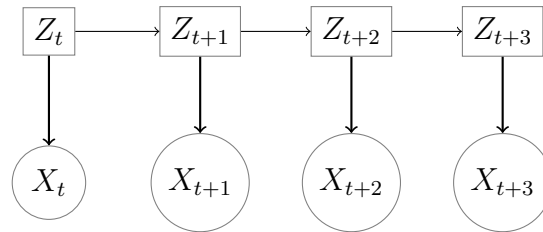


Figure 5.8. Trellis diagram for a hidden Markov model: Observations are denoted by X , latent states by Z .

For observations over N time points, in our case ECoG epochs, we assume there exists a corresponding sequence of N latent variable states, denoted by the discrete random variables $Z_1, \dots, Z_n \in \{1, \dots, k\}$, where k is the total number of possible hidden states. For the tetanus toxin data, there were two underlying hidden states, "ictal" and "non-ictal", which we assumed were provided by the hand-annotations. The observations are described by second set of random variables, and are referred to as $X_1, \dots, X_n \in 1, \dots, m$, where m is a number of distinct possible observations. In a hidden Markov model, these random variables are related via the graph shown in Figure 5.8 (assuming discrete time) and hidden Markov models can therefore be described by the following three parameters:

1. The transition probabilities between the hidden states, $p(Z_t|Z_{t-1})$, which are described by a $k \times k$ matrix A , where A_{ij} gives $p(Z_t = j|Z_{t-1} = i)$.
2. The emission probabilities ϕ_i , the conditional probabilities that a hidden state $Z_t = i$ will emit an observation X . $\phi_i(X) = p(X|Z_t = i)$
3. The initial hidden state distribution, $\pi(i) = p(Z_1 = i), i \in \{1, \dots, k\}$.

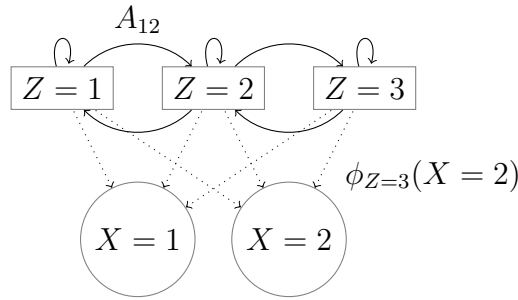


Figure 5.9. Graph diagram for a hidden Markov model with 3 hidden states $Z_i, i \in \{1, 2, 3\}$ and with two observable emissions $X_i, i \in \{1, 2\}$. The matrix A describes the probability of state transitions, and $\phi_{Z=i}(X=i)$ the probability that state $Z=i$ will emit $X=i$.

The joint probability over the latent and observed random variables (shown in Fig 5.8) factorises as follows:

$$p(X_1, \dots, X_N, Z_1, \dots, Z_N) = p(Z_1)p(X_1|Z_1) \prod_{t=2}^N p(Z_t|Z_{t-1})p(X_t|Z_t)$$

Which can then be written down in terms of the parameters of the hidden Markov model:

$$p(X_1, \dots, X_N, Z_1, \dots, Z_N) = \pi(Z_1)\phi_{Z_1}(X_1) \prod_{t=2}^N A_{(Z_{t-1}, Z_t)}\phi_{Z_t}(X_t)$$

5.2.8 Forward-backward algorithm

For off-line analysis we are interested in $p(Z_t|X)$: the probability of a hidden state Z at time t given all of the observations $X = X_{1:N}$. This probability, and the probabilities for all $Z_t \in 1, \dots, N$, can be calculated by the forward-backward algorithm, assuming that the three hidden Markov model parameters, (ϕ, π, A) , are known, and is derived below.

$$p(Z_t|X) \propto p(Z_t, X) = p(X_{t+1:N}|Z_t, X_{1:t})p(Z_t, X_{1:t})$$

First, $p(Z_t|X)$ is proportional to the joint probability $p(Z_t, X)$, which can be factored around Z_t . The conditional independence properties of hidden Markov models can then be applied to this factorisation, i.e. $p(X_t|Z_t) = p(X_t|Z_t, X_{1:t-1})$. Therefore:

$$p(Z_t|X) \propto p(Z_t, X) = p(X_{t+1:N}|Z_t)p(Z_t, X_{1:t})$$

The first term of this expression, $p(X_{t+1:N}|Z_t)$, is the backward part of the forward-backward algorithm, and the second term, $p(Z_t, X_{1:t})$ the forward part. The "trick" for both components of the forward-backward algorithm is to first marginalise over previous hidden states (in opposite directions for each part of the algorithm), as this then enables a factorisation that allows the hidden Markov model conditional independence properties to be applied to the expression. For future closed-loop optogenetic experiments, only the forward algorithm will be used, as this deals with observations up to and including X_t , whereas the the backward pass can only be used offline, when all of the observations are known.

5.2.8.1 Forward algorithm

Starting with the forward pass, we first marginalise over the possible hidden states at the previous time step.

$$p(Z_t, X_{1:t}) = \sum_{Z_{t-1}} p(Z_t, Z_{t-1}, X_{1:t})$$

This can be factored as

$$p(Z_t, X_{1:t}) = \sum_{Z_{t-1}} p(X_t|Z_t, Z_{t-1}, X_{1:t-1})p(Z_t, Z_{t-1}, X_{1:t-1})$$

$$p(Z_t, X_{1:t}) = \sum_{Z_{t-1}} p(X_t|Z_t, Z_{t-1}, X_{1:t-1})p(Z_t|Z_{t-1}, X_{1:t-1})p(Z_{t-1}, X_{1:t-1})$$

After applying conditional independence properties of the hidden Markov model

$$p(Z_t, X_{1:t}) = \sum_{Z_{t-1}} p(X_t|Z_t)p(Z_t|Z_{t-1})p(Z_{t-1}, X_{1:t-1})$$

The above expression involves a recursion - defining these explicitly

$$\alpha_t(Z_t) = p(Z_t, X_{1:t})$$

$$\alpha_{t-1}(Z_{t-1}) = p(Z_{t-1}, X_{1:t-1})$$

We arrive at the forward algorithm

$$\alpha_t(Z_t) = \sum_{Z_{t-1}} p(X_t|Z_t)p(Z_t|Z_{t-1})\alpha_{t-1}(Z_{t-1})$$

Which can also be written in terms of the model parameters (ϕ, π, A)

$$\alpha_t(Z_t) = \sum_{Z_{t-1}} \phi_{Z_t}(X_t)A_{(Z_{t-1}, Z_t)}\alpha_{t-1}(Z_{t-1})$$

This is valid for $t = 2, \dots, N$. For the case where $t = 1$:

$$\alpha_1(Z_1) = p(Z_1, X_{1:1}) = p(Z_1, X_1)$$

$$\alpha_1(Z_1) = p(X_1|Z_1)p(Z_1) = \phi_{Z_1}(X_1)\pi(Z_1)$$

To implement the forward algorithm, $\alpha_1(Z_1)$ is first initialised, and then we iterate through the remaining time points calculating $\alpha_t(Z_t)$ for $t = 2, \dots, N$.

5.2.8.2 Backward algorithm

Next, the backward pass

$$p(X_{t+1:N}|Z_t) = \sum_{Z_{t+1}} p(X_{t+1:N}, Z_{t+1}|Z_t)$$

Again, first marginalise over the possible hidden states for the previous time step (in this case the time step ahead as we are passing backwards over the data), Z_{t+1} , in order to then factorise around it.

$$p(X_{t+1:N}|Z_t) = \sum_{Z_{t+1}} p(X_{t+2:N}|Z_{t+1}, Z_t, X_{t+1})p(Z_{t+1}, X_{t+1}|Z_t)$$

$$p(X_{t+1:N}|Z_t) = \sum_{Z_{t+1}} p(X_{t+2:N}|Z_{t+1}, Z_t, X_{t+1})p(X_{t+1}|Z_{t+1}, Z_t)p(Z_{t+1}|Z_t)$$

After applying hidden Markov model conditional independence relationships:

$$p(X_{t+1:N}|Z_t) = \sum_{Z_{t+1}} p(X_{t+2:N}|Z_{t+1})p(X_{t+1}|Z_{t+1})p(Z_{t+1}|Z_t)$$

Again, the above expression involves a recursion, and after defining these explicitly

$$\beta_t(Z_t) = p(X_{t+1:N}|Z_t)$$

$$\beta_{t+1}(Z_{t+1}) = p(X_{t+2:N}|Z_{t+1})$$

We get to the backward algorithm

$$\beta_t(Z_t) = \sum_{Z_{t+1}} \beta_{t+1}(Z_{t+1})p(X_{t+1}|Z_{t+1})p(Z_{t+1}|Z_t)$$

Which can be written in terms of the hidden Markov model parameters (ϕ, π, A)

$$\beta_t(Z_t) = \sum_{Z_{t+1}} \beta_{t+1}(Z_{t+1})\phi_{t+1}(X_{t+1})A_{Z_t, Z_{t+1}}$$

This is valid for $t = N - 1, \dots, 1$. For the case where $t = N$:

$$\beta_N(Z_N) = 1, \text{ for all } Z_N$$

To implement the backward pass, $\beta_N(Z_N)$ is first initialised to a vector of ones, and the iterating backwards through the time points from Z_{N-1} to Z_1 .

5.2.9 Obtaining emission probabilities with cross-validation

Hidden state emission probabilities are one of the three model-defining parameters of hidden Markov models. For a given time point, the forward-backward algorithm requires knowledge of an observation's emission probability given the hidden state at the same time point, $(\phi_{Z_t}(X_t)$ or $p(X_t|Z_t)$). Unfortunately, a trained classifier does not provide this probability for an epoch of ECoG recording, instead, given our assumption of the hidden states corresponding to the hand-annotations, the classifier provides the opposite: $p(Z_t|X_t)$.

Emission probabilities, of some nature, can be obtained by assessing a classifier's performance on test data, the labels of which form the hidden states, and classifier's predictions the observations. To employ a seasonal analogy: a classifier is trained to predict the season to which a given day belongs using historical data such as

temperature and a target season label. Winter days will predominantly be cold and summer days hot, although there will be a certain number of warm winter days and cold summer days. Overall, given enough training data, a classifier will learn to predict "winter" for cold days and "summer" for warm days. Subsequently, when provided with unseen testing days, days that are cold but also from the summer will be incorrectly labelled as winter by the classifier. Conceptually, this can be thought of as the hidden state "summer" emitting a "winter"-like observation. The emission probabilities for state summer emitting "summer-like" and "winter-like" days can then be calculated over the unseen testing data. Correspondingly, within ictal states, periods of quiet baseline ECoG are often seen, and likewise inter-ictal states can emit brief periods of seizure-like activity. This is shown schematically in Figure 5.10.

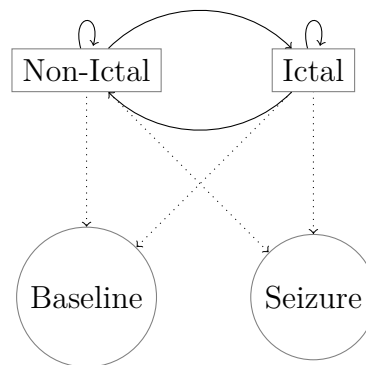


Figure 5.10. Diagram of a HMM in which Hidden States "non-ictal" and "ictal" emit "baseline" and "seizure" observations

Obtaining state emission probabilities using miss-classification of test-data labels - inspired by a model such as figure 5.10 - assumes that a classifier can learn an archetype of a hidden state: indeed it assumes that the state has an archetype. While this is perhaps fair for hidden states such as "winter" or "ictal", other hidden states may lack such an prototypical state. An alternative option would be to cluster the observations in an unsupervised manner, to obtain state emission probabilities of these clusters, and then assign new incoming observed data to these clusters. Ultimately, however, this approach still does not overcome the flaw that the hidden state has actually emitted the recorded data (or the features extracted from the data), not the classifier's prediction of the emission class. Indeed the attainment of emission probabilities, although taken in this thesis as a first approximation, is not motivated by any robust statistical reasoning.

5.2.10 Obtaining emission probabilities with Bayes' rule

Given training labels that correspond to hidden states, a classifier's prediction is the probability of a hidden state given an observation: $p(Z_t|X_t)$. However, the forward-backward algorithm requires $p(X_t|Z_t)$. It is possible to incorporate $p(Z_t|X_t)$ by modifying the forward-backward algorithm, using Bayes' rule to obtain $p(X_t|Z_t)$, as follows (Bishop et al., 2004). First obtain Bayes' rule by applying the commutative and product rules of probability:

$$\begin{aligned} p(X_t, Z_t) &= p(Z_t, X_t) \\ p(X_t, Z_t) &= p(X_t|Z_t)p(Z_t); \quad p(Z_t, X_t) = p(Z_t|X_t)p(X_t) \\ p(X_t|Z_t)p(Z_t) &= p(Z_t|X_t)p(X_t) \\ p(X_t|Z_t) &= \frac{p(Z_t|X_t)p(X_t)}{p(Z_t)} \end{aligned}$$

$p(X_t|Z_t)$ can then be incorporated into the forward-backward algorithm:

$$\begin{aligned} \alpha_t(Z_t) &= \sum_{Z_{t-1}} \frac{p(Z_t|X_t)p(X_t)}{p(Z_t)} A_{(Z_{t-1}, Z_t)} \alpha_{t-1}(Z_{t-1}) \\ \beta_t(Z_t) &= \sum_{Z_{t+1}} \beta_{t+1}(Z_{t+1}) \frac{p(Z_{t+1}|X_{t+1})p(X_{t+1})}{p(Z_{t+1})} A_{Z_t, Z_{t+1}} \end{aligned}$$

Here, $p(Z_t|X_t)$ is the hidden-state prediction probability provided by the classifier, $p(Z_t)$ the state probability provided by the stationary distribution, and $p(X_t)$ is the probability of the data. While we have no way of calculating $p(X_t)$, both α_t and β_t are functions of Z_t , whereas $p(X_t)$ is constant with respect to Z_t and can therefore be ignored.

Random forests assign class by majority vote, and the percentage of trees voting for the majority class can be used as a measure of the classifier's confidence. However, due to the underlying variance of the set of decision trees that are being averaged, random forests (and other bagging methods) are generally unable to correctly make confident predictions, near 0 or 1. For example, if the "correct" prediction probability

is $p = 1$, the random forest can only predict this if all of the decision trees predict the class, which is unlikely due to the enforced variance in the underlying trees caused by feature subsetting. While random forests are thought to be better calibrated than support vector machines and boosted models (Niculescu-Mizil and Caruana, 2005), in order to address this issue, random forests were calibrated by using cross validation to learn a sigmoid function that maps the original probability estimate to a more accurate value (Platt, 1999).

5.3 Results

A major contribution of the work in this chapter was the development of software used by other researchers within the laboratory, including graphical user interfaces for efficient manual inspection and the application of trained algorithms. These can be found at www.github.com/jcornford/pyecog.

5.3.1 Pilocarpine network-state classifier performance

Here we present the results of training a random forest classifier on a hand labelled dataset of pilocarpine injection induced epileptiform activity. Table 5.1 shows the results of applying the trained classifier on a test dataset of 204 ten second epochs of ECoG recording. In order to use measures such as precision and recall, which are performance metrics for binary classifiers, classifier performance was considered in turn for each state in a one-vs-all manner, i.e. for state one performance, positive epochs were state 1, and negative epochs state 2 or state 3. Our classifier achieved an average accuracy score of 0.94, and similar precision and recall scores (Table 5.1) across the three classes. This performance, in addition to verifying the use of the classifier for automated state assignment, indicates that indeed the pilocarpine-induced epileptiform activity does consistently manifest in the distinct modes that were originally identified by manual inspection.

State	Precision	Recall	F1 Score	no. examples
S1	0.95	0.89	0.92	63
S2	0.93	0.96	0.95	104
S3	0.95	0.97	0.96	37
avg\total	0.94	0.94	0.94	204

Table 5.1. Pilocarpine network-state classifier performance: results are show for testing dataset of 204 examples. In this dataset there were no baseline periods. Averages shown are simple "macro-averages", i.e. not weighted by number of examples.

Figure 5.11 shows precision and recall values at various thresholds of classier confidence for the three classes. Again, as for the Table 5.1, this is computed in a one-vs-all manner. A larger area under the curve indicates a well performing classifier. As shown in Figure 5.11, precision does not necessarily decrease with recall - this occurs when

the threshold for detection has been set too high, and new positive results returned by the classifier are true positives. Additionally, while the trade-off between precision and recall with threshold changes is generally relatively gradual, at thresholds closer to 0 or 1 larger changes in the relationship between precision and recall are observed in response to small changes in threshold.

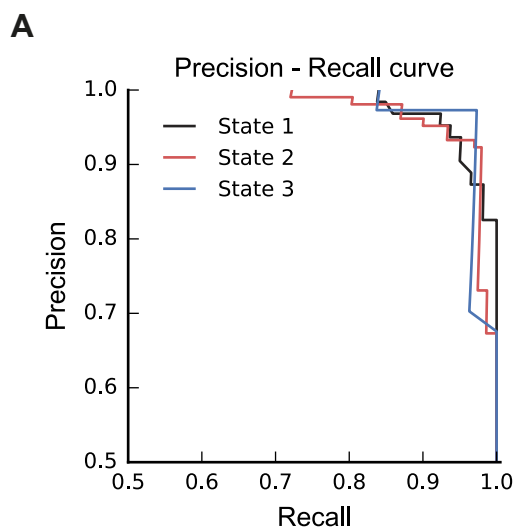


Figure 5.11. Precision-recall curves for pilocarpine-model dataset: (A) Precision-recall curves. Black: state 1 is the positive class. Red: state 2 is the positive class. Blue: state 3 the positive class.

5.3.2 The effect of PV⁺ interneuron activation on seizure duration is time-dependent

Figure 5.12 displays the relationship between the suppression of ictal-like bursts and the activation of PV⁺ interneurons. As ictal-like bursts had a large negative spike at the beginning of the burst (see Figs. 5.12A & 5.2) this spike was used to trigger PV⁺ activation with varying delays: from 0 to >2 seconds (mean delay for >2 second delay condition was 4.4 ± 0.6 seconds). The ictal-like bursts (state 2) used in this analysis were those that were assigned to state 2 by the classifier as described above. Light activation was triggered at every other threshold crossing, enabling the comparison between consecutive light-off and light-on discharges. For each animal, paired discharge durations were combined and averaged (mean was 7.2 paired discharges, minimum of 3 per animal). To enable comparison between animals, durations were normalised to the average light-off discharge duration. The average discharge duration for all events was 3.98 ± 0.21 s ($n = 166$, 10 mice). The number of animals averaged for each delay-condition was as follows: 0s $n = 8$, 0.5s $n = 7$, 2s $n = 7$, >2s $n = 5$.

Optogenetic activation of PV⁺ cells with no delay shortened the duration of the ictal-like discharges to 65.2 ± 7.6 %, $p = 0.003$, of light-off duration. Delaying the light activation by 0.5 seconds also led to a suppression of the mean discharge duration, however this was not statistically significant (78.8 ± 11.3 %, $p = 0.174$). Increasing the delay of activation to 2 seconds, in contrast, caused a non-significant increase in mean discharge duration (115.7 ± 16.2 %, $p = 0.217$). Finally, depolarising PV⁺ cells by time delays greater than 2 seconds (mean 4.4 ± 0.6 seconds) caused a statistically significant increase in discharge length, relative to light-off events (130.3 ± 7.4 %, $p=0.009$).

Figure 5.13 shows the relationship between % suppression and PV⁺ interneuron activation delay. Suppression was calculated as normalised light-off duration minus light-on duration. Values are therefore: 0s delay 34.82 ± 7.6 %, $p = 0.003$; 0.5s delay 21.2 ± 11.3 %, $p = 0.174$; 2s delay 15.7 ± 16.2 %, $p = 0.217$; >2s delay -30.3 ± 7.4 %, $p = 0.009$.

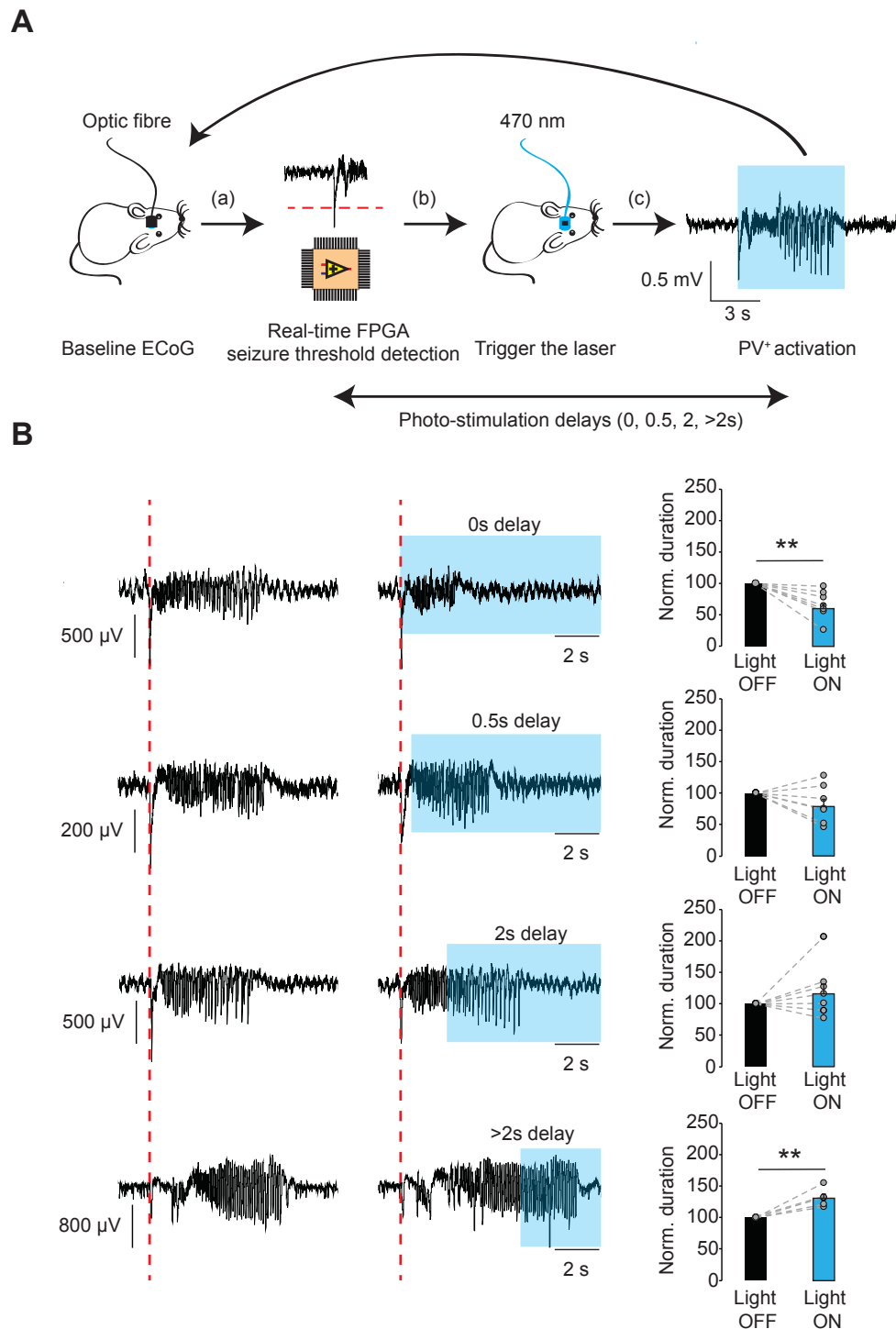


Figure 5.12. Temporal dependence of PV⁺ depolarisation on the duration of ictal-like discharges: **(A)** Optogenetic activation of PV⁺ interneurons was triggered upon ECoG recording amplitude crossing with varying delays. **(B)** Left: example consecutive ictal-like discharges, with PV⁺ interneuron depolarisation triggered on the second amplitude crossing for increasing delays of 0, 0.5, 2, and >2 seconds. Right: bar charts showing the average duration of ictal-like bursts, normalised to light-off discharge length, across animals. Animal numbers: 0s n = 8, 0.5s n = 7, 2s n = 7, >2s n = 5

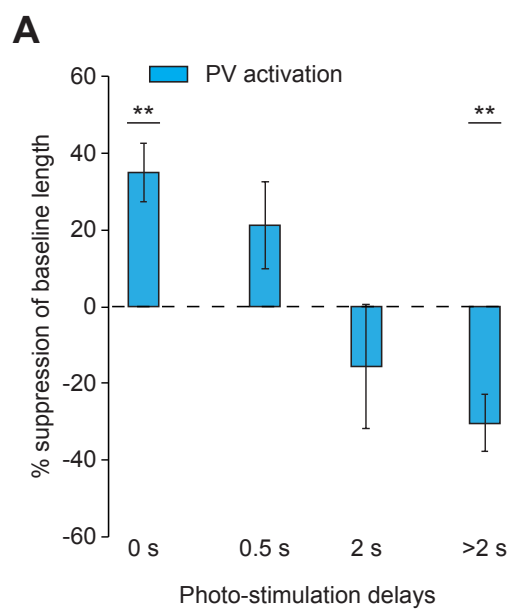


Figure 5.13. Bi-directional effect of PV⁺ interneuron activation: (A) Normalised duration suppression, calculated from normalised durations shown in Figure 5.12B plotted against the time delay of PV⁺ interneuron activation.

5.3.3 Tetanus toxin model spontaneous seizure detection

Here, we present preliminary work developing the a supervised learning strategy for detection of spontaneous seizures from chronic ECoG recordings. The total dataset used was composed of 2 weeks' continuous ECoG recordings from 10 epileptic rats, 14 - 28 days post tetanus toxin injection. Recording weeks were split by rat into training and test datasets in a checkerboard manner, such that for rats 1-5, week 1 was used for training and week 2 for testing, whereas for rats 6-10, week 2 was used for training and week 1 testing. This approach was taken in order to give an indication of the maximal classifier performance by minimising between-rat differences and temporal changes. One hour from the training dataset, in which the data were corrupted, was excluded, resulting in 1680 hours of training recordings and 1681 unseen testing recordings.

The classification process consisted of two steps. First, ECoG recordings were split into 5 second epochs and assigned non-ictal and ictal probabilities by a random forest classifier trained on features extracted from training data epochs. Next, smoothed posterior probabilities were calculated by application of the forward-backward algorithm to the initial probabilities. Figure 5.14 shows this smoothing process. Figure 5.14 A shows correctly identified ictal periods by both the smoothed probabilities and the initial probabilities assigned by the random forest classifier. In contrast, Figure 5.14 B shows the random forest classifier detecting three false positives, assuming a threshold of 0.5, whereas the smoothed probability correctly identifies these periods as non-ictal.

Tables 5.2 to 5.4 show the overall performance of the classifier on testing and training weeks, with emission probabilities incorporated into the forward-backward obtained in three different ways. Table 5.2 shows the performance of the random forest classifier, without hidden Markov model forward-backward algorithm smoothing. Using this strategy, while recall is good, far too many false positives are returned per true positive for the strategy to be used for automated seizure detection. Note that, unusually for supervised learning performance tasks, model performance - e.g. F1 score - evaluates more positively for the testing week than training. This is most likely due to the larger number of seizures present in the testing week increasing precision score. However, as expected, % recall of seizure seconds is less for the testing week.

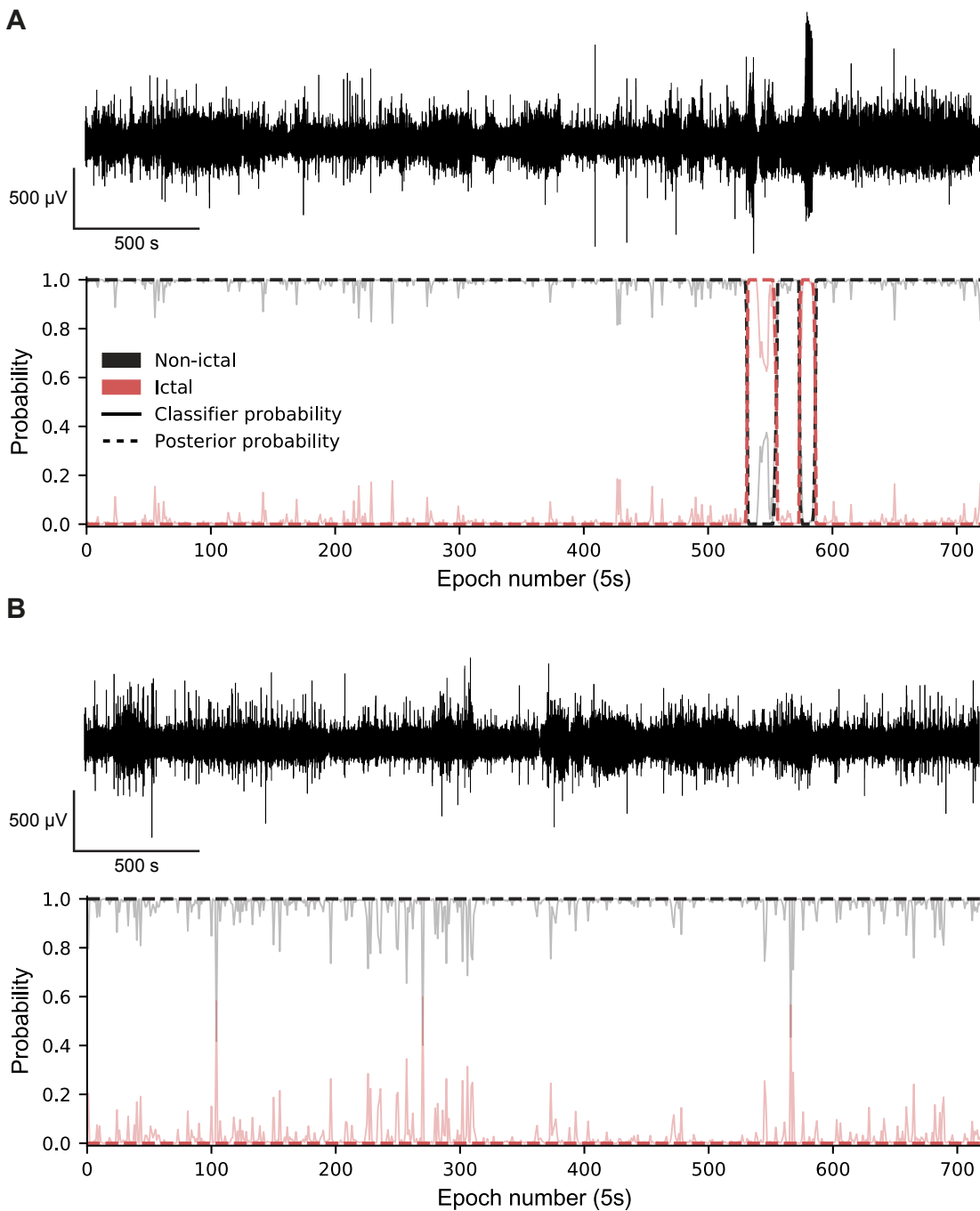


Figure 5.14. Forward-backward algorithm posterior probabilities: (A) ECoG recording with seizure and (B) without seizures. Traces show single hours of ECoG recordings, below, plot shows un-smoothed (solid faint lines), and posterior (dashed lines) probabilities for 5s epochs being ictal (red) or non-ictal (black).

In contrast, table 5.3 shows algorithm performance using cross validation to learn the hidden-state emission probabilities of classifier output. Here, smoothing to obtain

posterior probabilities results in decreased false positives by a factor of 10. In addition, % seconds recall is increased. Table 5.4 displays the results of using Bayes' theorem to directly incorporate the discriminative probabilistic output of the random forest. Here, false positive rate and recall is also improved from un-smoothed probabilities returned by the random forest classifier.

Table 5.2. Random forest performance on chronic tetanus toxin model ECoG recordings without hidden Markov model

Week	TP	FP	FN	Precision	Recall	F1	Recall (% s)	Hours
Training	183	2128	0	0.079	1.0	0.147	100.0	1680
Testing	388	3158	0	0.109	1.0	0.197	73.7	1681

Table 5.3. Algorithm performance with hidden state emission probabilities of classifier output

Week	TP	FP	FN	Precision	Recall	F1	Recall (% s)	Hours
Training	183	218	0	0.46	1.0	0.62	100.0	1680
Testing	388	343	0	0.53	1.0	0.69	80.6	1681

Table 5.4. Algorithm performance using $p(Z_t|X_t)/p(Z_t)$

Week	TP	FP	FN	Precision	Recall	F1	Recall (% s)	Hours
Training	183	582	0	0.24	1.0	0.39	100.0	1680
Testing	388	769	0	0.34	1.0	0.5	91.4	1681

5.4 Discussion

In this chapter we show that standard machine-learning approaches can be readily harnessed to augment research into the roles of interneurons, such as PV⁺ cells, during network disorders such as epilepsy. These methods are previously described in the scientific literature, and as such, no claim for implementation novelty is made, however, their successful application to the datasets reported in this chapter is novel.

5.4.1 Pilocarpine network-state classifier

The motivation underlying the use of a supervised-learning approach to classify pilocarpine-induced epileptiform activity was to remove any potential bias that might arise from manual data selection. However, this rests on the premise that the activity falls into distinct epileptiform states. The ability of the trained random forest classifier to correctly categorise features, which were extracted from ECoG recordings, indicates that activity does indeed fall into stereotyped states, in addition to validating its use for automated data selection.

It should also be noted that human annotation of the different network-states was inconsistent, especially at the boundary between the states. For example, state 3 was typically characterised by upward deflections, and by continuous activity, both of which evolved smoothly from state 2. Similarly, the ictal spikes seen in state 1 often gradually developed into the spike-discharge pattern seen in state 2. This, as well as motivating the need for an automated approach to state assignment, emphasises the performance of the classifier, as some of the training and testing examples are challenging even for a human to identify consistently.

5.4.2 Time dependent bi-phasic effect of PV⁺ interneuron activation

Our experiments show that the effect of PV⁺ interneuron depolarisation on the duration of discrete epileptiform discharges, in awake mice, evolves from an anti-epileptic to a pro-epileptic action over the time-course of a single discharge. In line with a E-I

balance model, activation of PV⁺ cells in a closed loop system decreases the discharge duration, however, surprisingly, delaying the activation of PV⁺ cells by 2 seconds or more from the start of the discharge, promotes the maintenance of epileptiform activity.

Of the mechanisms that could potentially explain this switch in function over time, two are perhaps the most plausible. First, PV⁺ cells may be entering into state of depolarisation-induced blockade, unable to fire action potentials due to voltage gated Na⁺ channel inactivation. In this case, optogenetic depolarisation would exacerbate the block. Second, the intense principal cell activity that occurs during the discharge may lead to a depolarising switch in the GABAergic reversal potential due to Cl⁻ accumulation. In this case, PV⁺ activation by light may excite the network, instead of inhibiting it.

Unfortunately, however, both of these theories are not entirely satisfactory. While it is true that pyramidal neurons readily enter into depolarisation block in response to somatic current injections, PV⁺ interneurons have particularly low input resistances and show large amplitude action-potential afterhyperpolarisation. They are therefore resistant to depolarisation-block, and in slices large somatic current injections (up to 1 nA) do not elicit firing block (experimental observations - not shown). In addition, in vivo, and particularly during epileptic network states, the large synaptic input barrage will decrease the input resistance, increasing the required excitatory current needed to generate depolarisation blockade of action-potential firing. Alternatively, for GABAergic signalling to have a distinct excitatory effect on the network, as has been suggested to occur in slices (Ellender et al., 2014), the driving force must be large enough to produce a current that overcomes inhibitory effect of the shunting conductance.

In order to test these two hypotheses, two further experiments could be performed. First, in order to investigate PV⁺ interneuron depolarisation blockade, targeted cell attached recordings could be made during epileptiform discharges. However, this is technically challenging. To test the second hypothesis, KCC2 could be over-expressed in pyramidal cells, making them more resistive to Cl⁻ accumulation, and experiments described above repeated. If excitatory GABAergic signalling in control conditions mediates the pro-epileptic role of PV⁺ cells, this approach should mitigate these effects.

5.4.3 Spontaneous seizure detection

While treatment of single 5 second epochs of ECoG recording treated in isolation can be used to detect ictal periods, we show that better performance can be achieved by incorporating surrounding information. This work is currently preliminary, and further work is required develop this approach and compare it to existing methods.

We also make a number of assumptions, that lead to inaccuracies in our model. The most important of these it to train the classifier from single hours, that each contain a seizure. This approach was taken in order to reduce the computational burden, and was motivated by the standard approach of down-sampling the more common class in situations of dataset imbalance. However, the transition probabilities and stationary distribution are then calculated from these hours in the library. As a result, these are not correct for the full test dataset.

For future work, deep learning and artificial neural networks offer an alternative approach to the problem of seizure detection. In contrast to extracting various features based on domain expertise, the approach of deep learning is to learn a non-linear functions that transforms raw ECoG to provide a new representation, analogous to feature extraction. A simple output layer then maps this representation to the desired target. While around from the 1950s, and used commercially from the 1990s, recently increased availability of computational resources and large datasets has led to an explosion of interest in deep learning. A next step, which should yield both insights and improved performance, would therefore be to leverage the large dataset, already collected by the laboratory, in order to train deep models.

Chapter 6

Discussion

6.1 General discussion

For cells that are largely understood in terms of their fast linear synaptic integration, and relative lack of input cooperation (Hu et al., 2014*a*), it is remarkable that the two main glutamatergic receptors expressed by PV⁺ interneurons have nonlinear conductance relationships with voltage. Moreover, these two receptors display diametrically opposing responses to voltage changes, requiring opposite postsynaptic membrane conditions to elicit maximal conductances. Previously, these receptors have been considered mainly in terms of their roles in mediating hebbian and anti-hebbian plasticity (Le Roux et al., 2013; Lamsa et al., 2007). In contrast, much of this thesis has focussed on assigning functional roles to the two current-voltage relationships mediated by NMDA or CP-AMPA receptors.

One of the main findings of our experiments was that NMDA receptors on PV⁺ interneurons can mediate synaptic input cooperativity for local feedback connections, which has a broad range of functions. First, for assemblies of neurons forming representations of external inputs, this form of synaptic integration leads to a sharpening of structured representations, in line with work showing a decrease in spatial precision of CA1 neurons in NR1^{PVCre}^{-/-} mice (Korotkova et al., 2010). This occurs because the number of neurons required to recruit the recurrent inhibition is dependent on the degree of synaptic cooperation. Assuming a positive relationship between synaptic co-

operation and coordinated presynaptic neuron activation, this number decreases with input cohesion. Further to sculpting single cell assemblies, synaptic cooperation of inputs onto PV⁺ cells also dictates the interaction between competing cell assemblies (Geisler et al., 2007). In this case, NMDAR-dependent synaptic integration allows the temporal stability and cohesion of a representation to be taken into account by the PV⁺ cell. Coordinated cell assemblies that cooperate post-synaptically are more able to recruit the PV⁺ interneuron, and thus drive lateral inhibition of an alternative cell assemblies. Finally, NMDA receptors allow dominant cell assemblies to be more stable in the face of input variations, which may underlie the contribution of both NMDA receptors and PV⁺ cells to cognitive disorders such as schizophrenia (Lewis et al., 2005; Gonzalez-Burgos and Lewis, 2012).

This work therefore resolves one of the central paradoxes in the literature surrounding PV⁺ cells: functionally, why would a slow conductance, such as that mediated by NMDA receptors, be found on a cell built for precision and speed? One explanation could be that the main function of NMDA receptors is to mediate synaptic plasticity, however, this role is less important for PV⁺ interneurons than principal cells, as CP-AMPA receptors are also capable of inducing synaptic weight changes. The functions of NMDA receptors on PV⁺ cells that we identify provide clear functional justifications for their expression, in addition to the mediation of synaptic plasticity, and also illuminate the network disorders that follow from NMDA receptor dysfunction (Carlén et al., 2012; Jadi et al., 2016; Bygrave et al., 2016; Korotkova et al., 2010).

We also corroborate a previous study (Le Roux et al., 2013), and show that NMDA receptors are enriched at feedback connections onto PV⁺ interneurons, relative to feedforward synapses. This differential expression also accounts for some of the conflicting data on PV⁺ interneuron physiology, namely, the apparent importance of NMDA receptors on PV⁺ cells, but coincident scarcity of their expression. Within the hippocampus, the existence of well defined afferent pathways allowed us to investigate the distinction between feedforward and feedback connections relatively easily. Unfortunately, this is not so elsewhere in the brain, and it is not known whether this afferent-specific expression profile exists as a common motif throughout the cortex. Nevertheless, the findings of this thesis could be applicable across all cortical sub-networks within which PV⁺ interneurons are found. Future work addressing this question, such as paired recordings or optogenetic strategies, might be required before more encompassing conclusions can be made.

It should be emphasised, however, that the categorisation of afferent fibres into feedback and feedforward connections, which is made both throughout this thesis and ubiquitously in the scientific literature, is an artificial distinction. Fundamentally, neurons exist in the context of larger networks, in which these terms ultimately lose their relevance. Furthermore, it is also not clear, even within the context of microcircuits, if these terms can be applied with consistent meaning: for example, dis-inhibitory connections can result in feedforward inhibition becoming excitatory. Additionally, lateral or recurrent connections from or to, local feedback inhibition mediate entirely separate outcomes for the principal cells driving the interneuron in these two situations. As an approach for understanding the roles of inhibition, the distinction of feedback and feedforward is useful, however care should be taken to not emphasise it blindly.

It was also surprising that the dendrites located in the stratum radiatum displayed linear synaptic integration. Given the role of PV⁺ cells in mediating precise feedforward inhibition, which regulates the temporal precision of pyramidal cell firing and expands network dynamic range (Pouille and Scanziani, 2001; Pouille et al., 2009), it might be expected that slow NMDA receptor-mediated supra-linear summation would be absent from these connections - though we do not provide any work to support this assertion. However, it is unexpected, given the conductance-based nature of synapses, that synaptic integration is linear as opposed to sublinear. We presume that Ca²⁺ channels underlie this observation, and that it reflects a requirement for synaptic inputs to be summed linearly at the network level.

Building upon the critical assumption that PV⁺ interneurons receive functionally clustered inputs, similar to principal cells (Wilson et al., 2016), we used patterned two-photon MNI-glutamate uncaging to study the integration of synaptic inputs. Experiments to address functional clustering of feedback synapses onto PV⁺ interneurons are therefore one clear avenue of further work. In addition, while two-photon MNI-glutamate uncaging is currently without peer for our purposes, it still has a number of caveats. Most pressing of these provisos is the unknown origin, i.e. synaptic or extra-synaptic, of the uncaging induced EPSPs used to investigate the synaptic integration. Unlike pyramidal cells, which helpfully have spines to somewhat guide the experimenter towards synaptic locations, PV⁺ cells are aspiny, though this does also reduce the surface area over which synapses are found. However, the use of MNI-glutamate also has other experimental shortcomings: it blocks GABA_A receptors, which potentially shifts the dendrites into an unphysiological state, and may cause

the slice to become epileptic; second, MNI-glutamate does not penetrate deep tissue well, biasing the experimenter towards superficial dendritic regions; and third drift, caused perhaps by the swelling of deeper cells as they die, can lead to photo-damage of the dendrite - though this is normally easily identified by blebbing or from the electrical recording.

Any investigation of synaptic inputs and the mechanisms of their interaction is ultimately motivated by an interest in understanding the behaviour and function of the postsynaptic neuron in a larger network context. One such area where the function of PV⁺ cells is contentious is epilepsy. Previous work has found PV⁺ interneuron activation to both contribute towards and against seizure termination. In this thesis, we present work that shows that the pro- or anti-epileptic nature of PV⁺ interneurons is dependent on the time from seizure onset. It is our hope this builds towards future work using more accurate rodent-models of epilepsy.

Finally, throughout this thesis, PV⁺ interneurons have been referred to as a single population of cells. However, as discussed in section 1.2.1, PV⁺ interneurons are a heterogeneous population, most easily separated by their axonal arborisation. For the hippocampal CA1 region, it could be argued that basket cells and axo-axonic cells are relatively similar, they both target perisomatic regions of the local pyramidal cells to deliver powerful divergent inhibition. In contrast bi-stratified cells, which make up almost a quarter of the PV⁺ cells in CA1, mainly target the dendrites of pyramidal neurons (Muller and Remy, 2014), and likely play distinct network roles. Furthermore, the PV⁺ Cre line used to identify PV⁺ cells is also not 100% specific for PV⁺ interneurons, for example PV is expressed transiently in a range of cells during development. While PV⁺ cell recordings in slice experiments were corroborated by the recording of fast-spiking firing patterns, a minority of other cells may be targeted in the optogenetic experiments presented in chapter 4. All of the work and experiments presented in this thesis would benefit from more selective targeting of a single subtype, such as the most common PV⁺ subtype - basket cells. One way in which this could be achieved for example, is to exclude bistratified cells, which also express SOM, by use of an inter-sectional strategy (e.g. Fenno et al., 2014).

6.2 Concluding remarks

By utilising a combined experimental and computational approach, it is possible to elucidate the workings of individual neurons and relate them to the circuits within which they are embedded. The experiments and simulations presented in this thesis provide a foundation for future work pinpointing the specific roles of PV⁺ interneurons during network functions and disorders, such as epilepsy and schizophrenia. By identifying network-level processes, and the cellular mechanisms that underpin them, we may come closer to the ultimate goal of not only understanding how systems of neurons function, but also to manipulate and control their malfunction.

Bibliography

- Aghazadeh, R., Shahabi, P., Frounchi, J. and Sadighi, M. (2015), An autonomous real-time single-channel detection of absence seizures in WAG/Rij rats, *Gen Physiol Biophys* 34(3), 285–291.
- Agmon-Snir, H. and Segev, I. (1993), Signal delay and input synchronization in passive dendritic structures., *Journal of neurophysiology* 70(5), 2066–2085.
- Andersen, P. (2007), *The hippocampus book*, Oxford University Press, Oxford; New York.
- Aponte, Y., Lien, C.-C., Reisinger, E. and Jonas, P. (2006), Hyperpolarization-activated cation channels in fast-spiking interneurons of rat hippocampus., *The Journal of physiology* 574(Pt 1), 229–243.
- Assaf, F. and Schiller, Y. (2016), The antiepileptic and ictogenic effects of optogenetic neurostimulation of PV-expressing interneurons, *Journal of Neurophysiology* 116(4), 1694–1704.
- Babadi, B. and Sompolinsky, H. (2014), Sparseness and Expansion in Sensory Representations, *Neuron* 83(5), 1213–1226.
- Baldassano, S. N., Brinkmann, B. H., Ung, H., Blevins, T., Conrad, E. C., Leyde, K., Cook, M. J., Khambhati, A. N., Wagenaar, J. B., Worrell, G. A. and Litt, B. (2017), Crowdsourcing seizure detection: algorithm development and validation on human implanted device recordings, *Brain* pp. 1680–1691.
- Bartos, M. and Elgueta, C. (2012), Functional characteristics of parvalbumin- and cholecystinin-expressing basket cells, *The Journal of physiology* .
- Behrens, M. M., Ali, S. S., Dao, D. N., Lucero, J., Shekhtman, G., Quick, K. L. and Dugan, L. L. (2007), Ketamine-Induced Loss of Phenotype of Fast-Spiking Interneurons Is Mediated by NADPH-Oxidase, *Science* 318(5856), 1645–1647.

- Bekkers, J. M. (2000), Properties of voltage-gated potassium currents in nucleated patches from large layer 5 cortical pyramidal neurons of the rat, *The Journal of Physiology* 525(3), 593–609.
- Belforte, J. E., Zsiros, V., Sklar, E. R., Jiang, Z., Yu, G., Li, Y., Quinlan, E. M. and Nakazawa, K. (2010), Postnatal NMDA receptor ablation in corticolimbic interneurons confers schizophrenia-like phenotypes., *Nature neuroscience* 13(1), 76–83.
- Bezaire, M. J. and Soltesz, I. (2013), Quantitative assessment of CA1 local circuits: Knowledge base for interneuron-pyramidal cell connectivity, *Hippocampus* 23(9), 751–785.
- Bi, G. Q. and Poo, M. M. (1998), Synaptic modifications in cultured hippocampal neurons: dependence on spike timing, synaptic strength, and postsynaptic cell type., *The Journal of neuroscience : the official journal of the Society for Neuroscience* 18(24), 10464–10472.
- Bishop, C. M. (2007), Pattern Recognition And Machine Learning, *Book* p. 738.
- Bishop, C. M., Svensen, M. and Hinton, G. E. (2004), Distinguishing text from graphics in on-line handwritten ink, *Proceedings - International Workshop on Frontiers in Handwriting Recognition, IWFHR* pp. 142–147.
- Bittner, K. C., Grienberger, C., Vaidya, S. P., Milstein, A. D., Macklin, J. J., Suh, J., Tonegawa, S. and Magee, J. C. (2015), Conjunctive input processing drives feature selectivity in hippocampal CA1 neurons, *Nature Neuroscience* 18(July), 1–13.
- Bloodgood, B. L. and Sabatini, B. L. (2007), Ca(2+) signaling in dendritic spines., *Current opinion in neurobiology* 17(3), 345–351.
- Borg-Graham, L. J., Monier, C. and Fregnac, Y. (1998), Visual input evokes transient and strong shunting inhibition in visual cortical neurons, *Nature* 393(6683), 369–373.
- Bowie, D. (2012), Redefining the classification of AMPA-selective ionotropic glutamate receptors., *The Journal of physiology* 590(Pt 1), 49–61.
- Bowie, D., Lange, G. D. and Mayer, M. L. (1998), Activity-dependent modulation of glutamate receptors by polyamines.
- Bowie, D. and Mayer, M. L. (1995), Inward rectification of both AMPA and kainate subtype glutamate receptors generated by polyamine-mediated ion channel block, *Neuron* 15(2), 453–462.

- Bragin, a., Jandó, G., Nádasdy, Z., Hetke, J., Wise, K. and Buzsáki, G. (1995), Gamma (40-100 Hz) oscillation in the hippocampus of the behaving rat., *The Journal of neuroscience : the official journal of the Society for Neuroscience* 15(1 Pt 1), 47–60.
- Branco, T., Clark, B. A. and Häusser, M. (2010), Dendritic discrimination of temporal input sequences in cortical neurons., *Science* 329(5999), 1671–1675.
- Breiman, L. (2001), Random forests, *Machine Learning* 45(1), 5–32.
- Buchanan, K. A., Petrovic, M. M., Chamberlain, S. E., Marrion, N. V. and Mellor, J. R. (2010), Facilitation of Long-Term Potentiation by Muscarinic M1 Receptors Is Mediated by Inhibition of SK Channels, *Neuron* 68(5), 948–963.
- Buetfering, C., Allen, K. and Monyer, H. (2014), Parvalbumin interneurons provide grid cell-driven recurrent inhibition in the medial entorhinal cortex., *Nature neuroscience* 17(5), 710–718.
- Buteneers, P., Verstraeten, D., Nieuwenhuyse, B. V., Stroobandt, D., Raedt, R., Vonck, K., Boon, P. and Schrauwen, B. (2013), Real-time detection of epileptic seizures in animal models using reservoir computing, *Epilepsy Research* 103(2-3), 124–134.
- Bygrave, A. M., Masiulis, S., Nicholson, E., Berkemann, M., Barkus, C., Sprengel, R., Harrison, P. J., Kullmann, D. M., Bannerman, D. M. and Kätzel, D. (2016), Knock-out of NMDA-receptors from parvalbumin interneurons sensitizes to schizophrenia-related deficits induced by MK-801, *Translational Psychiatry* 6(4), e778.
- Cais, O., Sedlacek, M., Horak, M., Dittert, I. and Vyklicky, L. (2008), Temperature dependence of NR1/NR2B NMDA receptor channels, *Neuroscience* 151(2), 428–438.
- Camire, O. and Topolnik, L. (2014), Dendritic calcium nonlinearities switch the direction of synaptic plasticity in fast-spiking interneurons., *The Journal of neuroscience : the official journal of the Society for Neuroscience* 34(11), 3864–3877.
- Cammarota, M., Losi, G., Chiavegato, A., Zonta, M. and Carmignoto, G. (2013), Fast spiking interneuron control of seizure propagation in a cortical slice model of focal epilepsy, *The Journal of Physiology* 591(4), 807–822.

- Campanac, E., Gasselín, C., Baude, A., Rama, S., Ankri, N. and Debanne, D. (2013), Enhanced Intrinsic Excitability in Basket Cells Maintains Excitatory-Inhibitory Balance in Hippocampal Circuits, *Neuron* 77(4), 712–722.
- Carlén, M., Meletis, K., Siegle, J. H., Cardin, J. A., Futai, K., Vierling-Claassen, D., Rühlmann, C., Jones, S. R., Deisseroth, K., Sheng, M., Moore, C. I. and Tsai, L.-H. (2012), A critical role for NMDA receptors in parvalbumin interneurons for gamma rhythm induction and behavior., *Molecular psychiatry* 17(5), 537–548.
- Carnevale, N. T. and Hines, M. L. (2009), *The NEURON Book*, Cambridge University Press.
- Caruana, R. and Niculescu-Mizil, A. (2006), An empirical comparison of supervised learning algorithms, *Proceedings of the 23rd international conference on Machine learning* C(1), 161–168.
- Cash, S. and Yuste, R. (1999), Linear summation of excitatory inputs by CA1 pyramidal neurons., *Neuron* 22(2), 383–394.
- Chen, C. (2004), ZD7288 inhibits postsynaptic glutamate receptor-mediated responses at hippocampal perforant path-granule cell synapses, *European Journal of Neuroscience* 19(3), 643–649.
- Chen, X., Leischner, U., Rochefort, N. L., Nelken, I. and Konnerth, A. (2011), Functional mapping of single spines in cortical neurons in vivo, *Nature* 475(7357), 501–505.
- Chevaleyre, V. and Castillo, P. E. (2002), Assessing the role of Ih channels in synaptic transmission and mossy fiber LTP., *Proceedings of the National Academy of Sciences of the United States of America* 99(14), 9538–9543.
- Chiovini (2013), Dendritic spikes induce ripples in parvalbumin interneurons during hippocampal sharp waves , pp. 1–59.
- Chiovini, B., Turi, G. F., Katona, G., Kaszás, A., Erdélyi, F., Szabó, G., Monyer, H., Csákányi, A., Vizi, E. S. and Rozsa, B. (2010), Enhanced dendritic action potential backpropagation in parvalbumin-positive basket cells during sharp wave activity., *Neurochemical research* 35(12), 2086–2095.
- Chiovini, B., Turi, G. F., Katona, G., Kaszás, A., Pálfi, D., Maák, P., Szalay, G., Szabó, M. F., Szabó, G., Szadai, Z., Káli, S. and Rozsa, B. (2014), Dendritic Spikes

- Induce Ripples in Parvalbumin Interneurons during Hippocampal Sharp Waves, *Neuron* 82(4), 908–924.
- Colgin, L. L., Denninger, T., Fyhn, M., Hafting, T., Bonnevie, T., Jensen, O., Moser, M.-B. and Moser, E. I. (2009), Frequency of gamma oscillations routes flow of information in the hippocampus., *Nature* 462(7271), 353–357.
- Connors, B. W. (1984), Initiation of synchronized neuronal bursting in neocortex, *Nature* 310(5979), 685–687.
- Cook, E. P. and Johnston, D. (1999), Voltage-dependent properties of dendrites that eliminate location-dependent variability of synaptic input., *Journal of neurophysiology* 81(2), 535–543.
- Cossart, R., Bernard, C. and Ben-Ari, Y. (2005), Multiple facets of GABAergic neurons and synapses: Multiple fates of GABA signalling in epilepsies, *Trends in Neurosciences* 28(2), 108–115.
- Craig, M. T. and McBain, C. J. (2015), Fast Gamma Oscillations Are Generated Intrinsically in CA1 without the Involvement of Fast-Spiking Basket Cells, *The Journal of neuroscience* .
- Csicsvari, J., Hirase, H., Czurko, A. and Buzsáki, G. (1998), Reliability and state dependence of pyramidal cell-interneuron synapses in the hippocampus: An ensemble approach in the behaving rat, *Neuron* 21(1), 179–189.
- Cuntz, H., Forstner, F., Borst, A. and Häusser, M. (2010), One rule to grow them all: a general theory of neuronal branching and its practical application., *PLoS computational biology* 6(8).
- de Almeida, L., Idiart, M. and Lisman, J. E. (2009a), A Second Function of Gamma Frequency Oscillations: An E%-Max Winner-Take-All Mechanism Selects Which Cells Fire, *Journal of Neuroscience* 29(23), 7497–7503.
- de Almeida, L., Idiart, M. and Lisman, J. E. (2009b), The Input-Output Transformation of the Hippocampal Granule Cells: From Grid Cells to Place Fields, *Journal of Neuroscience* 29(23), 7504–7512.
- DeFelipe, J. (2002), Cortical interneurons: From Cajal to 2001, *Progress in Brain Research* 136, 215–238.

- Destexhe, A., Mainen, Z. F. and Sejnowski, T. J. (1998), Biophysical models of synaptic transmission, *in* Koch, C. and I. Segev, eds, ‘Methods in Neuronal Modeling’, 2nd edn, MIT Pres, Cambridge, pp. 1–25.
- Druckmann, S., Feng, L., Lee, B., Yook, C., Zhao, T., Magee, J. C. and Kim, J. (2014), Structured Synaptic Connectivity between Hippocampal Regions, *Neuron* 81(3), 629–640.
- Dzhala, V. I., Talos, D. M., Sdrulla, D. A., Brumback, A. C., Mathews, G. C., Benke, T. A., Delpire, E., Jensen, F. E. and Staley, K. J. (2005), NKCC1 transporter facilitates seizures in the developing brain, *Nature Medicine* 11(11), 1205–1213.
- Ellender, T. J., Raimondo, J. V., Irkle, A., Lamsa, K. P. and Akerman, C. J. (2014), Excitatory Effects of Parvalbumin-Expressing Interneurons Maintain Hippocampal Epileptiform Activity via Synchronous Afterdischarges, *Journal of Neuroscience* 34(46), 15208–15222.
- Emri, Z. S., Antal, K., Gulyás, A. I., Megias, M. and Freund, T. F. (2001), Electrotonic profile and passive propagation of synaptic potentials in three subpopulations of hippocampal CA1 interneurons, *Neuroscience* .
- Fenko, L. E., Mattis, J., Ramakrishnan, C., Hyun, M., Lee, S. Y., He, M., Tucciarone, J., Selimbeyoglu, A., Berndt, A., Grosenick, L., Zalocusky, K. A., Bernstein, H., Swanson, H., Perry, C., Diester, I., Boyce, F. M., Bass, C. E., Neve, R., Huang, Z. J. and Deisseroth, K. (2014), Targeting cells with single vectors using multiple-feature Boolean logic., *Nature methods* 11(7), 763–72.
- Ferguson, K. a., Huh, C. Y. L., Amilhon, B., Williams, S. and Skinner, F. K. (2013), Experimentally constrained CA1 fast-firing parvalbumin-positive interneuron network models exhibit sharp transitions into coherent high frequency rhythms., *Frontiers in computational neuroscience* 7(October), 144.
- Ferguson, K. A., Huh, C. Y. L., Amilhon, B., Williams, S. and Skinner, F. K. (2014), Simple, biologically-constrained CA1 pyramidal cell models using an intact, whole hippocampus context., *F1000Research* 3(0), 104.
- Freund, T. F. and Buzsáki, G. (1998), Interneurons of the hippocampus, *Hippocampus* 6(4), 347–470.
- Fricker, D. and Miles, R. (2000), EPSP amplification and the precision of spike timing in hippocampal neurons., *Neuron* 28(2), 559–569.

- Galarreta, M. and Hestrin, S. (1999), A network of fast-spiking cells in the neocortex connected by electrical synapses., *Nature* 402(6757), 72–5.
- Galarreta, M. and Hestrin, S. (2001), Spike transmission and synchrony detection in networks of GABAergic interneurons., *Science* 292(5525), 2295–9.
- Geiger, J. R., Lübke, J., Roth, A., Frotscher, M. and Jonas, P. (1997), Submillisecond AMPA receptor-mediated signaling at a principal neuron-interneuron synapse., *Neuron* 18(6), 1009–1023.
- Geiger, J. R. P., Melcher, T., Koh, D. S. and Sakmann, B. (1995), Relative abundance of subunit mRNAs determines gating and Ca^{2+} permeability of AMPA receptors in principal neurons and interneurons in . . . , *Neuron* .
- Geisler, C., Robbe, D., Zugaro, M., Sirota, A. and Buzsáki, G. (2007), Hippocampal place cell assemblies are speed-controlled oscillators, *Proceedings of the National Academy of Sciences* 104(19), 8149–8154.
- Gidon, A. and Segev, I. (2012), Principles Governing the Operation of Synaptic Inhibition in Dendrites, *Neuron* 75(2), 330–341.
- Goldberg, E. M., Clark, B. D., Zaghera, E., Nahmani, M., Erisir, A. and Rudy, B. (2008), K^+ Channels at the Axon Initial Segment Dampen Near-Threshold Excitability of Neocortical Fast-Spiking GABAergic Interneurons, *Neuron* 58(3), 387–400.
- Goldberg, J. H., Tamás, G., Aronov, D. and Yuste, R. (2003), Calcium Microdomains in Aspiny Dendrites, *Neuron* 40(4), 807–821.
- Golding, N. L., Mickus, T. J., Katz, Y., Kath, W. L. and Spruston, N. (2005), Factors mediating powerful voltage attenuation along CA1 pyramidal neuron dendrites., *The Journal of physiology* 568(Pt 1), 69–82.
- Golding, N. L., Staff, N. P. and Spruston, N. (2002), Dendritic spikes as a mechanism for cooperative long-term potentiation., *Nature* 418(6895), 326–331.
- Goldstein, S. A., Bockenhauer, D., O’Kelly, I. and Zilberberg, N. (2001), Potassium leak channels and the KCNK family of two-P-domain subunits., *Nature reviews. Neuroscience* 2(3), 175–184.
- Gonzalez-Burgos, G. and Lewis, D. A. (2012), NMDA receptor hypofunction, parvalbumin-positive neurons, and cortical gamma oscillations in schizophrenia, *Schizophrenia Bulletin* 38(5), 950–957.

- Gotman, J. (1982), Automatic recognition of epileptic seizures in the EEG, *Electroencephalography and Clinical Neurophysiology* 54(5), 530–540.
- Greenfield, J. J. (2013), Molecular mechanisms of antiseizure drug activity at GABA A receptors, *Seizure: European Journal of Epilepsy* 22(8), 589–600.
- Grunze, H. C. R., Rainnie, D. G., Hasselmo, M. E., Barkai, E., Hearn, E. F., Mccarley, R. W. and Greene ', R. W. (1996), NMDA-Dependent Modulation of CA1 Local Circuit Inhibition, *The Journal of Neuroscience* 76(6), 2034–2043.
- Gulyás, A. I., Megías, M., Emri, Z. and Freund, T. F. (1999), Total number and ratio of excitatory and inhibitory synapses converging onto single interneurons of different types in the CA1 area of the rat hippocampus., *The Journal of neuroscience : the official journal of the Society for Neuroscience* 19(22), 10082–10097.
- Gulyás, A. I., Miles, R., Sik, A., Tóth, K., Tamamaki, N. and Freund, T. F. (1993), Hippocampal pyramidal cells excite inhibitory neurons through a single release site., *Nature* 366(6456), 683–687.
- Hao, J., Wang, X.-d., Dan, Y., Poo, M.-m. and Zhang, X.-h. (2009), An arithmetic rule for spatial summation of excitatory and inhibitory inputs in pyramidal neurons, *Proceedings of the National Academy of Sciences* 106(51), 21906–21911.
- Häusser, M. and Mel, B. (2003), Dendrites: Bug or feature?, *Current Opinion in Neurobiology* 13(3), 372–383.
- He, Y., Janssen, W. G. M. and Morrison, J. H. (1998), Synaptic coexistence of AMPA and NMDA receptors in the rat hippocampus: A postembedding immunogold study, *Journal of Neuroscience Research* 54(4), 444–449.
- Hines, M. L. and Carnevale, N. T. (1997), The NEURON simulation environment., *Neural computation* 9(6), 1179–1209.
- Hoffman, D. a., Magee, J. C., Colbert, C. M. and Johnston, D. (1997), K⁺ channel regulation of signal propagation in dendrites of hippocampal pyramidal neurons., *Nature* 387(6636), 869–875.
- Holmes, G. L. (1995), Role of glutamate and GABA in the pathophysiology of epilepsy, *Mental Retardation and Developmental Disabilities Research Reviews* 1(3), 208–219.

- Hopfield, J. J. (1982), Neural networks and physical systems with emergent collective computational abilities., *Proceedings of the National Academy of Sciences of the United States of America* 79(8), 2554–2558.
- Hopfield, J. J. and Tank, D. W. (1986), ‘Computing with neural circuits: a model.’
- Howarth, C., Gleeson, P. and Attwell, D. (2012), Updated energy budgets for neural computation in the neocortex and cerebellum., *Journal of cerebral blood flow and metabolism : official journal of the International Society of Cerebral Blood Flow and Metabolism* 32(7), 1222–32.
- Hu, H., Gan, J. and Jonas, P. (2014a), Interneurons. Fast-spiking, parvalbumin⁺ GABAergic interneurons: from cellular design to microcircuit function., *Science (New York, N.Y.)* 345(6196), 1255263.
- Hu, H., Gan, J. and Jonas, P. (2014b), Interneurons. Fast-spiking, parvalbumin⁺ GABAergic interneurons: from cellular design to microcircuit function., *Science* 345(6196), 1255263.
- Hu, H. and Jonas, P. (2014), A supercritical density of Na(+) channels ensures fast signaling in GABAergic interneuron axons., *Nature neuroscience* 17(5), 686–693.
- Hu, H., Martina, M. and Jonas, P. (2010), Dendritic mechanisms underlying rapid synaptic activation of fast-spiking hippocampal interneurons., *Science* 327(5961), 52–58.
- Hunyadi, B., Siekierska, A., Sourbron, J., Copmans, D. and de Witte, P. A. (2017), Automated analysis of brain activity for seizure detection in zebrafish models of epilepsy, *Journal of Neuroscience Methods* 287, 13–24.
- Iacaruso, M. F., Gasler, I. T. and Hofer, S. B. (2017), Synaptic organization of visual space in primary visual cortex, *Nature* 547(7664), 449–452.
- Iansek, R. and Redman, S. J. (1973), The amplitude, time course and charge of unitary excitatory post-synaptic potentials evoked in spinal motoneurone dendrites., *The Journal of physiology* 234(3), 665–688.
- Izhikevich, E. M. (2003), Simple model of spiking neurons, *IEEE Transactions on Neural Networks* 14(6), 1569–1572.
- Jadi, M. P., Behrens, M. M. and Sejnowski, T. J. (2016), Abnormal Gamma Oscillations in N-Methyl-D-Aspartate Receptor Hypofunction Models of Schizophrenia, *Biological psychiatry* 79(9), 716–726.

- Jadi, M., Polsky, A., Schiller, J. and Mel, B. W. (2012), Location-dependent effects of inhibition on local spiking in pyramidal neuron dendrites, *PLoS Computational Biology* 8(6).
- Jahr, C. E. and Stevens, C. F. (1990), Voltage dependence of NMDA-activated macroscopic conductances predicted by single-channel kinetics, *The Journal of neuroscience* 10(9), 3178–3182.
- Jia, H., Rochefort, N. L., Chen, X. and Konnerth, A. (2010), Dendritic organization of sensory input to cortical neurons in vivo, *Neuroforum* 16(3), 236–237.
- Jirsa, V. K., Stacey, W. C., Quilichini, P. P., Ivanov, A. I. and Bernard, C. (2014), On the nature of seizure dynamics, *Brain* 137(8), 2210–2230.
- Jonas, P., Bischofberger, J., Fricker, D. and Miles, R. (2004), Interneuron Diversity series: Fast in, fast out - temporal and spatial signal processing in hippocampal interneurons, *Trends in neurosciences* 27(1), 11.
- Jonas, P., Racca, C., Sakmann, B., Seeburg, P. H. and Monyer, H. (1994), Differences in Ca²⁺ permeability of AMPA-type glutamate receptor channels in neocortical neurons caused by differential GluR-B subunit expression., *Neuron* 12(6), 1281–1289.
- Jones, R. S. G. and Bühl, E. H. (1993), Basket-like interneurons in layer II of the entorhinal cortex exhibit a powerful NMDA-mediated synaptic excitation, *Neuroscience Letters* 149(1), 35–39.
- Kandel, E. R., Schwartz, J. H. and Jessell, T. M. (2000), *Principles of Neural Science*, Vol. 4.
- Kastellakis, G., Cai, D. J., Mednick, S. C., Silva, A. J. and Poirazi, P. (2015), Synaptic clustering within dendrites: An emerging theory of memory formation, *Progress in Neurobiology* 126, 19–35.
- Kavalali, E. T., Chung, C., Khvotchev, M., Leitz, J., Nosyreva, E., Raingo, J. and Ramirez, D. M. O. (2011), Spontaneous neurotransmission: an independent pathway for neuronal signaling?, *Physiology (Bethesda, Md.)* 26(1), 45–53.
- Khoshkhoo, S., Vogt, D. and Sohal, V. S. (2017), Dynamic, Cell-Type-Specific Roles for GABAergic Interneurons in a Mouse Model of Optogenetically Inducible Seizures, *Neuron* 93(2), 291–298.

- Klausberger, T. and Somogyi, P. (2008), Neuronal diversity and temporal dynamics: the unity of hippocampal circuit operations., *Science* 321(5885), 53–57.
- Kleindienst, T., Winnubst, J., Roth-Alpermann, C., Bonhoeffer, T. and Lohmann, C. (2011), Activity-dependent clustering of functional synaptic inputs on developing hippocampal dendrites, *Neuron* 72(6), 1012–1024.
- Koch, C., Douglas, R. and Wehmeier, U. (1990), Visibility of synaptically induced conductance changes: theory and simulations of anatomically characterized cortical pyramidal cells., *The Journal of neuroscience : the official journal of the Society for Neuroscience* 10(6), 1728–44.
- Koch, C., Poggio, T. and Torre, V. (1983), Nonlinear interactions in a dendritic tree: localization, timing, and role in information processing., *Proceedings of the National Academy of Sciences* 80(9), 2799–2802.
- Koch, C., Rapp, M. and Segev, I. (1996), A brief history of time (constants)., *Cerebral cortex (New York, N.Y. : 1991)* 6(2), 93–101.
- Koh, D. S., Burnashev, N. and Jonas, P. (1995), Block of native Ca(2+)-permeable AMPA receptors in rat brain by intracellular polyamines generates double rectification., *The Journal of physiology* 486 (Pt 2), 305–12.
- Korotkova, T., Fuchs, E. C., Ponomarenko, A., von Engelhardt, J. and Monyer, H. (2010), NMDA Receptor Ablation on Parvalbumin-Positive Interneurons Impairs Hippocampal Synchrony, Spatial Representations, and Working Memory, *Neuron* 68(3), 557–569.
- Krook-Magnuson, E., Armstrong, C., Oijala, M. and Soltesz, I. (2013), On-demand optogenetic control of spontaneous seizures in temporal lobe epilepsy, *Nature Communications* 4, 1376.
- Krystal, J., Karper, L., Seibyl, J., Freeman, G., Delaney, R., Bremner, D., Heninger, G., Bowers, M. and Charney, D. (1994), Subanesthetic effects of the NMDA antagonist, ketamine, in humans: psychotomimetic, perceptual, cognitive, and neuroendocrine effects., *Arch Gen Psychiatry* 51(3), 199–214.
- Kullmann, D. M. and Lamsa, K. P. (2007), Long-term synaptic plasticity in hippocampal interneurons, *Nature reviews. Neuroscience* 8(9), 687–699.
- Kwan, P., Schachter, S. C. and Brodie, M. J. (2011), Drug-resistant epilepsy, *N Engl J Med.* 365, 919–926.

- Lagae, L. (2006), Cognitive side effects of anti-epileptic drugs. The relevance in childhood epilepsy, *Seizure* 15(4), 235–241.
- Lahti, A. C., Holcomb, H. H., Medoff, D. R. and Tamminga, C. A. (1995), Ketamine activates psychosis and alters limbic blood flow in schizophrenia., *Neuroreport* 6(6), 869–872.
- Lalanne, T., Oyrer, J., Mancino, A., Gregor, E., Chung, A., Huynh, L., Burwell, S., Maheux, J., Farrant, M. and Sjöström, P. J. (2015), Synapse-specific expression of calcium-permeable AMPA receptors in neocortical layer 5, *J Physiol* 00000, 1–25.
- Lamsa, K. P., Heeroma, J. H., Somogyi, P., Rusakov, D. A. and Kullmann, D. M. (2007), Anti-Hebbian Long-Term Potentiation in the Hippocampal Feedback Inhibitory Circuit, *Science* 315(5816), 1262–1266.
- Lapray, D., Lasztóczy, B., Lagler, M., Viney, T. J., Katona, L., Valenti, O., Hartwich, K., Borhegyi, Z., Somogyi, P. and Klausberger, T. (2012), Behavior-dependent specialization of identified hippocampal interneurons., *Nature neuroscience* 15(9), 1265–1271.
- Larkman, A. U., Major, G., Stratford, K. J. and Jack, J. J. B. (1992), Dendritic morphology of pyramidal neurones of the visual cortex of the rat. IV: Electrical geometry, *The Journal of comparative neurology* 323(2), 137–152.
- Larkum, M. E. and Nevian, T. (2008), Synaptic clustering by dendritic signalling mechanisms, *Current Opinion in Neurobiology* 18(3), 321–331.
- Larkum, M. E., Zhu, J. J. and Sakmann, B. (1999), A new cellular mechanism for coupling inputs arriving at different cortical layers, *Nature* 398(6725), 338–341.
- Lavzin, M., Rapoport, S., Polsky, A., Garion, L. and Schiller, J. (2012), Nonlinear dendritic processing determines angular tuning of barrel cortex neurons in vivo, *Nature* 490(7420), 397–401.
- Le Roux, N., Cabezas, C., Böhm, U. L. and Poncer, J. C. (2013), Input-specific learning rules at excitatory synapses onto hippocampal parvalbumin-expressing interneurons., *The Journal of physiology* 591(Pt 7), 1809–1822.
- Lee, S. H., Marchionni, I., Bezaire, M., Varga, C., Danielson, N., Lovett-Barron, M., Losonczy, A. and Soltesz, I. (2014), Parvalbumin-positive basket cells differentiate among hippocampal pyramidal cells, *Neuron* 82(5), 1129–1144.

- Leutgeb, J. K., Leutgeb, S., Moser, M.-B. and Moser, E. I. (2007), Pattern Separation in the Dentate Gyrus and CA3 of the Hippocampus, *Science* 315(5814), 961–966.
- Lewis, D. a., Hashimoto, T. and Volk, D. W. (2005), Cortical inhibitory neurons and schizophrenia., *Nature reviews. Neuroscience* 6(4), 312–324.
- Liu, G. (2004), Local structural balance and functional interaction of excitatory and inhibitory synapses in hippocampal dendrites, *Nature Neuroscience* 7(4), 373–379.
- Liu, S. J. and Savtchouk, I. (2012), Ca(2+) permeable AMPA receptors switch allegiances: mechanisms and consequences., *The Journal of physiology* 590(Pt 1), 13–20.
- Llinás, R., Nicholson, C., Freeman, J. A. and Hillman, D. E. (1968), Dendritic spikes and their inhibition in alligator Purkinje cells., *Science (New York, N.Y.)* 160(3832), 1132–5.
- London, M., Segev, I., Magee, J. C. and Cook, E. P. (2001), Synaptic Scaling in vivo and in vitro, *Nature Neuroscience* 4(9), 853–855.
- Loscher, W. (2011), Critical review of current animal models of seizures and epilepsy used in the discovery and development of new antiepileptic drugs, *Seizure* 20(5), 359–368.
- Losonczy, A. and Magee, J. C. (2006), Integrative properties of radial oblique dendrites in hippocampal CA1 pyramidal neurons., *Neuron* 50(2), 291–307.
- Ludwig, M. and Pittman, Q. J. (2003), Talking back: Dendritic neurotransmitter release, *Trends in Neurosciences* 26(5), 255–261.
- Lumley, T., Diehr, P., Emerson, S. and Chen, L. (2002), The Importance of the Normality Assumption in Large Public Health Data Sets, *Annual Reviews of Public Health* 23, 151–169.
- Magee, J. C. (1998), Dendritic hyperpolarization-activated currents modify the integrative properties of hippocampal CA1 pyramidal neurons., *The Journal of neuroscience : the official journal of the Society for Neuroscience* 18(19), 7613–24.
- Magee, J. C. and Cook, E. P. (2000), Somatic EPSP amplitude is independent of synapse location in hippocampal pyramidal neurons., *Nature neuroscience* 3(9), 895–903.

- Makino, H. and Malinow, R. (2011), Compartmentalized versus global synaptic plasticity on dendrites controlled by experience, *Neuron* 72(6), 1001–1011.
- Manita, S., Miyakawa, H., Kitamura, K. and Murayama, M. (2017), Dendritic Spikes in Sensory Perception, *Frontiers in Cellular Neuroscience* 11(February), 1–7.
- Markram, H. and Sakmann, B. (1994), Calcium transients in dendrites of neocortical neurons evoked by single subthreshold excitatory postsynaptic potentials via low-voltage-activated calcium channels, *Proceedings of the National Academy of Sciences of the United States of America* 91(11), 5207–11.
- Marshall, L., Henze, D. a., Hirase, H., Leinekugel, X., Dragoi, G. and Buzsáki, G. (2002), Hippocampal pyramidal cell-interneuron spike transmission is frequency dependent and responsible for place modulation of interneuron discharge., *The Journal of neuroscience : the official journal of the Society for Neuroscience* 22(2), RC197.
- Matsuzaki, M., Ellis-Davies, G. C., Nemoto, T., Miyashita, Y., Iino, M. and Kasai, H. (2001), Dendritic spine geometry is critical for AMPA receptor expression in hippocampal CA1 pyramidal neurons., *Nature neuroscience* 4(11), 1086–92.
- Maurer, A. P., Cowen, S. L., Burke, S. N., Barnes, C. A. and McNaughton, B. L. (2006), Phase Precession in Hippocampal Interneurons Showing Strong Functional Coupling to Individual Pyramidal Cells.
- McBride, T. J., Rodriguez-Contreras, A., Trinh, A., Bailey, R. and DeBello, W. M. (2008), Learning Drives Differential Clustering of Axodendritic Contacts in the Barn Owl Auditory System, *Journal of Neuroscience* 28(27), 6960–6973.
- McCulloch, W. S. and Pitts, W. (1943), A Logical Calculus of the Idea Immanent in Nervous Activity, *Bulletin of Mathematical Biophysics* 5, 115–133.
- Muller, C. and Remy, S. (2014), Dendritic inhibition mediated by O-LM and bistratified interneurons in the hippocampus, *Frontiers in Synaptic Neuroscience* 6(SEP), 1–15.
- Niculescu-Mizil, A. and Caruana, R. (2005), Predicting good probabilities with supervised learning, *Proceedings of the 22nd international conference on Machine learning - ICML '05 (1999)*, 625–632.

- Nilsen, K. E., Walker, M. C. and Cock, H. R. (2005), Characterization of the tetanus toxin model of refractory focal neocortical epilepsy in the rat, *Epilepsia* 46(2), 179–187.
- Nörenberg, A., Hu, H., Vida, I., Bartos, M. and Jonas, P. (2010), Distinct nonuniform cable properties optimize rapid and efficient activation of fast-spiking GABAergic interneurons., *Proceedings of the National Academy of Sciences of the United States of America* 107(2), 894–9.
- Nowak, L., Bregestovski, P., Ascher, P., Herbet, A. and Prochiantz, A. (1984), Magnesium gates glutamate-activated channels in mouse central neurones, *Nature* 307(5950), 462–465.
- Nyíri, G., Stephenson, F. A., Freund, T. F. and Somogyi, P. (2003), Large variability in synaptic N-methyl-D-aspartate receptor density on interneurons and a comparison with pyramidal-cell spines in the rat hippocampus, *Neuroscience* 119(2), 347–363.
- Ovchinnikov, A., Lüttjohann, A., Hramov, A. and Van Luijtelaar, G. (2010), An algorithm for real-time detection of spike-wave discharges in rodents, *Journal of Neuroscience Methods* 194(1), 172–178.
- Pachernegg, S., Strutz-Seebohm, N. and Hollmann, M. (2012), GluN3 subunit-containing NMDA receptors: not just one-trick ponies., *Trends in neurosciences* 35(4), 240–249.
- Pape, H. C. (1996), Queer current and pacemaker: the hyperpolarization-activated cation current in neurons, *Annual review of physiology* .
- Pavlov, I., Kaila, K., Kullmann, D. M. and Miles, R. (2013), Cortical inhibition, pH and cell excitability in epilepsy: what are optimal targets for antiepileptic interventions?, *The Journal of physiology* 591(Pt 4), 765–774.
- Pavlov, I., Scimemi, A., Savtchenko, L., Kullmann, D. M. and Walker, M. C. (2011), Ih-mediated depolarization enhances the temporal precision of neuronal integration, *Nature Communications* 2, 199.
- Pernia-Andrade, A. J. and Jonas, P. (2014), Theta-Gamma-Modulated Synaptic Currents in Hippocampal Granule Cells InVivo Define a Mechanism for Network Oscillations, *Neuron* 81(1), 140–152.

- Perry, T., Buchanan, J., Kish, S. and Hansen, S. (1979), Gamma-aminobutyric-acid deficiency in brain of schizophrenic patients, *The Lancet* 313(8110), 237–239.
- Peters, A., Paley, S. L. and de Webster, H. F. (1976), *The fine structure of the nervous system: The neurons and supporting cells*.
- Pietersen, A. N. J., Ward, P. D., Hagger-Vaughan, N., Wiggins, J., Jefferys, J. G. R. and Vreugdenhil, M. (2014), Transition between fast and slow gamma modes in rat hippocampus area CA1 in vitro is modulated by slow CA3 gamma oscillations., *The Journal of physiology* 592(Pt 4), 605–620.
- Platt, J. (1999), Probabilistic outputs for support vector machines and comparisons to regularized likelihood methods, *Advances in large margin classifiers* 10(3), 61–74.
- Poirazi, P. and Mel, B. W. (2001), Impact of active dendrites and structural plasticity on the memory capacity of neural tissue, *Neuron* 29(3), 779–796.
- Polepalli, J. S., Wu, H., Goswami, D., Halpern, C. H., Südhof, T. C. and Malenka, R. C. (2017), Modulation of excitation on parvalbumin interneurons by neuroligin-3 regulates the hippocampal network, *Nature Neuroscience* 20(2), 219–229.
- Polkey, C. E. (2009), Complications of Epilepsy Surgery, *The Treatment of Epilepsy: Third Edition* pp. 993–1005.
- Postlethwaite, M., Hennig, M. H., Steinert, J. R., Graham, B. P. and Forsythe, I. D. (2007), Acceleration of AMPA receptor kinetics underlies temperature-dependent changes in synaptic strength at the rat calyx of Held., *The Journal of physiology* 579(Pt 1), 69–84.
- Pouille, F., Marin-Burgin, A., Adesnik, H., Atallah, B. V. and Scanziani, M. (2009), Input normalization by global feedforward inhibition expands cortical dynamic range, *Nature Neuroscience* 12(12), 1577–1585.
- Pouille, F. and Scanziani, M. (2001), Enforcement of temporal fidelity in pyramidal cells by somatic feed-forward inhibition., *Science (New York, N.Y.)* 293(5532), 1159–63.
- Pouille, F. and Scanziani, M. (2004), Routing of spike series by dynamic circuits in the hippocampus., *Nature* 429(6993), 717–723.
- Rall, W. (1964), Theoretical significance of dendritic trees for neuronal input-output relations., in ‘Reiss RF, editor. Neural theory and modeling. Palo Alto, CA: Stanford University Press.’, pp. 73–97.

- Roth, A. and van Rossum, M. C. W. (2009), Modeling Synapses, *Computational Modeling Methods for Neuroscientists* 06, 139–160.
- Royer, S., Zemelman, B. V., Losonczy, A., Kim, J., Chance, F., Magee, J. C. and Buzsáki, G. (2012), Control of timing, rate and bursts of hippocampal place cells by dendritic and somatic inhibition., *Nature neuroscience* 15(5), 769–775.
- Rudy, B. and McBain, C. J. (2001), Kv3 channels: voltage-gated K⁺ channels designed for high-frequency repetitive firing., *Trends in neurosciences* 24(9), 517–526.
- Scharfman, H. E. (2007), The neurobiology of epilepsy, *Current Neurology and Neuroscience Reports* 7(4), 348–354.
- Schiller, J. and Schiller, Y. (2001), NMDA receptor-mediated dendritic spikes and coincident signal amplification, *Current Opinion in Neurobiology* 11(3), 343–348.
- Schwindt, P. C. and Crill, W. E. (1995), Amplification of synaptic current by persistent sodium conductance in apical dendrite of neocortical neurons, *J Neurophysiol* 74(5), 2220–2224.
- Sciamanna, G. and Wilson, C. J. (2011), The ionic mechanism of gamma resonance in rat striatal fast-spiking neurons., *Journal of neurophysiology* 106(6), 2936–2949.
- Sik, A., Penttonen, M., Ylinen, A. and Buzsáki, G. (1995), Hippocampal CA1 interneurons: an in vivo intracellular labeling study, *The Journal of neuroscience : the official journal of the Society for Neuroscience* 15(10), 6651–6665.
- Sik, A., Tamamaki, N. and Freund, T. F. (1993), Complete Axon Arborization of a Single CA3 Pyramidal Cell in the Rat Hippocampus, and its Relationship With Postsynaptic Parvalbumin-containing Interneurons, *European Journal of Neuroscience* 5(12), 1719–1728.
- Smith, S. L., Smith, I. T., Branco, T. and Häusser, M. (2013), Dendritic spikes enhance stimulus selectivity in cortical neurons in vivo., *Nature* .
- Soto, D., Coombs, I. D., Gratacòs-Batlle, E., Farrant, M. and Cull-Candy, S. G. (2014), Molecular mechanisms contributing to TARP regulation of channel conductance and polyamine block of calcium-permeable AMPA receptors., *The Journal of neuroscience : the official journal of the Society for Neuroscience* 34(35), 11673–11683.

- Soto, D., Coombs, I. D., Kelly, L., Farrant, M. and Cull-Candy, S. G. (2007), Stargazin attenuates intracellular polyamine block of calcium-permeable AMPA receptors., *Nature neuroscience* 10(10), 1260–7.
- Spruston, N. and Johnston, D. (1992), Perforated patch-clamp analysis of the passive membrane properties of three classes of hippocampal neurons., *Journal of neurophysiology* 67(3), 508–529.
- Staley, K. J. and Mody, I. (1992), Shunting of excitatory input to dentate gyrus granule cells by a depolarizing GABAA receptor-mediated postsynaptic conductance., *Journal of neurophysiology* 68(1), 197–212.
- Stief, F., Zuschratter, W., Hartmann, K., Schmitz, D. and Draguhn, A. (2007), Enhanced synaptic excitation-inhibition ratio in hippocampal interneurons of rats with temporal lobe epilepsy, *European Journal of Neuroscience* 25(2), 519–528.
- Stuart, G. J. and Sakmann, B. (1994), Active propagation of somatic action potentials into neocortical pyramidal cell dendrites., *Nature* 367, 69–72.
- Stuart, G. J. and Spruston, N. (2015), Dendritic integration: 60 years of progress, *Nature Neuroscience* 18(12), 1713–1721.
- Stuart, G. and Spruston, N. (1998), Determinants of voltage attenuation in neocortical pyramidal neuron dendrites., *The Journal of neuroscience : the official journal of the Society for Neuroscience* 18(10), 3501–3510.
- Stuart, G., Spruston, N. and Häusser, M. (2008), *Dendrites*, Oxford University Press.
- Swanson, G. T., Kamboj, S. K. and Cull-Candy, S. G. (1997), Single-channel properties of recombinant AMPA receptors depend on RNA editing, splice variation, and subunit composition., *The Journal of neuroscience* 17(1), 58–69.
- Szabadics, J., Varga, C., Molnár, G., Oláh, S., Barzó, P. and Tamás, G. (2006), Excitatory effect of GABAergic axo-axonic cells in cortical microcircuits., *Science (New York, N.Y.)* 311(5758), 233–5.
- Takahashi, N., Kitamura, K., Matsuo, N., Mayford, M., Kano, M., Matsuki, N. and Ikegaya, Y. (2012), Locally Synchronized Synaptic Inputs, *Science* 335(6066), 353–356.
- Traynelis, S. F., Wollmuth, L. P., McBain, C. J., Menniti, F. S., Vance, K. M., Ogden, K. K., Hansen, K. B., Yuan, H., Myers, S. J. and Dingledine, R. (2010), Glutamate

- receptor ion channels: structure, regulation, and function., *Pharmacological reviews* 62(3), 405–496.
- Tremblay, R., Lee, S. and Rudy, B. (2016), GABAergic Interneurons in the Neocortex: From Cellular Properties to Circuits, *Neuron* 91(2), 260–292.
- Trevelyan, A. J., Sussillo, D., Watson, B. O. and Yuste, R. (2006), Modular Propagation of Epileptiform Activity: Evidence for an Inhibitory Veto in Neocortex, *Journal of Neuroscience* 26(48), 12447–12455.
- Trouche, S., Perestenko, P. V., van de Ven, G. M., Bratley, C. T., McNamara, C. G., Campo-Urriza, N., Black, S. L., Reijmers, L. G. and Dupret, D. (2016), Recoding a cocaine-place memory engram to a neutral engram in the hippocampus, *Nature Neuroscience* 19(4), 564–567.
- Tsodyks, M., Skaggs, W. E., Sejnowski, T. J. and McNaughton, B. L. (1997), Paradoxical effects of inhibitory interneurons, *The Journal of Neuroscience* 17(11), 4382–4388.
- Turrigiano, G. G. (1999), Homeostatic plasticity in neuronal networks: The more things change, the more they stay the same, *Trends in Neurosciences* 22(5), 221–227.
- Tzallas, A. T., Tsipouras, M. G., Tsalikakis, D. G., Karvounis, E. C., Astrakas, L., Konitsiotis, S. and Tzaphlidou, M. (2012), Automated Epileptic Seizure Detection Methods : A Review Study, *Epilepsy - Histological, Electroencephalographic and Psychological Aspects* pp. 75–87.
- Vaidya, S. P. and Johnston, D. (2013), Temporal synchrony and gamma-to-theta power conversion in the dendrites of CA1 pyramidal neurons., *Nature neuroscience* 16(12), 1812–1820.
- Varga, Z., Jia, H., Sakmann, B. and Konnerth, A. (2011), Dendritic coding of multiple sensory inputs in single cortical neurons in vivo., *Proceedings of the National Academy of Sciences of the United States of America* 108(37), 15420–5.
- Vyklicky, V., Korinek, M., Smejkalova, T., Balik, A., Krausova, B., Kaniakova, M., Lichnerova, K., Cerny, J., Krusek, J., Dittert, I., Horak, M. and Vyklicky, L. (2014), Structure, function, and pharmacology of NMDA receptor channels., *Physiological research / Academia Scientiarum Bohemoslovaca* 63 Suppl 1, S191–203.

- Wang, X. J. and Buzsáki, G. (1996), Gamma oscillation by synaptic inhibition in a hippocampal interneuronal network model., *The Journal of neuroscience* 16(20), 6402–6413.
- Williams, S. R. (2004), Spatial compartmentalization and functional impact of conductance in pyramidal neurons, *Nature Neuroscience* 7(9), 961–967.
- Williams, S. R. and Mitchell, S. J. (2008), Direct measurement of somatic voltage clamp errors in central neurons., *Nature neuroscience* 11(7), 790–798.
- Williams, S. R. and Stuart, G. J. (2002), Dependence of EPSP efficacy on synapse location in neocortical pyramidal neurons., *Science (New York, N.Y.)* 295(5561), 1907–10.
- Williams, S. R. and Stuart, G. J. (2003), Voltage- and site-dependent control of the somatic impact of dendritic IPSPs., *The Journal of neuroscience : the official journal of the Society for Neuroscience* 23(19), 7358–7367.
- Wilson, D. E., Whitney, D. E., Scholl, B. and Fitzpatrick, D. (2016), Orientation selectivity and the functional clustering of synaptic inputs in primary visual cortex., *Nature neuroscience* 19(8), 1003–9.
- Wilson, M. A. and McNaughton, B. L. (1993), Dynamics of the hippocampal ensemble code for space, *Science* 261(5124), 1055–1058.
- Wykes, R. C., Heeroma, J. H., Mantoan, L., Zheng, K., MacDonald, D. C., Deisseroth, K., Hashemi, K. S., Walker, M. C., Schorge, S. and Kullmann, D. M. (2012), Optogenetic and Potassium Channel Gene Therapy in a Rodent Model of Focal Neocortical Epilepsy, *Science Translational Medicine* 4(161), 161ra152–161ra152.
- Yang, W. and Yuste, R. (2017), In vivo imaging of neural activity, *Nature Methods* 14(4), 349–359.
- Yuste, R. (2011), Dendritic spines and distributed circuits, *Neuron* 71(5), 772–781.
- Zemankovics, R., Veres, J. M., Oren, I. and Hájos, N. (2013), Feedforward inhibition underlies the propagation of cholinergically induced gamma oscillations from hippocampal CA3 to CA1., *The Journal of neuroscience : the official journal of the Society for Neuroscience* 33(30), 12337–12351.
- Zhang, Z. J. and Reynolds, G. P. (2002), A selective decrease in the relative density of parvalbumin-immunoreactive neurons in the hippocampus in schizophrenia, *Schizophrenia Research* 55(1-2), 1–10.